EXCITATION AND ANALYSIS OF CHARACTERISTIC MODES ON COMPLEX ANTENNA STRUCTURES

Dissertation

Presented in Partial Fulfillment of the Requirements for The Degree
Doctor of Philosophy in the Graduate School of The Ohio State University

By

Brandan Thomas Strojny, M.S., B.S.

Graduate Program in Electrical and Computer Engineering

The Ohio State University

2011

Dissertation Committee

Professor Roberto G. Rojas, Adviser

Professor Fernando L. Teixeira

Professor Robert J. Garbacz

Abstract

Unmanned aerial vehicles (UAVs) have become increasingly popular for scientific research, remote sensing, transportation of goods, search and rescue as well as military applications. UAVs have several key advantages over piloted aircrafts including low cost and the ability to penetrate unattainable areas that would be classified as unsafe. Technological advances and miniaturization allow communication devices to be placed on small UAVs. To improve aerodynamics it is thus necessary to design antennas conformal to host structure of UAVs. However, at VHF/UHF the UAVs often become electrically small, making it challenging to design wideband communication antennas.

In this research, the theory of characteristic modes (CMs) is used for the analysis and design of complex conformal antennas. Traditionally, CM theory is used as an analysis tool. However, research efforts in this dissertation are focused on expanding characteristic mode theory for the design of antennas. First, two systematic simplification procedures are developed which reduce the number of characteristic modes considered for complex antenna structures. This lays the foundation for simplifying the analysis of complex antenna structures allowing the designer to focus on a small subset of critical modes. Later, thorough analysis of the input admittance of CMs is conducted. It is shown that if a mode contributes to the conductance, it ultimately contributes to the radiated pattern. For higher order modes this is typically undesirable. Thus, it will be shown how to suppress the effects of higher order modes by proper feed placement. By suppressing a higher order mode's admittance, the bandwidth of an antenna can be increased.

Using the simplification procedures, an investigation of electrically small square and rectangular ground planes is conducted. The analysis identified four important modes and allowed thorough analysis of the eigen properties of each mode. Results showed that antenna elements with electrically small ground planes should be fed like a dipole. Dipole excitation resulted in extended pattern bandwidth, relative to monopole excitation. Furthermore, the Q_{min} feed location was identified, by suppressing the first resonant higher order mode. Q_{min} feed location results in largest pattern bandwidth, for antennas considered. Rectangular ground plane effects were also investigated when the antenna element is offset on the ground plane. Design tradeoffs and practical limitations are discussed.

Finally, a 5-turn bifilar helix GPS antenna which fits inside the tail of the Dakota UAV covering L1-L5 GPS bands was designed and verified experimentally. The antenna uses a linearly varying pitch to enhance the bandwidth and was fabricated using a novel mesoplasma direct write technology. Furthermore, based on cumulative knowledge obtained from CM analysis of simplified electrically small structures, a wideband VHF/UHF antenna conformal to the vertical tail and fuselage of the Dakota UAV was designed. Utilization of the fuselage increases the occupied volume, lowering the Q. CM analysis shows that to extend the pattern bandwidth the antenna must be fed like a dipole.

Acknowledgement

I owe many thanks for the help and guidance throughout my graduate career. First and foremost I would like to thank my wife for all her love and support to keep me focused throughout my college years. Without her this would not have been possible. I would like to thank my advisor Prof. Rojas for his guidance. I have many friends and colleagues at the ElectroScience Lab to thank, especially Brian Raines, Justin Kasemodel, Mustafa Kuloglu, Ugur Olgun, and Nathaniel Smith. Numerous discussions have occurred increasing the quality of my research. Finally, I would like to thank my sponsors Dan Jennings at AFRL and Mesoscribe Technologies for supporting this research.

Vita

March 24, 1984……………………………………..	Born – Marinette, Wisconsin
May 2004………………………………………..	Associate of Applied Science in Electrical Engineering Technology, Fox Valley Technical College, Appleton, WI
May 2006………………………………………..	Bachelor in Science in Electrical Engineering Technology, Milwaukee School of Engineering, Milwaukee, WI
June 2010………………………………………..	Master in Science in Electrical Engineering, The Ohio State University, Columbus, OH

Publications

Journal

1. B.T. Strojny; R.G. Rojas, "Investigation of Ground Plane Effects Using the Theory of Characteristic Modes," *IEEE Transactions on Antennas and Propagation, 2011 [Under Review]*
2. N.K. Nahar, B.D. Raines, R.G. Rojas, and B.T. Strojny, "Wideband Antenna Array Beam Steering with Free-Space Optical True-Time Delay Engine" IET Microwaves, Antennas and Propagation, 2011
3. K.A. Obeidat, B.D. Raines, R.G. Rojas, and B.T. Strojny, "Design of Frequency Reconfigurable Antennas Using the Theory of Network Characteristic Modes," *IEEE Transactions on Antennas and Propagation*, vol. 58, no. 10, pp. 3106-3113, 2010

Conferences

1. B.D. Raines, B. T. Strojny and R. G. Rojas, "Systematic Characteristic Mode Aided Feed Design," *USNC/URSI/NRSM National Radio Science Meeting*, 2011
2. B. T. Strojny and R. G. Rojas, "Asymmetrical Low Frequency Conformal Antennas for Small Unmanned Aerial Vehicles: Dipole and Monopole Tradeoffs," in *Proc. Antennas Applications Symposium*, Allerton, IL, Sept. 2010
3. B. T. Strojny and R. G. Rojas, "Characteristic mode analysis of electrically large conformal bifilar helical antenna," *Proc. 4th European Conference on Antennas and Propagation*, pp. 1-5, 2010

4. B. T. Strojny and R. G. Rojas, "Volume integrated conformal UAV antennas," *USNC/URSI/NRSM National Radio Science Meeting*, 2010
5. N.K. Nahar, B.D. Raines, B. T. Strojny and R. G. Rojas, " A Practical Approach to Beam Steering with White Cell True-Time Delay Engine," *USNC/URSI/NRSM National Radio Science Meeting*, 2009
6. B. T. Strojny and R. G. Rojas, "Integration of conformal GPS and VHF/UHF communication antennas for small UAV applications," *Proc. 3rd European Conference on Antennas and Propagation,* pp. 2488-2492, 2009

Fields of Study

Major Field: Electrical Engineering

Studies in:

Applied Electromagnetics

Antenna Design

Material Characterization

Table of Contents

List of Tables

List of Figures

Chapter 1 Introduction

1.1 Motivation, Challenges and Objective

Unmanned aerial vehicles (UAVs) have become increasingly popular for scientific research, remote sensing, transportation of goods, search and rescue as well as military applications. UAVs have several key advantages over piloted aircrafts including low cost and the ability to penetrate areas that would be classified as unsafe. Technological advances and miniaturization allow communication devices to be placed on small UAVs. An unmanned aircraft system (UAS) is a complex system that includes the ground station, communication links and the UAV. To integrate the UAV into the UAS, it must have at a minimum GPS and VHF/UHF communication antennas. The GPS antenna is used to control the UAV over its programmed flight, while the VHF/UHF communication antenna provides a two-way link with personnel on the ground to relay information. VHF/UHF antennas can also be used for various sensing and tracking applications.

One of the challenges for communication, sensing and other applications is the limited area available on the fuselage, wings and tail section of the UAV for the installation of antennas, especially at VHF. At VHF the UAV may become electrically small implying electrically small antennas (ESAs). ESAs have many design challenges including large impedance mismatch losses and narrowband operation (high stored energy) [1], [2], [3]. Moreover, the vertical height of the UAV is generally limited to the tail section. In general, UAV antenna systems commonly require vertically polarized, omnidirectional radiation pattern, and large bandwidth covering VHF/UHF bands. Furthermore, when the UAV becomes electrically small the entire structure can become the radiating element, increasing cross-polarization levels.

In order to overcome the many challenges of designing conformal antennas for UAVs the theory of characteristic modes (CM) is used to give physical insight into the natural behavior of complex structures. CM theory has several properties which make it a useful tool for the analysis and design of antennas. The first properly is the orthogonality of the eigencurrents as well as the orthogonality of the eigenpatterns. The latter being true for lossless media. Second, the modes are excitation independent (eigenmodes), meaning they are natural modes dependent on the geometry and material properties. This allows the designer to analyze the modes and subsequently design a feeding network to excite the desired modes while suppressing the undesired modes based on design criteria. CMs can to be applied to a wide range of complex problems including radiation and scattering problems [4], [5], [6], [7], pattern synthesis [8], [9], antenna shape synthesis [10], and MIMO applications [11], [12]. Most recently Rojas et al. has used CM analysis for non-foster loading [13], reconfigurable antenna and multiband applications [14], to explain parallel and series resonance of input impedance in terms of CM excitation [15].

Traditionally, CM theory has been applied to electrically small to intermediate size antennas for simplicity. Furthermore, CM theory has been mainly used as an analysis tool. In this dissertation complex antennas including conformal UAV antennas, antennas modeled with plates and electrically large antennas ($d > 3\lambda$) will be analyzed. There are many challenges when using CM theory for the design of complex antennas, including a large generalized Z-matrix. Additionally, conformal UAV antennas often have electrically small asymmetric geometries that are modeled with plates in this dissertation. The number of CMs depends on the size of the Z-matrix. When modeling electrically large structures, the size of the Z-matrix becomes large resulting in an increased number of CMs to analyze. Therefore, a systematic approach for reducing the number of CMs is developed.

Another challenge when using CM theory as a design tool is determining how to excite or suppress CMs using a feeding network. As such, port placement is thoroughly emphasized throughout this dissertation. Design methods via proper port placement are shown for determining the location for the minimum quality factor (Q_{min}), extending pattern bandwidth and cross-polarization reduction. Analysis using the modal admittance and weighting coefficient is thoroughly used to show the excitation and suppression of modes. It will be shown that modes which contribute to the conductance radiate energy, whereas modes that mainly contribute to the susceptance store energy.

The methods developed in this dissertation allow CM theory to be applied to complex antennas, including conformal UAV antennas. A complex antenna structure is one in which there is no analytical solution. Often, for these antennas the designer resorts to running simulation and optimization routines to find an adequate design. This typically results in a satisfactory design, but little insight is gained about the fundamental problem. By simplifying CM analysis and developing systematic methods to conduct an analysis CM theory can be used for complex design problems.

The key contributions of this dissertation are:

- Development of a systematic procedure for reducing the number of CMs considered for complex antenna structures. This lays the foundation for simplifying the analysis of complex antenna structures.
- Thorough analysis of the input admittance of CMs. It will be shown that if a mode contributes to the conductance, it ultimately contributes to the radiated pattern. For higher order modes this is typically undesirable. Thus, it will be shown how to suppress the effects of higher order modes by proper feed placement. By suppressing a higher order mode’s admittance, the bandwidth of an antenna can be increased.

- Investigation of electrically small ground plane effects on feed location using the theory of CMs. This analysis shows that when a designer has an electrically small ground plane the antenna should be fed like a dipole. Q_{min} feed location for electrically small square and rectangular ground planes to maximize bandwidth was found. Design tradeoffs for an offset antenna element are shown.
- Design and measurement of a 5-turn bifilar helix GPS antenna which fits inside the tail of the Dakota UAV covering all GPS L-bands. The antenna uses a linearly varying pitch to enhance the bandwidth and was fabricated using a novel mesoplasma direct write technology [16].
- CM theory was used to design a VHF/UHF antenna conformal to the tail and fuselage of Dakota UAV.

This dissertation is organized as follows:

Chapter 2 starts with a brief introduction to the theory of CMs. The total current and pattern are shown to be a linear summation of weighted eigencurrents and eigenpatterns, respectively. The modal input admittance is then derived. Modal admittance is a very important parameter since it gives insight into the modes contribution to the radiated and stored energy. If a CMs conductance matches the total conductance, then the shape of the radiated pattern will be that of the mode. The impedance of a mode can also be investigated, however, when using CMs where the currents are expanded in terms of modes, the contributions from each mode's impedance add in parallel instead of series.

Chapter 3 introduces a systematic procedure for identifying important modes depending on the application and design criteria. Common design criteria are polarization, gain levels, pattern or bandwidth. As such, in this dissertation a vertically polarized omnidirectional radiation pattern will be the criteria when designing conformal VHF/UHF UAV antenna's.

Chapter 4 is an investigation of electrically small square ground planes. The investigation determines the important CMs when the width of the ground plane is $\lambda/8$, $\lambda/16$ and $\lambda/32$ at 150 MHz. It is determined that antenna elements on electrically small ground planes should not be fed like a monopole but rather like a dipole to achieve wideband pattern performance. Note similar to the square ground plane case, an investigation on rectangular ground planes is presented Appendix B. Rectangular ground planes are the more realistic case for conformal UAV antennas since the width of the UAV is severely restricted.

Chapter 5 outlines a method to determine the Q_{min} feed location for electrically small square and rectangular ground planes. It is determined that the first undesired higher order mode (CM 2) is the mode which dictates the Q_{min} feed location. To minimize the excitation of CM 2 the feed is placed in the null of the eigencurrent specifically at its corresponding resonant frequency.

Chapter 6 investigates electrically small rectangular ground planes with an offset antenna element. The feeding network tradeoffs and limitations are discussed. As expected, when the antenna element is offset the eigenpatterns are no longer symmetric. Additionally, the eigencurrents have a large horizontal current component in the ground plane increasing cross-polarization. Important modes are identified and a feed location to excite or suppress the modes is analyzed. Tradeoffs between bandwidth, high frequency cutoff and tolerable cross- polarization level are discussed.

Chapter 7 introduces the concept of volume integration of a GPS and VHF/UHF antenna conformal to a Dakota UAV. The design of a 5-turn bifilar helix antenna for GPS applications is presented. The GPS is a high performance antenna covering all L-bands and fits inside the tail of the Dakota UAV. The antenna is fabricated using mesoplasma direct write technology [16] and verified experimentally. Agreement between simulation and measurements were achieved. Furthermore, a VHF/UHF antenna conformal to the vertical tail and fuselage was designed using the insight gained through rigorous CM analysis of UAV structures examined in Chapters 4-7.

Chapter 2 Background

The main components of this dissertation develop tools using the theory of CMs for the analysis and design of complex antenna structures. The tools will be used for complex problems including ESAs, determining Q_{min} feed location and the excitation/suppression of modes. A brief background on these topics is given in this chapter.

2.1 Review of the Theory of Characteristic Modes

The theory of CMs was first devised by Garbacz and Turpin [4] and later elaborated by Harrington and Mautz [5], [6]. A brief introduction to the theory of CMs is given in this dissertation. A complete derivation can be found in the references. The total current on a conducting structure can be formulated as a linear summation of eigencurrents ($\vec{J}_n$) with associated weighting coefficients (α_n)

$$\vec{J} = \sum_{n}^{N} \alpha_n \vec{J}_n. \tag{2.1}$$

Eigencurrents or modal currents are natural currents that are geometry/material dependent and independent of excitation. They give insight into an antenna's natural characteristics, including total current, pattern, radiation efficiency and input admittance/impedance. The current weighting coefficients are complex coefficients that account for the excitation in the modal solution (2.1) and are given by

$$\alpha_n = \frac{\langle \vec{J}_n, \vec{E}^i \rangle}{1 + j\lambda_n} = \frac{V_n^i}{1 + j\lambda_n} \tag{2.2}$$

where ($\mathrm{V}_{\mathrm{n}}^{\mathrm{i}}$) is the modal excitation coefficient and physically represents whether the mode is excited by the feeding network; whereas, λ_n is the eigenvalue corresponding to the current mode. Note $\vec{E}^i$ is the excitation voltage vector defined. Substitution of (2.2) into (2.1) yields the modal solution for the total current given by

$$\vec{J} = \sum_{n}^{N} \frac{V_n^i}{1 + j\lambda_n} \vec{J}_n. \tag{2.3}$$

Eigenvalues in classical CM theory represent the modal stored reactive power relative to the dissipated power and proportional to the quality factor (Q) of the mode. Modes with extremely high Q have poor radiation efficiencies, since they are almost purely reactive. The smaller the eigenvalue the better the mode potentially radiates. Equation (2.3) illustrates the inverse relationship between the eigenvalue and the corresponding modal weighting coefficient. Modes with corresponding large eigenvalues (i.e. large Q) have a minimal contribution to the total current distribution.

Similarly a desired field can be expanded in terms of its weighted modal fields

$$\vec{E} = \sum_{n}^{N} \alpha_n \vec{E}_n \tag{2.4}$$

where $\vec{E}_n$ is the modal field radiated by the modal current $\vec{J}_n$. Reacting the total field with modal fields $\vec{E}_m$

$$\langle \vec{E}_m, \vec{E} \rangle = \langle \vec{E}_m, \sum_{n}^{N} \alpha_n \vec{E}_n \rangle \tag{2.5}$$

$$= \sum_{n}^{N} \alpha_n \langle \vec{E}_m, \vec{E}_n \rangle. \tag{2.6}$$

Due to orthogonality properties (i.e. $\langle \vec{E}_m, \vec{E}_n \rangle = 0$ for m ≠ n for lossless antenna) in the far-field (2.5) becomes

$$\langle \vec{E}_m, \vec{E} \rangle = \alpha_m \langle \vec{E}_m, \vec{E}_m \rangle \,. \tag{2.7}$$

Thus the modal field weight becomes

$$\alpha_n = \frac{\langle \vec{E}_n, \vec{E} \rangle}{\langle \vec{E}_n, \vec{E}_n \rangle}. \tag{2.8}$$

Computation of $\alpha_n$using the eigenpatterns has pattern synthesis applications, since the field $\vec{E}$ can be set as a desired far field specified by a desired magnitude or phase. In principle, this allows one to synthesize fields of arbitrary magnitude and polarization. For example, if $\vec{E}$ was chosen as a characteristic mode field $\vec{E}_n$ (a natural mode) $\alpha_n = 1$ for that mode and zero for all other modes.

2.2 Modal Admittance

Modal input admittance/impedance is an important analysis tool in the theory of CMs and has received little research attention. It is important because antennas need to be matched to minimize admittance/impedance mismatch loss. The input admittance of CMs was first presented in [17]. Quadratic forms were derived for the self- and mutual-admittances of delta gaps in thin wire structures in terms of the characteristic currents of the structures. In [18], the modal input impedance was derived in terms of current weighting coefficients. In both cases, only one port was excited for the antenna. It has been reported that the susceptance has slow convergence. The latter paper introduces a source mode to compensate for the convergence problem. It is believed that the slow convergence occurs because a single port (probe, slot, ect.) excites several modes and cannot suppress higher order modes.

The admittance of a CM is an important parameter to study when performing a CM analysis. The admittance gives insight into whether a mode is being excited or not. The admittance is made up of the conductance and susceptance. From the conductance one can determine if the mode contributes to the radiated pattern. If a single mode’s conductance matches the total conductance of the antenna then the radiated pattern will be equal to the modal pattern. If many modes contribute to the total conductance then the radiated pattern is a weighted summation of the modal patterns. Typically the susceptance is composed of many CMs and multiple ports on the antenna can be used to suppress undesirable modes. In this section the modal admittance will be derived and several examples will be shown.

2.2.1 Input Admittance Derivation

It is desirable to study the impact of each mode's admittance towards the total admittance. The input admittance at the antenna port is derived as follows

$$Y_{in} = \frac{I_P}{V_P} = \sum_n^N Y_n = \sum_n^N G_n + jB_n = \frac{\sum_n^N \alpha_n J_{P,n} \Delta W}{V_P}. \tag{2.9}$$

where I_P and V_P are they total current and voltage, respectively, at the antenna port. Subscript (P) denotes the current sampling point at the antenna port and ΔW is the width of the input port. It is assumed that the port voltage is 1V, therefore (2.9) simplifies to

$$Y_{in} = \sum_n^N \alpha_n J_{P,n} \Delta W. \tag{2.10}$$

The current weighting coefficient can be expanded as

$$\alpha_n = \frac{V_n^i}{(1 + j\lambda_n)} = \frac{V_n^i}{1 + \lambda_n^2} - j\frac{\lambda_n V_n^i}{1 + \lambda_n^2}. \tag{2.11}$$

Substituting equation (2.11) into (2.10) results in the preferred form of the total admittance

$$Y_{in} = \sum_n^N \left(\frac{V_n^i}{1 + \lambda_n^2} - j\frac{\lambda_n V_n^i}{1 + \lambda_n^2} \right) J_{P,n} \Delta W \tag{2.12}$$

where the total conductance is

$$G_{in} = \sum_n^N \frac{V_n^i}{1 + \lambda_n^2} J_{P,n} \, \Delta W \tag{2.13}$$

and the total susceptance is

$$B_{in} = -\sum_{n}^{N} \frac{\lambda_n V_n^i}{1+\lambda_n^2} J_{P,n}\,\Delta W. \tag{2.14}$$

From the above derivation it is clear to see that at resonance (i.e. $\lambda_n = 0$) the modal input admittance is purely real. By using the admittance formulation, each mode can be decomposed and analyzed to find total contribution to total admittance. This allows the designer to optimize port location to minimize mismatch losses. Additionally, each modes contribution to the overall radiated pattern can be determined from the conductance (assuming the antenna is lossless), since the radiated power can be written as

$$P_{rad} = \frac{1}{2} Re(VJ^*) = \frac{1}{2} |V^2| Re(Y_{in}^*) = \frac{1}{2} |V^2| G_{in}. \tag{2.15}$$

For example, if a mode's conductance matches the total conductance of the antenna, the mode's eigenpattern will be the radiated pattern. Alternatively, the input impedance can be formulated as

$$Z_{in,n} = \frac{V_P}{I_P} = R + jX = \frac{V_P}{\sum_n^N \alpha_n J_{P,n} \Delta W}. \tag{2.16}$$

However, because individual modes add in parallel it is difficult to predict the total impedance from several modal impedances, unless a single mode is excited. The modal input impedance can also be written in terms of modal admittances

$$R_{in,n} = \frac{G_{in,n}}{G_{in,n}^2 + B_{in,n}^2} \tag{2.17}$$

and

$$X_{in,n} = \frac{-B_{in,n}}{G_{in,n}^2 + B_{in,n}^2}. \tag{2.18}$$

Another important property to be explored further in this dissertation is the eigenvalue of a mode. The eigenvalue is proportional to the Q of a mode and can be written as

$$\lambda_n = \frac{B_n}{G_n} \tag{2.19}$$

where λ_n is the eigenvalue of a single mode. Additionally one can define λ_T as the ratio of the total susceptance to conductance

$$\lambda_T = \frac{B}{G}. \tag{2.20}$$

Since the total admittance is the summation of modal admittances (2.20) can be rewritten as

$$\lambda_T = \frac{\sum_n^N B_n}{\sum_n^N G_n}. \tag{2.21}$$

It is important to determine the dominant modes and their impact to λ_T. By suppressing the susceptance of higher order modes, λ_T of the antenna can be reduced. Therefore, by minimizing λ_T, the total Q is minimized.

2.3 Review of Electrically Small Antenna Challenges

An electrically small antenna (ESA) is an antenna with geometrical dimensions that are much smaller than the free-space wavelength at a desired operating frequency often generalized by $ka < 0.5$, where k is the wave number ($2\pi/\lambda$) and a is the radius of the smallest mathematical sphere enclosing the antenna. The fundamental limitations of ESAs were first discussed by Wheeler [1]. Wheeler claimed that ESAs behave similar to lumped circuit elements. Wheeler proved there is a fundamental free-space coupling efficiency limit for ESAs known as "radiation power factor." He also showed ESAs have a fundamental bandwidth limitation inversely related to Q. Chu [2] and later Harrington [19] expanded the radiating fields in terms of a complete set of orthogonal spherical modes. Chu proposed enclosing the antenna in a hypothetical sphere of radius a. Because each mode is orthogonal outside the sphere there is no coupling in power or energy between modes. Chu expanded the wave impedance to form equivalent ladder networks for each mode. From the equivalent network model he calculated the Q and also gave the well known minimum Q for ESAs based on the spherical occupied volume defined as

$$Q_{lb} = \eta\left(\frac{1}{(ka)^3} + \frac{1}{ka}\right) \tag{2.1}$$

where η is the antenna efficiency. The space outside the sphere was then replaced by individual equivalent circuits representing each mode. Harrington extended this work to unidirectional antennas and developed the well known maximum gain equation with realistic Q

$$G_{max} = N^2 + 2N \tag{2.2}$$

where $N = ka$.

Chu's analysis has two shortcomings: 1) the total radiated field outside the sphere cannot be separated into radiated and reactive fields, 2) method is restricted to spherical modes. A solution to this problem was first presented by Collin and Rothschild [20] who published a more exact theory based on calculating the evanescent energy stored within the sphere enclosing the antenna. The stored energy is then subtracted from the total energy in the far-field. Collin and Rothschild extended the computation of Q to cylindrical modes. Later Fante [21], followed Collin and Rothschild's method and extended the work to general antennas when a combination of TE and TM modes are excited. Recent work has focused on accurate numerical computation of the Q. Yaghjian and Best [3] developed an accurate computation of Q by using the input impedance of the antenna. Details of this method are given in Appendix A.

2.4 Pattern Synthesis

Pattern synthesis has been studied for many years. Synthesis is the inverse problem to analysis and typically more difficult since it is often non-linear and can have more than one solution. The goal of pattern synthesis techniques is to optimize antenna shape, polarization, impedance characteristics, excitation (Port) location, Q or bandwidth. A coherent approach has not been possible since it is difficult to specify the requirements in a rigorous way. Field pattern synthesis methods are usually specified in magnitude only or both magnitude and phase. A good overview of antenna pattern synthesis is given by Mautz and Harrington [22] and by Bucci [23].

The pattern synthesis methods reviewed focus on synthesis methods which use the theory of characteristic modes. In [7], a method for obtaining a desired radar scattering pattern by reactively loading a conducting body is given. The theory uses the concept of CMs of a loaded body to resonate any desired real current by reactive loads to make it the dominant mode current of that body. If no other mode is near resonance, the radar scattering pattern becomes nearly the same as the radiation pattern of the resonated current. A pattern synthesis procedure is developed for obtaining the induced current (real or constant phase) on the antenna whose radiation field pattern is the least mean-square approximation to a desired field pattern. Since the method focuses on resonating a real (or constant phase) current, the scattered field becomes predominantly that of the resonated mode assuming the antenna is electrically small or intermediate size. This condition may not hold if the antenna becomes electrically large.

In [8], a method is given for synthesizing a desired pattern by reactively loading an N-Port scatterer. The method is based on restricting the pattern magnitude only. The real port current or voltage which gives a least square approximation to a desired radiation field magnitude is found and resonated by reactive loads. If a sufficient number of ports is chosen and the body is electrically small to intermediate size, the scattered field is approximately the same as the synthesize radiation pattern. Since the pattern is synthesized using reactive loads, the method is narrowband. In [9], generalized characteristic modes (GCM) is applied towards magnitude pattern synthesis and directivity optimization. Most recently [24] used GCM for pattern synthesis of an electrically small near vertical-incidence skywave (NVIS) antenna mounted on a vehicle.

In this dissertation, desired patterns are used to identify important modes of an antenna structure. Once a desired pattern is specified, the eigenpatterns are tested against the desired pattern to compute a pattern weighting coefficient. From the weighting coefficients the designer can determine if the structure can naturally support the desired pattern.

2.5 Electrically Large Antennas

Traditionally, CM analysis is performed on electrically small antennas (ESAs) and intermediate size antennas for simplicity [6]. ESAs have only one or two dominant CMs which contribute to the total radiated pattern. Although other modes on the antenna can be excited, they have poor radiation efficiencies and contribute mostly to the input reactance of the antenna. ESAs are also usually resonant antennas with narrow bandwidths.

The number of CMs for a structure depends on its dimensions in terms of wavelength and is directly related to the size of the Z-matrix if the Method of Moments (MoM) is used to simulate the structure. For ESAs, the Z-matrix is small, resulting in only a few CMs. A limited number of CMs make it easy to determine the dominant modes contributing to the total current. However, when the antenna is electrically large, it can have many CMs which contribute to the total current. It is therefore necessary to have guidelines for conducting a CM analysis for electrically large antennas. A practical method to reduce the number of CMs considered in the design of an antenna is discussed in Chapter 3.

Chapter 3 Identifying Important Modes

The theory of CMs is a powerful tool for the design and analysis of conformal UAV antennas. It allows the designer to analyze the natural modes on a conductive and/or dielectric structure and design a feeding network to excite the desired modes and suppress the undesirable modes. Although in this study CM design is applied only to conductive structures, the tools developed here can easily be used with structures consisting of metallic as well as dielectric materials. With conductive surfaces, the CM currents are surface currents; however, the CM currents become volumetric when dielectric materials are included.

The number of characteristic modes is determined by the size of the Z-matrix; while the size of the matrix depends on the electrical size of a structure (size in terms of wavelengths). Therefore, the size of the matrix will increase if the frequency of the EM signal increases, or when the actual physical size of the structure increases for a fix frequency, or when both, the physical size of the structure as well as the frequency become larger. However, fortunately, not all modes are important. What makes a current mode important in an antenna is its contribution to the total current, radiation pattern and input impedance. A systematic procedure for identifying the important modes for a bifilar helix was shown in [25]. The procedure for reducing the number of modes is expanded in this chapter.

The reason the Method of Moments (MoM) matrix becomes larger as the frequency increases is because the mesh size cannot exceed a certain size (usually > λ/10, where λ is the wavelength). Although the mesh size determines the number of CMs for a structure, practically only a finite number need to be analyzed. Higher order modes suffer from numerical errors which ultimately deteriorates the orthogonality between modes. Thus, if possible, only a limited number of CMs should be considered in the analysis. It is first necessary to understand what makes a mode important and when to include the mode in the analysis. Modes with low eigenvalue are potentially good radiators. When the eigenvalue of the mode is 0 dB, this means the ratio between the susceptance and conductance is equal. Thus exciting the mode would have equal contribution to the stored and radiated energy. When the eigenvalue is larger than 0 dB, the mode mainly contributes to the susceptance or stored energy of the antenna. Below 0 dB, the mode mainly contributes to the conductance, thus potentially making the mode a good radiator. Since CMs are identified without an excitation, a feeding network still needs to be designed. However, modes can be identified based on their contribution to a desired pattern. This technique will be outlined in Section 3.1. A second method which limits the analysis to only modes which resonate in the frequency range is shown in Section 3.2. The advantages and disadvantages of each method will be discussed.

3.1 Mode Identification Using a Desired Pattern

In this section a mode identification procedure is introduced. This method is basically a pattern synthesis technique, because it tells you whether the desired pattern can naturally be created based on the structure under test. Pattern synthesis is strictly being used for mode identification purposes in this dissertation and was briefly reviewed in Section 2.4. It should be emphasized that guidelines introduced in this section have been developed after extensive numerical simulation on resonant type antennas. Guidelines would not likely hold for traveling wave antennas.

The first step in the mode reduction is to only consider modes with eigenvalues less than 30 dB at a frequency where the diameter of an imaginary sphere enclosing the antenna is $\lambda/1.85$ for plate antennas and $\lambda/1.5$ for wire antennas. When the antenna occupies more volume the dominant modes are shifted lower in frequency, thus the frequency which you are identifying important modes can therefore be lowered. For resonant antennas this typically means the dominant mode has already resonated and the higher order modes are below 30 dB, thus will be included in the analysis. The modes can be tracked to lower frequencies where the eigenvalues may become larger than 30 dB. Note that, the eigenvalue is proportional to the Q of the corresponding mode.

To further reduce the number of modes considered, the desired radiation pattern and the remaining eigenpatterns are tested using (2.8) to determine the pattern weighting coefficients. The desired field $\vec{E}$ is defined by both magnitude and phase. This allows one to synthesize circular, elliptical and linear polarization patterns. If $\vec{E}$ was chosen as a CM field (a natural mode) α_n would be one for the corresponding mode and would equal zero for all other modes. The modes with the largest α_n potentially have the largest impact on the input admittance and pattern. The advantage of using a desired pattern instead of the current to compute weighting coefficients is that the method is now truly independent of a feeding network. Additionally, it is difficult to specify the desired current distribution on complex antenna structures, whereas the desired radiation pattern can be generated with a simple antenna which radiates the pattern.

Realization of the feeding network is the next step, as port locations and voltages need to be determined. By looking at the eigencurrent of the mode, port locations are chosen. To couple strongly to a given eigencurrent, the ports need to be placed at the eigencurrents' maxima. Depending on the number of port locations chosen one may be able to easily predict the needed port voltages.

3.1.1 Identifying Dominant Characteristic Modes of a Flat Plate

To illustrate the identification of important CMs on an antenna structure, a λ/2 plate at 150 MHz is considered as shown in Figure 3.1. The flat plate is a relatively simple structure and will be used to give baseline results before the antenna element is loaded with a ground plane in later chapters. The height (H) and width (P_W) of the plate are 0.5 and 0.05 m, respectively. The plate is modelled as a perfect electric conductor (PEC) with an average edge length mesh size of 0.04 m for the mesh, resulting in a Z matrix size of 80×80, therefore 80 CMs. The eigenvalue spectrum is shown in Figure 3.2 including all modes.

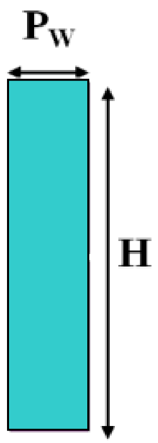

Figure 3.1: Reference antenna

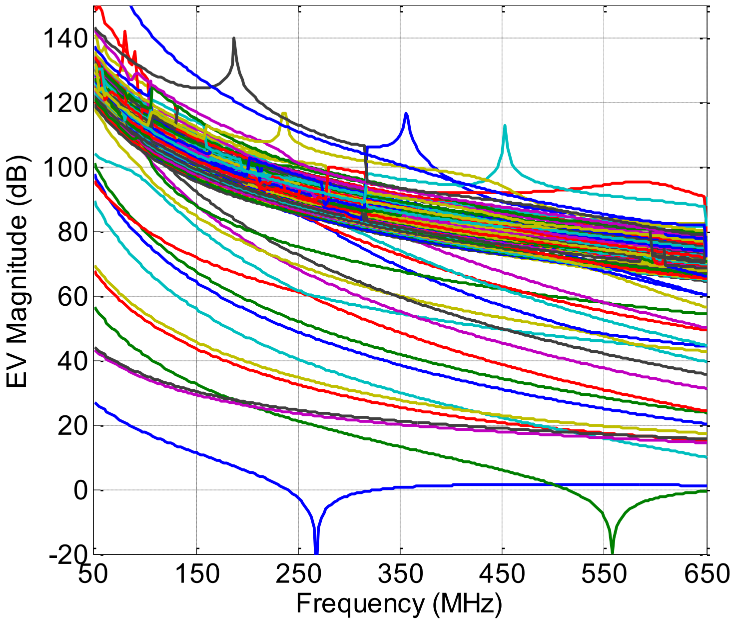

Figure 3.2: Eigenvalue spectrum of flat plate including all modes.

Since the antenna is a plate the λ/1.85 guideline will be used. The diameter of the sphere enclosing the antenna is 0.5025 m, thus the reduction frequency takes place at 355 MHz. The modes less than 30 dB at 355 MHz are listed in Table 3.1 in ascending order. In addition the eigenvalues for each mode are listed at 50 and 550 MHz. The reduced eigenvalue spectrum is shown in Figure 3.3. Note modes are numbered in ascending at reduction frequency of 355 MHz.

Table 3.1: CMs with |EV| less than 30 dB at 355 MHz

CM	50 MHz	355 MHz	550 MHz
1	27.0640	0.6605	1.4236
2	56.5046	12.8411	-8.5614
5	43.2017	19.9324	15.9705
7	44.1166	21.0284	17.0504
3	67.5092	25.1135	17.3848
6	69.5811	27.3425	19.5799
3	89.2521	29.5337	15.7658

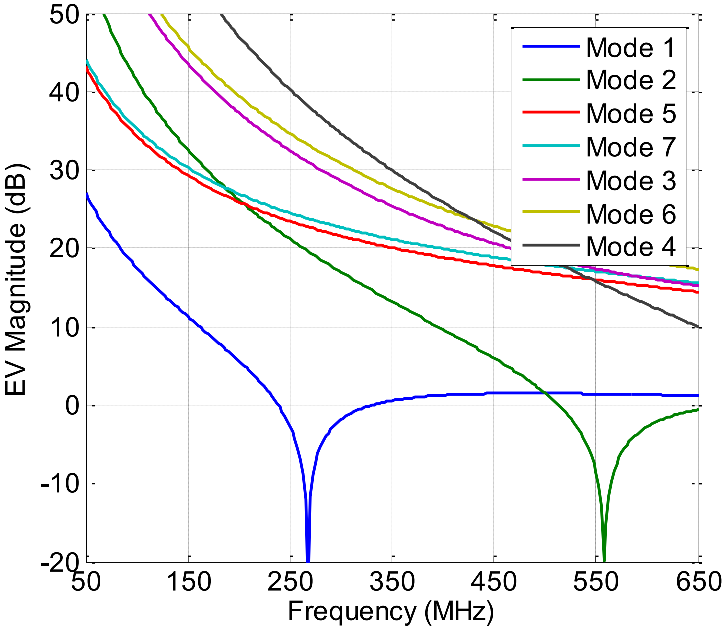

Figure 3.3: Reduced eigenvalue spectrum.

Next a desired pattern (i.e. $\vec{E}$ of (2.8)) is specified. The desired pattern for conformal UAV antenna throughout this dissertation is an omnidirectional vertically polarized pattern, thus will be used in this example. The desired pattern is shown Figure 3.4. The desired pattern is tested with the remaining CMs at 50, 355 and 550 MHz to get the weighting coefficient. Of the remaining modes only three modes have weighting coefficients above -40 dB and are listed in Table 3.2. Below -40 dB the modes contribution can be neglected. The final reduced eigenvalue spectrum after the two step procedure is shown in Figure 3.5. Thus, the reduction procedure in this section has reduced the number of modes considered from 80 down to 3 modes.

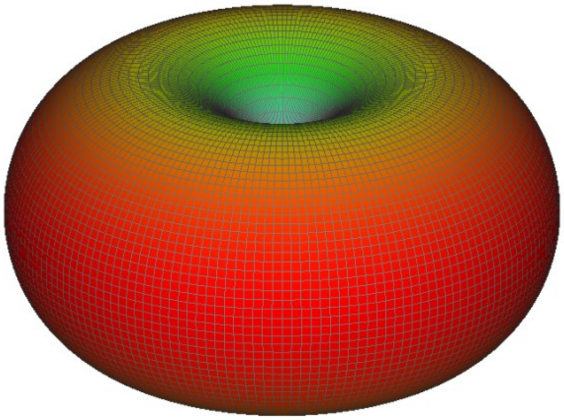

Figure 3.4: Desired vertically polarized omnidirectional radiation pattern.

Table 3.2: $|\alpha_n|$ in dB normalized to maximum at each frequency

CM	50 MHz	355 MHz	550 MHz
1	0.0	0.0	-1.53
2	-9.59	-0.72	0.0
4	-12.42	-4.35	-1.60

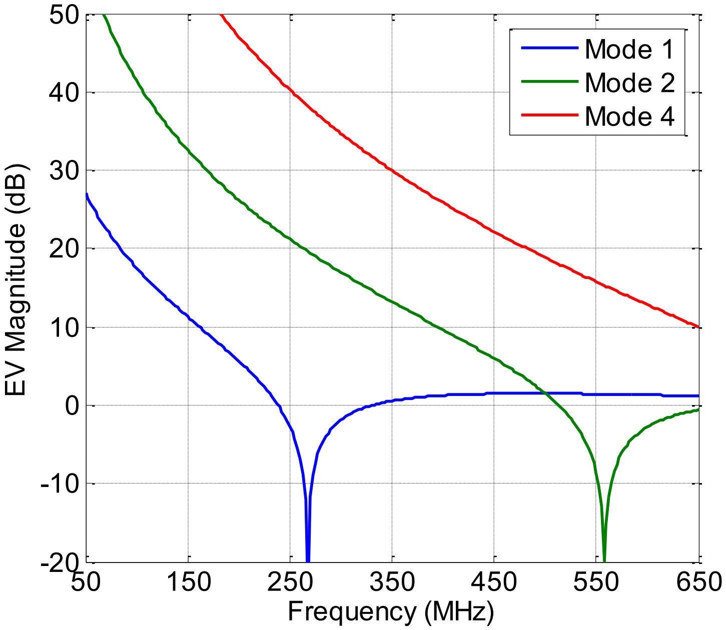

Figure 3.5: Reduced eigenvalue spectrum after testing modes with desired pattern.

3.2 Identifying Dominant Characteristic Modes via Resonance Method

Another technique to reduce the number of modes considered is a visual inspection of the eigenvalue spectrum. The goal is to identify resonant modes in the frequency range of interest. When a CM resonates it can easily be excited by a feeding network. Thus, the eigenvalue of all modes is computed and tracked vs. frequency. This reduction procedure is useful to identify modes that contribute to the radiated pattern; however it neglects the higher order modes that mostly contribute to the susceptance. In terms of feed placement this is generally adequate. In Figure 3.2 it can be seen that two modes resonate over the frequency range of interest. CM 1 resonates at 267.5 MHz and CM 2 resonates at 557.5 MHz. Thus, this reduction procedure reduces the number of modes considered from 80 to only two modes.

3.3 Summary

Two methods for identifying important modes for CM analysis have been proposed. The first method identifies modes based on a desired pattern. Weighting coefficients for the modes are computed with respect to the desired pattern. Modes with largest weighting coefficient are the most important modes. If a structure's weighting coefficients are extremely small, then the structure cannot naturally radiate the desired pattern. The advantage of this method is that, it can be used over a narrow bandwidth. The disadvantage is it includes some higher order modes. Weighting coefficients corresponding to higher order modes may result in large numerical errors.

The second identification method only analyzes modes which resonate over a desired frequency range. Near resonance modes are easily excitable. Depending on a mode's contribution to the radiated pattern it may be desirable to excite or suppress this mode. Thus the eigencurrent near resonance can be studied for feed placement. The advantage of this method is that, it very easy to identify resonant modes. However, a large frequency range may have to be computed in order to identify a sufficient number of modes. Depending on the structure this may be computationally expensive. Both methods will be used extensively throughout this dissertation.

Chapter 4 Characteristic Mode Investigation of Square Ground Plane Effects

The theory of CMs can be used in the design and analysis of antennas conformal to the structure of UAVs. For many applications, it is desirable to design conformal antennas for VHF/UHF frequency bands for UAVs; however, size constraints can severely degrade the performance. The theory of CMs will be used to analyze a representative vertically polarized antenna model conformal to the UAV. Dominant modes will be identified and feeding network considerations will be discussed. A comparison of the dominant modes' weighting coefficients, admittance and realized gain will be shown for both dipole- and monopole-type excitations. By using CMs, it will be shown that the dipole feed configuration strongly excites the desired omnidirectional modes while suppressing higher order modes.

With limited vertical height and fuselage width, it is necessary to understand the design tradeoffs and limitations of low frequency antennas conformal to a UAV structure. Derivatives of dipole and monopole antennas are commonly used for VHF/UHF communication. Typically, monopole antennas are preferred over dipoles due to their lower operating frequency for a fixed height [26]. However, a monopole antenna requires a ground plane whose radius should be larger than λ/4 at the operating frequency. The fuselage of the UAV can be used for this purpose but is limited by the width, resulting in a rectangular ground plane. Finite ground plane effects on pattern and input impedance have been studied in [27],[28],[29],[30],[31]. Small UAVs have very limited area to create a ground plane, so the question becomes whether it is better to create a monopole with an electrically small ground plane or use the available height to create a dipole.

To emphasize the need to investigate ground plane effects, a simplified version of the Dakota UAV is shown in Figure 4.1.The three regions of the UAV are labeled as the tail (I), top section of fuselage that would be utilized as a ground plane (II) and fuselage itself (III). Electrical dimensions are listed in Table 4.1 at 50 and 150 MHz, respectively. Note that W1 of the top section of the fuselage is electrically small at both 50 and 150 MHz. Therefore, the width of the ground plane would be electrically small.

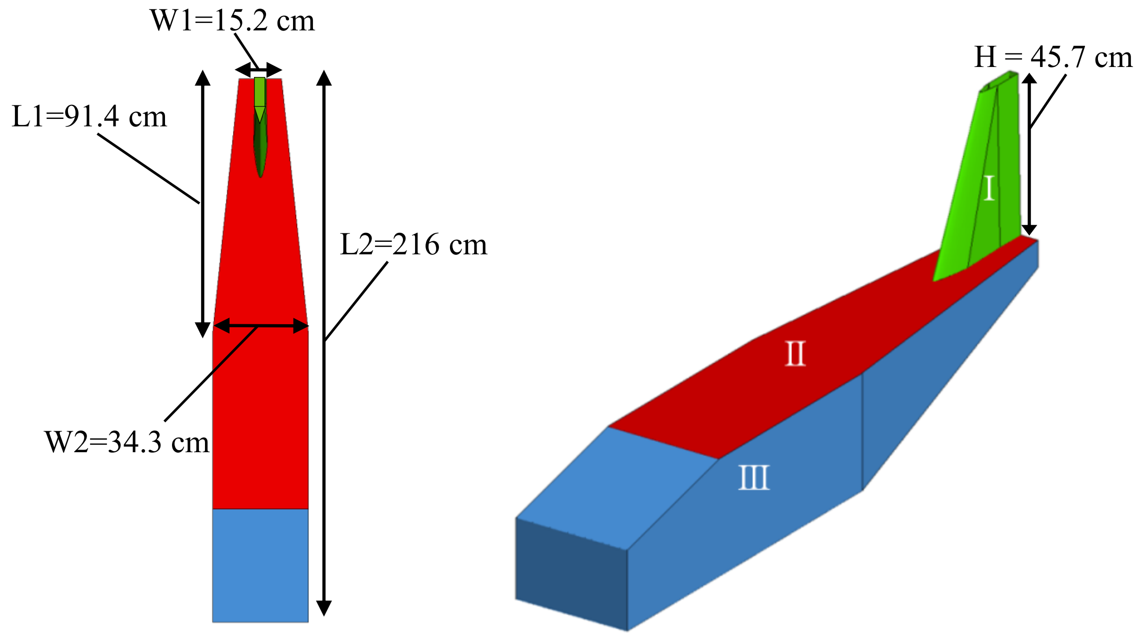

(a) (b)

Figure 4.1: Simplified Dakota UAV: (a) top view, (b) perspective view.

Table 4.1: Dakota UAV electrical dimensions at 50 and 150 MHz

	50 MHz	150 MHz
W1	λ/39.4	λ/13.2
W2	λ/17.5	λ/5.8
L1	λ/6.6	λ/2.2
L2	λ/2.7	λ/0.9
H	λ/13.1	λ/4.4

This chapter focuses on the analysis and design of conformal vertically polarized UAV antennas using the theory of CMs when the ground plane is square. Throughout this chapter λ_M is defined as the wavelength at 150 MHz. At 150 MHz the height of the tail corresponds to the $\lambda/4$ monopole operation frequency. In Section 4.2 the analysis is conducted when the length and width of a square ground plane equals $\lambda_M/8$. Then the ground plane size is reduced to $\lambda_M/16$ in Section 4.3 and $\lambda_M/32$ in Section 4.4. To simplify the model, while maintaining the relevant physics, a general UAV model will be created using the tail and fuselage sections of the UAV. The dominant CMs will be identified and dipole and monopole feeding networks will be explored. The vertical height and width of the tail section will remain the same to make a direct comparison. By using CMs to study the ground plane effects on the feeding network or type of antenna, one can predict the natural behavior of the structure; thus improving its radiation and input admittance (or impedance) properties.

4.1 Antenna Configuration

Conformal UAV antennas often have size constraints on the width of the ground plane and height of the vertical antenna element. To generalize the investigation, a model is used that represents many common UAVs, shown in Figure 4.2. The conformal antenna under investigation has two regions. Region I is a vertical plate with height (H) and width (T_W) of 0.5 and 0.05 m. The vertical plate represents an antenna element conformal to the tail of UAVs. Region II is a horizontal plate representing the ground plane conformal to the fuselage of UAVs. The width (W_G) and length (L_G) will be varied to study electrically small square ground plane effects. The feed height (H_F) will also be varied to create both a monopole and dipole excitation.

The model has two assumptions about the UAV. First, it is assumed the UAV is a composite with low conductivity and a relative permittivity of 1. Second, it is assumed the designer has the freedom to use the vertical tail and fuselage as the antenna. These assumptions allow the designer to embed copper into the skin of the UAV to form the antenna. Two different feed locations are used to create a dipole and monopole antenna. For both feed configurations the port is placed in the center of the gap. When creating the feeding network, the geometry is being altered since a section of the vertical tail is removed to create a gap; however, the modified geometry is minor and does not change any of the dominant modes under investigation. Therefore, the dominant modes will be shown without any feeding network.

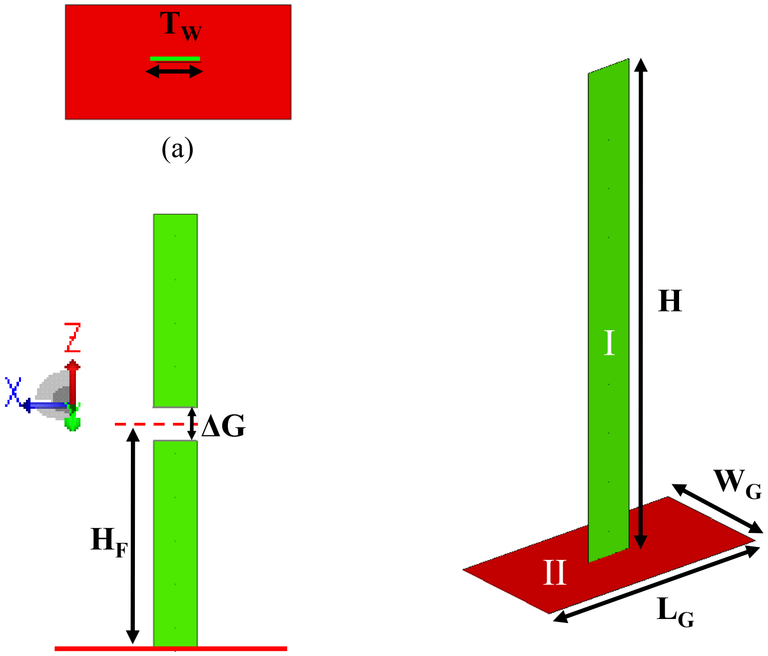

(a)

(b)

(c)

Figure 4.2: UAV antenna element centered on ground plane: (a) top view, (b) side view, (c) perspective view.

4.2 $\lambda_M/8 \times \lambda_M/8$ Square Plate

First, the ground plane will be modelled as a square $L_G = W_G = \lambda_M/8$. The square ground plane with a vertical element is a common antenna typically fed like a monopole. Generally it is accepted that the diameter of the ground plane should be larger than λ/2. Unfortunately, for small

UAVs the dimensions are typically less than λ/2 at operating frequency. For that reason, it is necessary to study the effects of the ground plane and determine the optimum feed location to radiate the desired pattern over the frequency of interest.

The dominant CMs were identified from the process outlined in Section 3.1. The reduced eigenvalue spectrum vs. frequency is shown in Figure 4.3. CM 1 and 2 resonate at 150 and 432.5 MHz, respectively. CM 1 is identified as the overall dominant mode below 400 MHz. This is because a CM becomes dominant when its eigenvalue is near zero or small relative to those of the other CMs supported by the structure. Its eigencurrent and eigenpattern are shown in Figure 4.4. Note CM 1 is a desired mode, since it radiates a vertically polarized omnidirectional pattern. Studying the eigencurrent of CM 1, it can be observed that the current distribution remains strong over the majority of the vertical element starting at the base. This gives the designer freedom to move the feed along the vertical element (Region I) to a location that will weakly excite undesirable modes. Next, the higher order CMs (i.e. CM 2, 3 and 4) are studied. CM 2 is shown in Figure 4.5. This mode has a null in its eigencurrent near the center of the vertical element creating an undesirable null in the radiated pattern at broadside. CM 2 eigenpattern forms two main lobes with maximum at θ = 45 and 135°. Similarly, CM 3 eigencurrent (Figure 4.6(a)) has a null near the center of the vertical element. However the radiated pattern has three main lobes with maxima at θ = 32, 90 and 148°. CM 4 eigencurrent (Figure 4.7(a)) has two nulls along the vertical element. The nulls occur around a quarter and three quarters up the vertical element. The corresponding eigenpattern has four main lobes with maxima at θ = 25, 70, 110 and 155°.

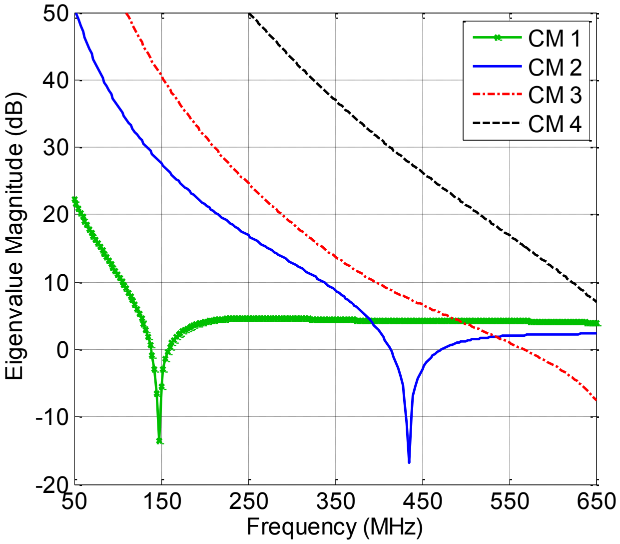

Figure 4.3: Eigenvalue spectrum of characteristic modes under consideration ($L_G = W_G = \lambda_M/8$).

Table 4.2: |EV| (dB) when $L_G = W_G = \lambda_M/8$

CM	50 MHz	150 MHz	300 MHz	550 MHz
1	22.33	-17.42	4.32	1.08
2	47.62	27.59	12.93	1.81
3	74.12	40.66	18.78	4.15
4	89.85	63.85	42.84	17.00

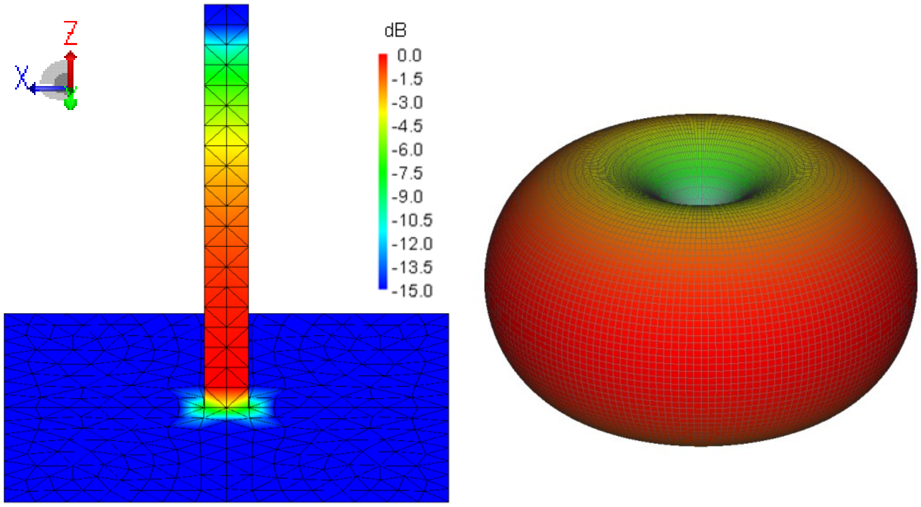

(a) (b)

Figure 4.4: Normalized characteristic mode 1 eigen properties at 150 MHz; (a) eigencurrent, (b) eigenpattern.

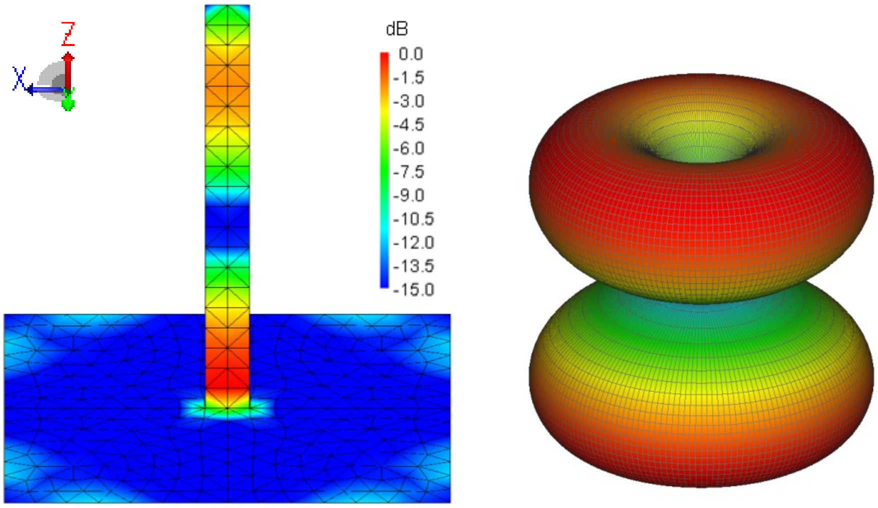

(a) (b)

Figure 4.5: Normalized characteristic mode 2 eigen properties at 150 MHz; (a) eigencurrent, (b) eigenpattern.

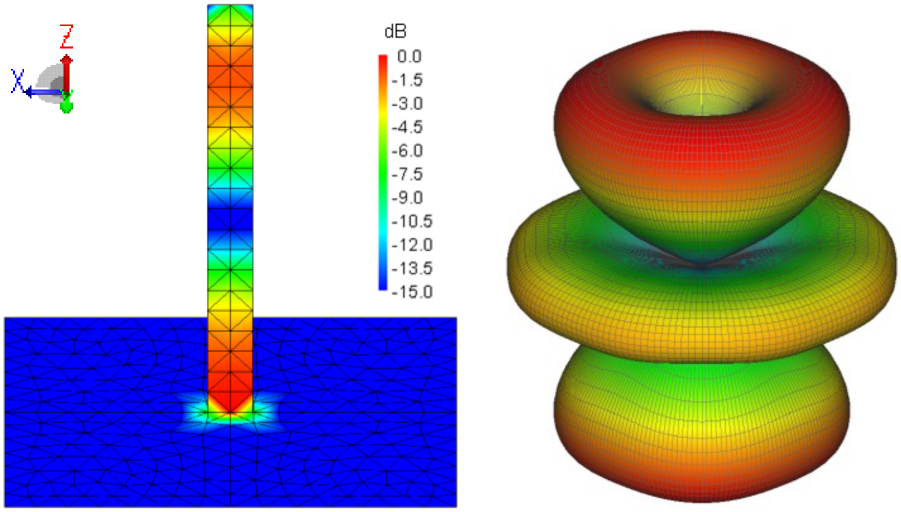

(a) (b)

Figure 4.6: Normalized characteristic mode 3 eigen properties at 150 MHz; (a) eigencurrent, (b) eigenpattern.

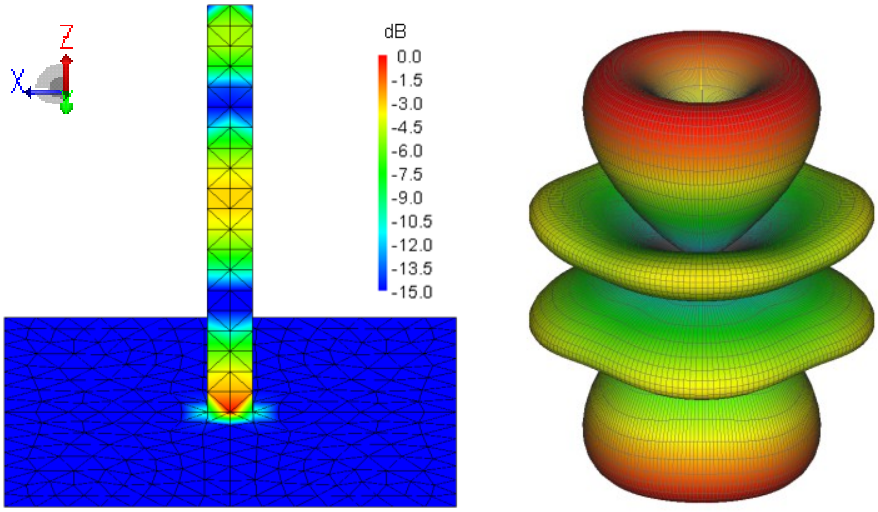

(a) (b)

Figure 4.7: Normalized characteristic mode 4 eigen properties at 150 MHz; (a) eigencurrent, (b) eigenpattern.

By analyzing the properties of the dominant modes, it was found that, after CM 2 resonates, CM 1 and 2 go through a transition where their properties essentially switch. The transition occurs above 450 MHz where the eigenpatterns of CM 1 and CM 2 start to switch. CM 1 develops a null at broadside whereas CM 2 becomes more omnidirectional. The change in pattern can be explained by the change in eigencurrent of the modes. At 150 MHz CM 1 eigencurrent has near constant amplitude starting from the base of the ground plane and extending to the top where it transitions into a null (Figure 4.4 (a)). As the frequency increases the eigencurrent null moves down the vertical element towards the ground plane. At 550 MHz the null resides near the middle of the vertical element with another strong current component forming near the top as shown in Figure 4.8(a). The change in eigencurrent results in an eigenpattern with a null at broadside as shown in Figure 4.8(b). The eigencurrent for CM 2 starts out with two dominant current components along the vertical element (Figure 4.5(a)) resulting in an eigenpattern with a null at broadside (Figure 4.5(b)). As the frequency increases the current component near the top of the vertical element moves towards the bottom, while the one at the bottom becomes weaker. The end result is one current component offset near the top of the vertical element as shown in Figure 4.9(a). Since one current component resides on the element, the radiated pattern is near omnidirectional as shown in Figure 4.9(b). It should be emphasized that these effects are believed to be caused by the plate loading the antenna. The switching of the modes does not occur without the plate.

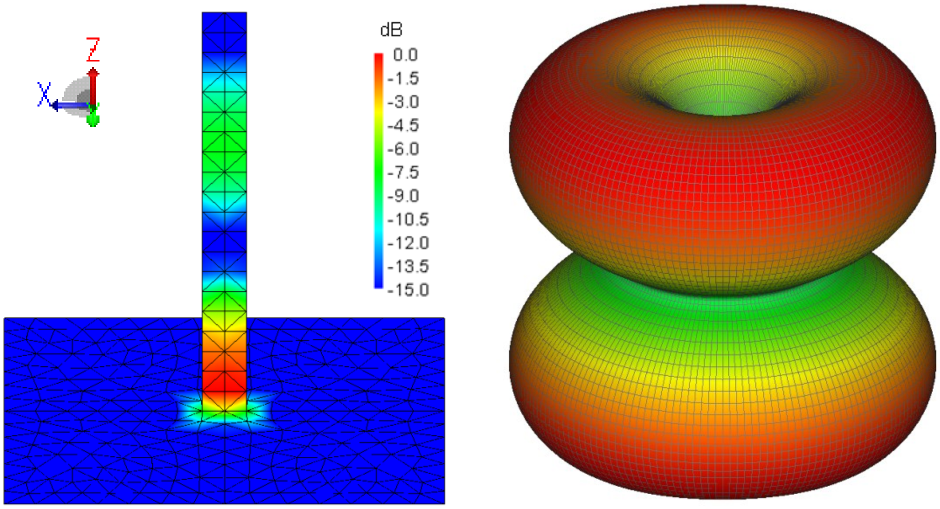

(a) (b)

Figure 4.8: Normalized characteristic mode 1 eigen properties at 550 MHz; (a) eigencurrent, (b) eigenpattern.

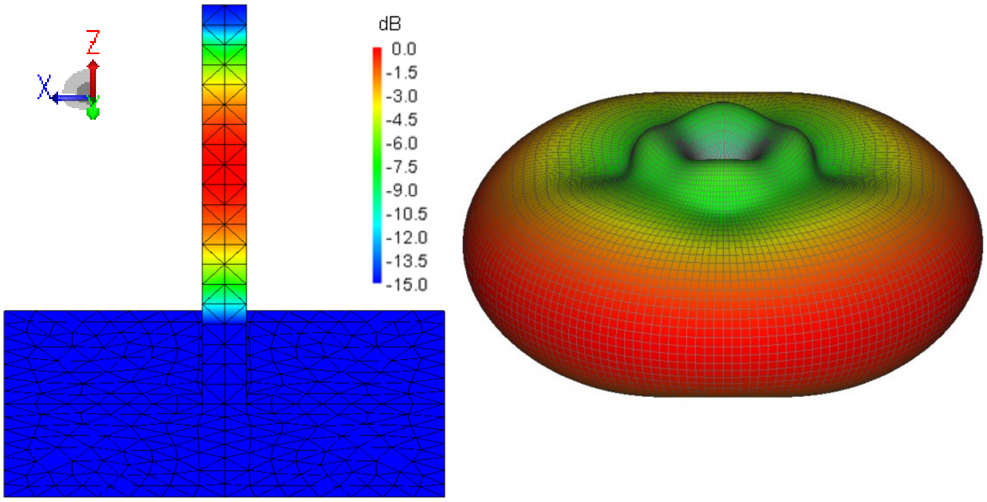

(a) (b)

Figure 4.9: Normalized characteristic mode 2 eigen properties at 550 MHz; (a) eigencurrent, (b) eigenpattern.

After identification of the dominant CMs, the feeding networks need to be considered. From the eigencurrent analysis, the designer gains insight into the preferred location. Since CM 1 has a strong current extending from the base upward along the element, a feed can be placed at 0.1625 m. This feed is referred to as the dipole feed/excitation. It is expected to strongly excite the dominant mode while weakly exciting the higher order modes since this location would reside near a null in their eigencurrents.

4.2.1 Dipole Feed $\lambda_M/8 \times \lambda_M/8$ Square Plate

When modeling an antenna, you must carefully model the feed region and let $V = 0$ to calculate the modes. In this case, that means introducing a gap and shorting it with a thin wire where the voltage source is located. The dipole feed is formed by creating a gap in the vertical element starting at $H_F = 0.1575$ m. The gap is 1 cm and extends across the vertical element forming two arms. A voltage port is placed at the gap center. Creating a gap for a feed is a slight modification to the geometry, but has negligible effects on the dominant modes previously identified. Modification to the geometry may change the mode numbering depending on the numerical tracker, therefore to be consistent the mode numbering will be the same as the modes previously identified. The $|\alpha_n|$ in dB of the dominant modes is shown in Figure 4.10. As expected, the dipole feed configuration strongly excites CM 1. CM 1 remains the dominant mode excited up to 500 MHz. Above 500 MHz, CM 2 transitions into the dominant mode excited, but all modes remain within 7 dB of the dominant mode, therefore they contribute to the total input admittance and radiated pattern. The dominant mode's contribution to the total admittance is shown in Figure 4.11. It can be seen that with the dipole feed, the total conductance and CM 1 conductance match from 50 to 450 MHz. At 450 MHz the total conductance and that of CM 1 diverge because CM 2 is becoming excited. The sum of all four dominant CM's conductance is also shown Figure 4.11, where the total and sum agree. In the susceptance comparison the total and CM 1 susceptance agree at low frequencies and diverge around 250 MHz. This is a typical result where higher order modes have a larger impact in the susceptance although their impact on the conductance is not significant.

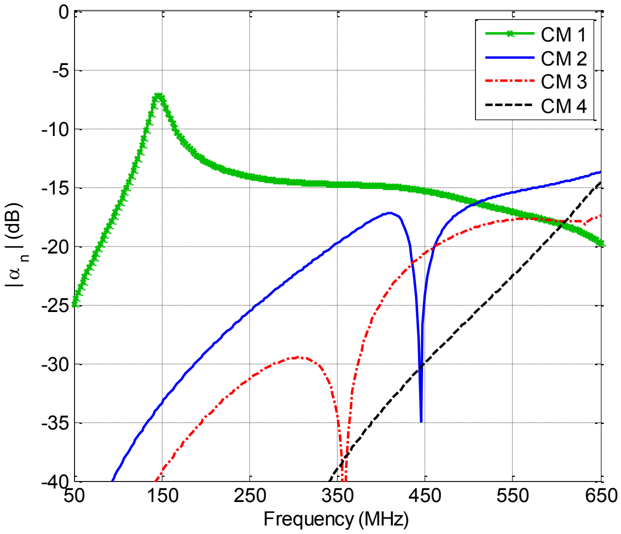

Figure 4.10: $|\alpha_n|$ (dB) of characteristic modes under consideration for dipole feed ($L_G = W_G = \lambda_M/8$).

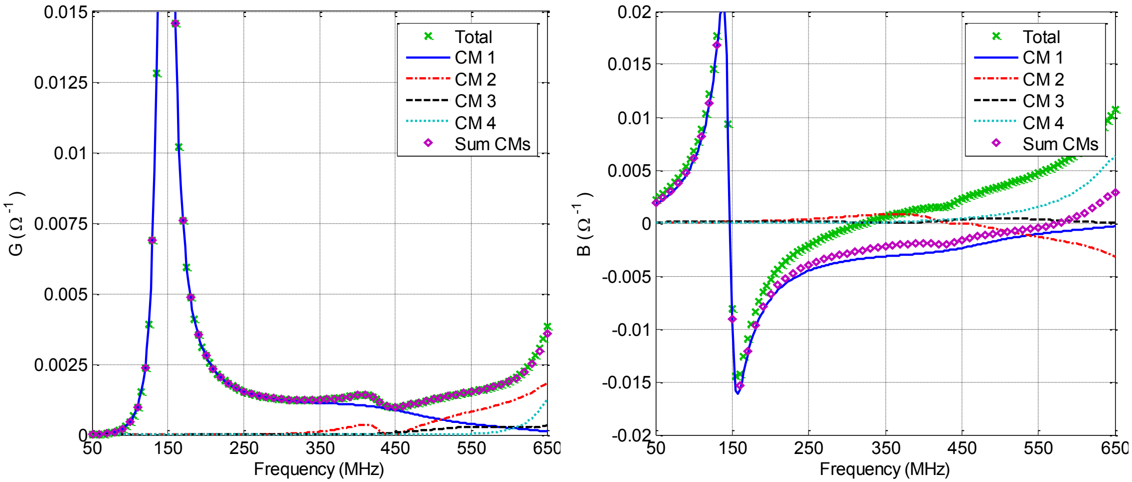

(a) (b)

Figure 4.11: Dipole feed comparing total, characteristic mode and sum of characteristic mode admittance; (a) conductance, (b) susceptance.

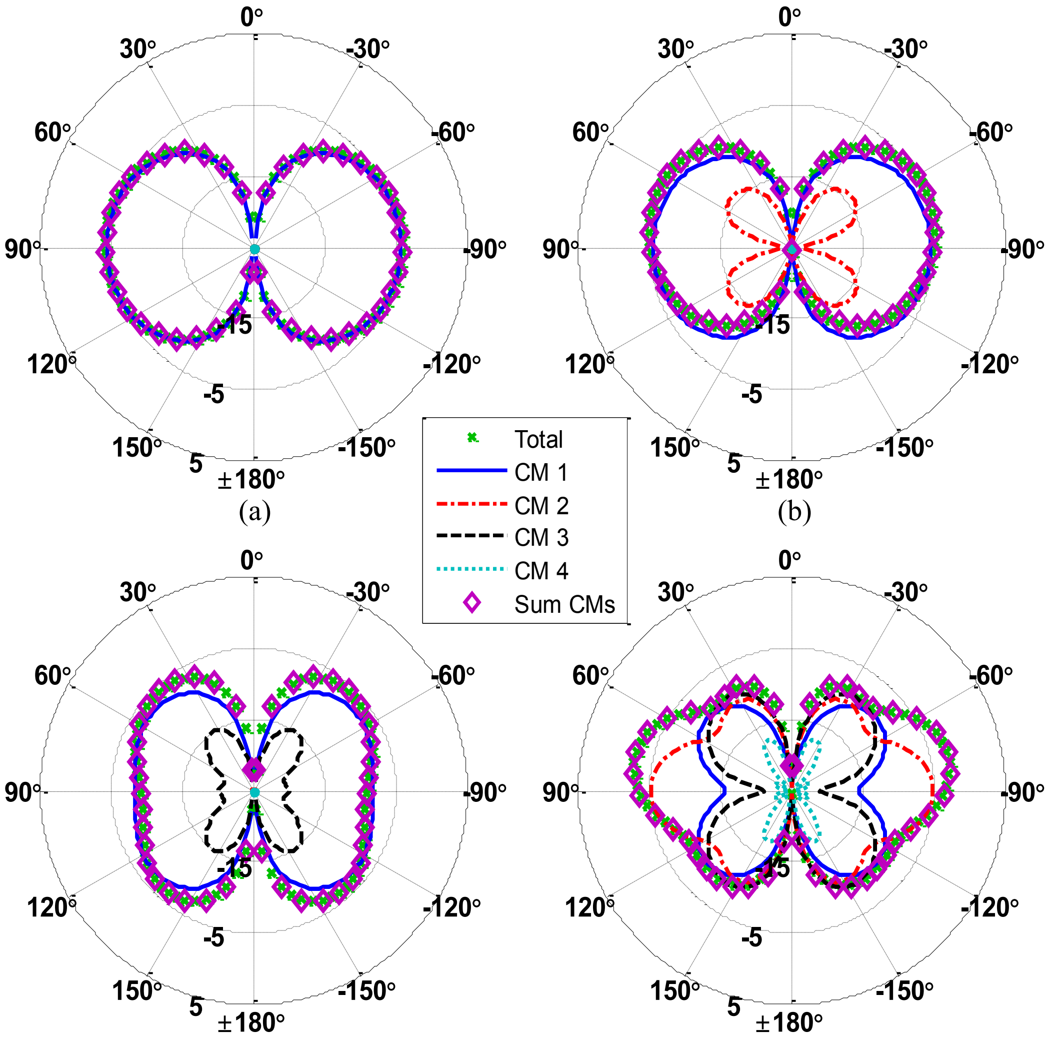

(a) (b)

(c) (d)

Figure 4.12: Dipole feed realized total gain (dBi) comparing total pattern, eigenpatterns and sum of eigenpatterns in the XZ-plane; (a) 250 MHz, (b) 350 MHz, (c) 450 MHz, (d) 550 MHz.

The realized total gain (referenced to 50 Ω) of the dominant modes is shown in Figure 4.12 for the XZ-plane at 250, 350, 450 and 550 MHz. No noticeable differences can be seen between the XZ- and YZ-plane, thus the YZ-plane is omitted in this chapter. Below 250 MHz CM 1 is the dominant mode contributing to the radiated pattern. Note CMs 2-4 at 250 MHz, 3 and 4 at 350 MHz, and 2 and 4 at 450 MHz have realized gains less than -25 dBi and thus do not show up in the figures. At 550 MHz all four dominant modes have contributions to the radiated pattern.

When these four modes are summed, the resulting pattern matches the total pattern. Note that with the dipole feed there are no major nulls at broadside.

The patterns in the XY-plane are shown in Figure 4.13. It is desirable for the pattern to remain omnidirectional in the XY-plane. At 250, 350 and 450 MHz total and CM 1 radiation pattern match and CM 1 is the only mode with realized gain above -25 dBi except at 450 where CM 3 is slightly excited. Between 450 and 550 MHz CM 2 becomes the dominant mode as discussed previously.

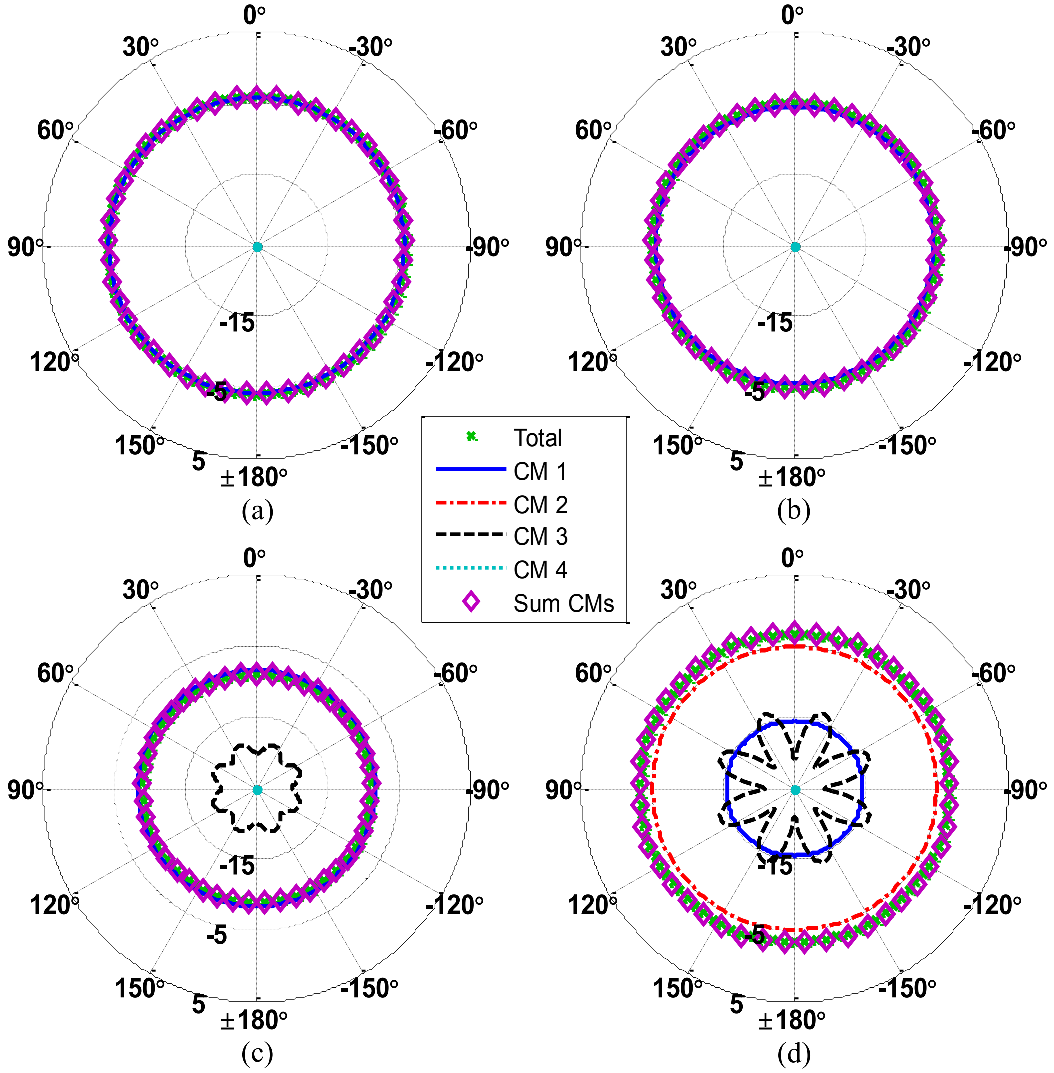

(a) (b) (c) (d)

Figure 4.13: Dipole feed realized total gain (dBi) comparing total pattern, eigenpatterns and sum of eigenpatterns in the XY-plane; (a) 250 MHz, (b) 350 MHz, (c) 450 MHz, (d) 550 MHz.

4.2.2 Monopole Feed $\lambda_M/8 \times \lambda_M/8$ Square Plate

The monopole feed is formed by creating a 1 cm gap between the plate and the vertical element. This is accomplished by connecting the two structures together via a voltage port at the base of the vertical element. The $|\alpha_n|$ (dB) of the dominant modes is shown in Figure 4.14. CM 1 is the dominant mode excited up to 350 MHz. CM 2 is strongly excited from 350-460 MHz then CM 1 is dominant until 650 MHz. CM 1 and 2 have the largest contribution to the admittance as seen in Figure 4.15. The monopole feed does not suppress the excitation of CM 2 since the feed is not placed in the null of that mode. At 250 MHz $|\alpha_2|$ is increased by 4 dB relative to dipole feed.

The realized total gain (referenced to 50 Ω) of the dominant modes is shown in Figure 4.16 for the XZ-plane at 250, 350, 450 and 550 MHz. Below 250 MHz CM 1 is the dominant mode contributing to the radiated pattern, however with the monopole feed, CM 2 is excited although it is weaker. Note CMs 3 and 4 at 250 MHz and 4 at 350 MHz have realized gains less than -25 dBi and thus do not show up in the figures. At 550 MHz all modes have contributions to the radiated pattern with CM 1 having the largest impact and CM 2 having the least impact. When the four dominant modes are summed the resulting pattern matches the total pattern. The monopole feed creates an undesirable null at broadside above 350 MHz.

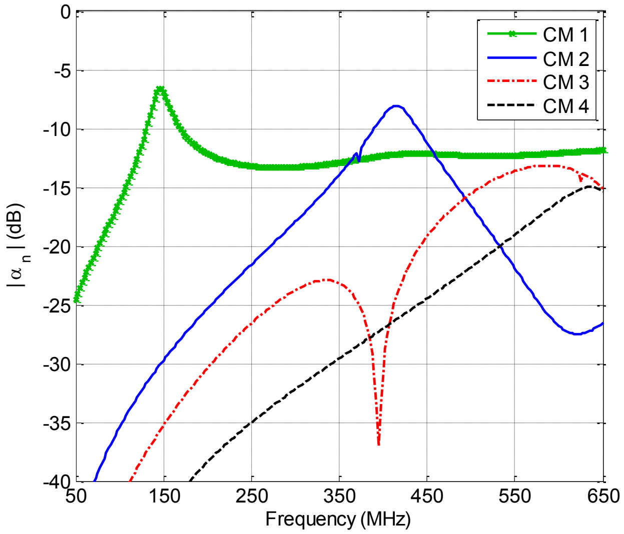

Figure 4.14: $|\alpha_n|$ (dB) of characteristic modes under consideration for monopole feed ($L_G = W_G = \lambda_M/8$).

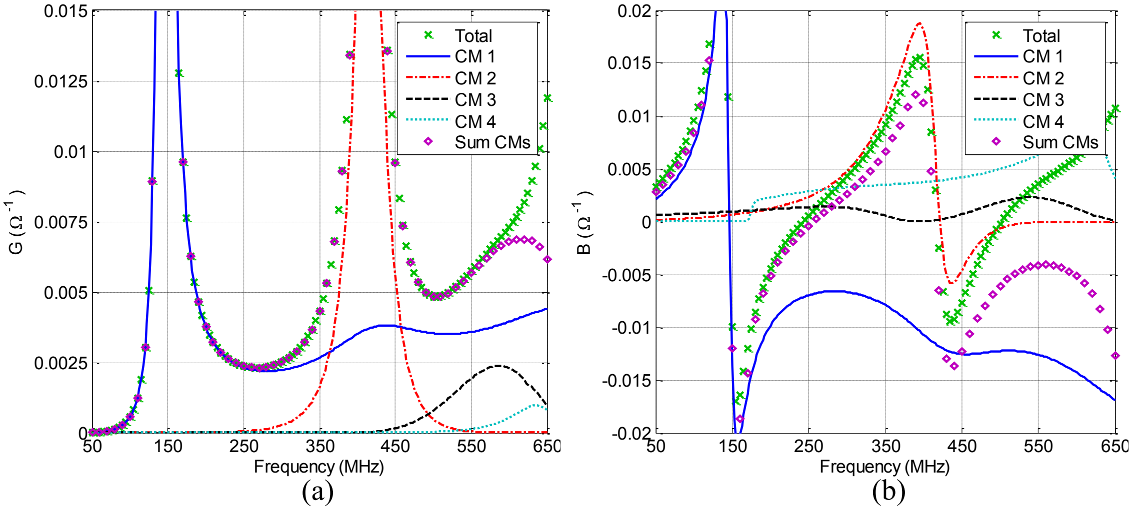

(a)

(b)

Figure 4.15: Monopole feed comparing total, characteristic mode and sum of characteristic mode admittance; (a) conductance, (b) susceptance.

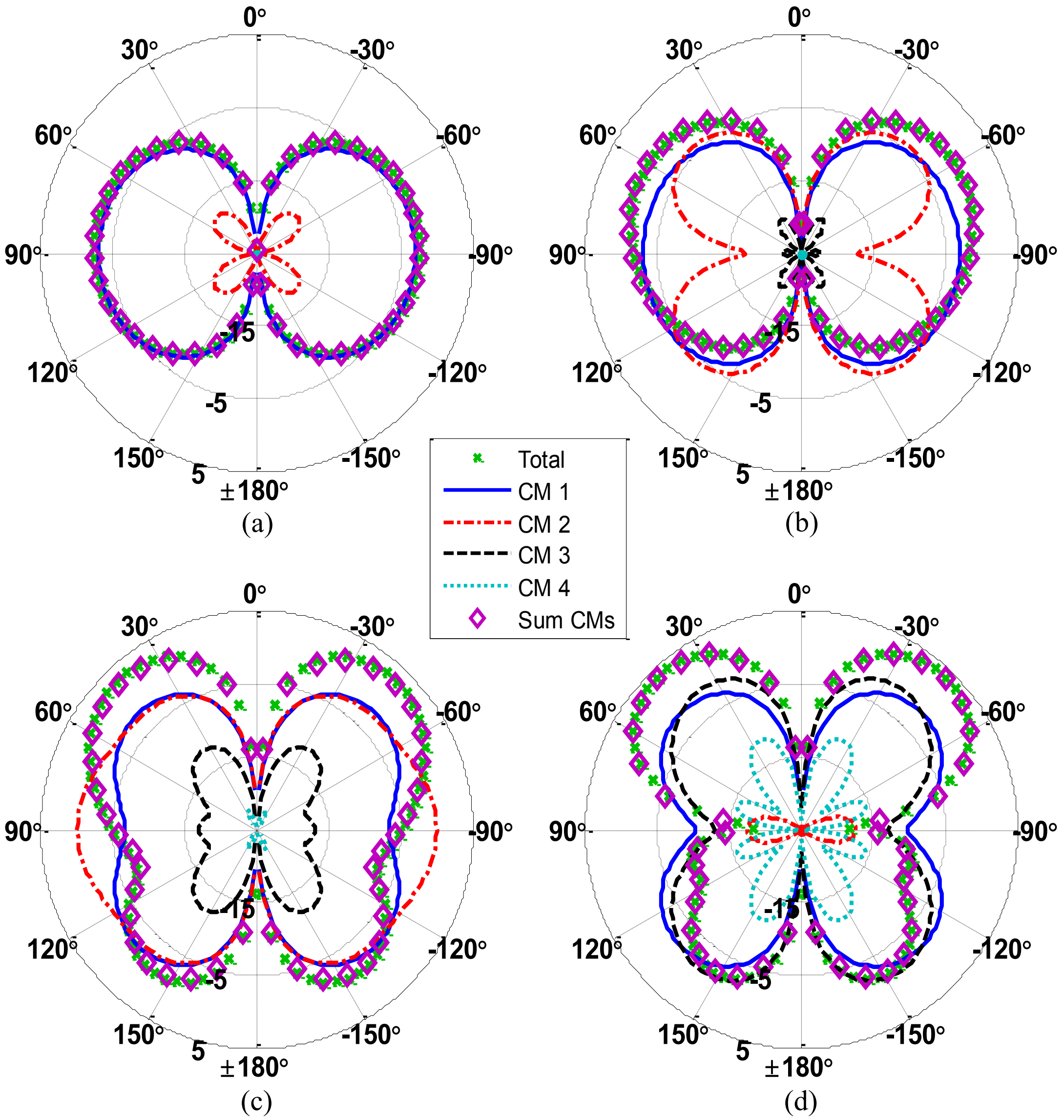

Figure 4.16: Monopole feed realized total gain (dBi) comparing total pattern, eigenpatterns and sum of eigenpatterns in the XZ-plane; (a) 250 MHz, (b) 350 MHz, (c) 450 MHz, (d) 550 MHz.

The realized gain in the XY-plane is shown in Figure 4.17. It is desirable for the pattern to remain omnidirectional in the XY-plane. At 250 MHz CM 1 is the only mode with a realized gain larger than -25 dBi. At 350, 450 and 550 MHz all modes have a realized gain larger than -25 dBi except CM 4. Between 350 and 450 MHz CM 2 becomes the dominant mode. At 550 MHz CM 3 closely resembles the total realized gain and is no longer omnidirectional.

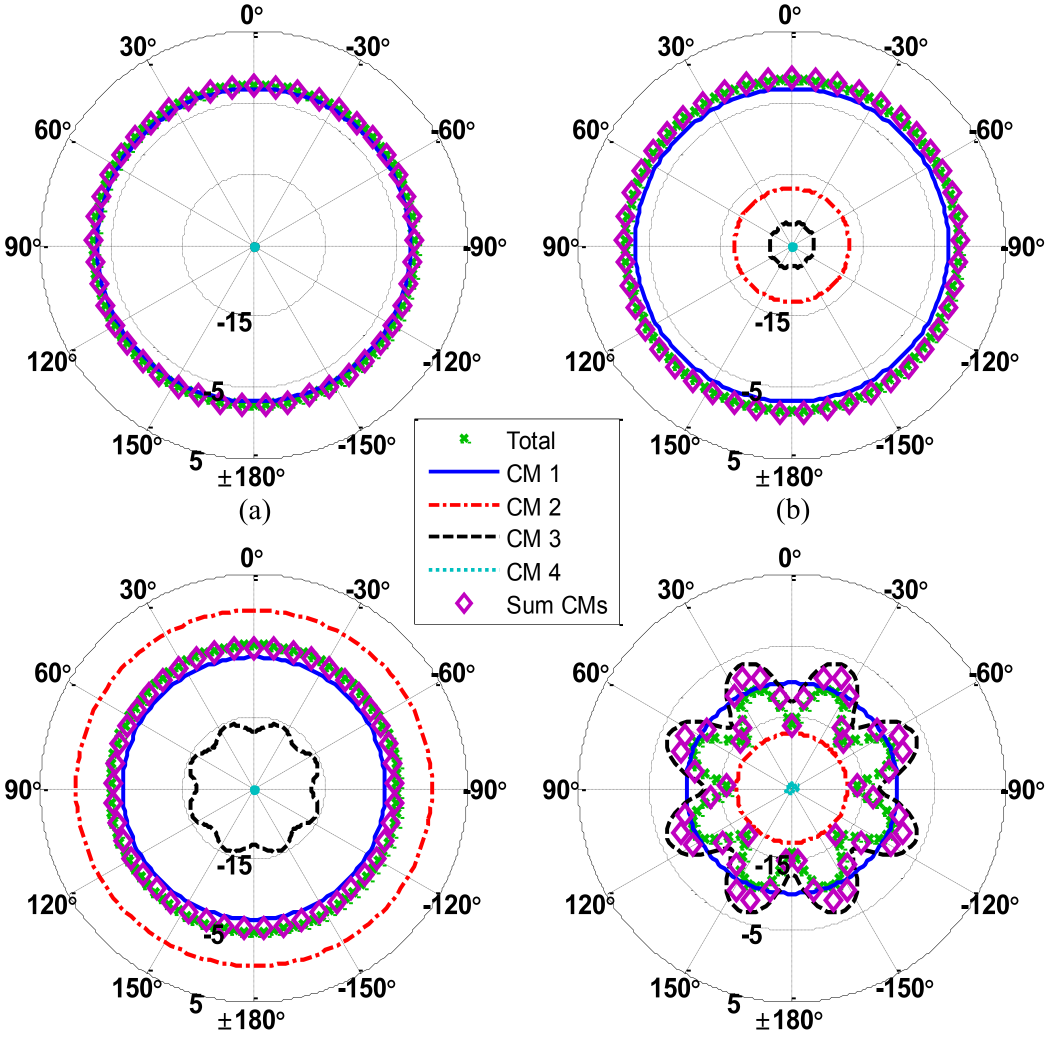

(a) (b) (c) (d)

Figure 4.17: Monopole feed realized total gain (dBi) comparing total pattern, eigenpatterns and sum of eigenpatterns in the XY-plane; (a) 250 MHz, (b) 350 MHz, (c) 450 MHz, (d) 550 MHz.

4.3 $\lambda_M/16 \times \lambda_M/16$ Square Plate

The analysis is now performed when $L_G = W_G = \lambda/16$. Three dominant CMs were identified from the process outlined in Section 3.1. The fourth mode that was identified when $L_G = W_G = \lambda/8$ was pushed higher in frequency and thus is not considered in this analysis. The eigenvalue spectrum is shown in Figure 4.18 and a table listing the eigenvalues (dB) at 50, 150, 300 and 550

MHz is given in Table 4.3. The most noticeable affect is the increased separation of CM 2 and CM 3. CM 3 eigenvalue increases by almost 10 dB at 50 MHz relative to λ/8 case. CM 1 and 2 have a resonant frequency of 172.5 and 445 MHz respectively, an increase of 12.5 MHz from the λ/8 case. CM 1 is identified as the overall dominant mode below 400 MHz and its eigenvalue increases by 1.06 dB at 50 MHz relative to λ/8 case. The increase is expected since the occupied volume of the antenna decreased. The first three dominant modes are essentially the same as the λ/8 case. Their eigencurrent and eigenpatterns are shown in Figure 4.19-Figure 4.21 at 172.5 MHz which corresponds to the resonant frequency of CM1. Note CM 1 is a desired mode, since it radiates a vertically polarized omnidirectional pattern. Studying the eigencurrent of CM 1 the current distribution remains strong over the majority of the vertical element starting at the base. This gives the designer freedom to move the feed along the vertical element (Region I) to a location that will weakly excite undesirable modes. Next, CM 2 is investigated since it is the next mode to resonate and the eigenvalue is the closest to CM 1. CM 2 is shown in Figure 4.20. This mode has a null in its eigencurrent near the center of the vertical element creating an undesirable null in the radiated pattern at broadside. CM 2 eigenpattern forms two main lobes with maximum at θ = 45 and 135°. Similarly, CM 3 eigencurrent Figure 4.21(a)) has two nulls along the vertical element. The nulls occur around a quarter and three quarters up the vertical element. However the radiated pattern has three main lobes with maximums at θ = 32, 90 and 148°. A similar modal transition/switch occurs between CM 1 and 2 above the resonant frequency of CM 2 as previously described for the λ/8 case. This transition occurs high in frequency since the resonant frequency of CM2 has increased relative to the $\lambda_M/8$ case. The eigencurrent and pattern are not shown for brevity.

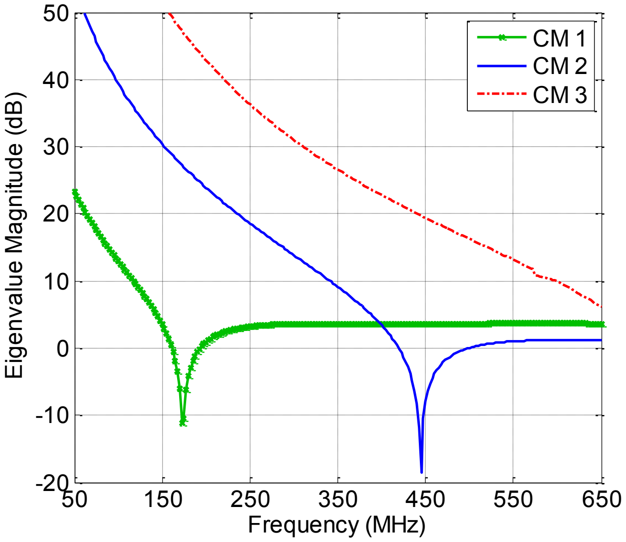

Figure 4.18: Eigenvalue spectrum of characteristic modes under consideration ($L_G = W_G = \lambda_M/16$).

Table 4.3: |EV| dB when $L_G = W_G = \lambda_M/16$

CM	50 MHz	150 MHz	300 MHz	550 MHz
1	23.39	3.54	3.61	1.01
2	54.53	30.43	13.85	3.72
3	84.05	51.45	31.02	13.17

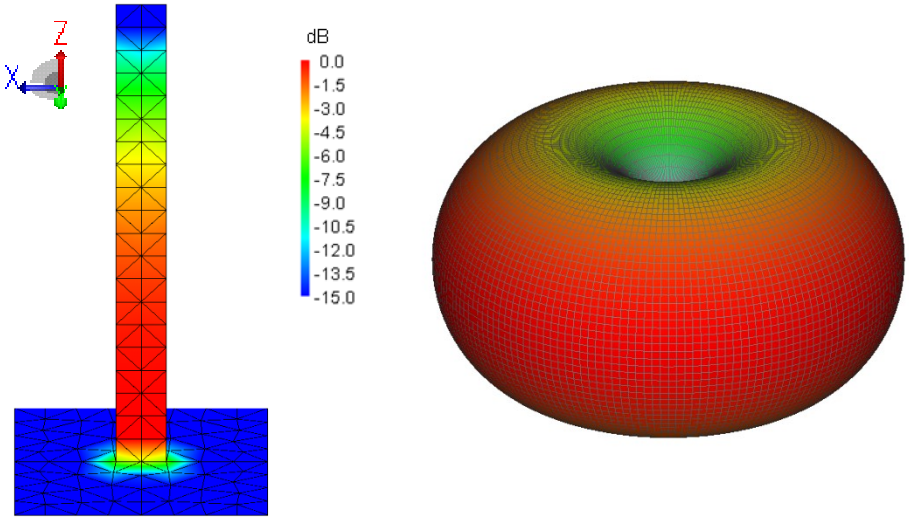

(a) (b)

Figure 4.19: Normalized characteristic mode 1 eigen properties at 172.5 MHz; (a) eigencurrent, (b) eigenpattern.

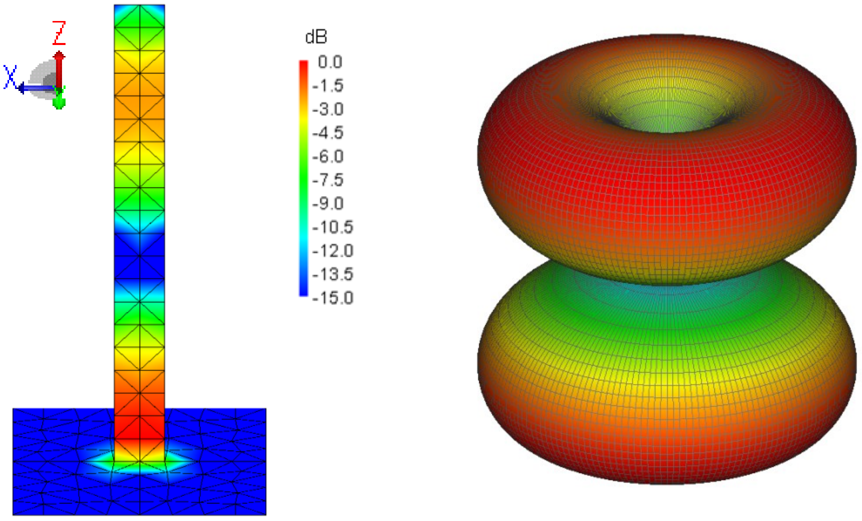

(a) (b)

Figure 4.20: Normalized characteristic mode 2 eigen properties at 172.5 MHz; (a) eigencurrent, (b) eigenpattern.

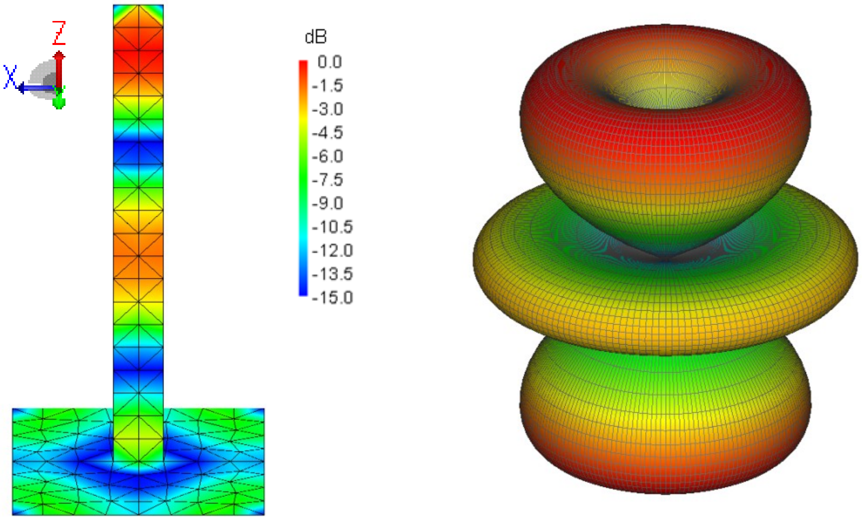

(a) (b)

Figure 4.21: Normalized characteristic mode 3 eigen properties at 172.5 MHz; (a) eigencurrent, (b) eigenpattern.

4.3.1 Dipole Feed $\lambda_M/16 \times \lambda_M/16$ Square Plate

The dipole feed is identical to the feed described in Section 4.2.1. The $|\alpha_n|$ (dB) of the dominant modes is shown in Figure 4.22. As expected the dipole feed configuration strongly excites CM 1. CM 1 remains the dominant mode excited up to 575 MHz. Above 575 MHz, CM 2 transitions into the dominant mode excited; all modes remain within 5 dB of the dominant mode, therefore they all contribute to the input admittance and radiated pattern. The dominant modes contribution to the total admittance is shown in Figure 4.23. It can be seen that with the dipole feed the total conductance and CM 1 conductance match from 50 to 520 MHz, except around CM 2 resonant frequency (i.e. 400-450 MHz) since the mode is easily excited. Note, although CM 2 resonates at these frequencies, the dipole feed suppresses its effects and CM 1 still has the largest contribution towards the total conductance. At 520 MHz the total conductance and that of CM 1 diverge because CM 2 is transitioning into the dominant mode. The sum of all three dominant CM's conductance is also shown in Figure 4.23, where the total and sum agree. In the susceptance comparison, the total and CM 1 susceptance agree well at low frequencies and diverge around 200 MHz.

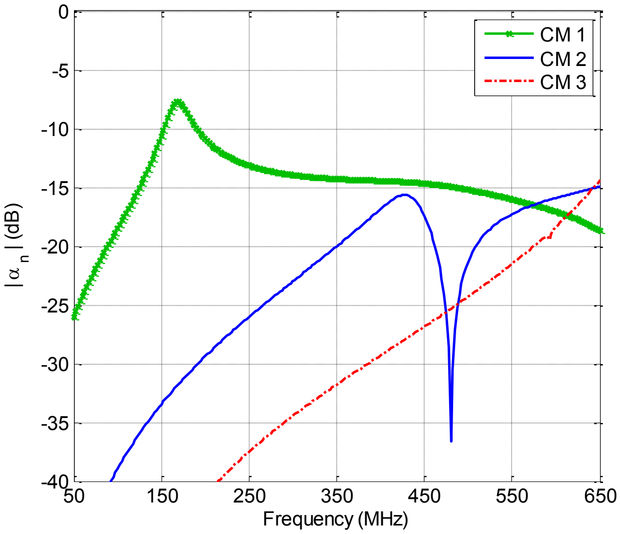

Figure 4.22: $|\alpha_n|$ (dB) of characteristic modes under consideration for dipole feed ($L_G = W_G = \lambda_M/16$).

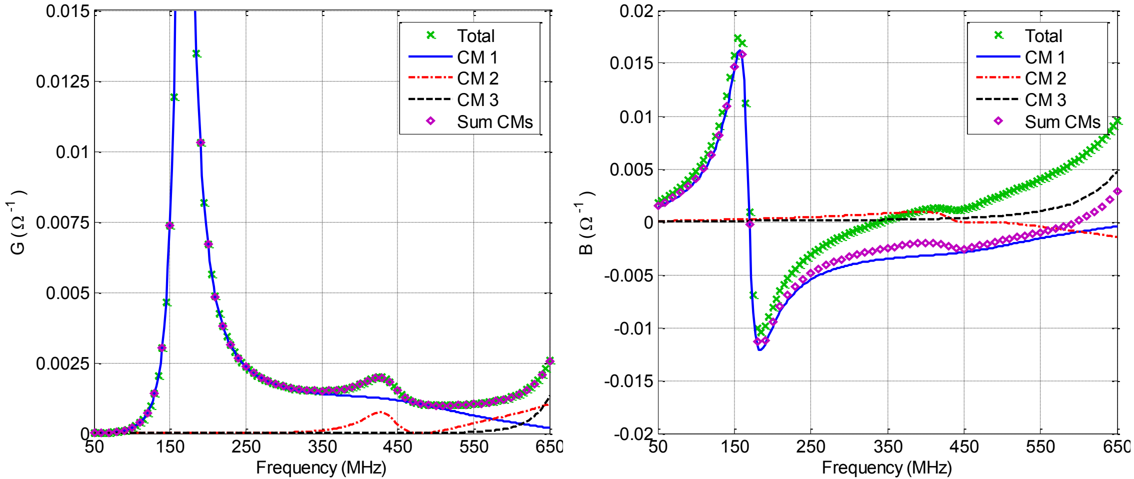

(a) (b)

Figure 4.23: Dipole feed comparing total, characteristic mode and sum of characteristic mode admittance; (a) conductance, (b) susceptance.

The realized total gain referenced to 50 Ω of the dominant modes is shown in Figure 4.24 for the XZ-plane at 250, 350, 450 and 550 MHz. Below 250 MHz CM 1 is the dominant mode contributing to the radiated pattern. Note CMs 2 and 3 at 250 MHz and 3 at 350 and 450 MHz have realized gains less than -25 dBi and thus do not show up in the figures. At 550 MHz all modes have contributions to the radiated pattern. When the four dominant modes are summed the resulting pattern matches the total pattern. Note that with the dipole feed there are no major nulls at broadside.

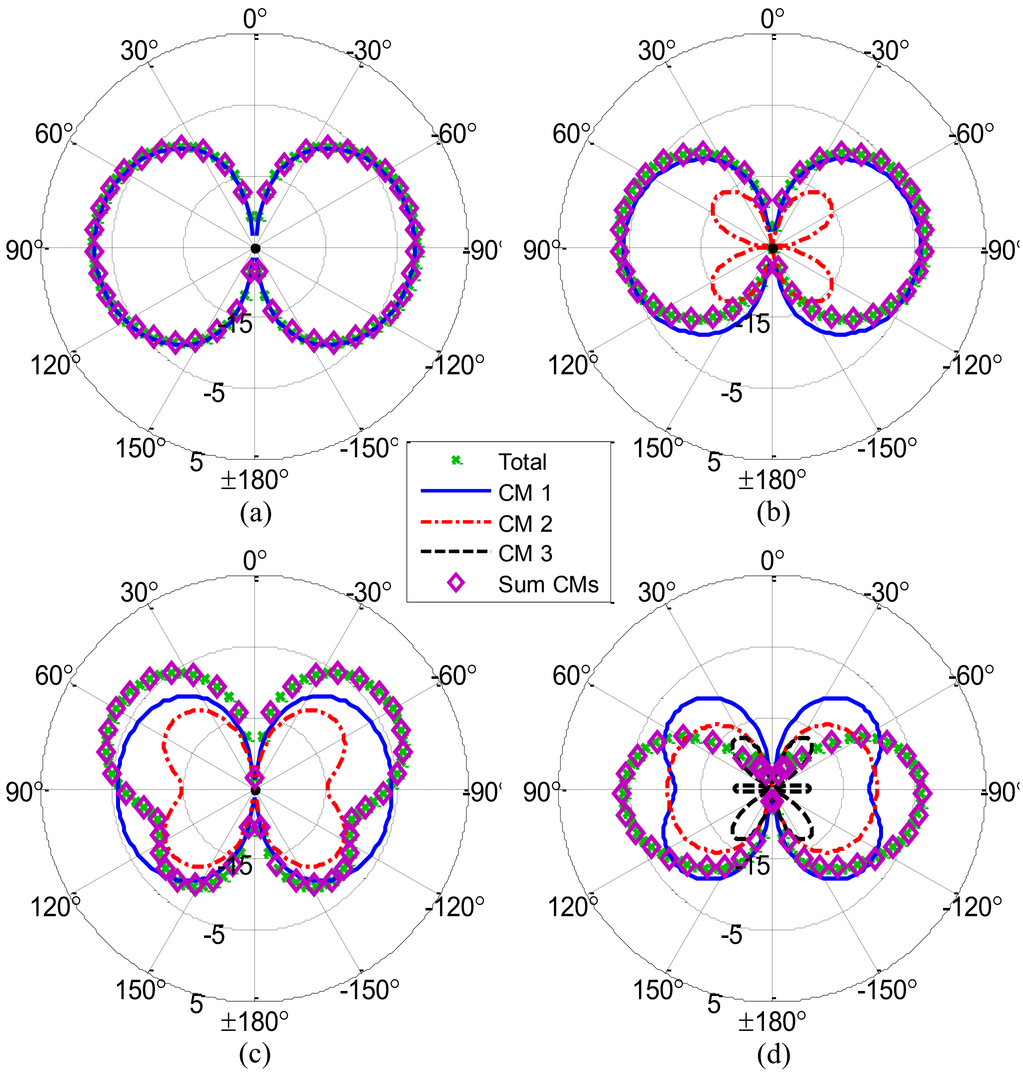

Figure 4.24: Dipole feed realized total gain (dBi) comparing total pattern, eigenpatterns and sum of eigenpatterns in the XZ-plane; (a) 250 MHz, (b) 350 MHz, (c) 450 MHz, (d) 550 MHz.

The patterns in the XY-plane are in shown Figure 4.25. It is desirable for the pattern to remain omnidirectional in the XY-plane. At 250, 350 and 450 MHz total and CM 1 radiation pattern match. CM 1 is the only mode with a realized gain above -25 dBi, except at 450 where CM 3 is slightly excited. Between 450 and 550 MHz CM 2 becomes the dominant mode.

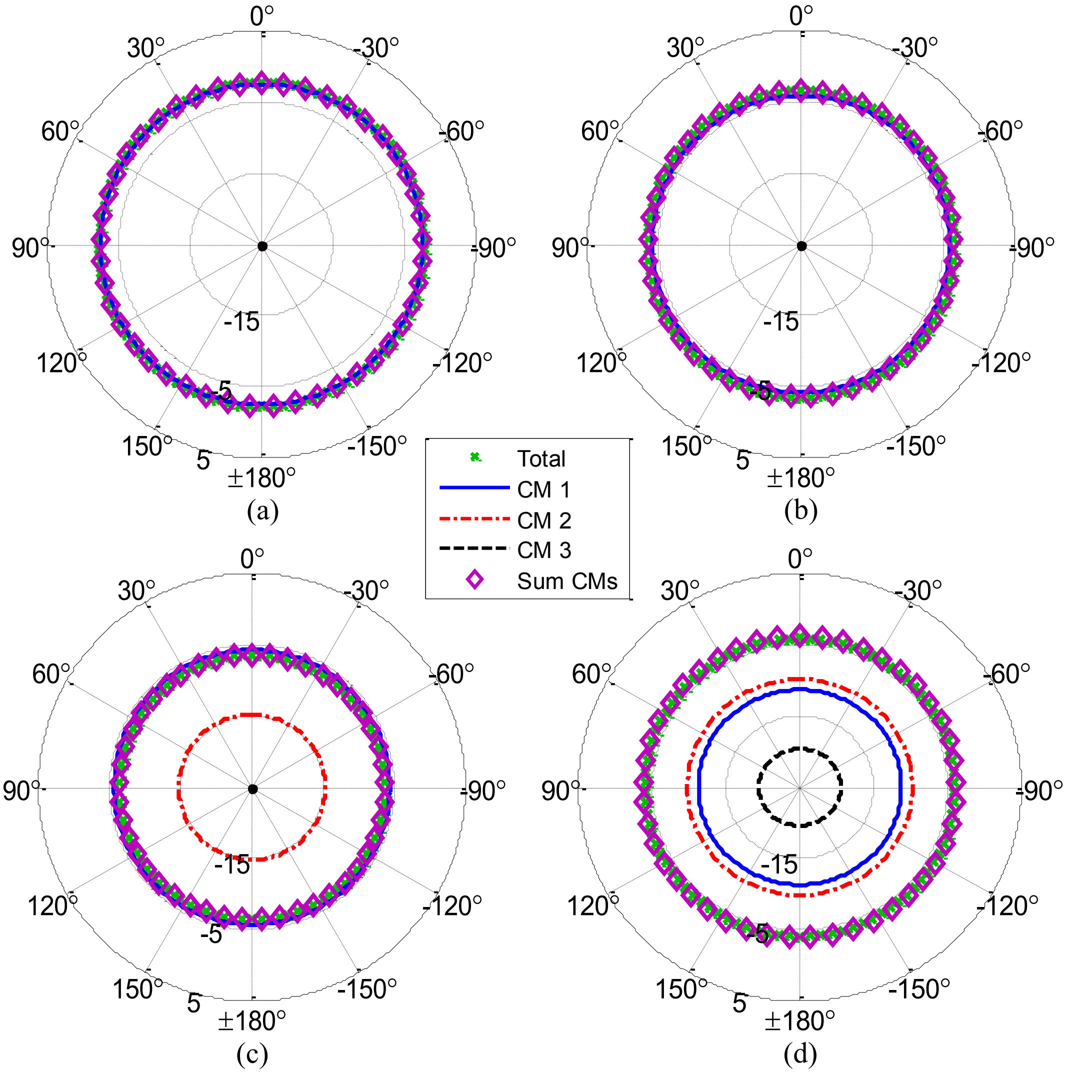

(a) (b) (c) (d)

Figure 4.25: Dipole feed realized total gain (dBi) comparing total pattern, eigenpatterns and sum of eigenpatterns in the XY-plane; (a) 250 MHz, (b) 350 MHz, (c) 450 MHz, (d) 550 MHz.

4.3.2 Monopole Feed $\lambda_M/16 \times \lambda_M/16$ Square Plate

The monopole feed is identical to the feed described in Section 4.2.2. The $|\alpha_n|$ (dB) of the dominant modes is shown in Figure 4.26. CM 1 is the dominant mode excited up to 350 MHz. CM 2 is strongly excited from 365-475 MHz then CM 1 is dominant till 630 MHz, then CM 3 starts to become dominant after 630 MHz. CM 1 and 2 have the largest contribution to the admittance below 630 MHz, as seen in Figure 4.27. The monopole feed does not suppress the excitation of CM 2 since the feed is not placed in the null of the mode. At 250 MHz $|\alpha_2|$ is increased by 4.66 dB relative to dipole feed.

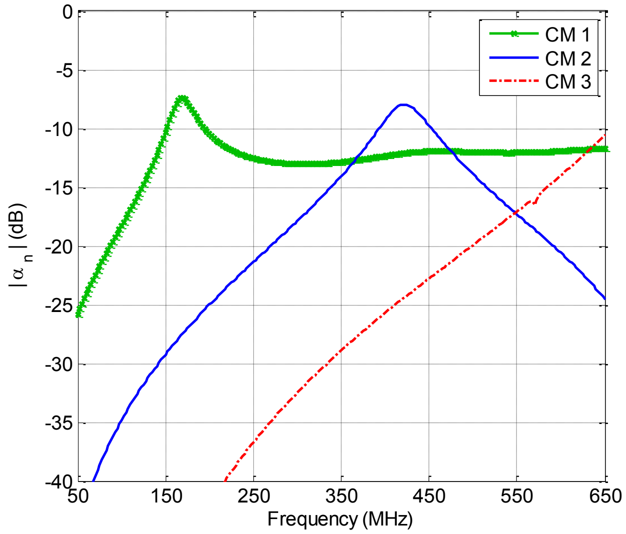

Figure 4.26: $|\alpha_n|$ (dB) of characteristic modes under consideration for monopole feed ($L_G = W_G = \lambda_M/16$).

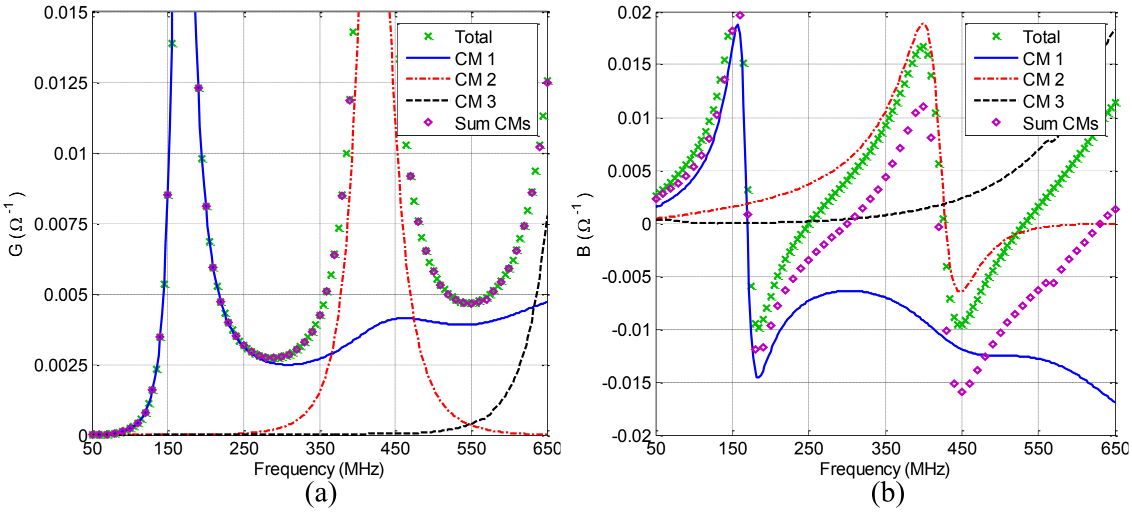

(a)

(b)

Figure 4.27: Monopole feed comparing total, characteristic mode and sum of characteristic mode admittance; (a) conductance, (b) susceptance.

The realized total gain referenced to 50 Ω of the dominant modes is shown in Figure 4.28 for the XZ-plane at 250, 350, 450 and 550 MHz. Below 250 MHz CM 1 is the dominant mode contributing to the radiated pattern, however with the monopole feed, CM 2 is excited although weakly. Note CM 3 at 250 MHz and 350 MHz has a realized gain less than -25 dB and thus does not show up in the figures. At 450 and 550 MHz all modes have contributions to the radiated pattern with CM 1 and 2 having the largest impact and CM 3 having the least impact. When the three dominant modes are summed the resulting pattern matches the total pattern. Note the monopole feed creates an undesirable null at broadside, especially at 550 MHz.

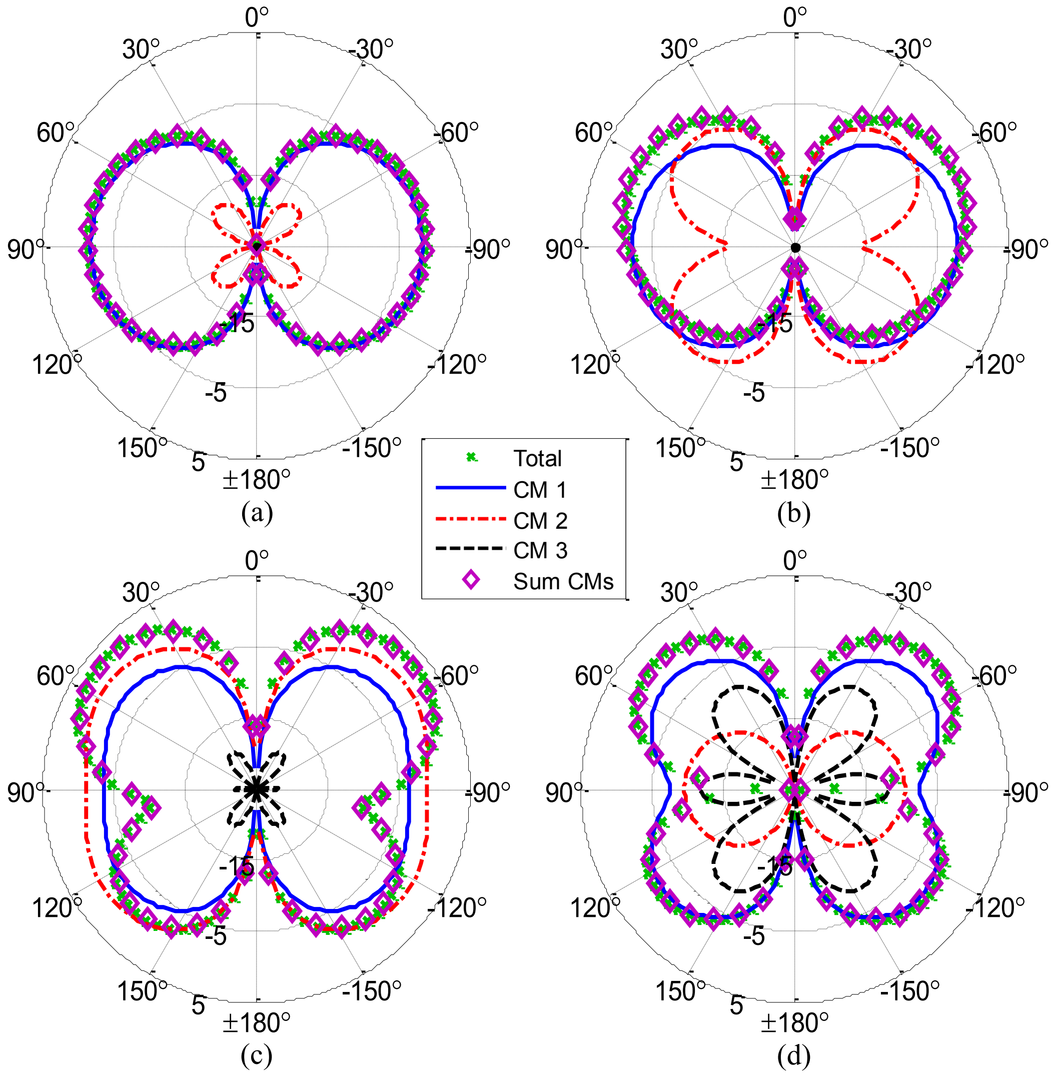

(a) (b) (c) (d)

Figure 4.28: Monopole feed realized total gain (dBi) comparing total pattern, eigenpatterns and sum of eigenpatterns in the XZ-plane; (a) 250 MHz, (b) 350 MHz, (c) 450 MHz, (d) 550 MHz.

The realized gain in the XY-plane is shown in Figure 4.29. It is desirable for the pattern to remain omnidirectional in the XY-plane. At 250 MHz CM 1 is the only mode with a realized gain larger than -25 dBi. At 450 and 550 MHz all modes have a realized gain larger than -25 dBi. Between 350 and 450 MHz CM 2 becomes the dominant mode. At 550 MHz the dominant modes add destructively, resulting in a total realized gain less than -25 dBi.

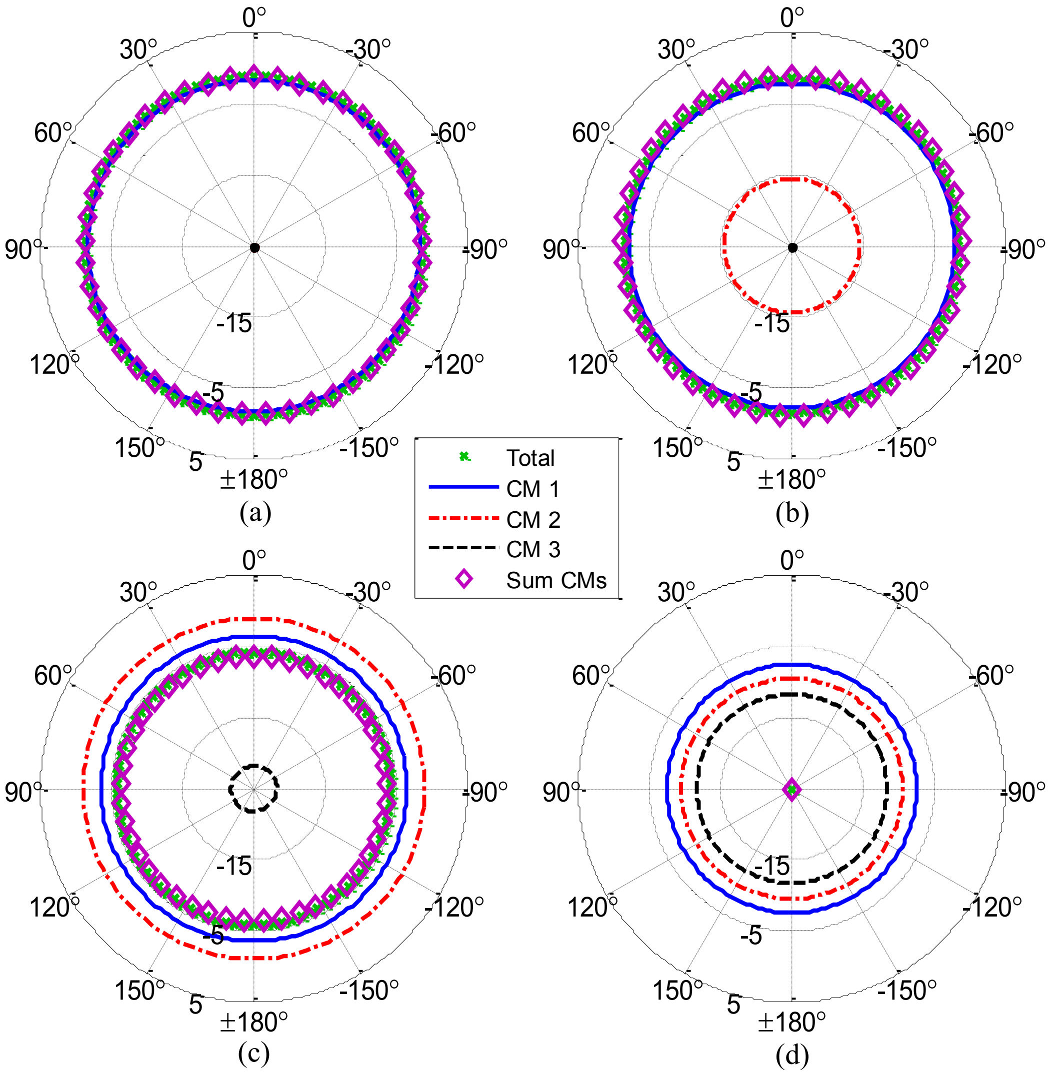

Figure 4.29: Monopole feed realized total gain (dBi) comparing total pattern, eigenpatterns and sum of eigenpatterns in the XY-plane; (a) 250 MHz, (b) 350 MHz, (c) 450 MHz, (d) 550 MHz.

4.4 $\lambda_M/32 \times \lambda_M/32$ Square Plate

Finally the last square ground plane considered is when $L_G = W_G = \lambda_M/32$. Three dominant CMs were identified from the process outlined in Section 3.1. Similar to the $\lambda_M/16$ case, the 4th mode identified in the $\lambda_M/8$ case was pushed higher in frequency and thus is not considered in this analysis. The eigenvalue spectrum is shown in Figure 4.30 and a table listing the eigenvalues (dB) at 50, 150, 300 and 550 MHz is given in Table 4.4. CM 1 and 2 have a resonant frequency of 210 and 470 MHz, respectively, an increase of 60 and 37.5 MHz relative to the $\lambda_M/8$ case. CM 1 is identified as the overall dominant mode below 400 MHz and its eigenvalue increases by 2.54 dB at 50 MHz relative to $\lambda_M/8$ case. The increase is expected since the occupied volume of the antenna decreased. The first three dominant modes are essentially the same as $\lambda_M/8$ and $\lambda_M/16$ case. Their eigencurrent and eigenpatterns are shown in Figure 4.31-Figure 4.33 at 210 MHz which corresponds to the resonant frequency of CM1. Note CM 1 is a desired mode, since it radiates a vertically polarized omnidirectional pattern. Studying the eigencurrent of CM 1, the current distribution remains strong over the majority of the vertical element starting at the base. This allows the designer freedom to move the feed along the vertical element (Region I) to a location that will weakly excite undesirable modes. Next, CM 2 is investigated since it is the next mode to resonate and the eigenvalue is closest to CM 1. CM 2 is shown in Figure 4.32. This mode has a null in its eigencurrent near the center of the vertical element creating an undesirable null in the radiated pattern at broadside. CM 2 eigenpattern forms two main lobes with maximum at $\theta = 45$ and 135°. Similarly, CM 3 eigencurrent Figure 4.33(a)) has two nulls along the vertical element. The nulls occur around a quarter and three quarters up the vertical element. However, the radiated pattern has three main lobes with maximums at $\theta = 32$, 90 and 148°. A similar modal transition/switch occurs between CM 1 and 2 above the resonant frequency of CM 2 as previously described for the $\lambda/8$ case. The transition starts to occur higher in frequency since the resonant frequency of CM 2 has increased relative to $\lambda_M/8$ and $\lambda_M/16$ cases. The eigencurrent and pattern are not shown for brevity.

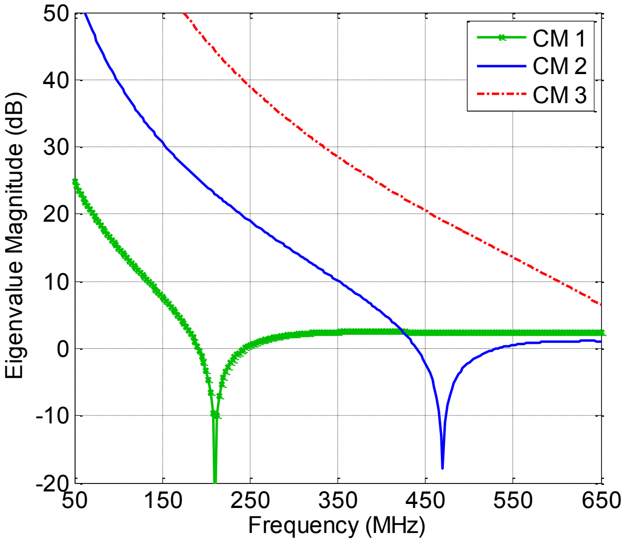

Figure 4.30: Eigenvalue spectrum of characteristic modes under consideration ($L_G = W_G = \lambda_M/32$).

Table 4.4: |EV| dB when $L_G = W_G = \lambda_M/32$

CM	50 MHz	150 MHz	300 MHz	550 MHz
1	24.86	7.74	2.09	0.51
2	54.71	30.65	14.42	2.37
3	78.18	54.32	33.36	13.57

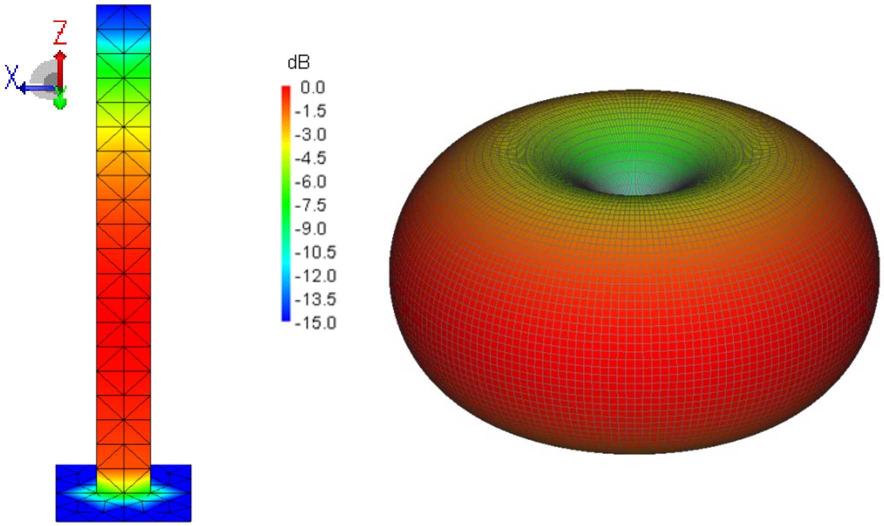

(a) (b)

Figure 4.31: Normalized characteristic mode 1 eigen properties at 210 MHz; (a) eigencurrent, (b) eigenpattern.

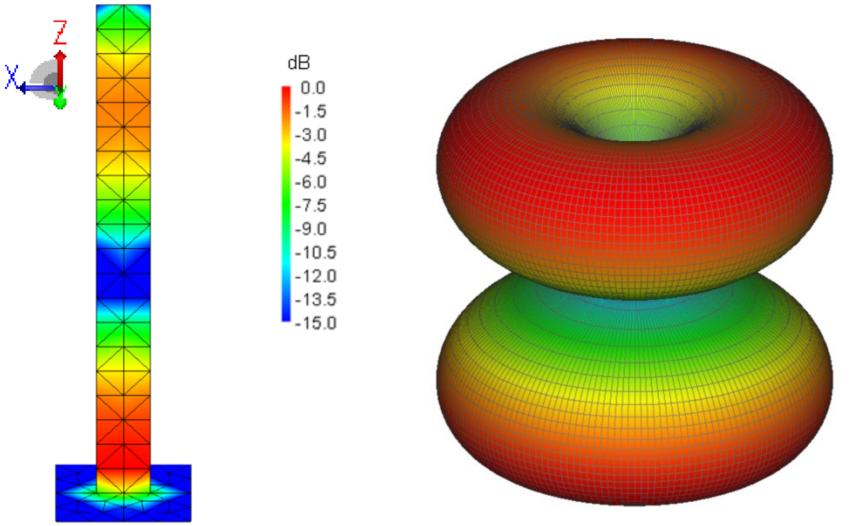

(a) (b)

Figure 4.32: Normalized characteristic mode 2 eigen properties at 210 MHz; (a) eigencurrent, (b) eigenpattern.

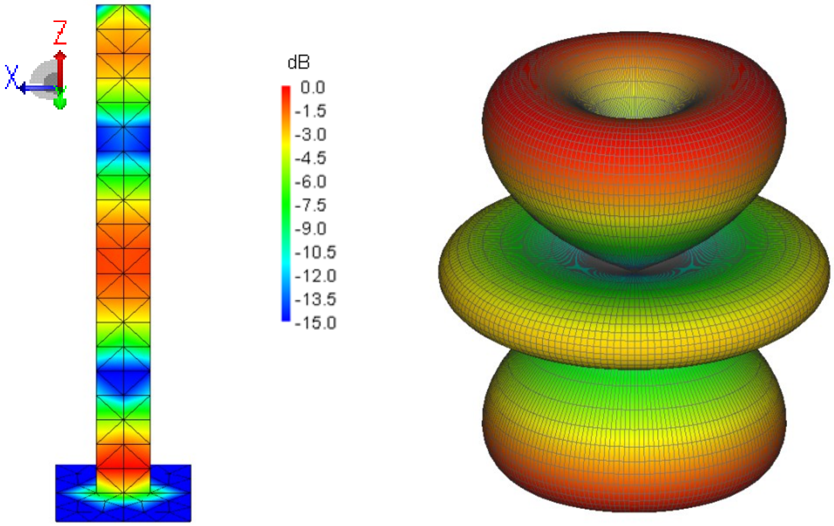

(a) (b)

Figure 4.33: Normalized characteristic mode 3 eigen properties at 210 MHz; (a) eigencurrent, (b) eigenpattern.

4.4.1 Dipole Feed $\lambda_M/32 \times \lambda_M/32$ Square Plate

The dipole feed is identical to the feed described in Section 4.2.1. The $|\alpha_n|$ (dB) of the dominant modes is shown in Figure 4.34. As expected the dipole feed configuration strongly excites CM 1. CM 1 remains the dominant mode excited up from 50 – 650 MHz except near the resonant frequency of CM 2. The dominant modes contribution to the total admittance is shown in Figure 4.35. It can be seen that with the dipole feed the total conductance and CM 1 conductance match from 50 to 650 MHz except around CM 2 resonance frequency (i.e. 385-515 MHz) since the mode is easily excited. Although CM 2 resonates at these frequencies, the dipole feed suppresses its effects. Unlike the $\lambda_M/8$ and $\lambda_M/16$ cases, in the $\lambda_M/32$ case, the conductance of CM 2 has the largest contribution to the total conductance. This occurs because the dipole feed is not placed in the optimum location to suppress CM 2 for the $\lambda_M/32$ case. Optimum feed location will be discussed in Chapter 5. The sum of all three dominant CM’s conductance is also shown in

Figure 4.35, where the total and sum agree. In the susceptance comparison, the total and CM 1 susceptance agree well at low frequencies and diverge around 225 MHz.

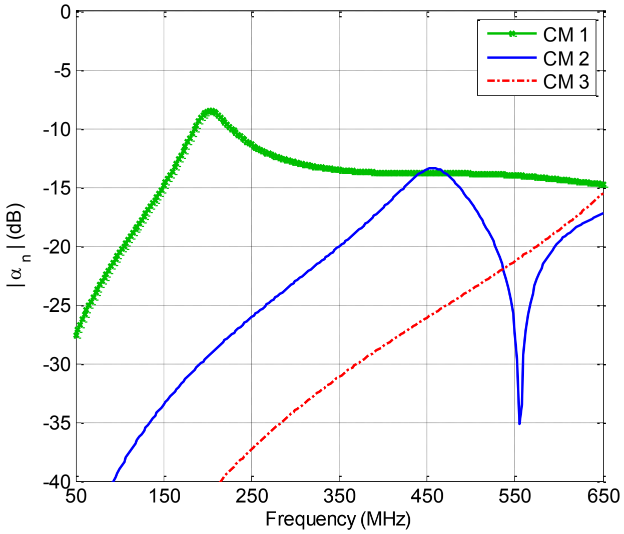

Figure 4.34: $|\alpha_n|$ (dB) of characteristic modes under consideration for dipole feed ($L_G = W_G = \lambda_M/32$).

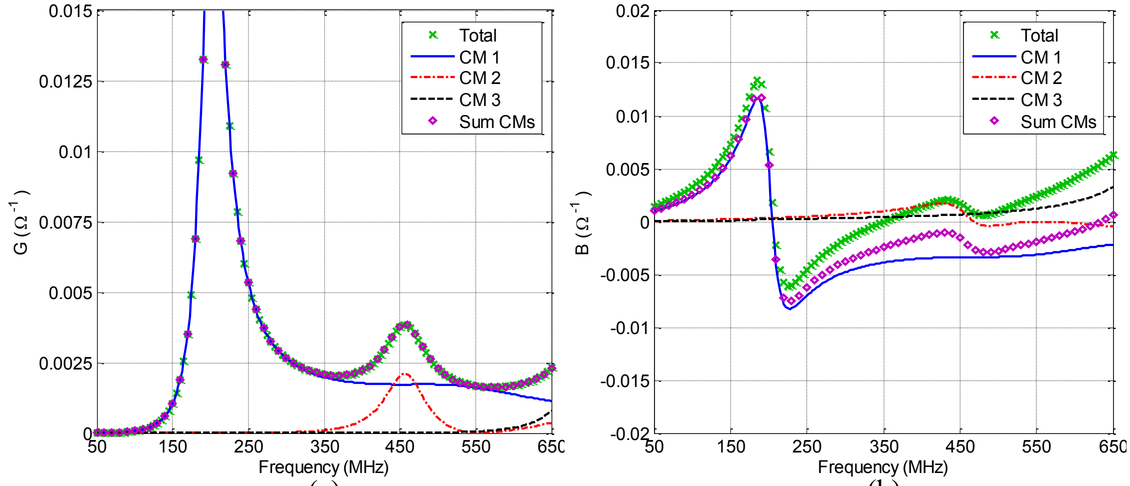

(a) (b)

Figure 4.35: Dipole feed comparing total, characteristic mode and sum of characteristic mode admittance; (a) conductance, (b) susceptance.

The realized total gain referenced to 50 Ω of the dominant modes is shown in Figure 4.36 for the XZ-plane at 250, 350, 450 and 550 MHz. Below 250 MHz CM 1 is the dominant mode contributing to the radiated pattern. Note that CMs 2 and 3 at 250 MHz, 3 at 350 and 450 MHz and 2 at 550 MHz have realized gains less than -25 dBi and thus do not show up in the figures. At 550 MHz all modes have contributions to the radiated pattern. When the four dominant modes are summed, the resulting pattern matches the total pattern. Note that with the dipole feed there are no major nulls at broadside. At 450 MHz a null forms at ±115°. This is due to the increased excitation of CM 2 for the $\lambda_M/32$ case.

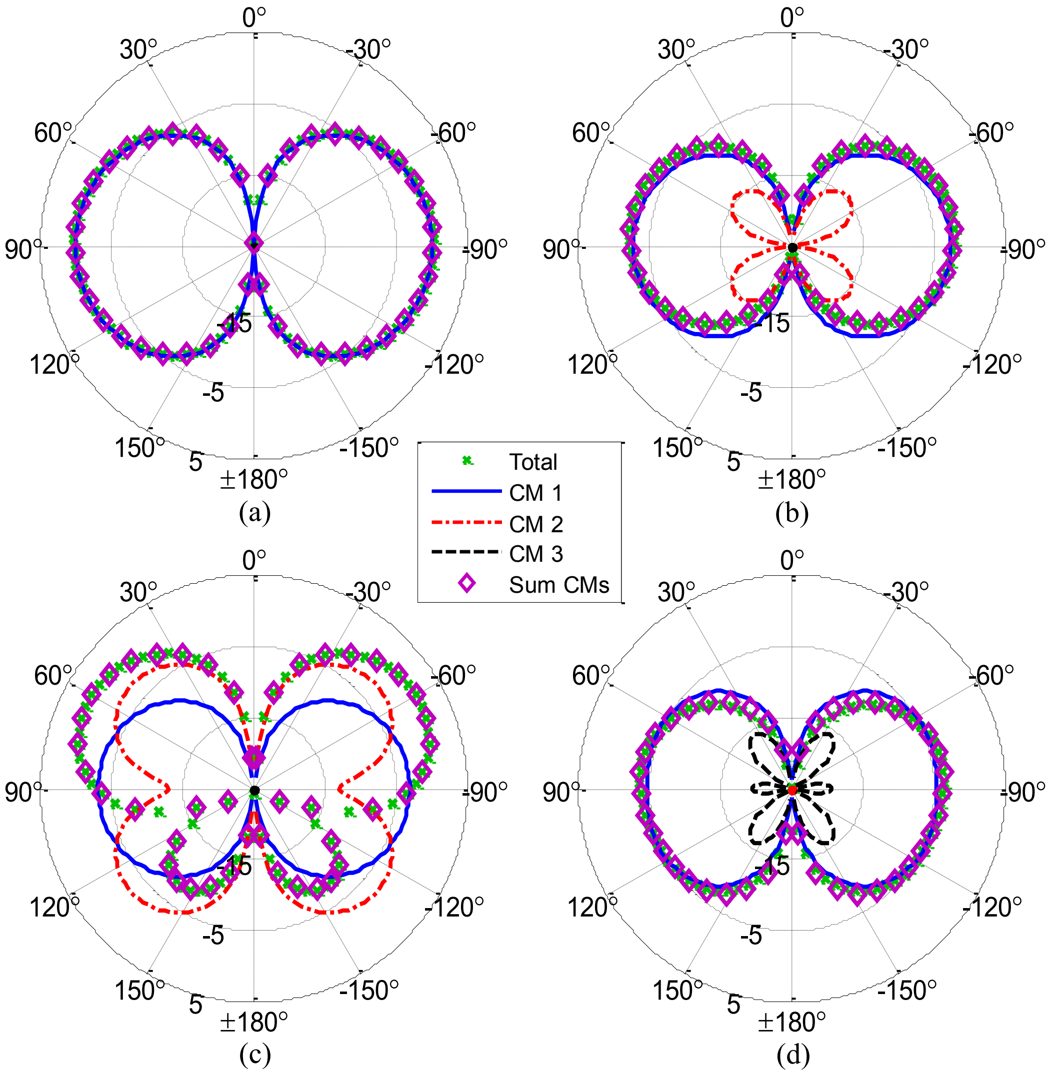

Figure 4.36: Dipole feed realized total gain (dBi) comparing total pattern, eigenpatterns and sum of eigenpatterns in the XZ-plane; (a) 250 MHz, (b) 350 MHz, (c) 450 MHz, (d) 550 MHz.

The patterns in the XY-plane are in shown Figure 4.37. It is desirable for the pattern to remain omnidirectional in the XY-plane. At 250, 350 and 450 MHz total and CM 1 radiation pattern match and is the only mode with realized gain above -25 dBi except at 450 where CM 2 is slightly excited.

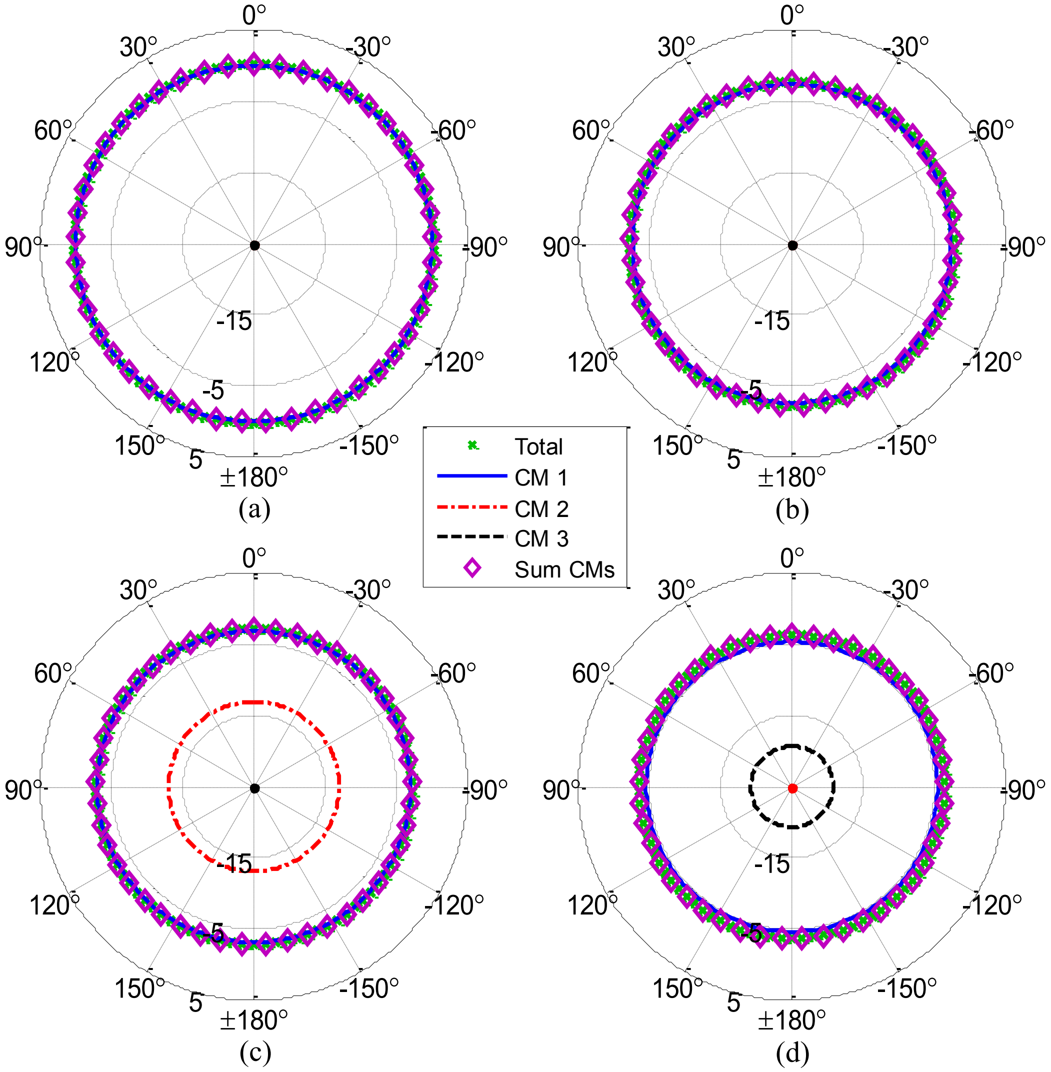

Figure 4.37: Dipole feed realized total gain (dBi) comparing total pattern, eigenpatterns and sum of eigenpatterns in the XY-plane; (a) 250 MHz, (b) 350 MHz, (c) 450 MHz, (d) 550 MHz.

4.4.2 Monopole Feed $\lambda_M/32 \times \lambda_M/32$ Square Plate

The monopole feed is the same as the one described in Section 4.2.2. The $|\alpha_n|$ (dB) of the dominant modes is shown in Figure 4.38. CM 1 is the dominant mode excited up to 375 MHz. CM 2 is strongly excited from 375-510 MHz then CM 1 is dominant till 650 MHz. CM 1 and 2 have the largest contribution to the admittance as seen in Figure 4.39. The monopole feed does not suppress the excitation of CM 2 since the feed is not placed in the null of the mode. At 450 MHz $|\alpha_2|$ is increased by 5.51 dB relative to the dipole feed.

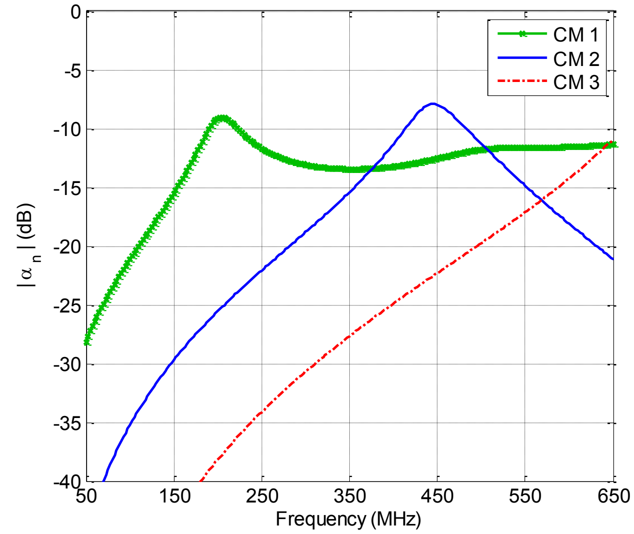

Figure 4.38: $|\alpha_n|$ (dB) of characteristic modes under consideration for monopole feed ($L_G = W_G = \lambda_M/32$).

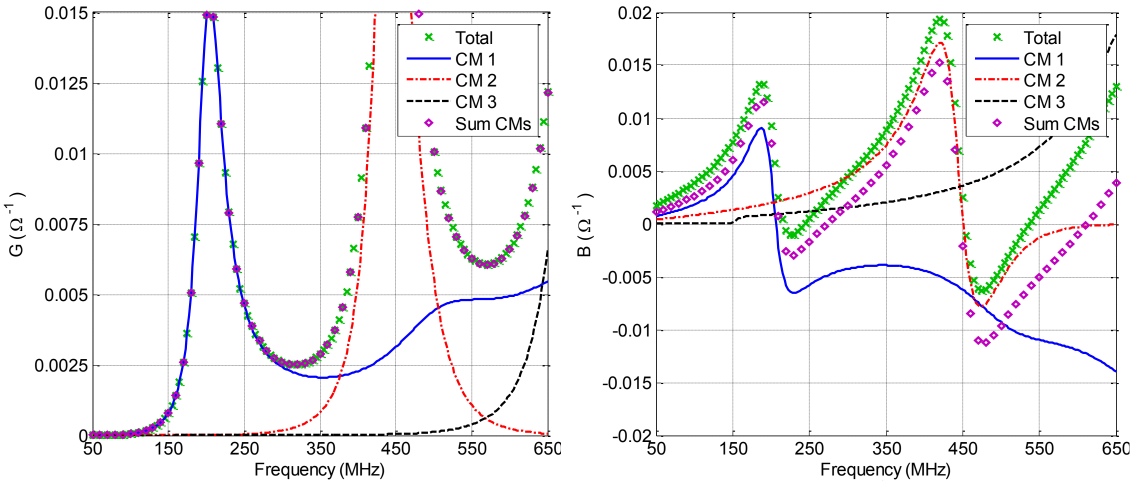

(a) (b)

Figure 4.39: Monopole feed comparing total, characteristic mode and sum of characteristic mode admittance; (a) conductance, (b) susceptance.

The realized total gain referenced to 50 Ω of the dominant modes is shown in Figure 4.40 for the XZ-plane at 250, 350, 450 and 550 MHz. Below 250 MHz CM 1 is the dominant mode contributing to the radiated pattern, however with the monopole feed, CM 2 is weakly excited. Note CM 3 at 250 MHz and 350 MHz has a realized gain less than -25 dBi and thus does not show up in the figures. At 450 and 550 MHz all modes have contributions to the radiated pattern with CM 1 and 2 having the largest impact. When the three dominant modes are summed the resulting pattern matches the total pattern. Note the monopole feed creates an undesirable null at broadside, especially at 550 MHz.

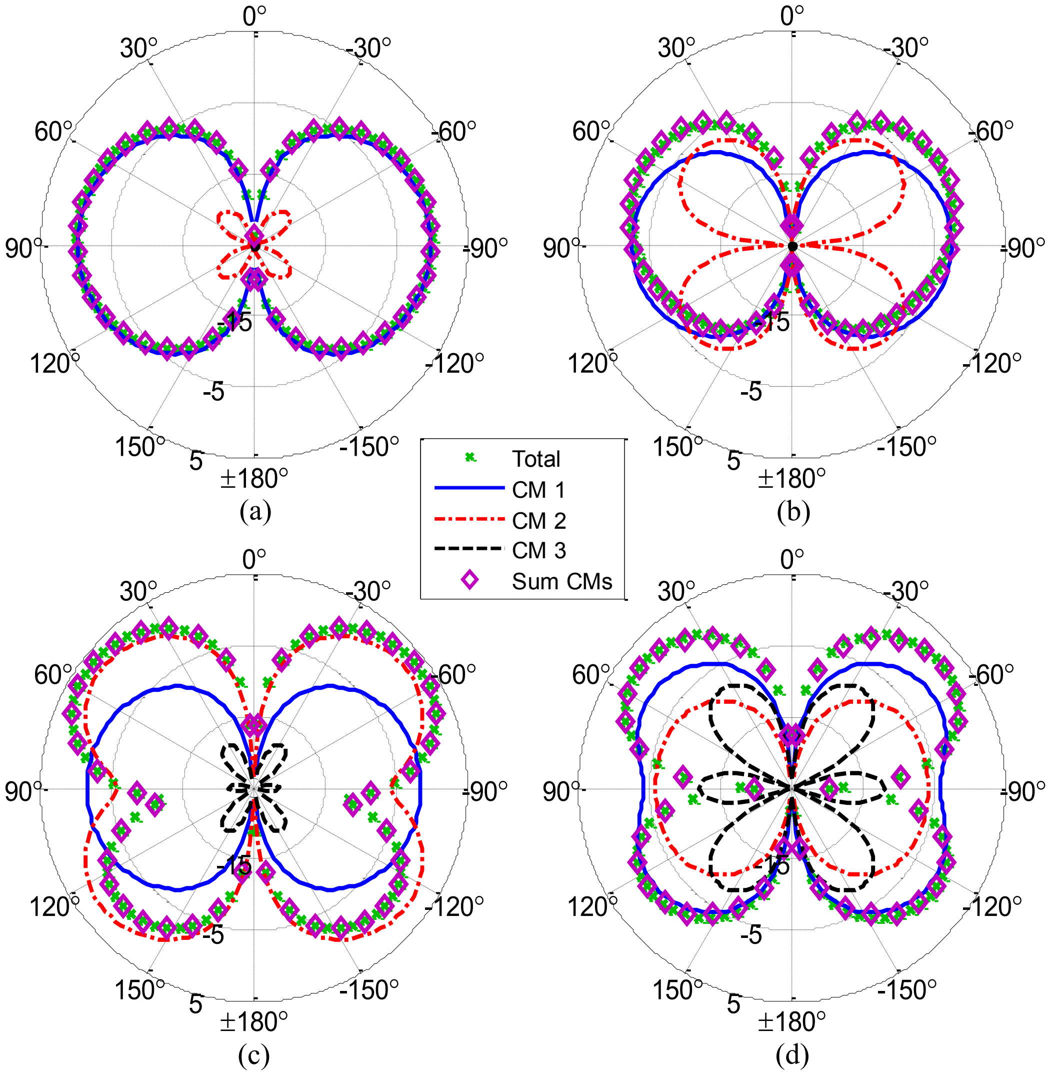

Figure 4.40: Monopole feed realized total gain (dBi) comparing total pattern, eigenpatterns and sum of eigenpatterns in the XZ-plane; (a) 250 MHz, (b) 350 MHz, (c) 450 MHz, (d) 550 MHz.

The realized gain in the XY-plane is shown in Figure 4.41. It is desirable for the pattern to remain omnidirectional in the XY-plane. At 250 MHz, CM 1 is the only mode with a realized gain larger than -25 dBi and at 350 MHz CM 2 is weakly excited. At 450 and 550 MHz, all modes have a realized gain larger than -25 dBi. In all cases CM 1 is the strongest mode excited. Between 350 and 450 MHz CM 2 becomes the dominant mode. At 550 MHz the dominant modes add destructively, resulting in a total realized gain less than -25 dBi.

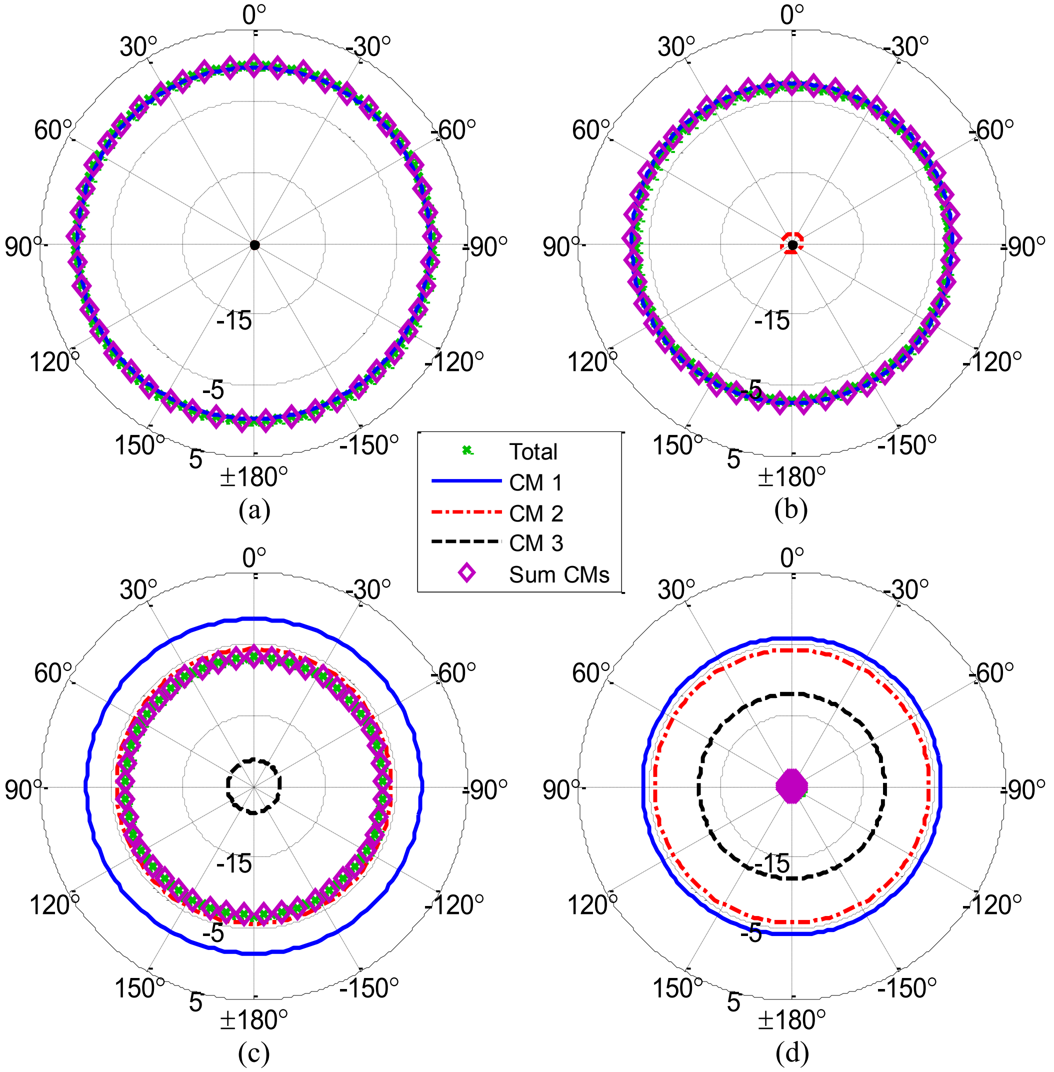

(a) (b) (c) (d)

Figure 4.41: Monopole feed realized total gain (dBi) comparing total pattern, eigenpatterns and sum of eigenpatterns in the XY-plane; (a) 250 MHz, (b) 350 MHz, (c) 450 MHz, (d) 550 MHz.

4.5 Summary

The effects of having an electrically small square ground plane ($L_G \times W_G$) in size were analyzed in this chapter. Results were shown for $L_G = W_G = \lambda_M/8$, $\lambda_M/16$ and $\lambda_M/32$. Dipole and monopole excitations were used to emphasize the excitation/suppression of the dominant modes on each antenna configuration. For both feed types (i.e. dipole and monopole) the conformal antennas radiate an omnidirectional radiation pattern below 350 MHz. At 550 MHz the dipole feed maintains an omnidirectional radiation pattern whereas the monopole feed has a null at broadside. By analyzing the weighting coefficients alone it would appear that the monopole feed would provide an omnidirectional pattern at the higher frequencies because CM 1 remains the dominant mode excited. However, CMs are frequency dependent and CM 1 and CM 2 undergo a transition over frequency where they essentially switch roles. The transition occurs above the resonant frequency of CM 2 where the eigenpatterns of CM 1 and CM 2 start to switch. CM 1 develops a null at broadside, whereas CM 2 becomes more omnidirectional. The change in pattern was explained by the change in eigencurrents of the modes for $\lambda_M/8$. The same modal transition occurs for all cases. It should be emphasized that these effects are caused by the plate loading of the antenna. The switching of the modes does not occur without the plate. The result of the mode transformation is that, the dipole feed location is preferred as it excites an omnidirectional pattern over the entire frequency band.

The resonant frequency of CM 1 without a plate was 267.5 MHz. Adding the plate increases the occupied volume of the antenna. When $L_G = W_G = \lambda_M/8$ the resonant frequency of CM 1 is reduced by 43.93% to 150 MHz. Similarly, the resonant frequency of CM 1 is reduced by 35.51% and 21.5% in the $\lambda_M/16$ and $\lambda_M/32$ cases, respectively.

It should be noted that the optimum dipole feed height to suppress CM 2 changes with the ground plane size. Decreasing the size requires the height to be raised to keep the feed in the eigencurrent null of CM 2. In the preceding work the height was held constant for a direct comparison. The optimum feed height to produce Q_{min} will be explored in Chapter 5.

Chapter 5 Determining Q_{min} Feed Location for Electrically Small Ground Planes

In this chapter, a design methodology based on the theory of CMs is introduced to determine the optimum feed location of conformal UAV antennas. For the purpose of this study, the optimum feed location is defined as the feed which provides the lowest quality factor while radiating an omnidirectional vertically polarized pattern. Exciting the antenna at the lowest Q location is important for designing a matching network to complement the antenna design. Designing a matching network decreases the mismatch factor of the antenna, thus improving the realized gain. The total Q is composed of the individual modal Qs, while the Q of a single mode is directly related to the mode's eigenvalue. For monopole and dipole antennas, the individual mode with the lowest Q is the dominant mode. However, to realize the lowest possible total Q, a feed location is chosen such that it strongly couples to the dominant mode, in addition it must weakly exciting higher order modes. This is true under the assumption that the dominant mode yields the desired radiation pattern. For ESAs, this assumption is generally applicable. In general, for an untuned antenna, several CMs will be excited by the feeding network contributing to the overall total Q. Since higher order CMs get excited by the feed network, the lowest possible Q is not always the location which strongly excites the dominant mode. Instead it will be shown in this research that a combination of exciting the dominant mode while simultaneously placing the feed in the null of the higher order modes yields the overall lowest total Q.

It is desirable to design conformal UAV antennas to cover the SINCGARS communication band from 30-88 MHz. At these frequencies, UAVs become electrically small implying electrically small antennas. Electrically small UAVs also have electrically small ground planes if excited as a monopole antenna. It is important to then determine the optimum height to feed the antenna for the Q_{min}.

Previously in Chapter 4 and Appendix B, the ground plane effects of an electrically small square and rectangular ground planes were investigated. The antenna element was centered on the ground plane. The dominant modes were identified and analyzed. CM 1 was found to be the desired mode for all cases since it radiated a vertically polarized omnidirectional radiation pattern. Its excitation is relatively insensitive to feed placement on the lower half of the vertical element. In order to minimize the stored energy around antenna it is necessary to suppress the higher order modes, specifically CM 2. CM 2 is the first higher order mode to get excited and also can have the largest contribution to the total susceptance depending on feeding network. It was shown that the dipole feed suppressed the excitation of CM 2 relative to the monopole feed. In previous studies the height of the dipole feed was held fixed at $H_F = 0.1625$ m for a direct comparison. However, the optimum location to suppress CM 2 depends on the ground plane size. It will be shown in this chapter that the Q_{min} feed location for electrically small square and rectangle ground planes corresponds to the eigencurrent null of CM 2, specifically at its resonant frequency. The resonant frequency of a CM is the frequency at which the mode is most excitable. Thus placing the feed in the deepest null minimizes excitation resulting in reduced stored energy. Previously it was shown that placing the feed in the eigencurrent null reduced excitation, however it was not known that the Q_{min} feed location needs to be placed in the null at its resonant frequency. Since CMs are frequency dependent, the eigencurrent null at 50 MHz is at a different location that the null at its resonant frequency. Several feed locations will be tested to investigate the Q_{min} location.

The antenna under consideration is shown in Figure 4.2, where the vertical flat plate height (H) in this analysis is 0.5 m and tail width (T_W) is 0.05 m. Note, throughout this chapter λ_M is defined as the wavelength at 150 MHz. The Q_{min} feed location at VHF is investigated in Section 5.1 for square ground planes and 5.2 for rectangular ground planes.

5.1 Q_{min} of Electrically Small Square Ground Plane

The Q_{min} feed location of square ground planes is determined in this section. Previously in Chapter 4 the dominant modes of square ground planes were studied. The same three ground plane sizes are considered in this section. CM 1 was found to be the dominant mode excited below 300 MHz for all cases. When a dominant mode exists on a structure, it is easily excitable and relatively insensitive to feed location. The dominant mode sets the baseline Q for the structure. The total Q cannot be lowered less than that of CM 1. The eigenvalue of a mode is proportional to the Q and can be calculated from its admittance as shown in (2.19). The total eigenvalue (λ_T) can be computed from the total admittance (2.20). It is important to understand the main modes contributing to λ_T. Feed location which minimizes λ_T results in Q_{min}.

CM 2 is the first higher order mode excited, it is believed that the feed which has the weakest excitation to CM 2 results in the feed with the lowest stored energy, thus Q_{min}. The normalized eigencurrents of CM 2 at their corresponding resonant frequencies are shown in Figure 5.1, when $L_G = W_G = \lambda_M/8$, $\lambda_M/16$ and $\lambda_M/32$ respectively. The location of the eigencurrent nulls (blue region) in the vertical section are listed in Table 5.1 where Z_s and Z_e correspond to the nulls starting and ending height, respectively. Note as the ground plane size is increased the eigencurrent null moves towards the ground plane. Five different feed locations are tested for each case to cover the entire null. Additionally, for each case a monopole feed ($H_F = 0$ m) is used as a reference resulting in six different feed locations. Each excitation is created by removing a 1 cm section across the vertical element at a height $H_F \pm 0.005$ m. A port is placed in the center of the gap.

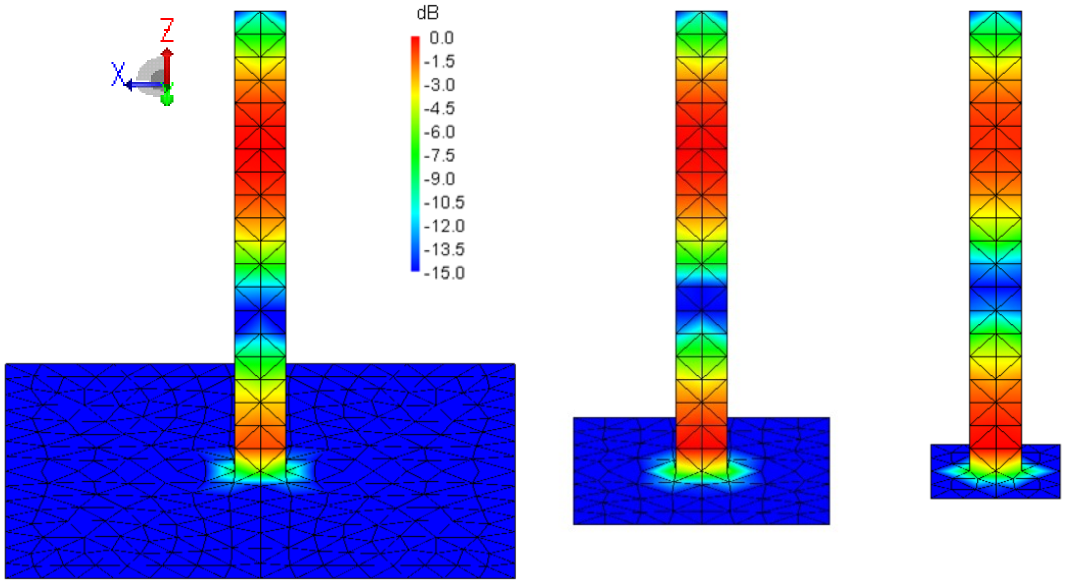

(a) (b) (c)

Figure 5.1: Normalized characteristic mode 2 eigencurrents at resonance; (a) $\lambda_M/8$ case at 432.5 MHz, (b) $\lambda_M/16$ case at 445 MHz, (c) $\lambda_M/32$ case at 470 MHz.

Table 5.1: Location of eigencurrent null of CM 2 for square ground planes sizes.

Case	Z_s (m)	Z_e (m)
$\lambda/8$	0.1375	0.2000
$\lambda/16$	0.1500	0.2125
$\lambda/32$	0.1750	0.2250

The total Q at 50 MHz for each feed location is listed in Table 5.2. The monopole feed location results in the largest Q for all cases. As the ground plane size increases the difference between largest Q and Q_{min} decreases. Q_{min} for all cases corresponds to the center of the eigencurrent null. Note that the Q does not drastically change over the eigencurrent null. The largest variation between feed locations occurs for the $\lambda_M/32$ case. The difference between max and min Q of the feed locations tested is 48.52, 92.11 and 285.00 for the $\lambda_M/8$, $\lambda_M/16$ and $\lambda_M/32$ cases, respectively. The Q_{min} feed location for the $\lambda_M/8$ case occurs at H_F = 0.175 m, closely followed by H_F = 0.15 m. For the $\lambda_M/16$ and $\lambda_M/32$ case, Q_{min} occurs at H_F = 0.175 and 0.2 m respectively.

Table 5.2: Square ground plane total Q at 50 MHz vs. H_F

H_F (m)	$\lambda/8$	$\lambda/16$	$\lambda/32$
0.000	286.66	405.21	756.66
0.125	240.00	318.03	495.63
0.150	238.47	314.16	478.18
0.175	238.14	313.10	474.34
0.200	240.80	316.77	471.67
0.225	243.62	320.40	474.53

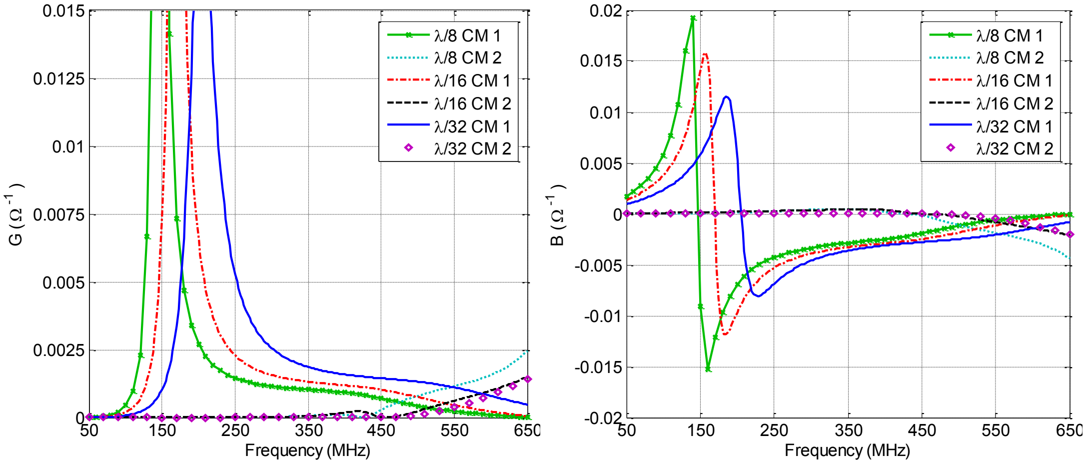

(a)

(b)

Figure 5.2: Q_{min} feed locations comparing CM 1 and CM 2 admittance for $\lambda_M/8$, $\lambda_M/16$ and $\lambda_M/32$ square ground planes; (a) conductance, (b) susceptance.

The admittance of CM 1 and 2 for all ground plane sizes are shown in Figure 5.2. From CM 1, it can be seen that the operation frequency increases as the size of the ground plane decreases. Note the suppression of CM 2 at its corresponding resonant frequency for each case. Previously in Chapter 4, CM 2 was suppressed for $\lambda_M/8$ case, however in $\lambda_M/16$ case was slightly excited (Figure 4.23(a)) and in $\lambda_M/32$ case was excited even more (Figure 4.35(a)). This occurred, because the feed was not placed at the optimum location to suppress CM 2. The excitation of CM

2 above its resonant frequency is due to the mode switching as discussed in Chapter 4 and Appendix B.

The realized vertical gain at broadside is shown in Figure 5.3-Figure 5.5, for the $\lambda_M/8$, $\lambda_M/16$, and $\lambda_M/32$ ground plane sizes, respectively. For each case, two plots are shown which compare the monopole excitation to the corresponding Q_{min} dipole excitation. Note the increased pattern bandwidth of the Q_{min} dipole excitation. Above 500 MHz the realized vertical gain is larger than -5 dBi, whereas the monopole excitation has transitioned into a null. Near 450 MHz, for $\lambda_M/8$ dipole excitation, the realized gain has a dip. This occurs because of the mode switching. As the ground plane size decreases the dip is less noticeable. Although the pattern becomes more uniform with smaller ground plane size, the tradeoff is the lowest frequency of operation. Decreasing the size of the ground plane increases the Q and shifts the resonant frequency of the dominant mode higher in frequency. Additionally, having a dipole excitation away from Q_{min} location, worsens the transition. Exciting the antenna using a dipole feed at any height between $H_F = 0.0$ m (i.e. monopole) and $H_F = Q_{min}$ increases the realized gain below the resonant frequency of CM 2. However, the tradeoff is a decreased excitation of the omnidirectional mode (i.e. CM 2) at higher frequencies, thus decreasing the realized gain at higher frequencies. Exciting the antenna using a dipole feed at a height above Q_{min} (i.e. $H_F > Q_{min}$) decreases the realized gain below the resonant frequency of CM 2. At higher frequencies the feed has a stronger excitation to the omnidirectional mode thus improving the realized gain.

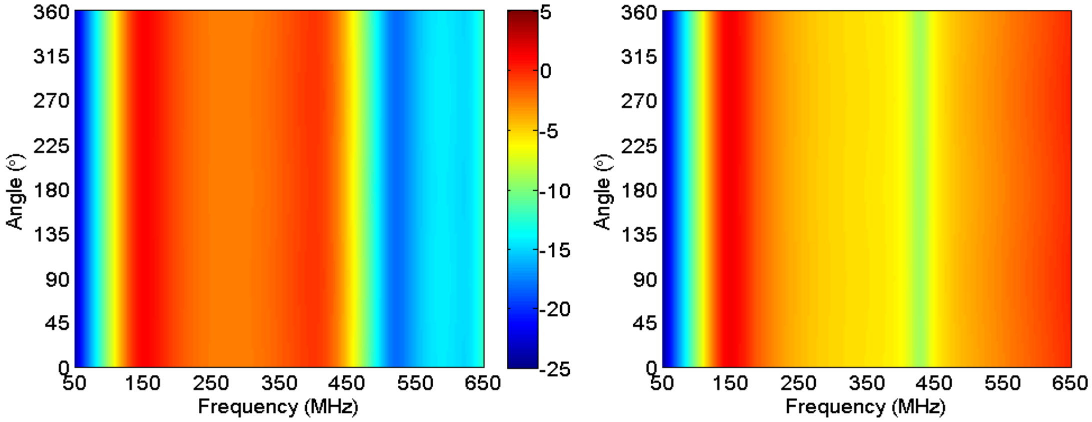

(a) (b)

Figure 5.3: Realized vertical gain (dBi) of $\lambda_M/8$ square ground in XY-plane; (a) H_F = 0.0 m, (b) H_F = 0.175 m (Q_{min}).

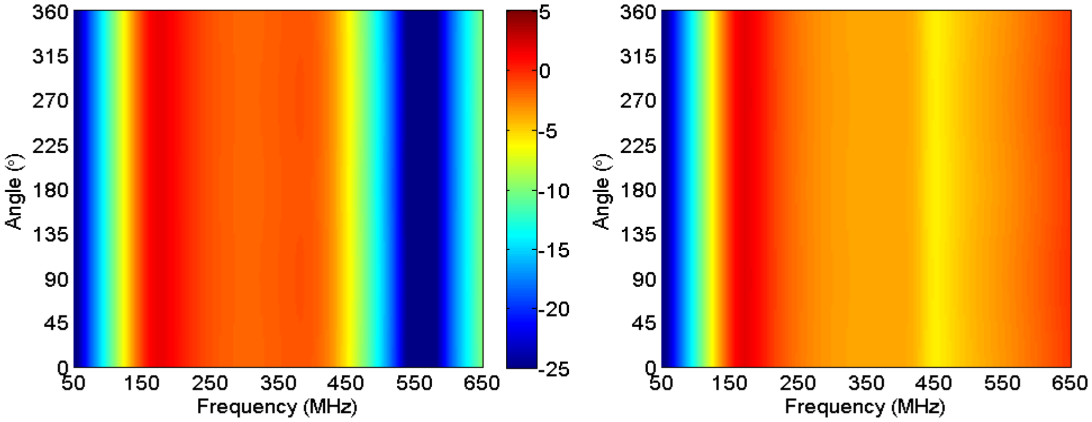

(a) (b)

Figure 5.4: Realized vertical gain (dBi) of $\lambda_M/16$ square ground in XY-plane; (a) H_F = 0.0 m, (b) H_F = 0.175 m (Q_{min}).

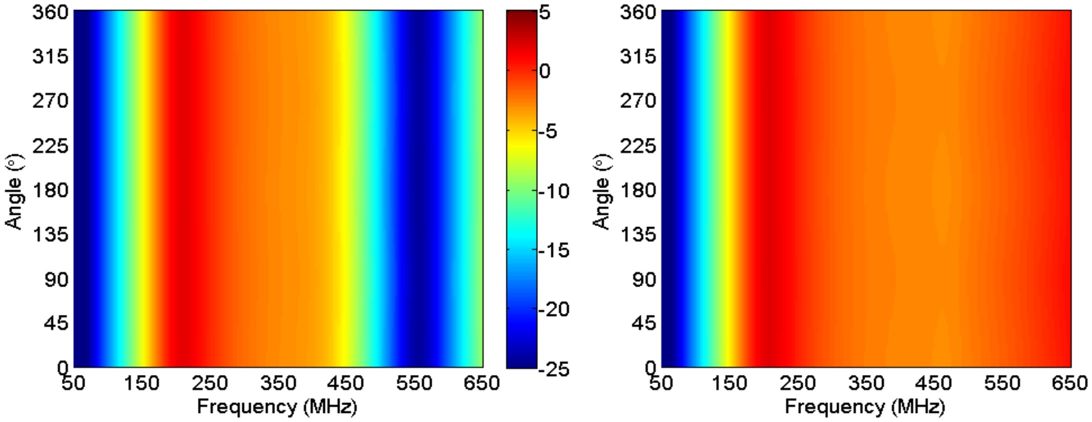

(a) (b)

Figure 5.5: Realized vertical gain (dBi) of $\lambda_M/16$ square ground in XY-plane; (a) H_F = 0.0 m, (b) H_F = 0.2 m (Q_{min}).

5.2 Q_{min} of Electrically Small Rectangular Ground Plane

The Q_{min} feed locations of rectangular ground planes are determined in this section. Previously, in 0, the dominant modes of rectangular ground planes were studied. The same cases are considered in this section. Similar to the analysis of the electrically small square ground plane, CM 2 dictates the Q_{min} feed location. The normalized eigencurrents of CM 2 at their corresponding resonant frequencies are shown in Figure 5.6, when $L_G = \lambda_M/8 \times W_G = \lambda_M/32$ and $L_G = \lambda_M/16 \times W_G = \lambda_M/32$.

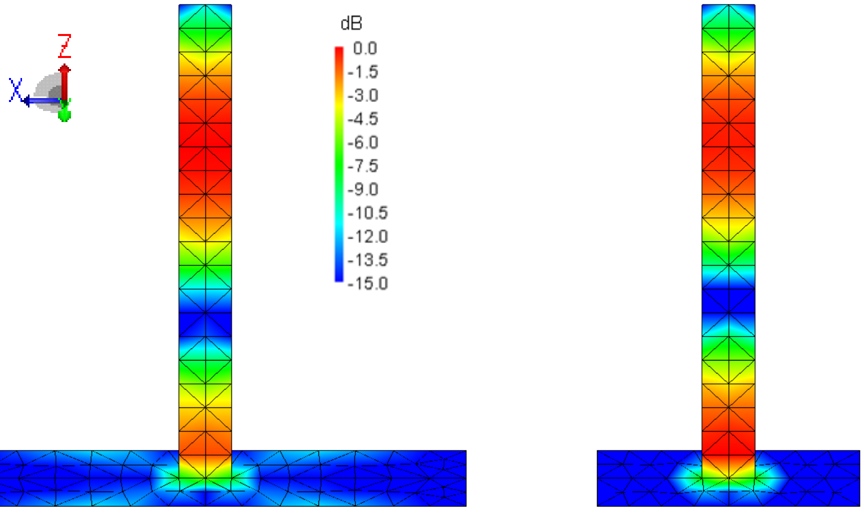

(a) (b)

Figure 5.6: Normalized characteristic mode 2 eigencurrents at resonance; (a) $L_G = \lambda_M/8 \times W_G = \lambda_M/32$ case at 430 MHz, (b) $L_G = \lambda_M/16 \times W_G = \lambda_M/32$ case at 452.5 MHz.

The location of the eigencurrent nulls of CM 2 residing in the vertical element are listed in Table 5.3. Similar to the square case, as the ground plane size is increased the eigencurrent null moves towards the ground plane. Six different feed locations are tested for each case to cover the entire null and the additional monopole feed.

Table 5.3: Location of eigencurrent null of CM 2 for different ground planes.

Case	Z_s (m)	Z_e (m)
$\lambda/8\times\lambda/32$	0.1375	0.2000
$\lambda/16\times\lambda/32$	0.1625	0.2125

The total Q of each feed location is listed in Table 5.4. Q_{min} feed location corresponds to the center of the eigencurrent null at CM 2 resonant frequency. When $L_G = \lambda_M/8 \times W_G = \lambda_M/32$ the Q_{min} feed location occurs at $H_F = 0.175$ m. Note the Q at $H_F = 0.15$ m is only 0.36 larger (0.12 % difference). The maximum deviation in Q across the eigencurrent null is 6.77, however the Q increase by 85.21 when fed like a monopole. When $L_G = \lambda_M/16 \times W_G = \lambda_M/32$ the Q_{min} feed location occurs at H_F = 0.175 m. The maximum deviation in Q across the null is 10.34 with an increase of 149.21 when fed like a monopole.

Table 5.4: Rectangle plate total Q at 50 MHz vs. H_F

H_F (m)	$\lambda/8 \times \lambda/32$	$\lambda/16 \times \lambda/32$
0.000	385.69	525.67
0.125	304.78	386.80
0.150	300.84	378.95
0.175	300.48	376.46
0.200	302.94	379.01
0.225	307.25	382.75

The admittance of CM 1 and 2 at the Q_{min} feed location for both rectangular ground planes are shown in Figure 5.7. Decreasing the ground plane size increases the operating frequency.

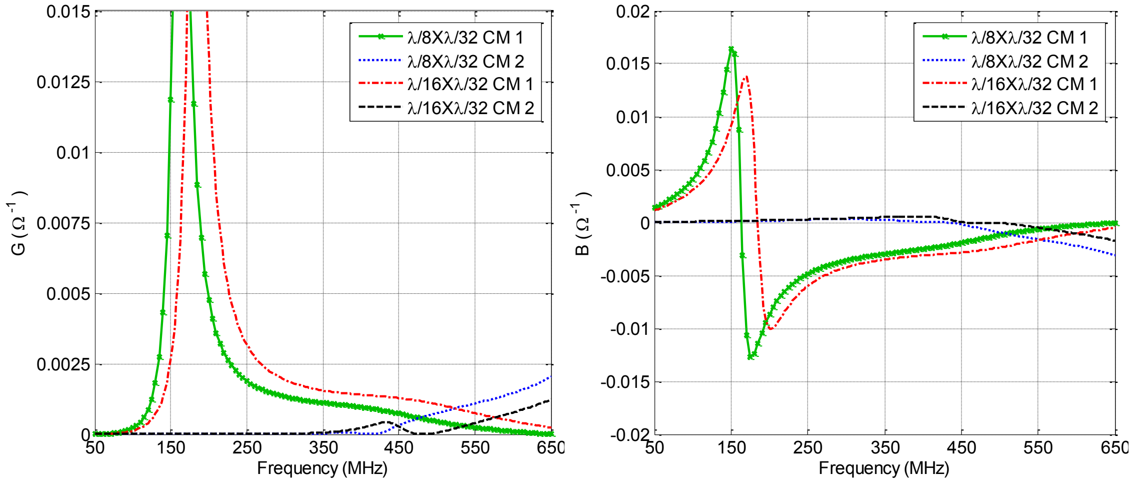

(a) (b)

Figure 5.7: Q_{min} feed locations comparing CM 1 and CM 2 admittance for $L_G = \lambda_M/8 \times W_G = \lambda_M/32$ and $L_G = \lambda_M/16 \times W_G = \lambda_M/32$ rectangular ground planes; (a) conductance, (b) susceptance.

The realized vertical gain at broadside is shown in Figure 5.8 and Figure 5.9, for the $\lambda_M/8 \times \lambda_M/32$ and $\lambda_M/16 \times \lambda_M/32$ rectangular ground plane sizes, respectively. For each case, two plots are shown which compare the monopole excitation to the corresponding Q_{min} dipole excitation. Similar to the square ground plane case, the Q_{min} feed location results in an increased pattern bandwidth. Again a dip in the realized gain occurs for Q_{min} feed due to the mode transition (i.e. switch between CM 1 and CM2). Decreasing the size of the ground plane creates a smoother transition however increases the operation frequency.

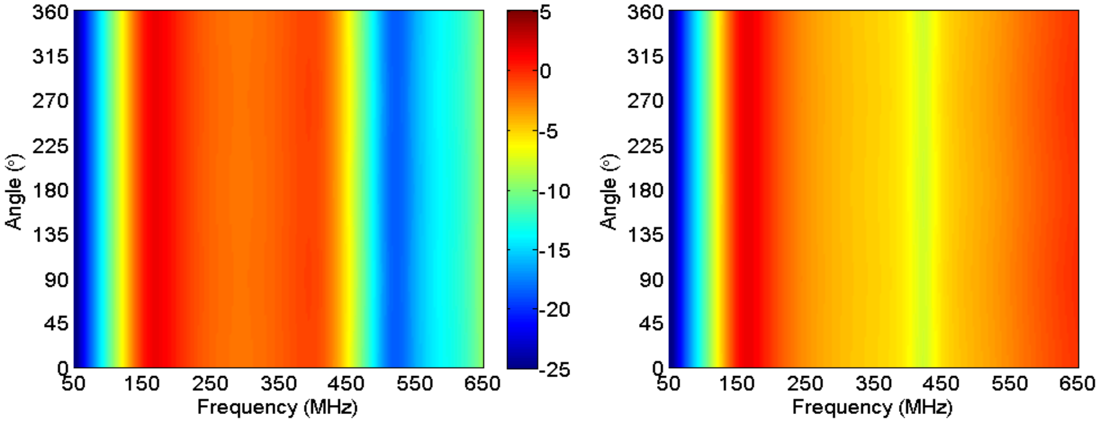

(a) (b)

Figure 5.8: Realized vertical gain (dBi) of $L_G = \lambda_M/8 \times W_G = \lambda_M/32$ rectangular ground in XY-plane; (a) $H_F = 0.0$ m, (b) $H_F = 0.175$ m (Q_{min}).

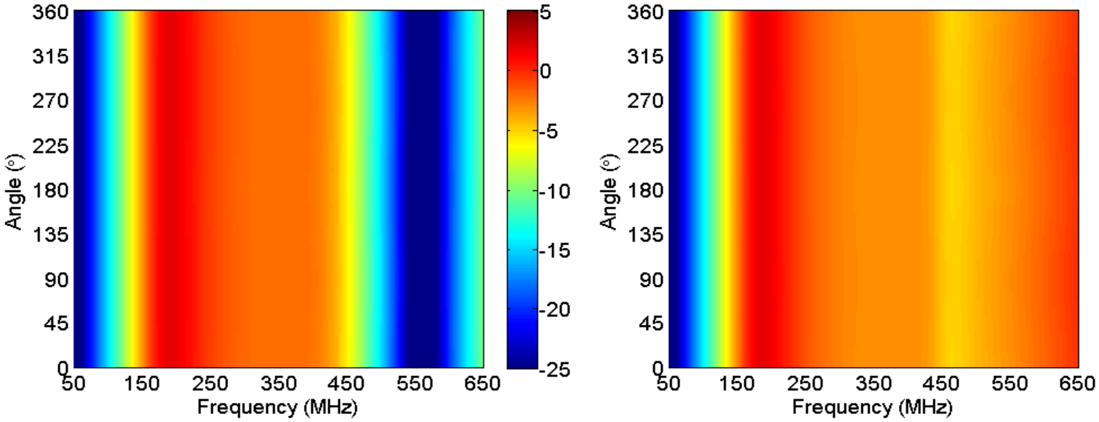

(a) (b)

Figure 5.9: Realized vertical gain (dBi) of $L_G = \lambda_M/16 \times W_G = \lambda_M/32$ rectangular ground in XY-plane; (a) $H_F = 0.0$ m, (b) $H_F = 0.175$ m (Q_{min}).

5.3 Summary

The Q_{min} feed location for electrically small square and rectangular ground planes was investigated in this chapter. It was numerically determined that the first higher order mode (CM 2) dictates the Q_{min} feed location. When the feed is placed in the null of CM 2, specifically at resonance the location corresponds to Q_{min}. Properties of the ground planes, specifically, the area (A), CM 1 resonant frequency (f_r) and CM 2 f_r are directly compared in Table 5.5 for both square and rectangular ground planes. Cases are ordered in terms of overall lowest Q. The $\lambda_M/8$ square ground plane has the largest area resulting in the overall lowest Q, while the $\lambda_M/32$ case has the smallest area resulting in the largest Q of all the cases considered. Note the $\lambda_M/16$ square ground plane has the same area as the $\lambda_M/8 \times \lambda_M/32$ rectangular ground plane; however, the rectangular ground plane has a lower Q. This is because CM 1 resonant frequency (f_r) of $\lambda_M/8 \times \lambda_M/32$ rectangular is lower than the $\lambda_M/16$ square ground plane. Directly comparing any two cases, the one which has a lower CM 1 resonant frequency has a lower Q. Thus by analyzing the dominant mode's resonant frequency one can gain insight into its relative Q behavior. CM 2 f_r also behaves in a similar manner except for the $\lambda_M/8 \times \lambda_M/32$ rectangular ground plane case which ultimately has the lowest f_r of all cases considered. Note the eigenpattern for CM 2 $\lambda_M/8 \times \lambda_M/32$ case is substantially different than all other cases (Figure B.2(b)), thus making it not suitable for a direct comparison.

Table 5.5: Q_{min} feed location comparison

Case	Q_{min}	A (m^2)	f_r CM 1 (MHz)	f_r CM 2 (MHz)
$\lambda/8\times\lambda/8$	238.14	0.2500	150.0	432.5
$\lambda/8\times\lambda/32$	300.48	0.0625	165.0	430.0
$\lambda/16\times\lambda/16$	313.10	0.0625	172.5	445.0
$\lambda/16\times\lambda/32$	376.46	0.0313	190.0	452.5
$\lambda/32\times\lambda/32$	471.67	0.0156	210.0	470.0

Chapter 6 Offset Antenna Element

In this chapter the antenna element (Region I) on the UAV is offset to the end of ground plane (Region II) as shown in Figure 6.1. The ground plane dimensions are fixed at $L_G = \lambda_M/8 \times W_G = \lambda_M/32$ at 150 MHz, where λ_M is defined as the wavelength at 150 MHz. This model represents many common UAVs such as the Prowler and NOAA UAV, shown in Figure 6.2. It can be seen that the fuselage width of the UAV is severely limited. It is assumed that copper can be embedded on the tail and fuselage to form the antenna. When the antenna element is offset, the geometry no longer has symmetry about the XZ- and YZ-planes.

In Section6.1 the dominant CMs are identified. Four CMs are considered to understand the tradeoffs and limitations of the UAV model. CM 1 is identified as the desired mode since it closely resembles the omnidirectional vertically polarized radiation pattern. However, unlike previous cases, the eigenpattern is no longer symmetric. Since modes are easily excited near resonance, CM 1 is shown at the resonant frequencies of all modes. CMs 2, 3 and 4 are only shown at their resonant frequencies.

In Section 6.2 the feeding network considerations are discussed. Tradeoffs exist between the operation bandwidth, high frequency cutoff and tolerable cross-polarization level. Three different feeding networks will be investigated to emphasize the excitation and or suppression of the dominant modes. The feeding networks will be placed on the vertical element. The feed heights are placed at H_F = 0.1625, 0.1125 and 0.0 m to illustrate the tradeoffs. The different feed cases are shown in Sections 6.3-6.5. To compare the different feed configurations the $|\alpha_n|$ (dB), modal admittance and realized gain will be shown. When the antenna element is offset on the ground plane, the dominant modes have a large current in the ground plane creating cross-polarization. The tradeoffs and limitations of the structure will be discussed. Note throughout this chapter unless otherwise stated, the eigenpatterns shown are the total pattern.

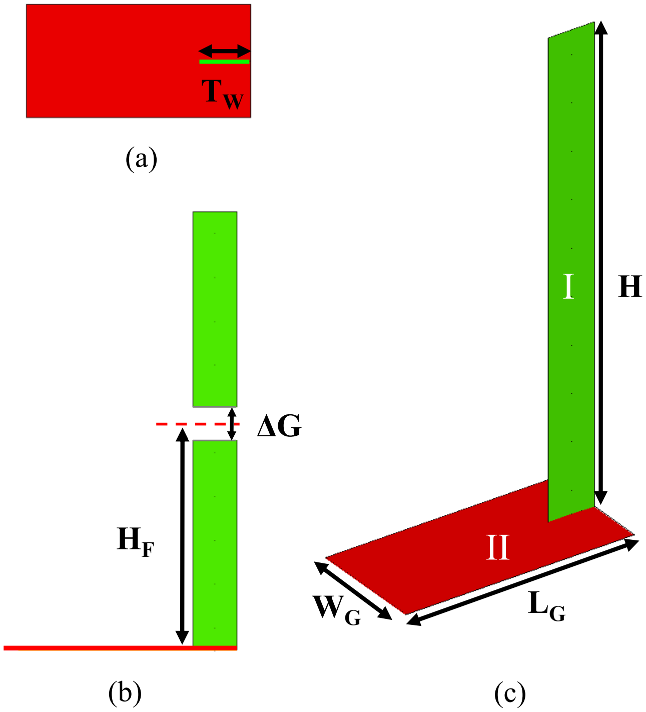

Figure 6.1: UAV antenna element offset on ground plane; (a) top view, (b) side view, (c) perspective view.

(a)

(b)

Figure 6.2: Modern UAVs with tail/vertical stabilizer centered at the end of fuselage; (a) Prowler UAV, (b) NOAA UAV.

6.1 $\lambda_M/8 \times \lambda_M/32$ Rectangular Plate

A CM analysis is performed on the UAV model when $L_G = \lambda_M/8 \times W_G = \lambda_M/32$. The dominant CMs are determined by the reduction process outlined in Chapter 3. Four dominant CMs are identified and the eigenvalue spectrum vs. frequency is shown in Figure 6.3. The modes resonate at 145, 300, 460 and 605 MHz. The eigenvalues (dB) are tabulated (Table 6.1) at 50, 150, 300 and 550 MHz to directly compare each mode. By studying the eigenpattern of CM 1, it was determined that this is the desired mode to excite, since its eigenpattern is the closest to the desired vertically polarized omnidirectional radiation pattern criteria over the desired frequency range. Since four dominant modes resonate in the frequency range of 50–650 MHz the eigencurrent and eigenpattern of CM 1 are shown at the resonant frequencies for each mode in Figure 6.4-Figure 6.7. The eigencurrent of CM 1 is predominantly contained in the lower half of Region 1 except at 605 MHz where it develops a current component in the upper half. Unlike when the antenna element is centered on the ground plane, the offset antenna element has a strong current component in the ground plane. Radiation from the ground plane will be shown to increase the cross-polarization. The cross-polarization in the XY-plane will be shown by decomposing the realized gain into the vertical and horizontal components.

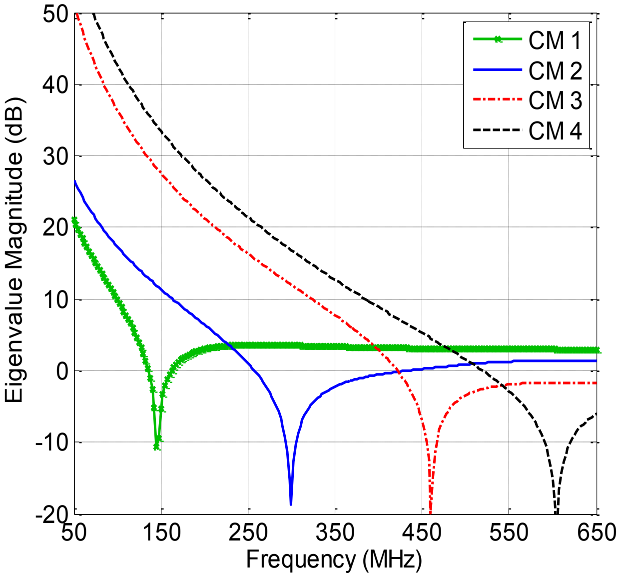

Figure 6.3: Eigenvalues spectrum of characteristic modes under consideration, $L_G = \lambda_M/8 \times W_G = \lambda_M/32$.

Table 6.1: |EV| (dB) when $L_G = \lambda_M/8 \times W_G = \lambda_M/32$

CM	50 (MHz)	150 (MHz)	300 (MHz)	550 (MHz)
1	21.1193	-5.2602	3.5406	3.0514
2	26.6641	11.3736	-18.7637	1.2628
3	51.3217	27.5546	11.9708	-1.9472
4	57.9601	33.4720	16.8127	-2.8683

When the antenna element is offset to the end of the ground plane, CM 1 is tilted at low frequencies (Figure 6.4(b)). As frequency increases the tilt decreases and the CM 1 becomes more omnidirectional (Figure 6.6(b)). This occurs because the eigencurrent component in the ground plane decreases with increased frequency and becomes more contained in the vertical element as seen in Figure 6.4-Figure 6.7(a). As a result, the cross-polarization from CM 1 decreases with frequency. At 605 MHz a strong current component forms in the upper half of the vertical element in addition to the strong component in the lower half, which leads to a pattern null at broadside, as seen in Figure 6.7(b).

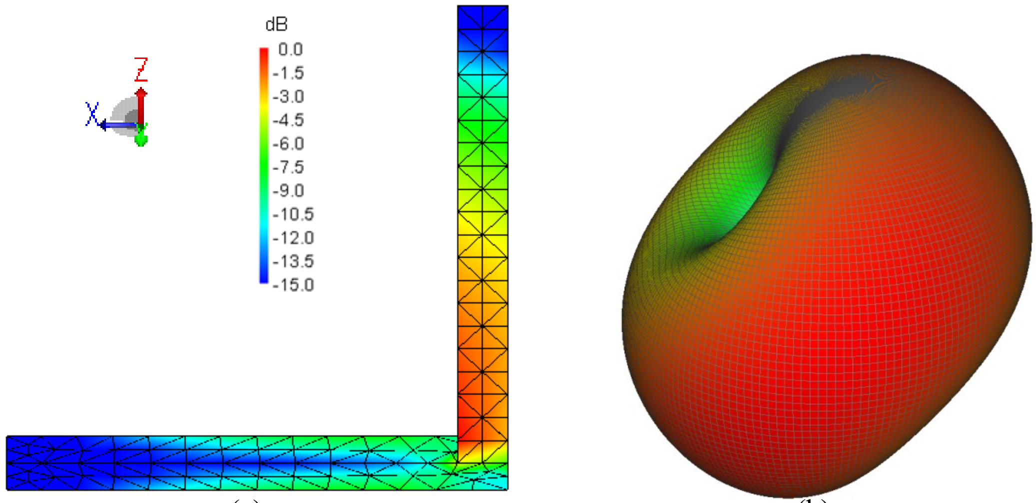

(a) (b)

Figure 6.4: Normalized characteristic mode 1 eigen properties at 145 MHz; (a) eigencurrent, (b) eigenpattern.

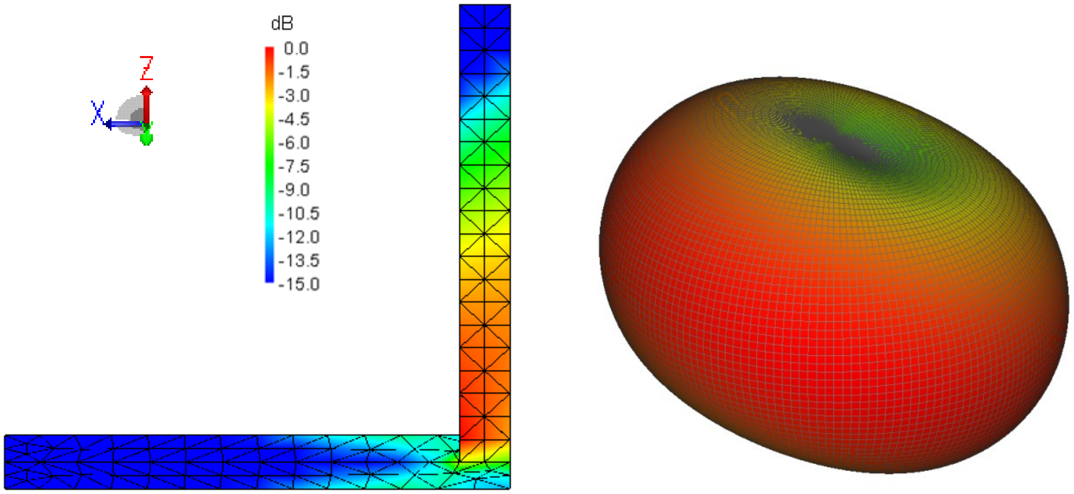

(a) (b)

Figure 6.5: Normalized characteristic mode 1 eigen properties at 300 MHz; (a) eigencurrent, (b) eigenpattern.

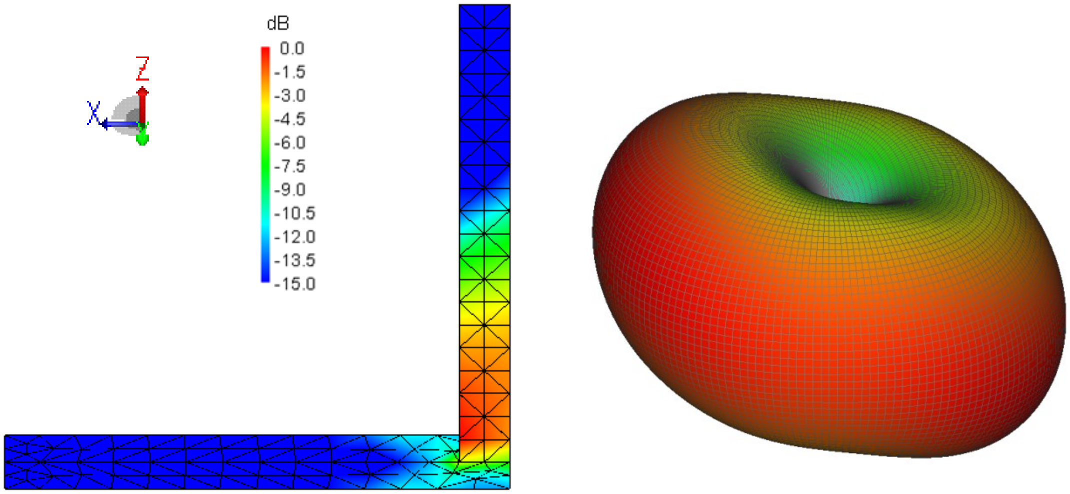

(a) (b)

Figure 6.6: Normalized characteristic mode 1 eigen properties at 460 MHz; (a) eigencurrent, (b) eigenpattern.

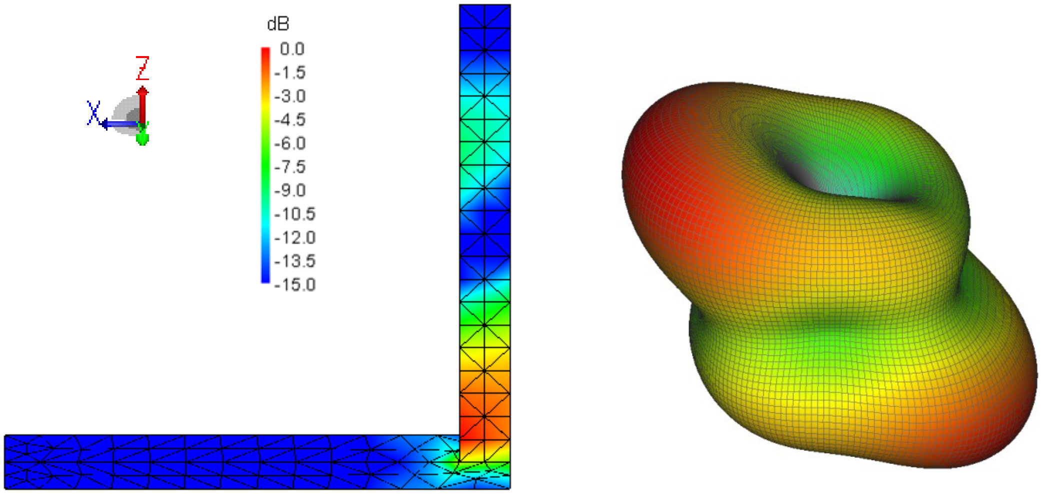

(a) (b)

Figure 6.7: Normalized characteristic mode 1 eigen properties at 605 MHz; (a) eigencurrent, (b) eigenpattern.

The remaining dominant characteristic modes are shown at their resonant frequencies as shown in Figure 6.8-Figure 6.10. Higher order modes tend to be excited over a narrow bandwidth near their resonant frequency. Thus, it is important to analyze each modes eigenpattern and eigencurrent to determine whether it is a desirable mode to excite or suppress. CM 2 is the first higher order mode considered since it has a resonant frequency of 300 MHz. At 300 MHz the eigenpattern has a near omnidirectional behavior about the YZ-plane. A feed placed near the center of the vertical element ($H_F = 0.25$ m) would strongly excite CM 2. At this height CM 1 eigencurremt is transitioning into a null and would be weakly excited. Therefore, the feed needs to be lowered since CM 1 has a more omnidirectional pattern. Additionally, CM 2 has a strong horizontal current component in the ground plane whereas CM 1 eigencurrent at 300 MHz has been reduced relative to that at 145 MHz. Thus, CM 2 will have a large cross-polarization component in the YZ-plane. By not fully exciting CM 2, the cross-polarization can be reduced.

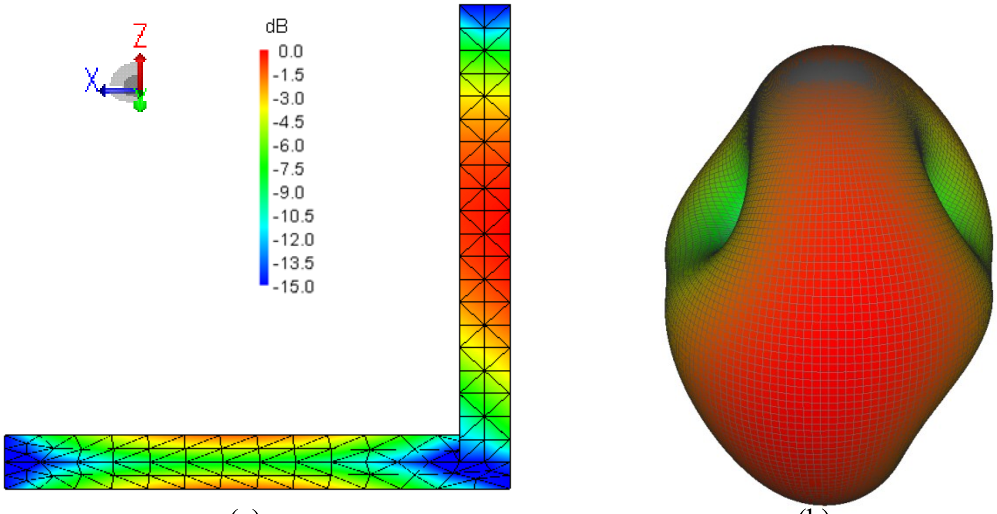

(a) (b)

Figure 6.8: Normalized characteristic mode 2 eigen properties at 300 MHz; (a) eigencurrent, (b) eigenpattern.

Above 300 MHz the next important mode to analyze is CM 3. Its eigencurrent and eigenpattern are shown in Figure 6.9 at its resonant frequency of 460 MHz. The eigenpattern has a null at broadside; therefore it is desirable to suppress this mode. To suppress CM 3 the feed needs to be placed in the null of the eigencurrent. The weakest excitation to the mode would occur when the feed is place in the region starting at $H_F = 0.15$ m extending upward till $H_F = 0.2$ m. The region described corresponds to the edges of the eigencurrent null (blue region) in the vertical element.

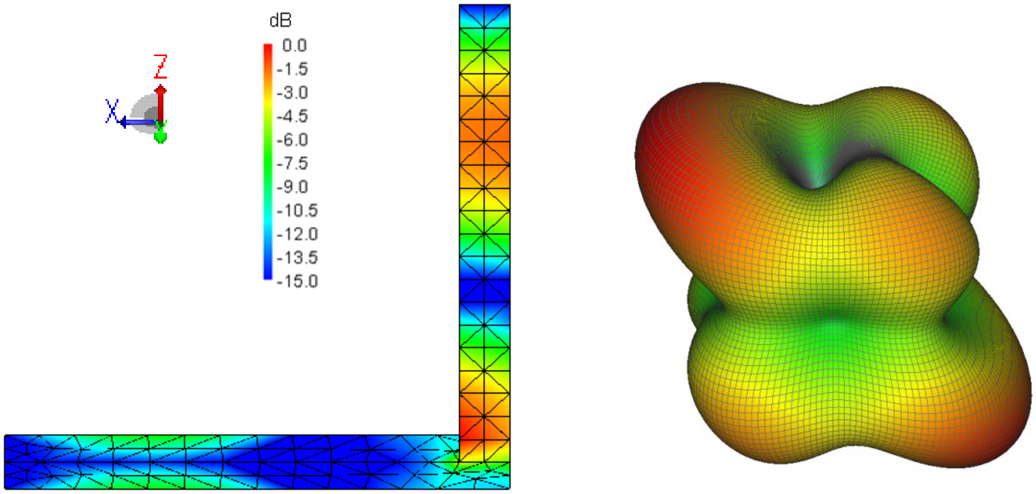

(a) (b)

Figure 6.9: Normalized characteristic mode 3 eigen properties at 460 MHz; (a) eigencurrent, (b) eigenpattern.

Finally, CM 4 is investigated. Its eigencurrent and eigenpattern are shown in Figure 6.10 at its resonant frequency of 605 MHz. The radiated eigenpattern is undesirable and typically a feeding network would be designed to suppress this mode. However, at 605 MHz CM 1 has also transformed into an undesirable mode. Since the desired criteria cannot be realized over the entire bandwidth, CM 4 is not consider when determining feed location.

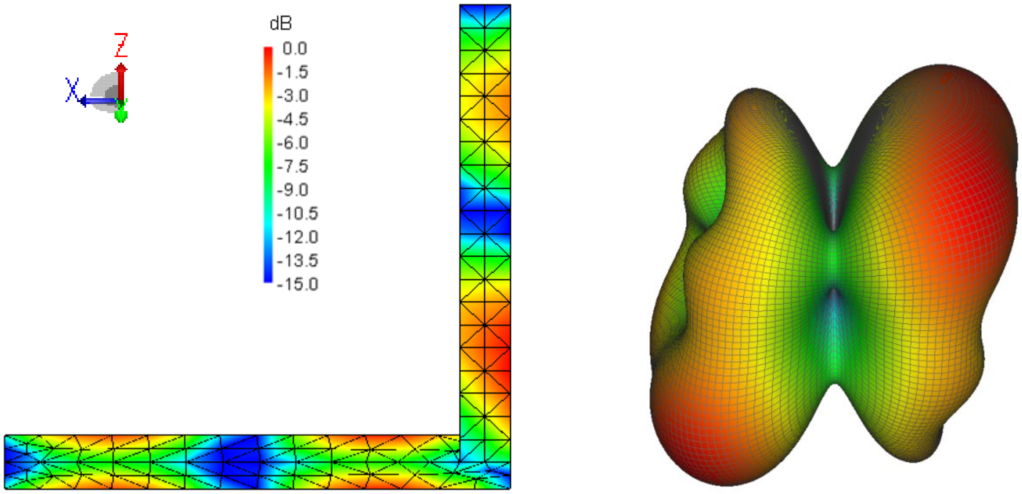

(a) (b)

Figure 6.10: Normalized characteristic mode 4 eigen properties at 605 MHz; (a) eigencurrent, (b) eigenpattern.

6.2 Feeding Network Considerations

The previous discussion helps the designer understand the tradeoffs and limitations of the structure under consideration. Three feeding networks will be considered to emphasize the increase excitation or suppression of the modes previously identified. Feed 1 (F1) will be place as $H_F = 0.1625$ m. This feed location will result in the strongest excitation of CM 2 at 300 MHz and weakest excitation on CM 3. Feed 2 (F2) will be placed at $H_F = 0.1125$ m. Lowering the height from F1 will decrease the excitation of CM 2 while increasing the excitation of CM 3. Finally, feed 3 (F3) is the monopole feed placed at $H_F = 0.0$ m. This feed has strong excitation to all modes, except CM 2.

Tradeoffs a designer may consider are; (1) Optimization for low frequency operation (VHF-band), (2) Lowest cross-polarization over desired frequency range, (3) largest bandwidth which maintains an omnidirectional radiation pattern, (4) a combination of (1)-(3). To meet criteria (1) the designer needs to feed the antenna in a location which provides the lowest Q. When the antenna becomes electrically small large impedance mismatches occur. Thus, to have an acceptable realized gain the antenna will require a matching network. By feeding the antenna in the Q_{min} location, the bandwidth and performance of the matching network can be improved. At VHF, CM 1 is the dominant mode that will be excited with a single port located on the vertical element.

To meet criteria (2) the desired frequency range would first have to be specified. If the antenna is to operate around 300 MHz, the goal would be to feed the antenna in a location which would weakly excite CM 2, as it has a strong horizontal current in the ground plane creating a cross-polarization component.

If the designer decides criteria (3) is most important, a feeding network will have to designed to extend the bandwidth of the antenna. This ultimately requires studying the dominant modes and how they change with frequency, since CMs are frequency dependent. CM 1 meets the required vertically polarized omnidirectional radiation pattern at 460 MHz. CM 3 is undesirable around its resonant frequency, thus to meet the criteria a feeding network needs to suppress this mode. The eigencurrent null in the vertical element start at a height of 0.15 m and continues till a height of 0.225 m. Placing the feed in the eigencurrent null will weakly excite CM 3, thus extending the antennas bandwidth to higher frequencies. Criteria (4) is really a compromise given the tradeoffs previously discussed.

6.3 Feed 1 $\lambda_M/8 \times \lambda_M/32$ Rectangular Plate

The first feed that is considered is F1. F1 will be placed at $H_F = 0.1625$ m corresponding to the eigencurrent null of CM 3 as shown in Figure 6.9(a). The objective is to suppress CM 3 to extend the bandwidth of the antenna. F1 feed location also strongly couples to CM 2 near its resonant frequency of 300 MHz. The tradeoff to extending the bandwidth past 460 MHz is accepting the effects of CM 2 at 300 MHz.

F1 is a dipole excitation and is created as described in Section 4.2.1. The $|\alpha_n|$ (dB) of the dominant modes is shown in Figure 6.11. As expected, CM 1 is the dominant mode excited at low frequencies up to 240 MHz. CM 1 remains one of the dominant modes excited; however, near the resonant frequencies of CM 2 and 4, there is large contribution from the input admittance of these modes as seen in Figure 6.12.

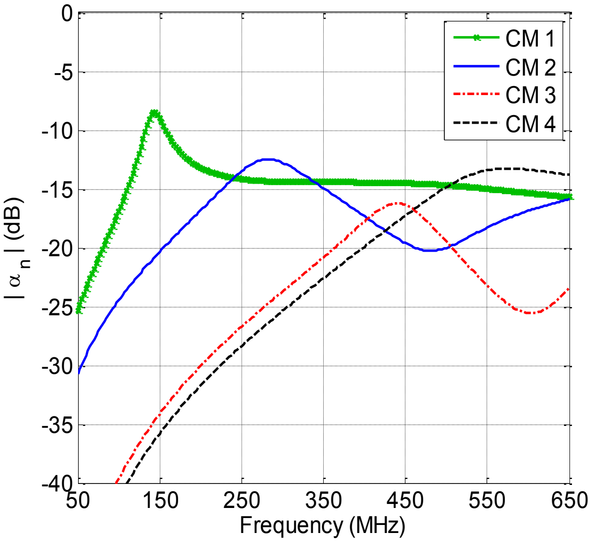

Figure 6.11: $|\alpha_n|$ (dB) of characteristic modes under consideration for dipole feed 1 ($L_G = \lambda_M/8 \times W_G = \lambda_M/32$).

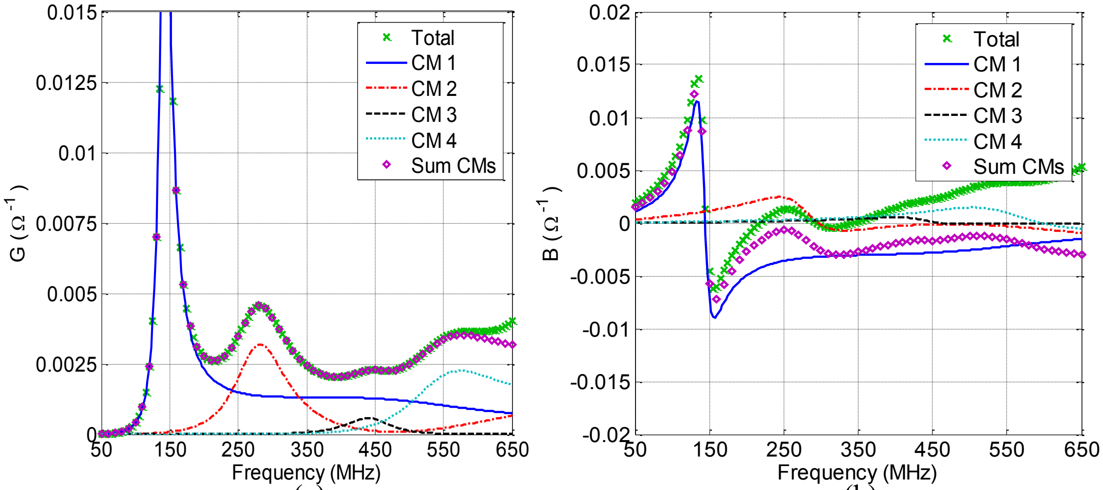

(a) (b)

Figure 6.12: F1 comparing total, characteristic mode and sum of characteristic mode admittance; (a) conductance, (b) susceptance.

The realized total gain (referenced to 50 Ω) of the dominant modes is shown in Figure 6.13 and Figure 6.14 for the XZ- and YZ-planes, respectively, at 145, 300, 460 and 605 MHz. Note the XZ- and YZ- planes correspond to elevation cuts at φ = 0 and 90°, respectively. CM 1 is strongly excited at all frequencies; however, is the only mode contributing to the radiated pattern below 145 MHz. F1 strongly excites CM 2 at its resonant frequency of 300 MHz. At 460 MHz all modes contribute to the radiated pattern and again at 605 MHz, except CM 3 is not excited. For all cases, when the dominant modes are summed, the resulting pattern matches the total pattern. Since the antenna structure is symmetric in the YZ-plane the eigenpatterns are also symmetric. No major nulls form at broadside in the YZ-plane. Note that CMs 3 and 4 at 145 MHz and 3 at 605 MHz have realized gains less than -25 dBi in the XZ-plane and thus do not show up in the figures. In the YZ-plane, CMs 3 and 4 at 145 and 300 MHz and CM 3 at 605 MHz have realized gains less than -25 dBi.

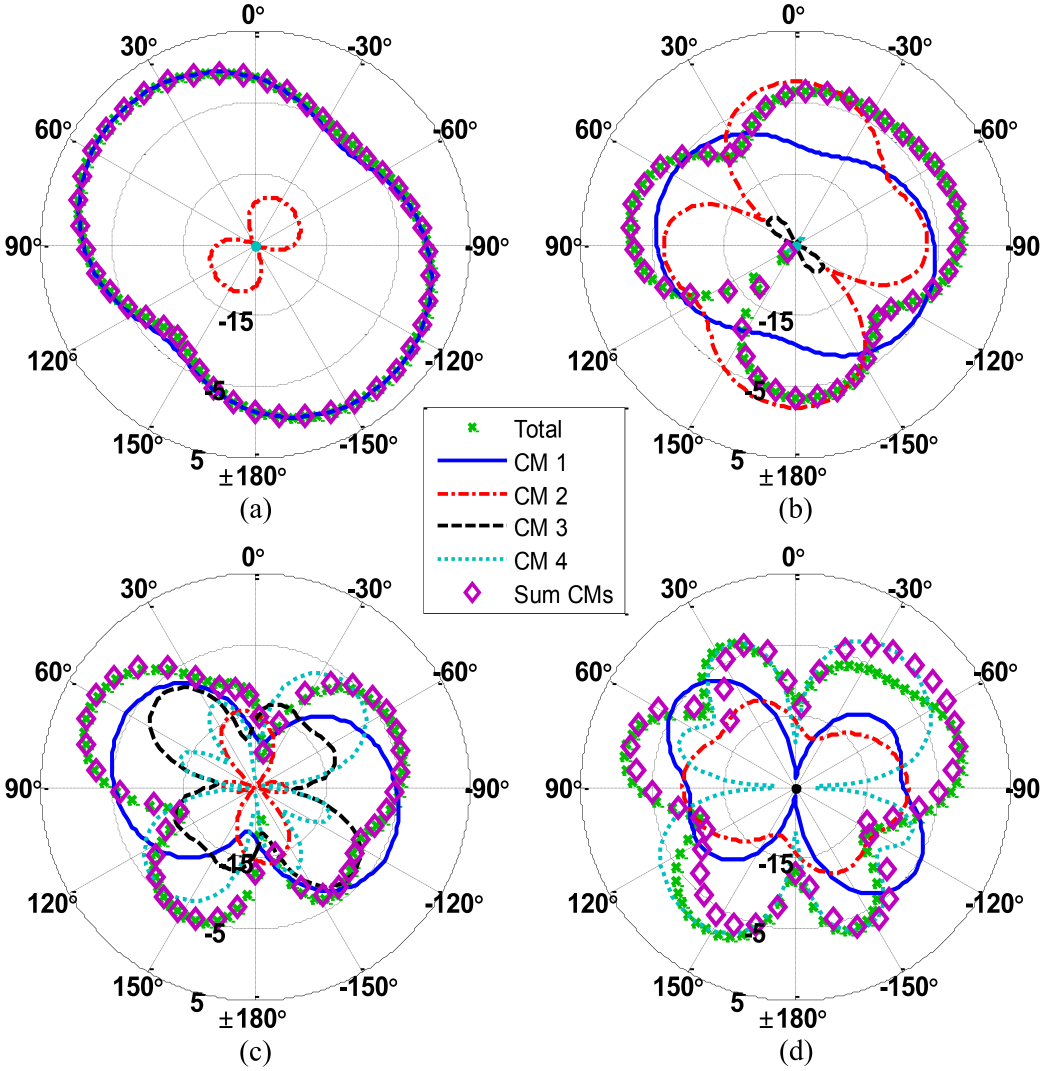

(a) (b) (c) (d)

Figure 6.13: F1 realized total gain (dBi) comparing total pattern, eigenpatterns and sum of eigenpatterns in the XZ-plane; (a) 145 MHz, (b) 300 MHz, (c) 460 MHz, (d) 605 MHz.

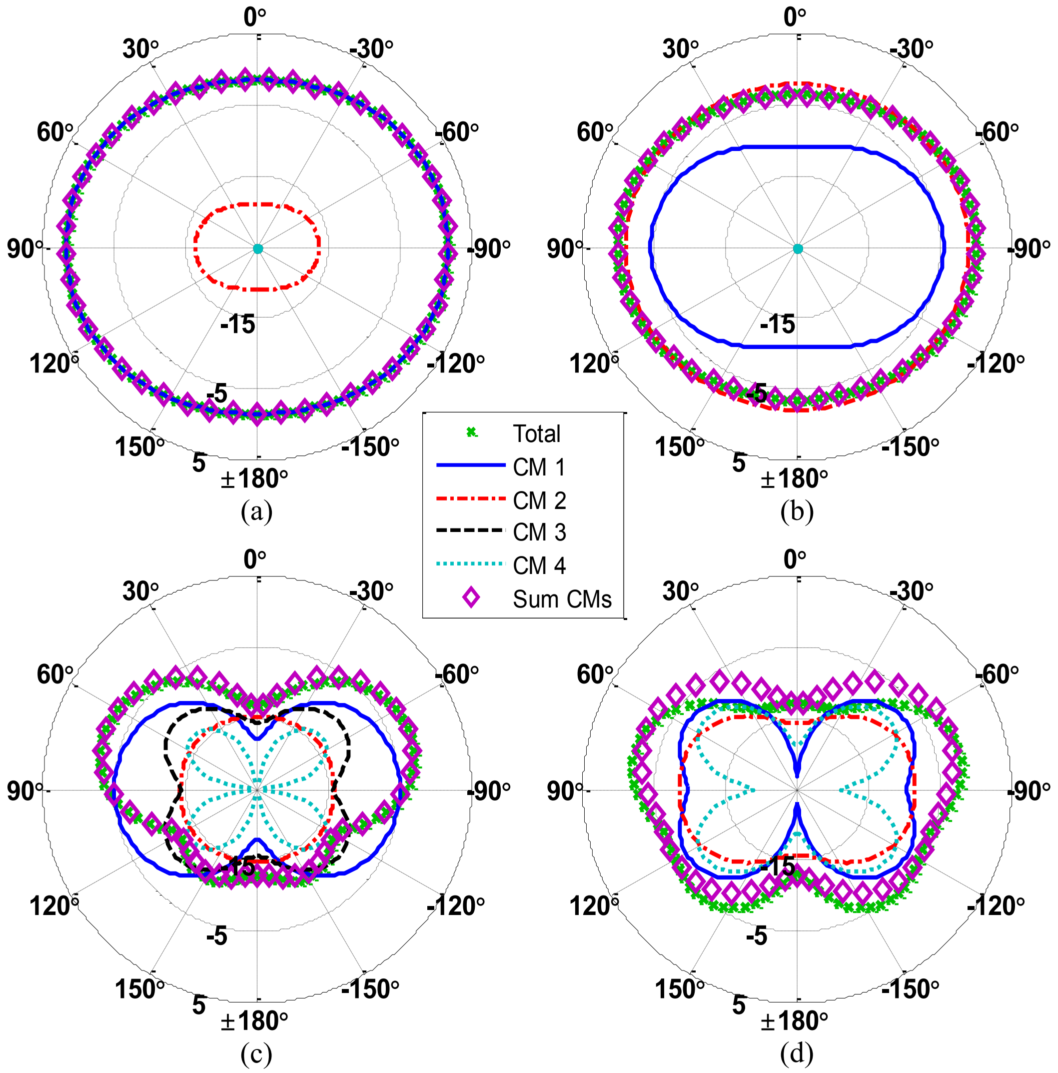

Figure 6.14: F1 realized total gain (dBi) comparing total pattern, eigenpatterns and sum of eigenpatterns in the YZ-plane; (a) 145 MHz, (b) 300 MHz, (c) 460 MHz, (d) 605 MHz.

The patterns in the XY-plane (i.e. θ = 90°) are shown in Figure 6.15 and Figure 6.16 for vertical- and horizontal-polarizations, respectively. It is desirable for the vertical-polarization to remain omnidirectional and have a low horizontal-polarization component. Since CM 1 is the dominant mode excited at low frequencies, CM 1 and total vertical and horizontal gain match. CM 3 and 4 do not have a vertical component larger than -25 dBi except CM 3 at 460 MHz. At 300 and 605 MHz, CM 1 and 2 have approximately equal vertical gain. CM 2 is the dominant mode contributing to the horizontal-polarization at 300 MHz. All modes contribute the horizontal -polarization at 460 MHz. CM 4 horizontal-polarization and the total have good agreement at 605 MHz.

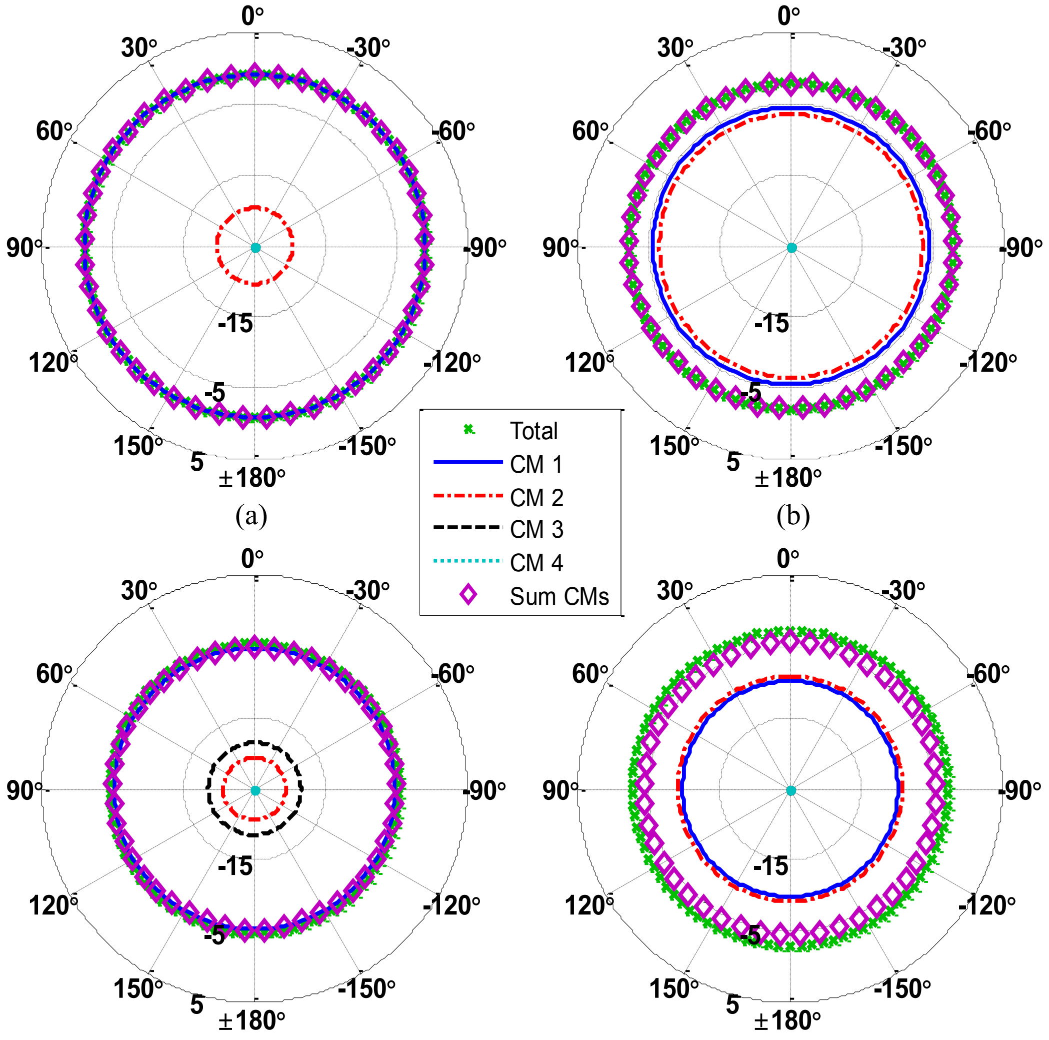

(a)

(b)

(c)

(d)

Figure 6.15: F1 realized vertical gain (dBi) comparing total pattern, eigenpatterns and sum of eigenpatterns in the XY-plane; (a) 145 MHz, (b) 300 MHz, (c) 460 MHz, (d) 605 MHz.

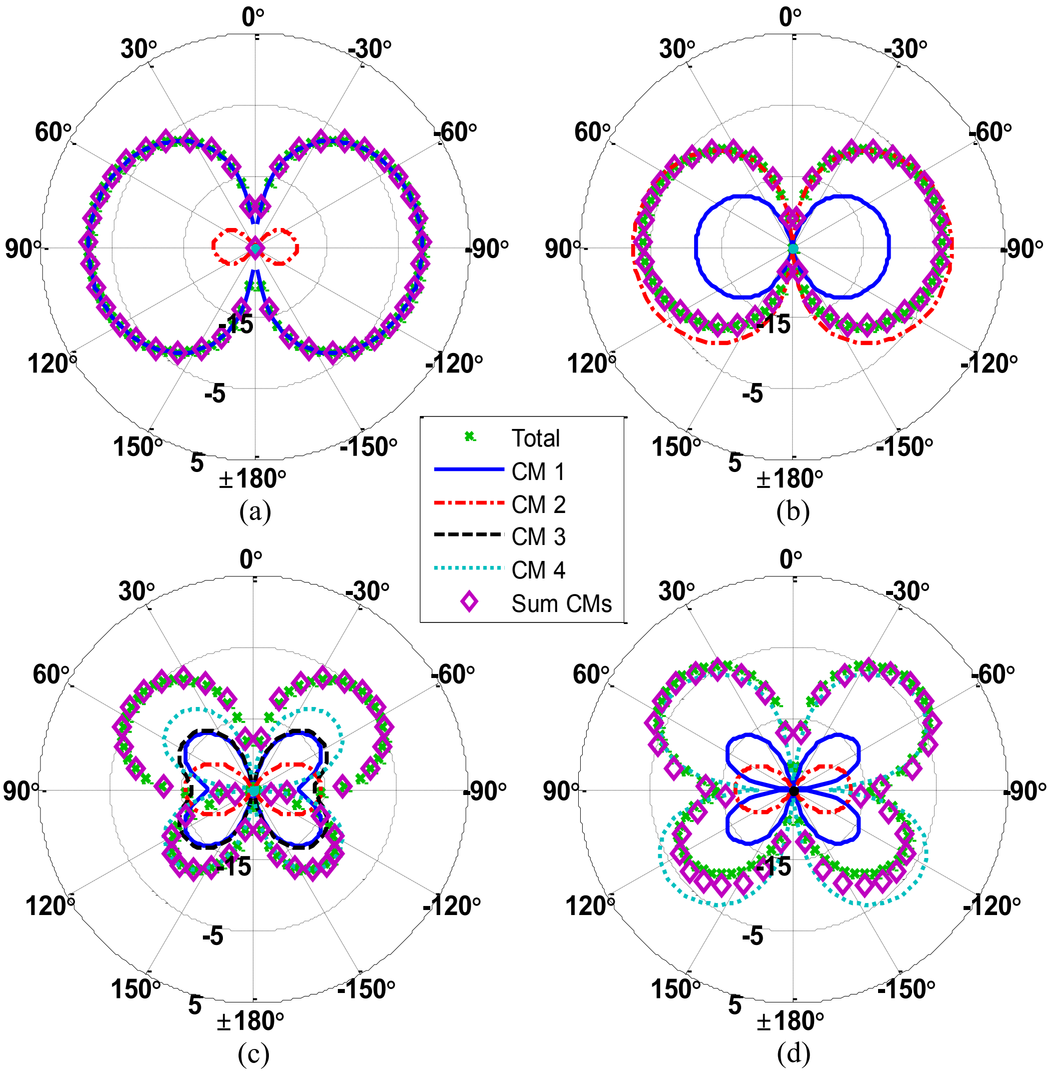

(a) (b) (c) (d)

Figure 6.16: F1 realized horizontal gain (dBi) comparing total pattern, eigenpatterns and sum of eigenpatterns in the XY-plane; (a) 145 MHz, (b) 300 MHz, (c) 460 MHz, (d) 605 MHz.

F1 realized gain (dBi) in the XY-plane is shown in Figure 6.17 for both vertical- and horizontal-polarization. Vertical-polarization remains omnidirectional vs. frequency with a realized gain larger than -10 dBi from 120-650 MHz. From 125-325 MHz the horizontal-polarization component has contributions from CM 1 and 2. Above 450 MHz the horizontal-polarization is mainly from CM 4.

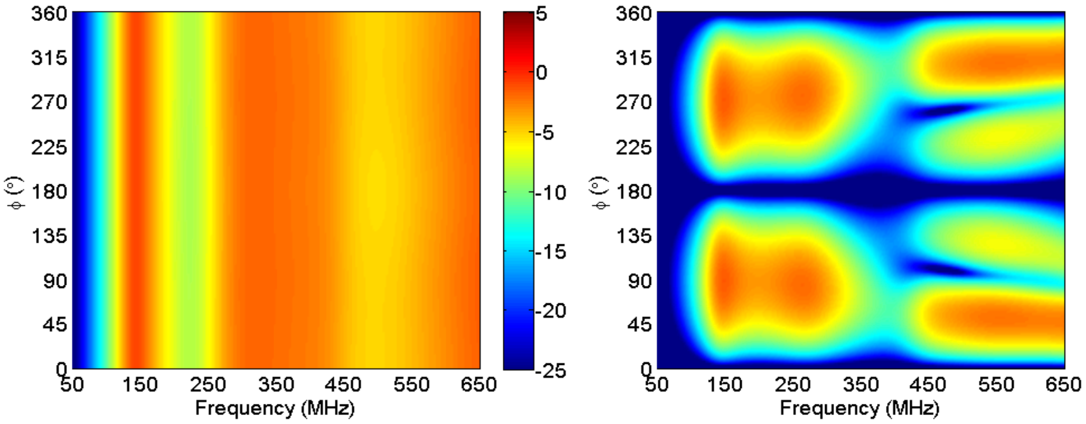

(a)

(b)

Figure 6.17: F1 realized gain (dBi) vs. frequency in XY-plane; (a) vertical-polarization, (b) horizontal-polarization.

6.4 Feed 2 $\lambda_M/8 \times \lambda_M/32$ Rectangular Plate

The second feed that is considered is F2. F2 will be placed at $H_F = 0.1125$ m. By decreasing the height relative to F1 the feed will result in a decreased excitation of CM 2 and an increased excitation of CM 3. The tradeoff with F2 is a reduction in cross-polarization around 300 MHz at the cost of exciting CM 3 higher in frequency, thus reducing the bandwidth of the antenna.

F2 is again a dipole excitation as described in Section 4.2.1 The $|\alpha_n|$s (dB) of the dominant modes are shown in Figure 6.18. Note that $|\alpha_2|$ is decreased by 1.02 dB and $|\alpha_3|$ is increased by 4.49 dB at their corresponding resonant frequencies of 300 and 460 MHz respectively. The admittance is shown in Figure 6.19. The changes in $|\alpha_n|$ can be seen in the conductance, where CM 2 conductance has decreased relative to F1. The result is CM 1 and 2 similar conductance levels near CM 2 resonant frequency. Additionally, CM 3 conductance has significantly increased becoming the dominant mode contributing to the radiated pattern near its resonance frequency of 460 MHz.

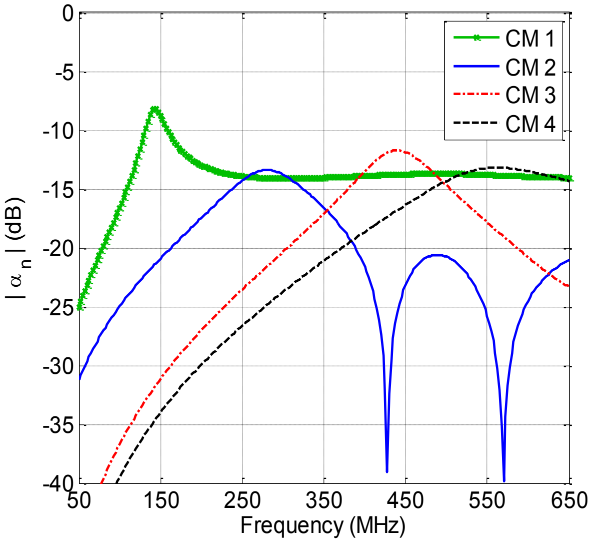

Figure 6.18: $|\alpha_n|$ (dB) of characteristic modes under consideration for dipole feed 2 ($L_G = \lambda_M/8 \times W_G = \lambda_M/32$).

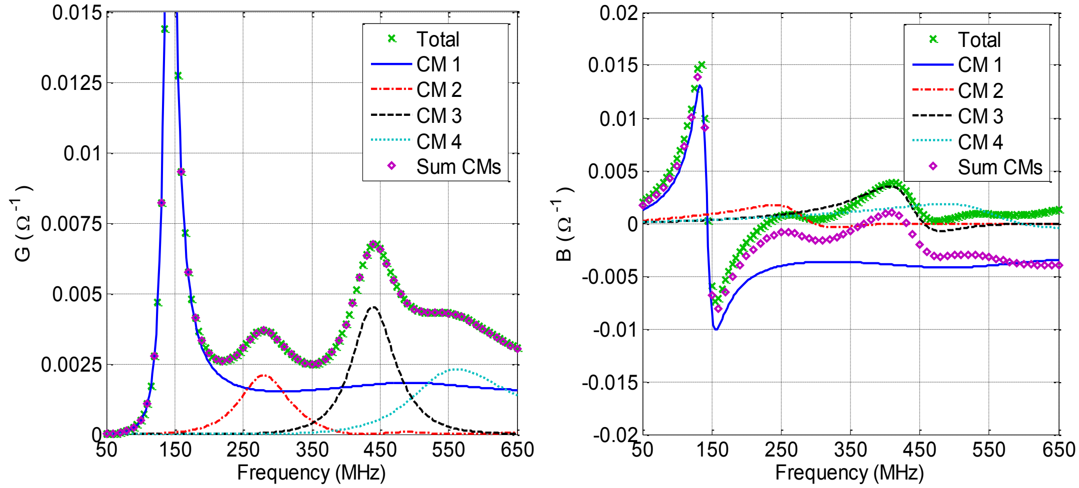

(a)

(b)

Figure 6.19: F2 (H_F = 0.1125 m) comparing total, characteristic mode and sum of characteristic mode admittance; (a) conductance, (b) susceptance.

The realized total gain (referenced to 50 Ω) of the dominant modes is shown in Figure 6.20 and Figure 6.21 for the XZ- and YZ-plane, respectively at 145, 300, 460 and 605 MHz. Although, CM 2 excitation has been decreased relative to F1, the mode still has a large contribution to radiated pattern, as seen in Figure 6.20(b). Furthermore, as discussed in the conductance analysis, one of the major changes is the increased excitation of CM 3 near its resonance frequency. Therefore, CM 3 has the largest impact on the radiated pattern as seen in Figure 6.20(c).

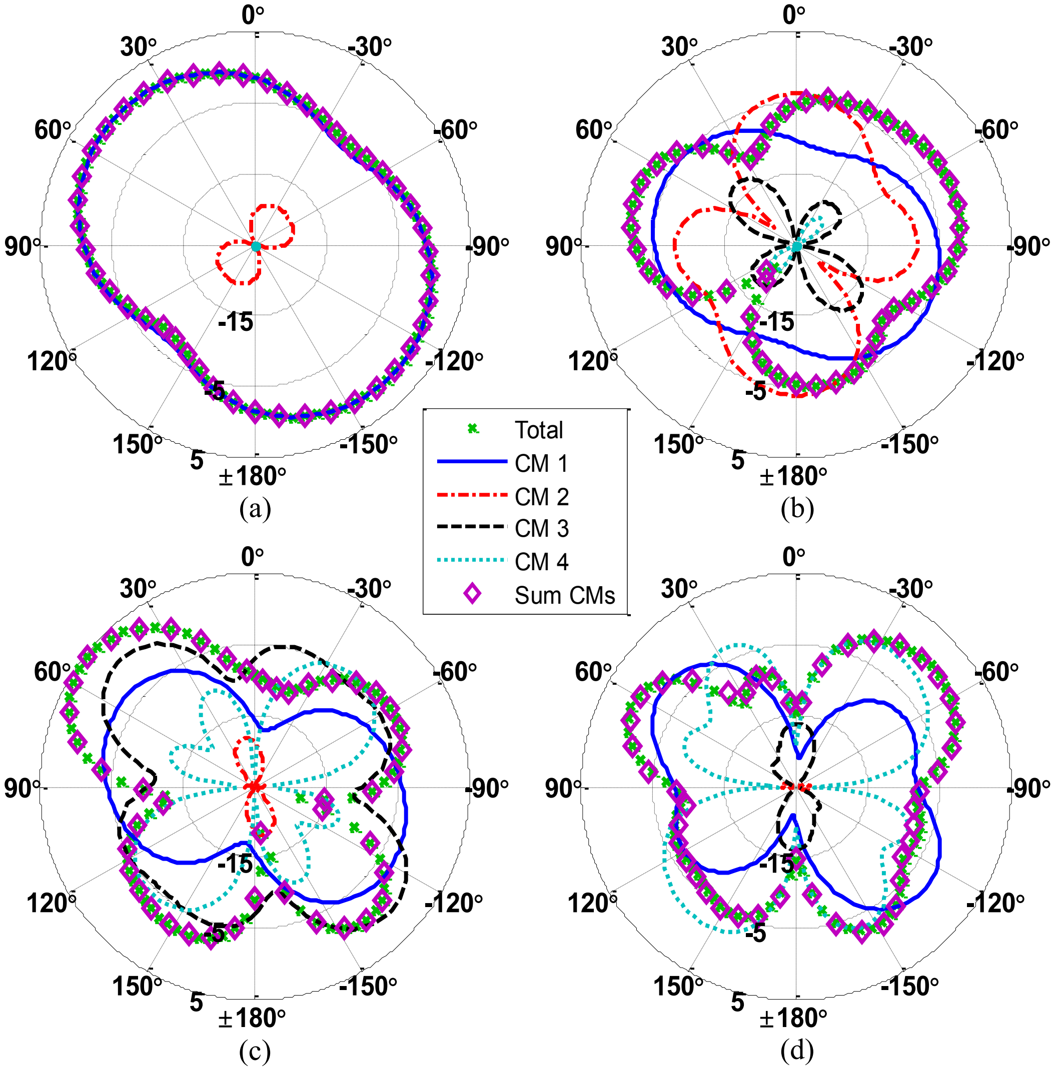

(a) (b) (c) (d)

Figure 6.20: F2 realized total gain (dBi) comparing total pattern, eigenpatterns and sum of eigenpatterns in the XZ-plane; (a) 145 MHz, (b) 300 MHz, (c) 460 MHz, (d) 605 MHz.

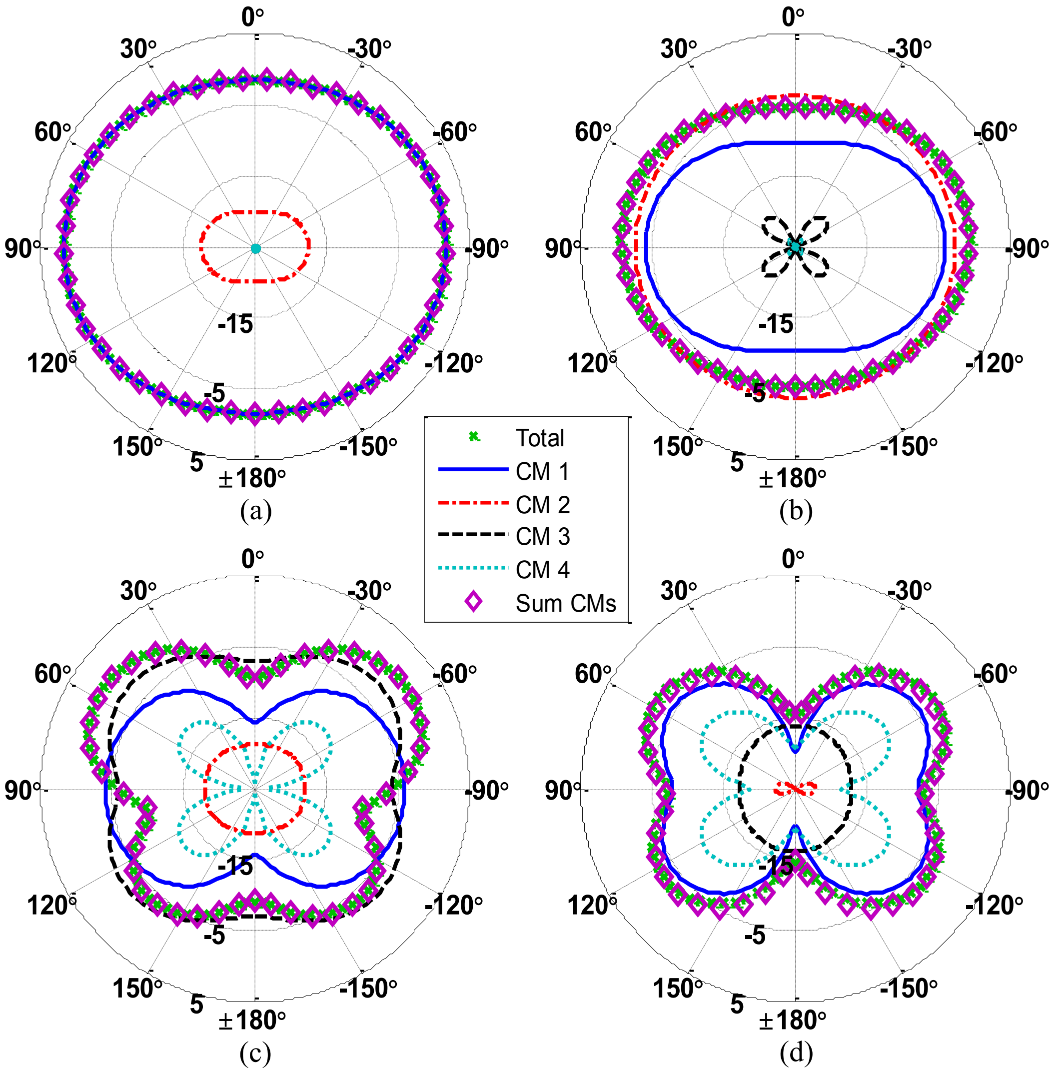

(a) (b) (c) (d)

Figure 6.21: F2 realized total gain (dBi) comparing total pattern, eigenpatterns and sum of eigenpatterns in the YZ-plane; (a) 145 MHz, (b) 300 MHz, (c) 460 MHz, (d) 605 MHz.

Again, the patterns in the XY-plane (i.e. $\theta = 90°$) are shown in Figure 6.22 and Figure 6.23 for vertical and horizontal polarizations, respectively. Note the eigenpatterns vertical-polarization is omni-directional. Comparing F1 and F2, F2 has almost a 2 dB decrease in cross-polarization as seen in Figure 6.23(b); however remains the dominant mode contributing to the horizontal-polarization at 300 MHz. Again, all modes contribute the horizontal-polarization at 460 MHz. CM 4 horizontal-polarization and the total have good agreement at 605 MHz.

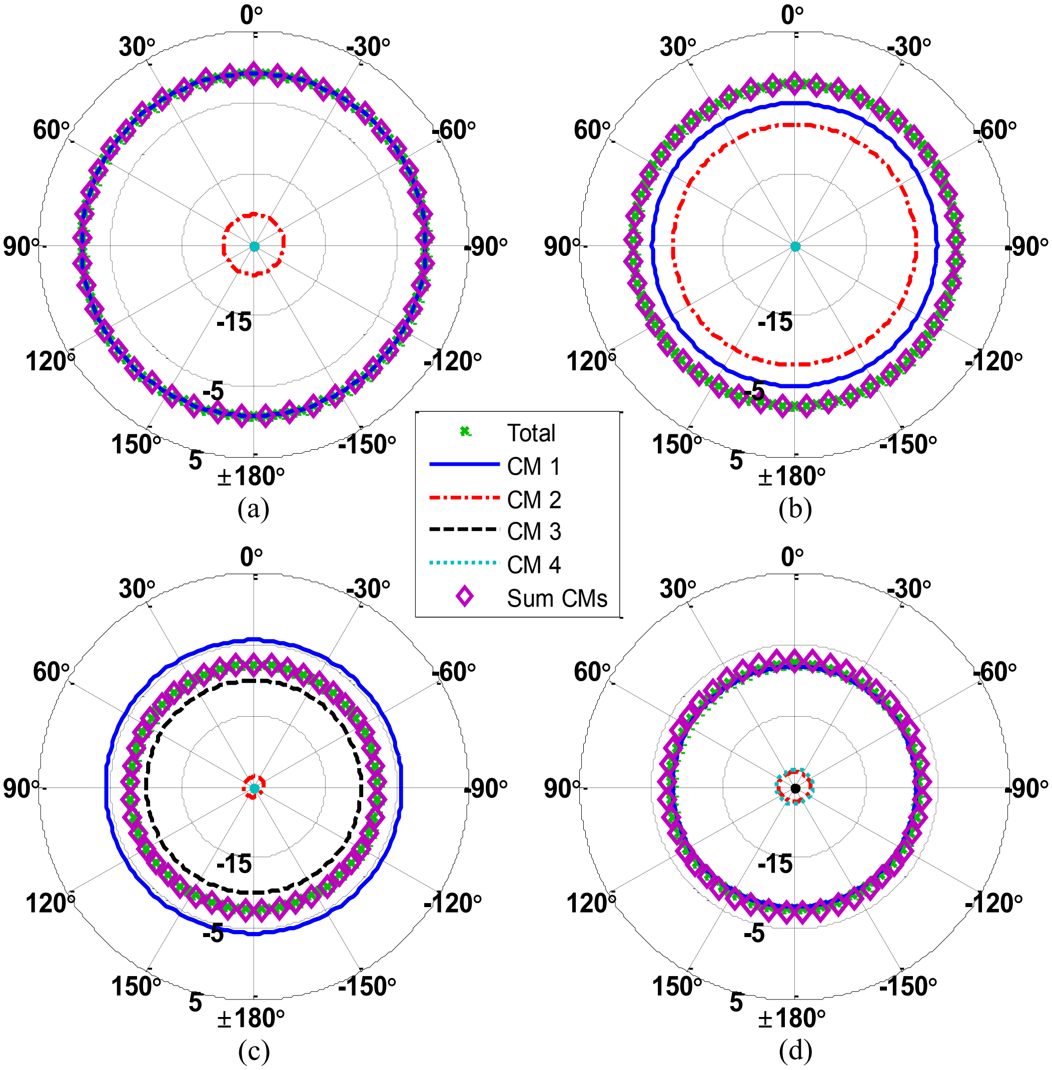

Figure 6.22: F2 realized vertical gain (dBi) comparing total pattern, eigenpatterns and sum of eigenpatterns in the XY-plane; (a) 145 MHz, (b) 300 MHz, (c) 460 MHz, (d) 605 MHz.

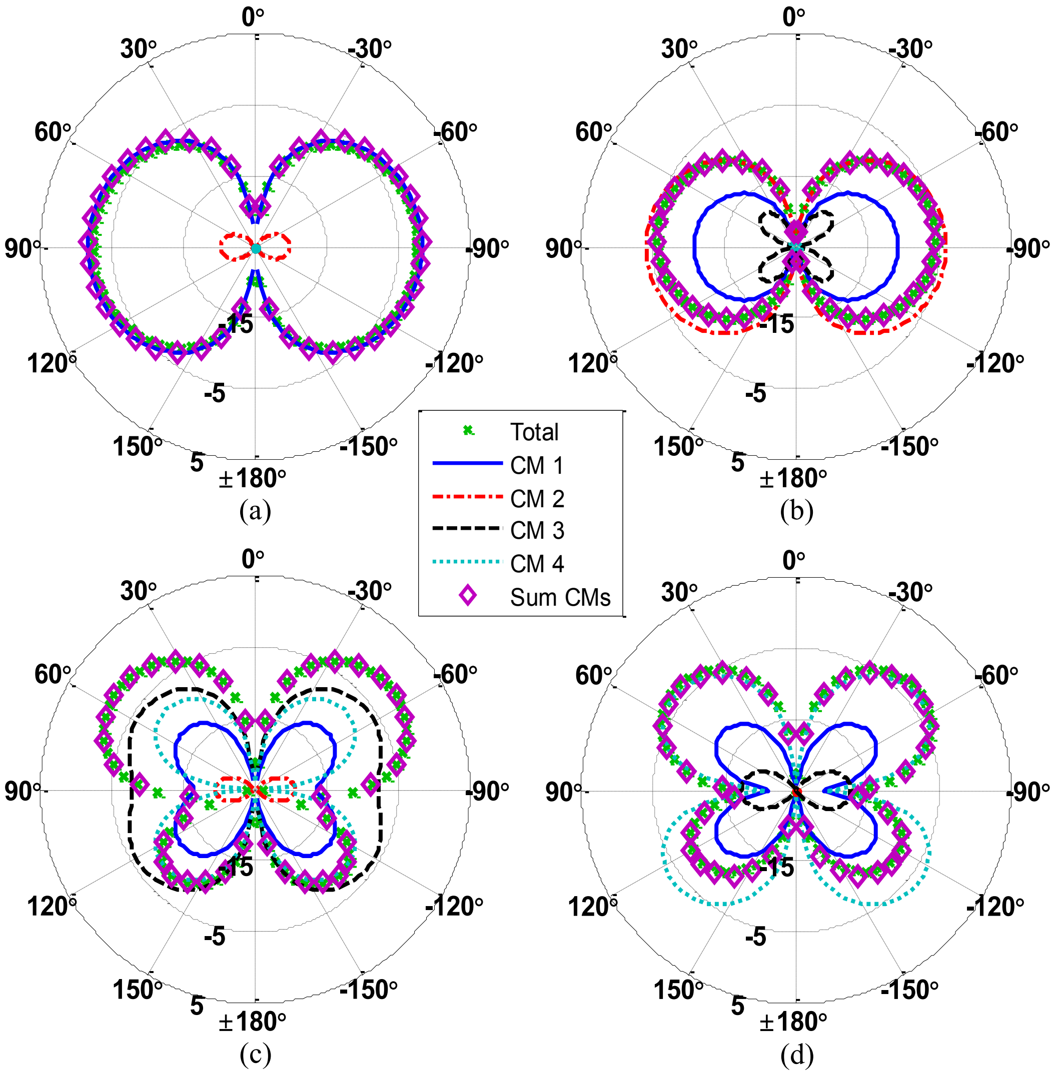

Figure 6.23: F2 realized horizontal gain (dBi) comparing total pattern, eigenpatterns and sum of eigenpatterns in the XY-plane; (a) 145 MHz, (b) 300 MHz, (c) 460 MHz, (d) 605 MHz.

F2 total realized gain (dBi) in the XY-plane is shown in Figure 6.24 for both vertical- and horizontal-polarization. Vertical-polarization remains omnidirectional vs. frequency with a realized gain larger than -10 dBi from 120-650 MHz. From 125-325 MHz the horizontal-polarization component has contributions from CM 1 and 2. Above 450 MHz the horizontal-polarization is mainly from CM 4.

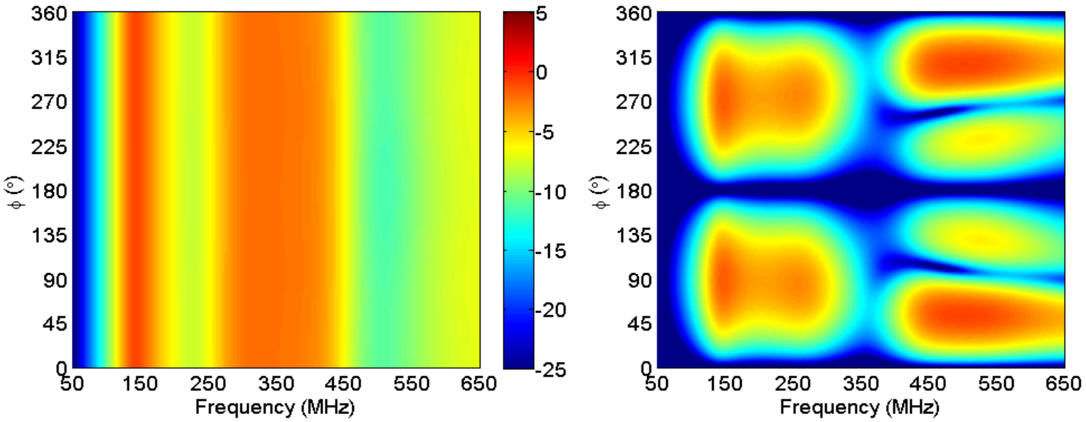

(a)

(b)

Figure 6.24: F2 realized gain (dBi) vs. frequency in XY-plane; (a) vertical-polarization, (b) horizontal-polarization.

6.5 Feed 3 $\lambda_M/8 \times \lambda_M/32$ Rectangular Plate

Finally, F3 will be placed at $H_F = 0.0$ m. This feed further decreases the height with respect to F1, resulting in a decreased excitation of CM 2 and an increased excitation of CM 3. This feed results in the best suppression of CM 2, thus has the lowest expected cross-polarization. However, the feed strongly excited the undesirable higher order modes (i.e. CM 3 and 4).

F3 is a monopole excitation as described in Section 4.2.2. The $|\alpha_n|$s (dB) of the dominant modes are shown in Figure 6.25. Note that $|\alpha_2|$ is decreased by 4.57 dB and $|\alpha_3|$ is increased by 6.40 dB at their corresponding resonant frequencies respectively, relative to F1. The admittance is shown in Figure 6.26. As expected the conductance level of CM 2 has further decreased while CM 3 conductance has increased around 460 MHz.

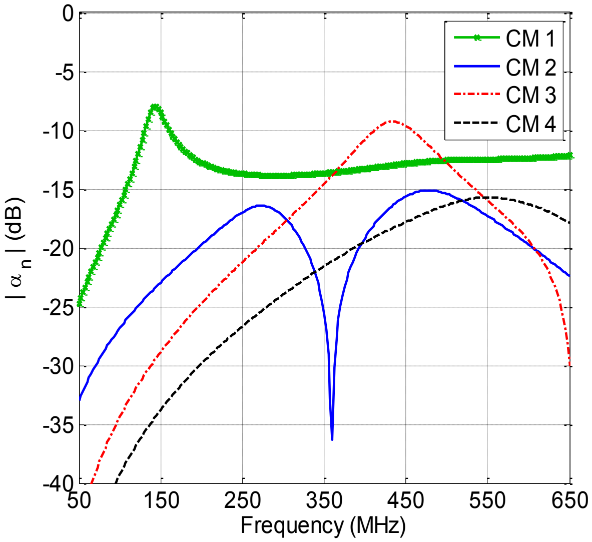

Figure 6.25: $|\alpha_n|$ (dB) of characteristic modes under consideration for dipole feed 3 ($L_G = \lambda_M/8 \times W_G = \lambda_M/32$).

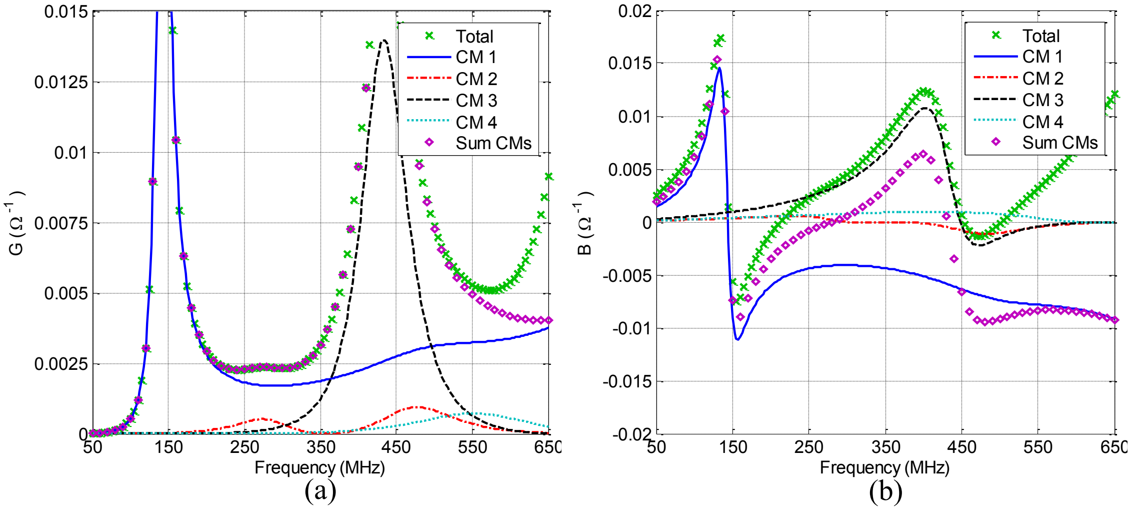

Figure 6.26: F3 (H_F = 0) comparing total, characteristic mode and sum of characteristic mode admittance; (a) conductance, (b) susceptance.

The realized total gain in the XZ- and YZ-plane is shown in Figure 6.27 and Figure 6.28. Due to the decrease in excitation of CM2 at 300 MHz, CM 1 now has the largest impact on the overall pattern at both 145 and 300 MHz. At 460 MHz CM 3 resembles the overall shape of the pattern. At 605 MHz the sum and total realized gain have a slight disagreement. The disagreement is a result of not including enough modes at high frequencies. With the monopole feed the vertical polarization remains omnidirectional in XY-plane (Figure 6.29).

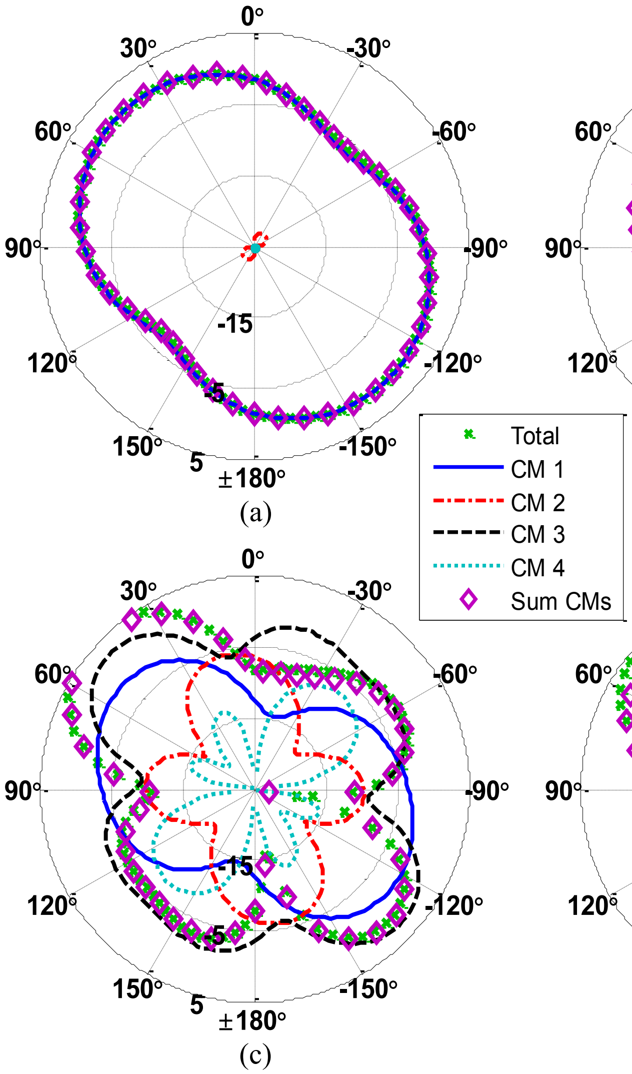

(a) (b) (c) (d)

Figure 6.27: F3 realized total gain (dBi) comparing total pattern, eigenpatterns and sum of eigenpatterns in the XZ-plane; (a) 145 MHz, (b) 300 MHz, (c) 460 MHz, (d) 605 MHz.

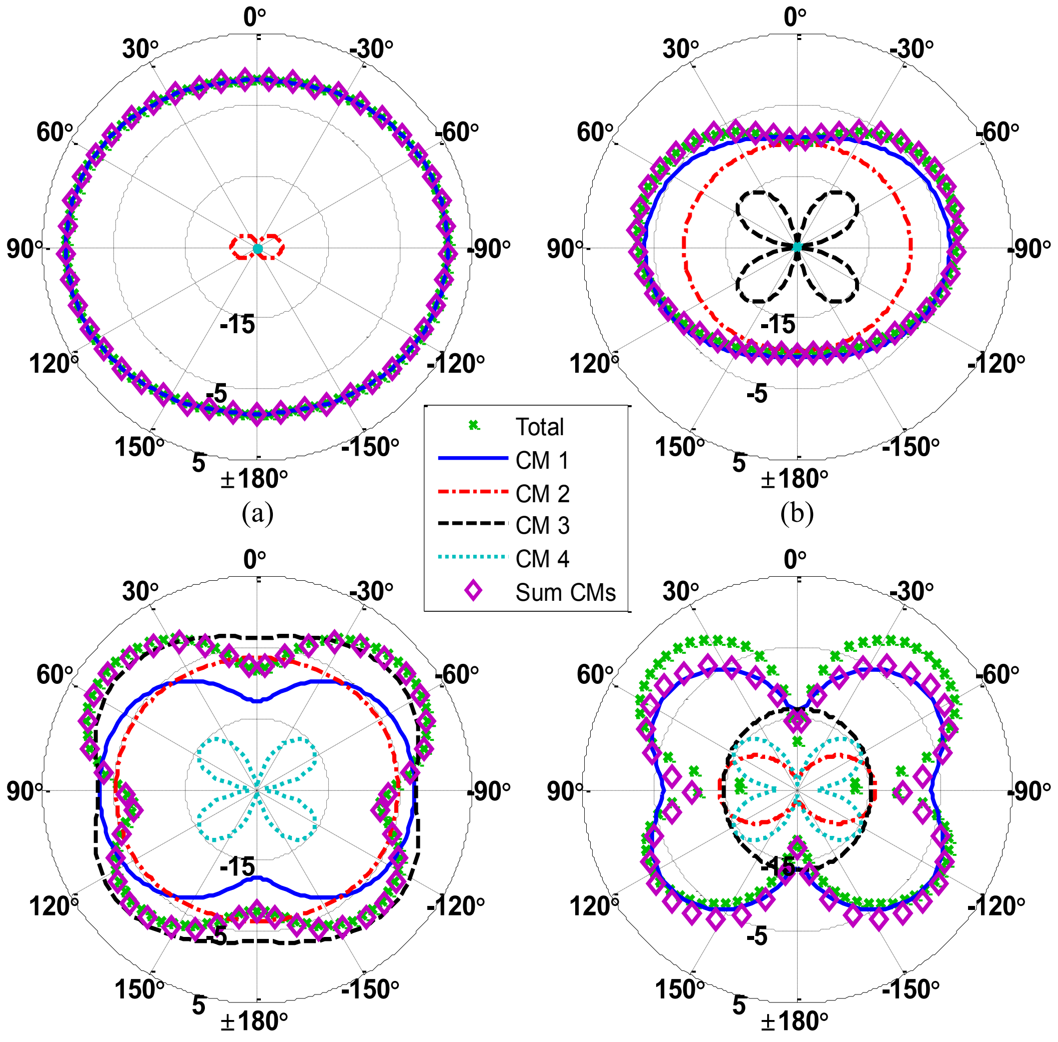

(a) (b) (c) (d)

Figure 6.28: F3 realized total gain (dBi) comparing total pattern, eigenpatterns and sum of eigenpatterns in the YZ-plane; (a) 145 MHz, (b) 300 MHz, (c) 460 MHz, (d) 605 MHz. Pattern look the same

Figure 6.29 shows the realized vertical gain in the XY-plane. The pattern remains omnidirectional at all frequencies. Note the decrease in vertical gain at higher frequencies relative to the dipole excitation.

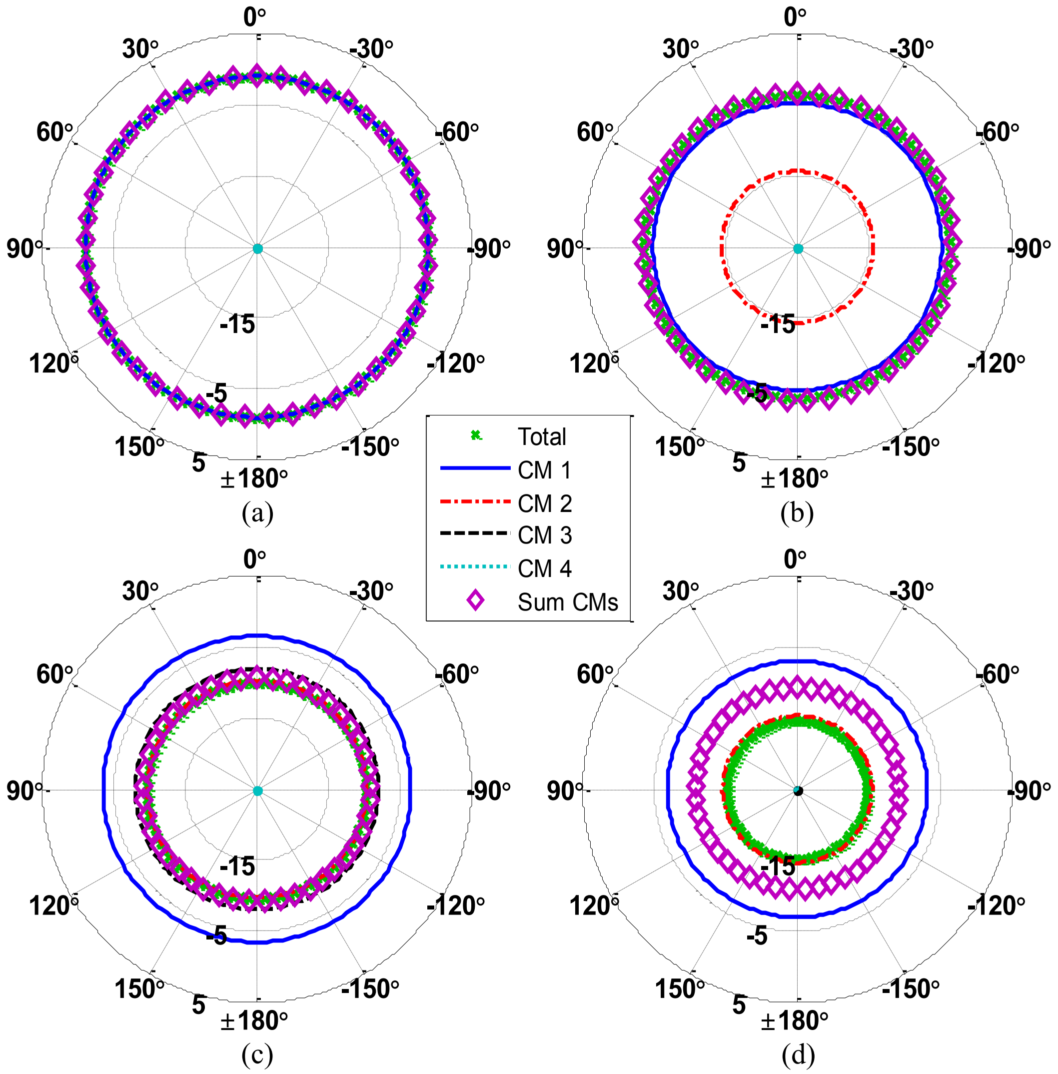

Figure 6.29: F3 realized vertical gain (dBi) comparing total pattern, eigenpatterns and sum of eigenpatterns in the XY-plane; (a) 145 MHz, (b) 300 MHz, (c) 460 MHz, (d) 605 MHz.

Note that with the monopole feed there is a significant reduction in cross-polarization at 300 MHz as seen in Figure 6.30(b). The total cross-polarization level is reduced to -10.55 dB. Both CM 1 and 2 cross-polarization levels are below -10 dB.

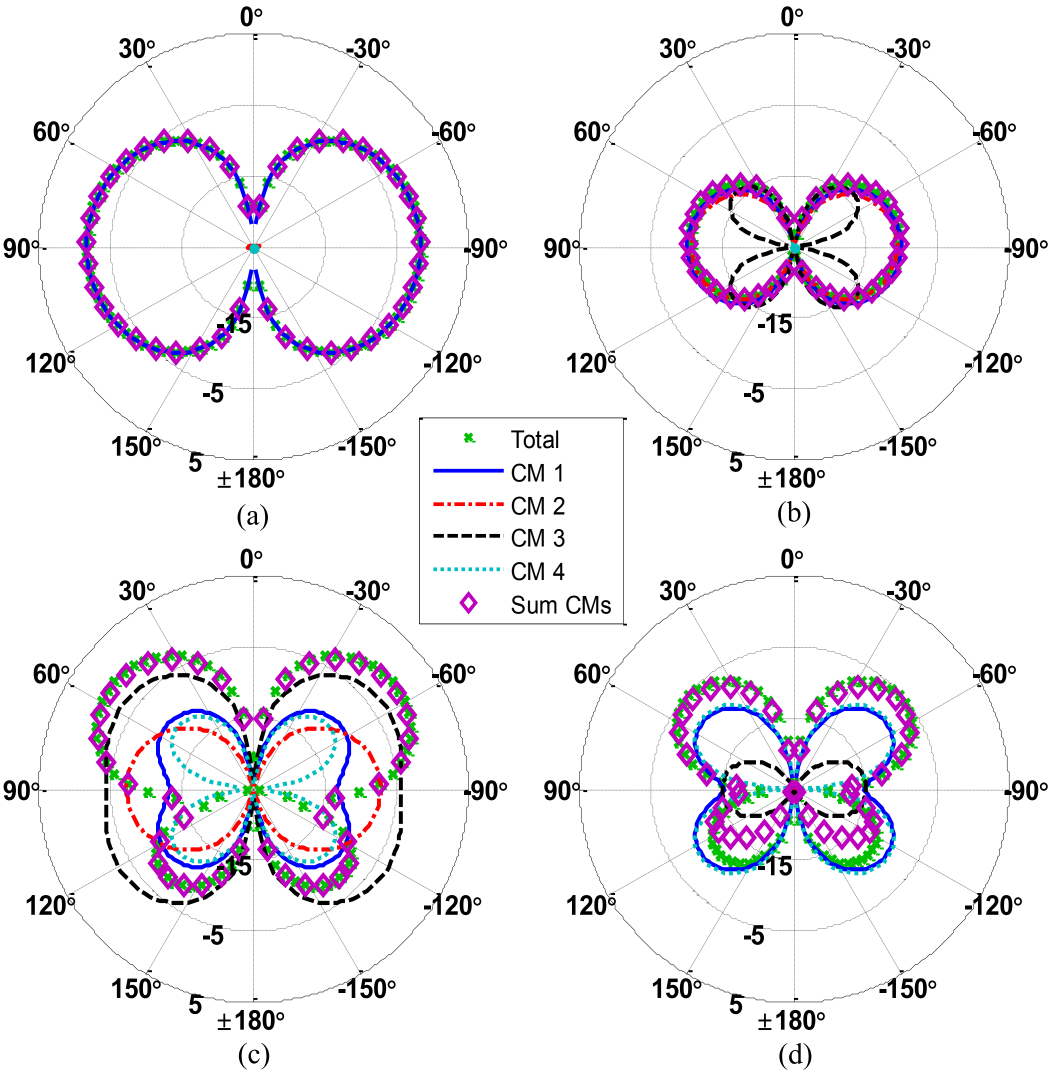

Figure 6.30: F3 realized horizontal gain (dBi) comparing total pattern, eigenpatterns and sum of eigenpatterns in the XY-plane; (a) 145 MHz, (b) 300 MHz, (c) 460 MHz, (d) 605 MHz.

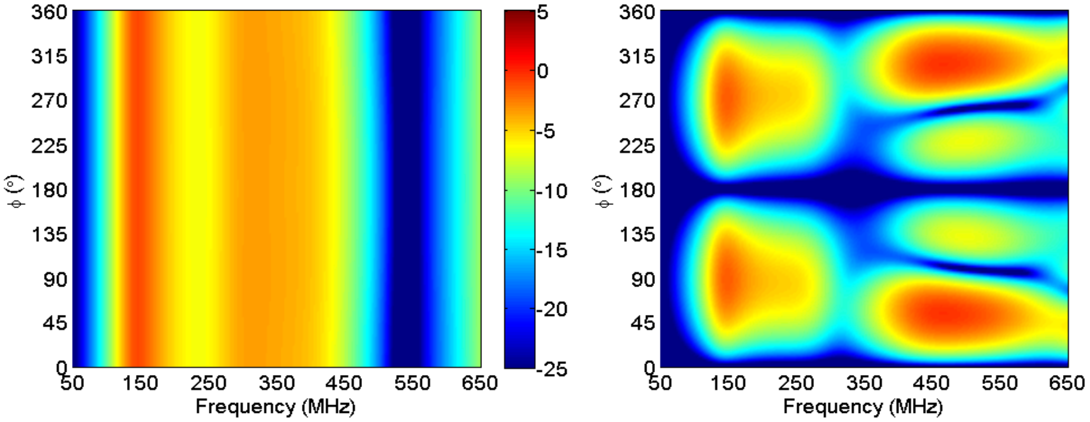

(a) (b)

Figure 6.31: F3 realized gain (dBi) vs. frequency in XY-plane; (a) vertical-polarization, (b) horizontal-polarization.

6.6 Summary

In this chapter, the design tradeoffs and limitations were shown for an offset antenna element on a rectangular ground plane. Three feed networks were considered to emphasize the predictable tradeoffs of the dominant CMs identified. The tradeoffs are between bandwidth and cross-polarization. As illustrated in Table 6.2, the horizontal polarization at broadside changes significantly with feed height. CM 2 is the dominant mode contributing to the total cross-polarization for F1 and F2. Decreasing the height decreases the excitation of CM 2. Therefore lowering the cross-polarization at 300 MHz. F3 is the feed on the vertical element which weakly excites CM 2. This feed corresponds to a monopole excitation. The tradeoff for reducing the cross-polarization is a reduced pattern bandwidth. F3, which weakly excites CM 2 and strongly excites CM 3.

Table 6.2: Realized horizontal gain (dBi) comparison at broadside (θ = 90°, φ = 90°, 300 MHz)

CM	F1	F2	F3
Total	-3.82	-5.61	-10.55
CM 1	-11.28	-10.75	-10.04
CM 2	-2.43	-4.07	-10.66

The $|\alpha_n|$s (dB) at each mode's resonant frequency for the three feeds considered are shown in Table 6.3. Note CM 1 is relatively insensitive to feed location. Thus if this mode does not meet the design criteria the structure needs to be modified. All other modes are sensitive to feed location allowing the designer to make tradeoffs to meet their desired criteria.

Table 6.3: $|\alpha_n|$ (dB) feed comparison at each modes resonant frequency

CM	F1	F2	F3
1	-8.46	-8.22	-7.98
2	-12.77	-13.79	-17.34
3	-16.75	-12.26	-10.17
4	-13.39	-13.55	-16.41

Chapter 7 Design of Volume Integrated GPS and VHF/UHF Antennas Conformal to Dakota UAV

Volume integration of conformal GPS and VHF/UHF antennas on small UAVs was proposed in [32], [33]. The idea is to better utilize the limited space available on the UAV by combining antennas into the same volume. Volume integration of antennas increases available space on the UAV for installation of additional antennas, increasing the UAVs functionality. Traditionally, each antenna requires its own volume, thus limiting the number of antennas on a small UAV. In this chapter, a 5-turn bifilar helix GPS antenna is designed to fit inside the tail of the Dakota UAV. Furthermore, a VHF/UHF communication antenna is designed to be conformal to the surface of the tail and fuselage of the UAV. Successful volume integration requires both antennas to maintain input impedance, polarization, gain as well as front-to-back (F/B) ratio, axial ratio (AR), etc.

In Section 7.1, the design of a 5-turn bifilar helix antenna for GPS applications is presented. The bifilar helix antenna proposed here has continuous bandwidth covering L1-L5 GPS bands. A feeding network insert is designed with a 4:1 balanced to unbalance transformation, resulting in $|S_{11}| < -10$ dB at all bands. The antenna is fabricated on a tapered dielectric rod using mesoplasma direct write technology [16]. Finally, the performance of this volume integrated antenna is verified experimentally to access the accuracy of all the design tools developed in this study.

In Section 7.2, the design of a VHF/UHF conformal to the tail and fuselage of the Dakota is presented. The insight gained through rigorous CM analysis of general UAV structures in Chapters 4-7 allows proper utilization of the available volume to achieve VHF/UHF communications via an omnidirectional vertically polarized pattern. The antennas are integrated into the same volume, directly improving the functionality of the UAV.

7.1 GPS Antenna

The GPS antenna provides communication between the UAV and satellites. GPS antennas require right hand circular polarization (RHCP) with a large half power beamwidth (HPBW) to receive signals from at least four satellites simultaneously. The F/B ratio, bandwidth, axial ratio (AR) and cross-polarization rejection (CPR) are important parameters when designing a GPS antenna. In this dissertation, the F/B ratio is defined as the difference between total gain (dB) in the forward direction to the total gain (dB) in reverse direction. The forward direction is typically $\theta = 0^\circ$ (i.e. boresight) while the reverse direction is typically $\theta = \pm 180^\circ$. A F/B ratio of at least 10 dB is desirable to ensure radiation mostly in the upper hemisphere. Radiation in the lower hemisphere is wasted energy. For ground based antennas or when multipath is an issue, the F/B ratio is an important parameter. CPR is defined as the difference (dB) between the co- and cross-polarization (i.e. RHCP and LHCP respectively) at any elevation angle. A CPR of 15 dB is desirable for GPS antennas for a tolerable signal to noise ratio and to ensure AR is less than 3 dB.

The GPS antenna must be either multiband or wideband to cover L1-, L2- and L5-bands. Microstrip patch antennas such as the one used in [34] are commonly used to cover both bands while maintaining performance. Such an antenna will not work in this application due to the large ground plane needed for the patch.

A GPS antenna was designed to fit in the tail of the Dakota UAV. The dimensions of the tail restrain the size of the GPS limiting the possible types of GPS antennas to either a helical or bifilar helical antenna. There are some key differences between these antennas, but more importantly the bifilar helix does not need a ground plane. This is critical because the dimensions needed for a ground plane which provides a F/B ratio greater than 10 dB would be too large to fit inside the tail. Therefore, a bifilar helix is used to design the GPS antenna.

7.1.1 Design of Bifilar Helix

Bifilar helix is a two arm travelling wave antenna which radiates a backfire mode [35]. Figure 7.1 shows a bifilar helix. Key parameters are the height (H), turn separation (S), top radius (R_t) and bottom radius (R_b). In order to excite the backfire mode radiating an RHCP pattern the antenna must be fed from the top with the arms rotating downward in a counter clockwise manner. The backfire mode region of the bifilar helix is shown in Figure 7.2(a). The radius and spacing at any point in the shaded region can be used to excite the backfire mode. The pitch of the bifilar helix is defined as [36]

$$\alpha = \tan^{-1}\frac{S}{2\pi R}. \tag{8.1}$$

Bifilar helical antennas have some well defined tradeoffs between bandwidth, F/B ratio and pitch. As the pitch of the bifilar helix increases, the F/B ratio and beamwidth increase, however the bandwidth decreases. Tapering the arms of the bifilar helix improves the F/B ratio and extends the bandwidth [37], [38]. A 5-turn bifilar helical was designed with a varying pitch starting at 23.57° at the base and increasing to 25.72° to operate at L5, L2 and L1-bands. Additionally, since the antenna is a traveling wave antenna with continuous bandwidth, the antenna also operates at L3 (1.381 GHz) and L4-bands (1.379 GHz). Thus, the proposed GPS antenna covers all five L-bands (1.175-1.575 GHz).

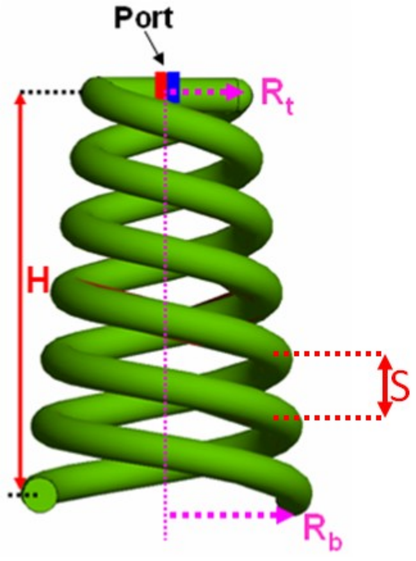

Figure 7.1: 5-turn bifilar helix antenna with total height (H), turn separation (S), top radius (R_t) and bottom radius (R_b).

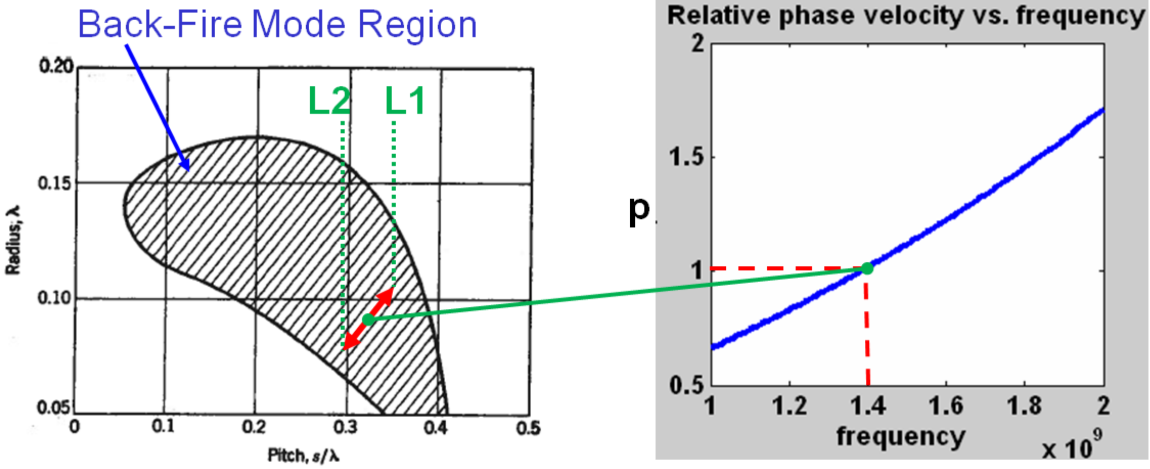

(a)

(b)

Figure 7.2: Bifilar helix properties; (a) backfire mode region (The figure was taken from Figure 8-22 in reference [39]), (b) relative phase velocity vs. frequency.

To cover L5, L2 and L1-bands a center frequency of 1.4 GHz was chosen as the design frequency. At the center frequency, the antenna is designed such that the relative phase velocity is 1. The relative phase velocity vs. frequency is shown in Figure 7.2(b) and defined as

$$p = \frac{L}{\lambda_o\left(1+\frac{1}{2n}\right) - S} \tag{8.2}$$

where L is the length per turn, n is number of turns and S is the turn separation. At L5-band the relative phase velocity is 0.8 in which the mode is just getting excited. At L1-band the relative phase velocity is 1.2 in which the desired mode is dying out. The rate of change of the phase velocity is dependent on the pitch of the antenna. Increasing the pitch of the antenna increases the F/B ratio while reducing the cross-polarization. However the slope of the relative phase velocity increases, thus the bandwidth of the antenna is decreased.

The height of the tail limits the maximum number of turns and the width of the tail limits the radius of the bifilar helix. Two techniques were used to miniaturize the antenna. First a dielectric rod was used. Miniaturization of antenna using dielectrics reduces the bandwidth of antennas. Thus, the relative permittivity of the rod was kept low ($\varepsilon_r = 3.3$) to maintain the bandwidth. Second, the bifilar helix was designed using square turn. Square and circular turns have the same performance as long as the electrical circumference is held constant. Thus, a 20% reduction in radius is achieved when using square loops. The reduction in radius is emphasized in Figure 7.3. Since the circumference of the turn did not change, the bandwidth of the antenna is unaffected.

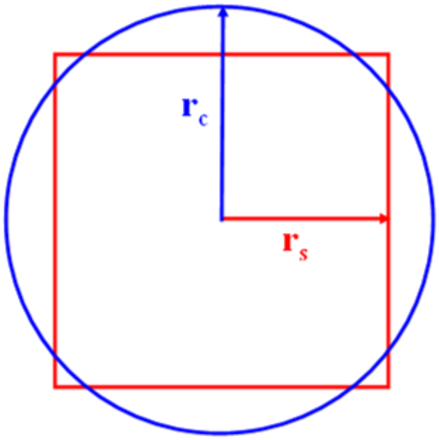

Figure 7.3: Square vs. circle radius comparison.

The dimensions of the GPS antenna are shown in Figure 7.4. Specifically the total height (H), top width (W_t), bottom width (W_b) and trace thickness are illustrated in Figure 7.4(a). For fabrication purposes, the antenna has a linear taper, since the rod will has to be machined. Additionally, the corners are rounded as shown in Figure 7.4(b, c), where the top corner radius (r_{ct}) and bottom corner radius (r_{cb}) are shown. The dimension per turn are given in Table 7.2, where r_{avg} is the average radius over the turn. Note, turn 1 is closest to the feeding network. Additionally, the electrical length per turn for L5, L2 and L1-bands are listed in Table 7.3.

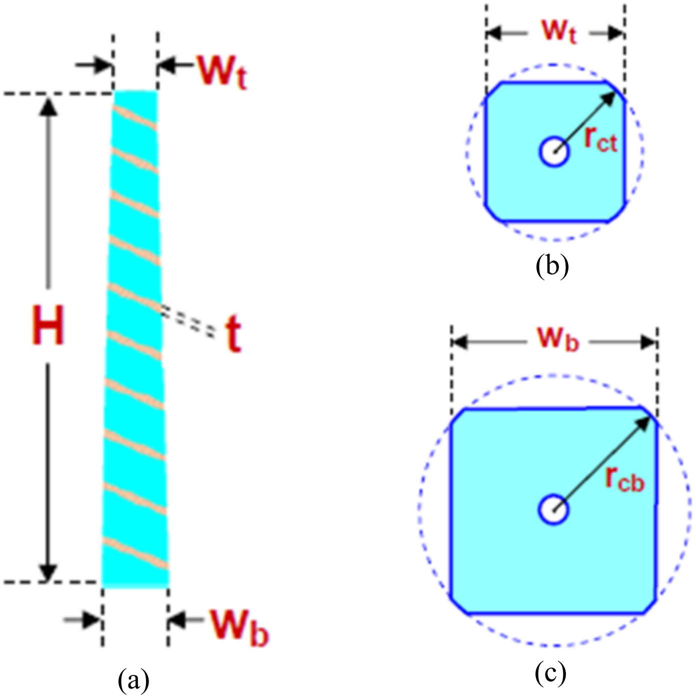

(a)

Figure 7.4: GPS dimension; (a) side view, (b) top view, (c) bottom view.

Table 7.1: 5-turn bifilar helix dimensions (mm)

H	287.95
W_t	25.72
W_b	38.00
t	3.00
r_{ct}	16.19
r_{cb}	24.89

Table 7.2: R_{avg}, S and pitch of each turn

Turn	r_{avg} (mm)	S (mm)	α (°)
1	13.47	50.80	25.25
2	14.58	53.55	24.66
3	15.76	56.60	24.18
4	17.00	60.05	23.82
5	18.32	63.95	23.57

Table 7.3: Electrical length per turn for L5, L2 and L1-bands

Turn	L5	L2	L1
1	0.3865	0.4030	0.5181
2	0.4156	0.4333	0.5571
3	0.4466	0.4656	0.5987
4	0.4799	0.5004	0.6433
5	0.5158	0.5378	0.6914

7.1.2 Fabrication of GPS Antenna

The bifilar helix was fabricated on a polyetheretherketone (PEEK) dielectric rod with $\varepsilon_r = 3.3$. The dielectric rod was machined at Mesoscribe Technologies facilities. Copper was sprayed on dielectric rod to form antenna traces via mesoplasma direct write technology [16]. Reference impedance of the bifilar helix is 200 Ω, moreover, it requires a 180° balanced feed. To provide a matched balanced output, a feeding network insert is created using a Rogers Corporation RO3203 microwave laminate. Feeding network insert is 1.52 mm thick and placed at the top of GPS antenna. Figure 7.5 shows the top of the GPS antenna before and after insertion of the feeding insert. Note that the holes in the dielectric rod are tooling holes used to hold the antenna during machining and later during the direct write thermal spray process. A 5 mm hole was milled through the center of the dielectric rod. This allows a 50 Ω RG-405 coaxial cable to run through the center of the dielectric rod to excite microstrip input of feed insert.

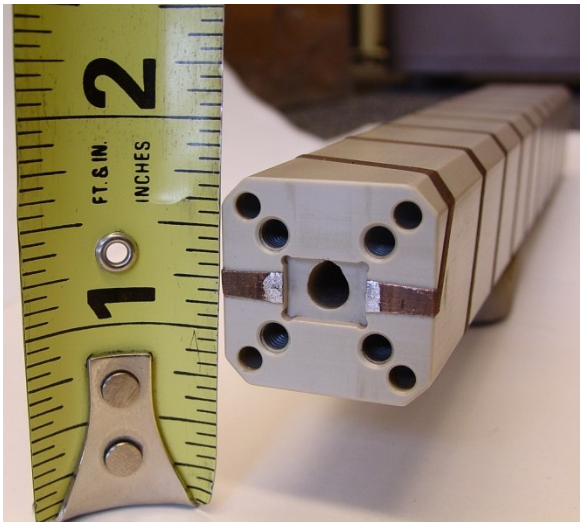

(a)

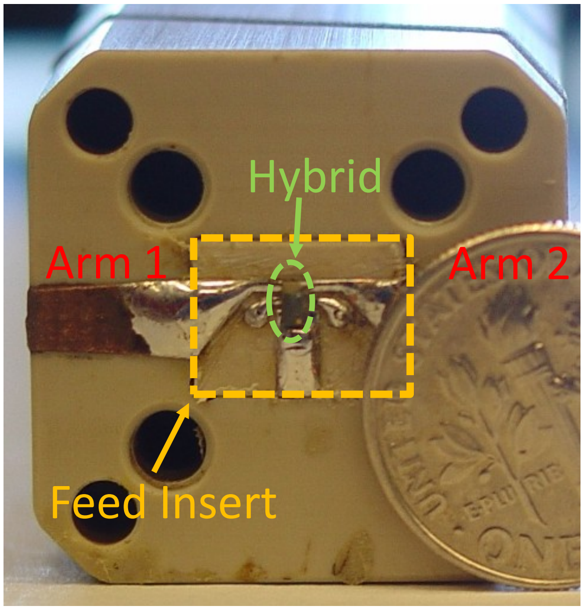

(b)

Figure 7.5: Manufactured GPS antenna; (a) top view illustrating notched area for feeding network insert, (b) insertion of feeding network insert.

The hybrid used for this design is a Xinger series, part number BD0826J50200A00, manufactured by Anaren. Table 7.4 list the connection to each of the six pads of the Xinger hybrid. Dimensions of the feeding network insert are shown in Figure 7.6. Additionally, the feeding network insert with hybrid placed on the layout is shown in Figure 7.7. Note the bottom of the insert is copper, except a 1 mm radius circle is removed. This allows the RG-405 coaxial cable running through the center of the antenna to connect to the feeding network insert, forming a coaxial to microstrip transition. To create the probe a 2 mm section of the shield and dielectric of the coaxial cable is removed exposing the center conductor. The shield of the coaxial cable is soldered to the feeding network insert ground plane, while the center conductor runs through the substrate and soldered to the microstrip input trace. Since pin 6 has no connection, the microstrip input trace can be placed symmetrically on the board. Pins 3 and 4 are the microstrip outputs which taper to connect to the arms of the bifilar helix. Pins 2 and 5 are connected to ground through a via.

Table 7.4: Xinger Hybrid BD0826J50200A00 pin layout

Pin	Connection
1	Unbalanced Input
2	Ground
3	Balanced Output
4	Balanced Output
5	Ground
6	No Connection

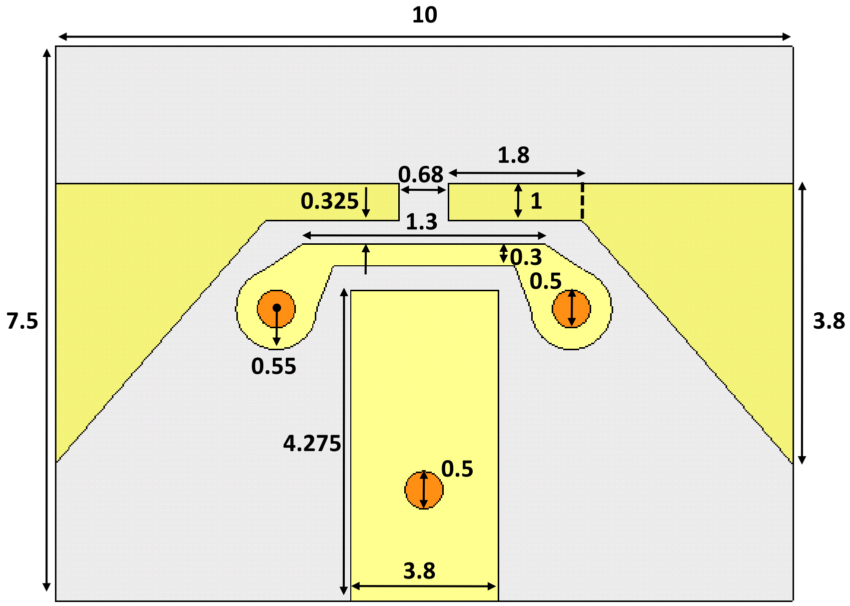

Figure 7.6: GPS feed network insert illustrating dimensions (mm).

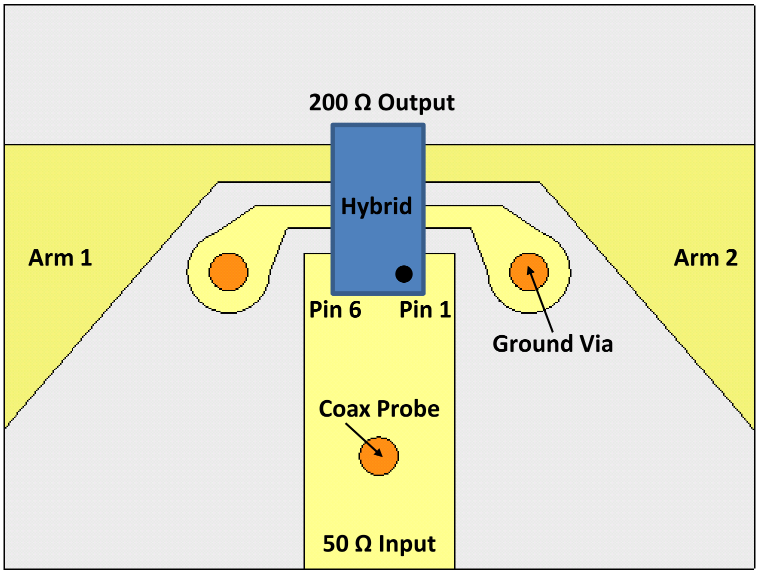

Figure 7.7: GPS feed network insert populated with Xinger hybrid Part # BD0826J50200A00.

The first step to install the feeding network insert is to solder the Xinger hybrid to the milled board. Next a 50 Ω coaxial cable is inserted from the bottom of the antenna running the length of the antenna connecting to the feeding network insert as shown in Figure 7.8(a). The coaxial cable inner conductor runs through the RO3203 microwave laminate and soldered to the input trace, while the coaxial ground (i.e. shield) is soldered to the ground plane on the bottom of the insert. Next, the milled feeding insert is pressed into the top of the GPS antenna. When the top surface of the board is level with the dielectric rod the insert is all the way in. Finally, the junction between the feeding network output traces and antenna arms are soldered.

(a) (b)

Figure 7.8: (a) Fabricated GPS antenna, (b) insertion of GPS antenna into vertical stabilizer (bottom view).

7.1.3 Measured GPS Antenna

Measured results <u>before integration</u> are presented in this section. The $|S_{11}|$ (dB) is shown in Figure 7.9. Simulated and measured results are in good agreement. Measured $|S_{11}|$ (dB) remains less than -10 dB from 1.159-1.949 GHz (1.68:1 bandwidth). Note, simulated $|S_{11}|$ is referenced to 200 Ω, since it does not include the balun, whereas the measurement is referenced to 50 Ω. Note the simulation port is placed between output pads of pin 3 and 4. Table 7.5 lists the $|S_{11}|$ (dB) at L-bands in ascending frequency band order.

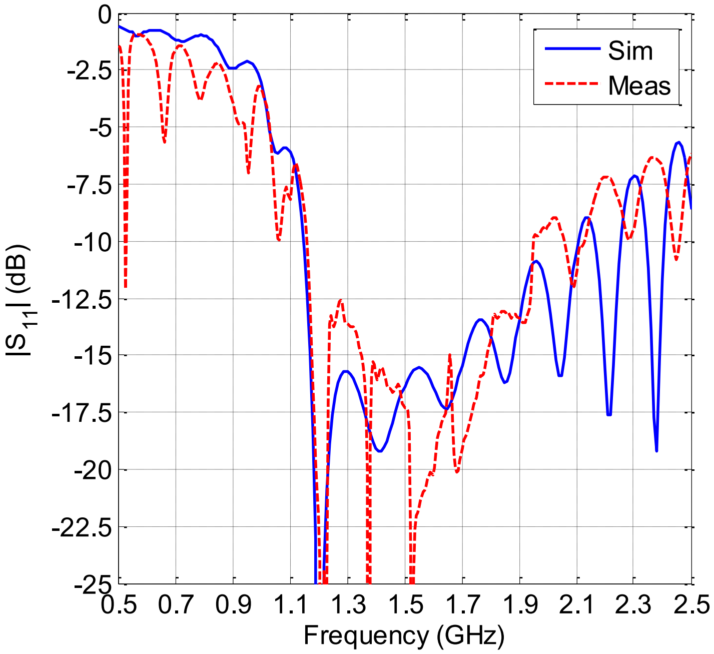

Figure 7.9: $|S_{11}|$ (dB) of 5-turn bifilar helical GPS antenna; (Blue) simulation results referenced to 200 Ω port impedance, (Red) measured results referenced to 50 Ω port impedance.

Table 7.5: $|S_{11}|$ (dB) simulated vs. measured at L5, L2, L4, L3 and L1-bands

Band	Sim.	Meas.
L5	-16.69	-14.71
L2	-27.22	-22.02
L4	-18.37	-23.91
L3	-18.46	-18.90
L1	-13.10	-15.21

Next the realized gain, both RHCP and LHCP is presented for both XZ- (φ = 0°) and YZ- (φ = 90°) elevation planes. Additionally, the AR is shown for both elevation cuts. First, the realized gain at L5-band is shown in Figure 7.10. Good agreement between simulated and measured results is observed. Small discrepancies exist between simulated and measured LHCP. Discrepancies mainly affect the AR and which is shown in Figure 7.11.

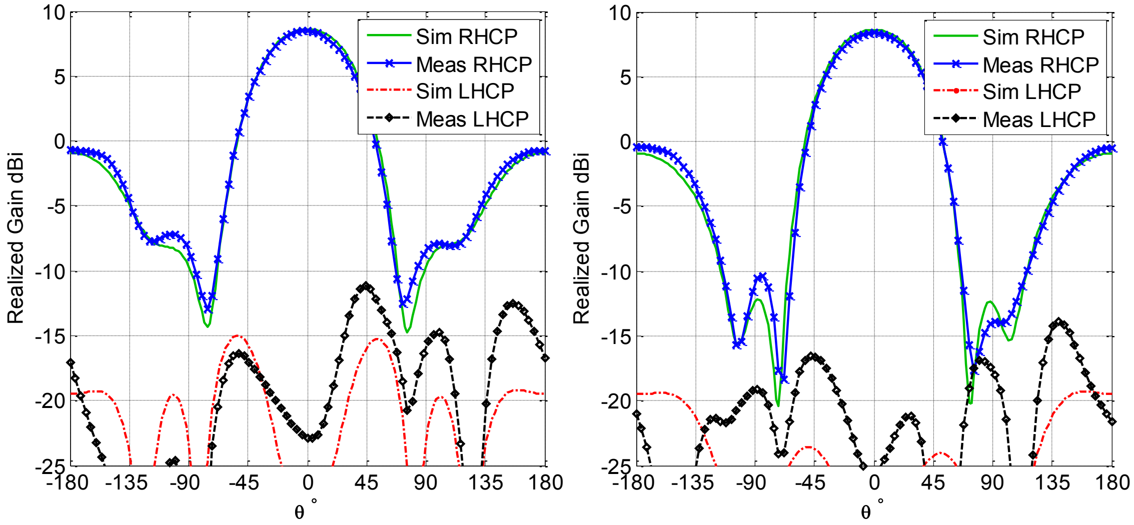

(a) (b)

Figure 7.10: L5-band realized gain (dBi); (a) XZ-plane, (b) YZ-plane.

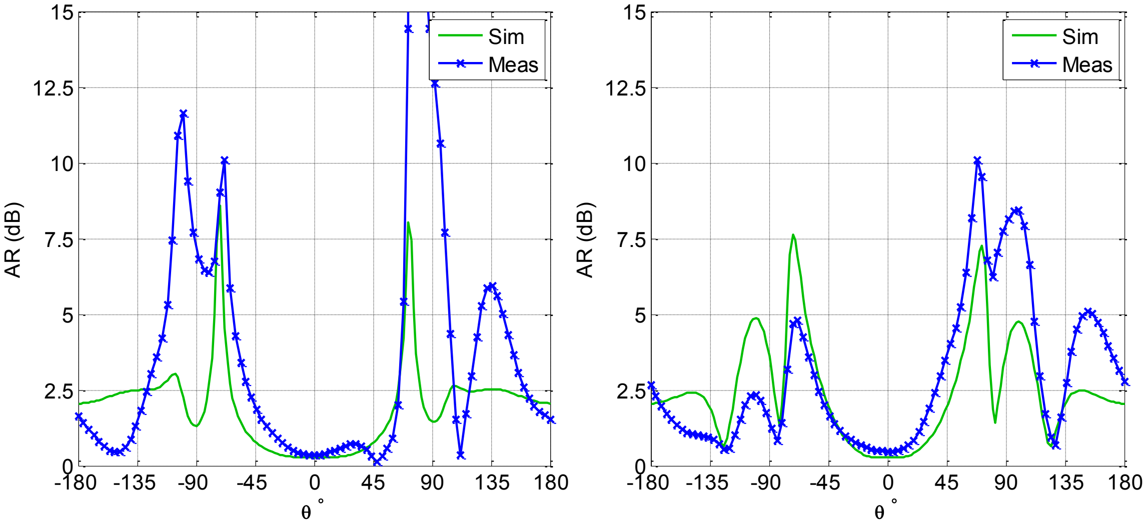

(a) (b)

Figure 7.11: L5-band axial ratio (dB); (a) XZ-plane, (b) YZ-plane.

The realized gain at L2-band is shown in Figure 7.12. L2-band measured gain at boresight is 1.34 dB less than simulation. Again, good agreement between simulation and measurements is achieved. The axial ratio is shown in Figure 7.13 for both XZ- and YZ-planes.

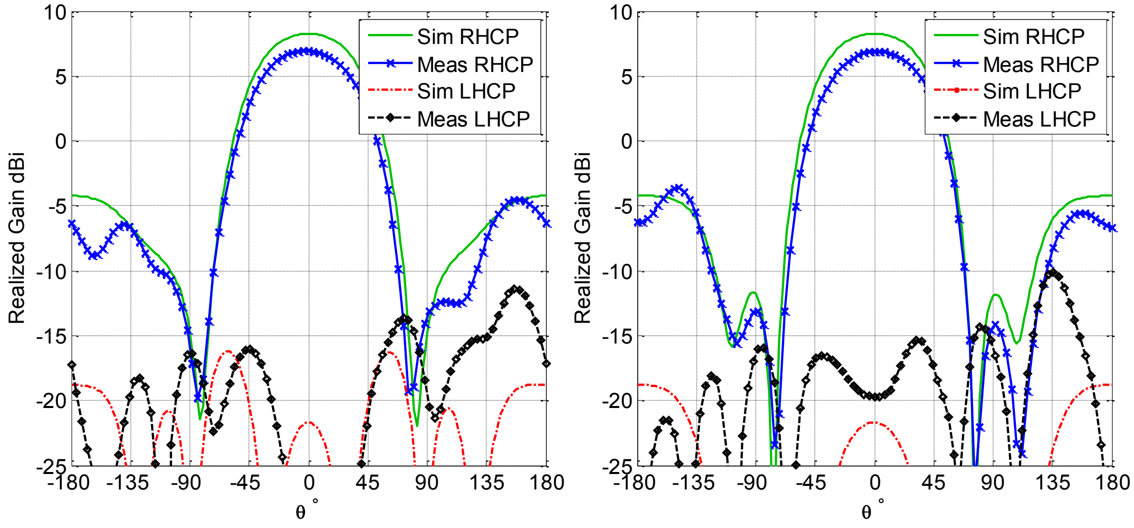

(a) (b)

Figure 7.12: L2-band realized gain (dBi); (a) XZ-plane, (b) YZ-plane.

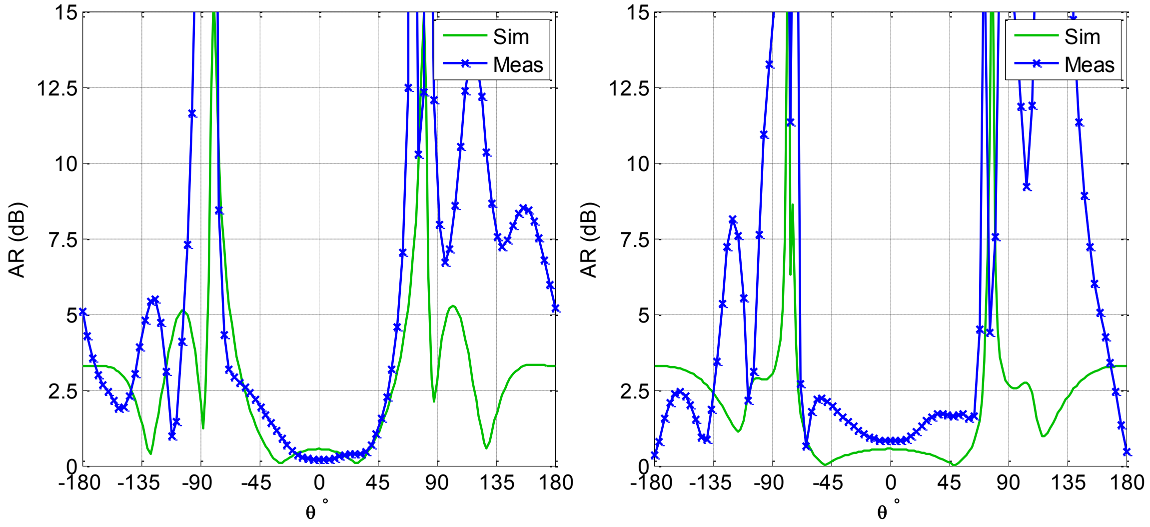

(a) (b)

Figure 7.13: L2-band axial ratio (dB); (a) XZ-plane, (b) YZ-plane.

Since the antenna has continuous bandwidth from 1.175 -1.575 MHz the antenna can be used at L3- and L4-bands. Thus, the realized gain at 1.4 GHz (near L3/4-bands) is shown in Figure 7.14. The measured gain is 1.17 dB less than simulation at boresight. The cross-polarization remains less than 15 dB for almost all elevation angles. The AR is shown in Figure 7.15, where its main beam AR is less than 3 dB for over 140° range.

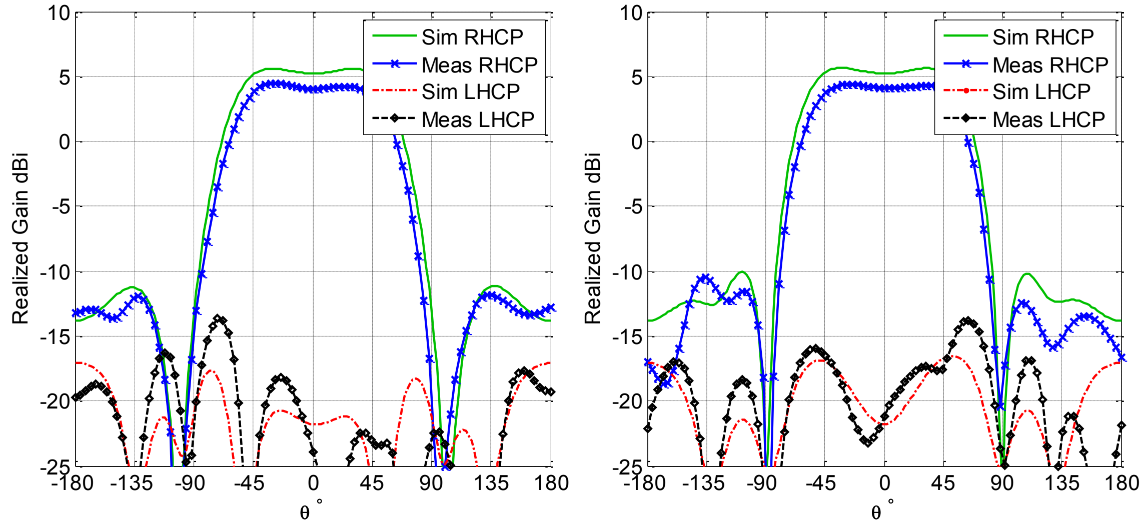

(a) (b)

Figure 7.14: 1.4 GHz realized gain (dBi); (a) XZ-plane, (b) YZ-plane.

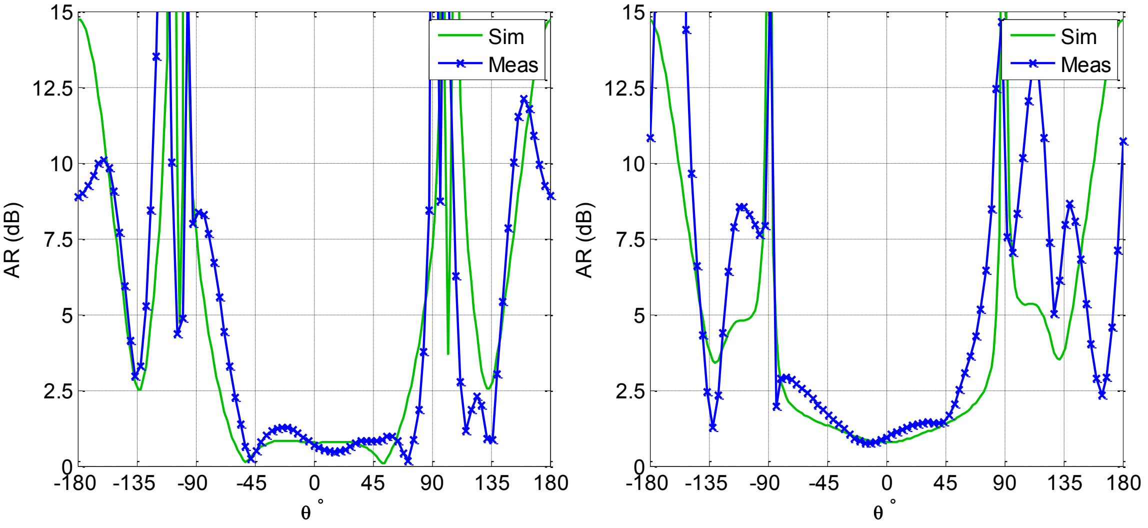

(a) (b)

Figure 7.15: 1.4 GHz axial ratio (dB); (a) XZ-plane, (b) YZ-plane.

L1-band is shown in Figure 7.16. It can be seen that as the frequency increase the beam is broadening, increasing the beamwidth. As the beam spreads the gain at boresight no longer is the maximum gain in the main beam. There is a 1.14 dB difference between measured and simulated gain at boresight. Very good agreement between measured and simulated results is achieved. Although the main beam is spreading, this is actually a desirable property since it provides increased gain levels at low grazing angles. The measured gain remains above 0 dB at boresight. As expected the F/B ratio increased while the cross-polarization level is decreased. The cross-polarization is less than -15 dBi in XZ-plane. Similarly, the cross-polarization is less than -15 dBi in the YZ-plane except at θ = -70 and 55°. Reduction in cross-polarization results in good agreement in the AR (Figure 7.17).

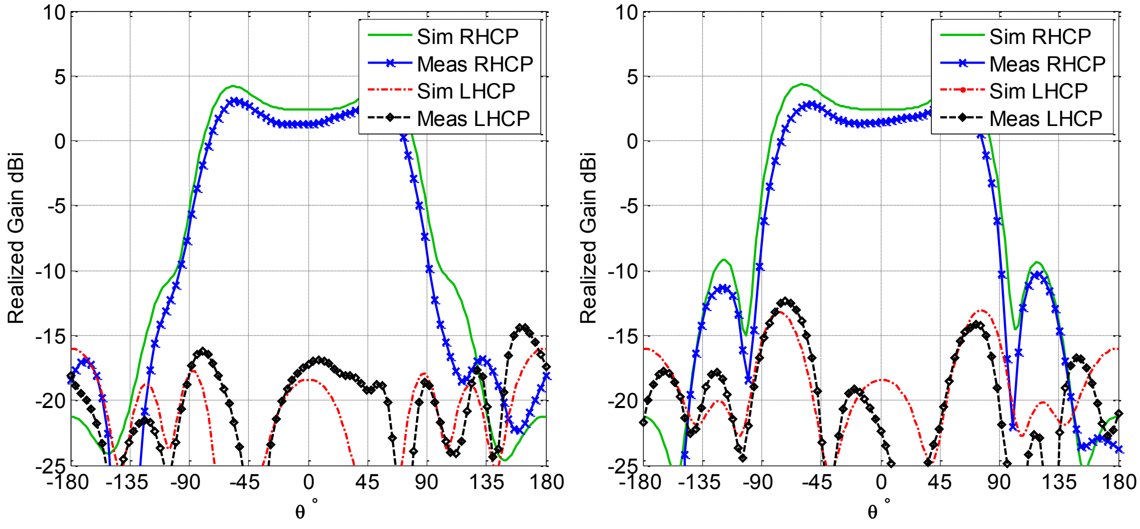

(a) (b)

Figure 7.16: L1-band realized gain (dBi); (a) XZ-plane, (b) YZ-plane.

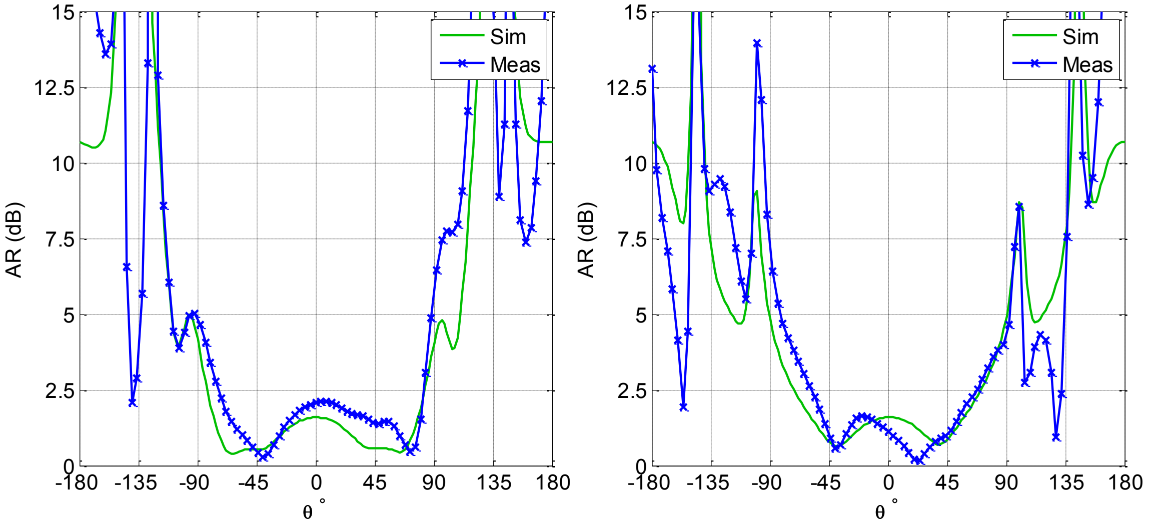

(a) (b)

Figure 7.17: L1-band axial ratio (dB); (a) XZ-plane, (b) YZ-plane.

Some of the relevant performance metrics, namely, the HPBW, F/B ratio, grazing angle gain level (i.e. θ = 80˚) and AR are listed in Table 7.6 and Table 7.7 for the XZ- and YZ-plane, respectively. First the HPBW is compared. It is generally desirable to have a HPBW of at least 100˚ to ensure communication with at least 4 satellites. The HPBW meets this criteria for L3/4-, L1-bands. Next the F/B ratio is compared. It is desirable to have a F/B ratio of at least 10 dB to ensure radiation is in the upper hemisphere. The measured F/B is better than 10 dB except at the L5-band. The low grazing angle gain level (θ = 80˚) is then compared. It is desirable to have a realized gain near -10 dBi at grazing angles. L3/4 and L1-bands meet this criteria because of the broadening of the beam with increase in frequency. Finally the AR is compared. An AR less than 3 dB is desirable, since it ensures the difference between co- and cross-polarization is 15 dB. The AR is given in degrees (beamwidth) in which it is less than 3dB over the main beam. For all bands the beamwidth is larger than 100˚.

Table 7.6: XZ-plane measured HPBW, F/B ratio, realized gain at θ = 80˚ and AR

Band	HPBW (˚)	F/B (dB)	θ = 80˚ (dBi)	AR 3dB (˚)
L5	72	9.16	-11.89	107
L2	80	13.25	-18.37	114
L3/L4	114	17.75	-7.72	145
L1	148	21.48	-1.92	161

Table 7.7: YZ-plane measured HPBW, F/B ratio, realized gain at θ = 80˚ and AR

Band	HPBW (˚)	F/B (dB)	θ = 80˚ (dBi)	AR 3dB (˚)
L5	70	8.82	-11.27	119
L2	76	13.20	-16.96	134
L3/L4	116	21.38	-10.95	144
L1	156	28.39	-1.58	138

7.1.4 Integrated GPS Antenna Results

A simplified model of the Dakota UAV is used is this research effort. Fuselage was created by Mesoscribe Technologies using Spyder foam. Style 6781 S2-Glass fabric from Fibre Glast Inc. was used to skin the Spyder foam. Fiberglass was adhered to the fuselage using AEROPOXY epoxy resin. Furthermore, SuperFil Filler and UV Smooth Primer by Poly-Fiber was used to finish the composite surface. Filler smoothes the surface, while UV primer protects the structure from environment conditions, specifically, UV radiation, since epoxy resins are subject to deterioration when exposed to sunlight. The Dakota UAV was fabricated with three separate regions and shown in Figure 7.18. Additionally, Figure 7.19 shows the three regions of the fuselage with the placement of the vertical stabilizer on Region III. The measured relative permittivity and loss tangent of the simplified Dakota UAV skin is 2.65 and 0.015, respectively. Properties were characterized using an Agilent E4991A RF Impedance/Material analyzer from 0.03 - 1 GHz. Multiple samples were characterized and the results were averaged.

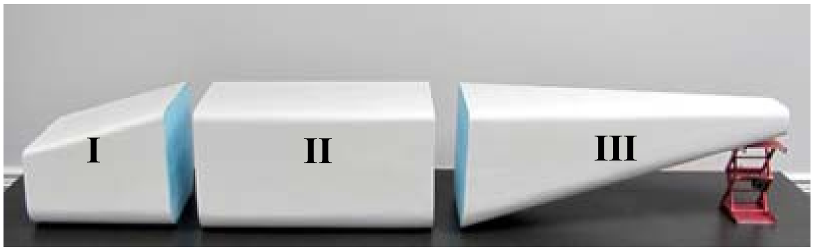

Figure 7.18: Three regions of simplified Dakota UAV fuselage.

Figure 7.19: Three regions of simplified Dakota UAV fuselage with the vertical stabilizer.

The integrated GPS results are now presented. Integration is inserting the GPS antenna into the tail of the Dakota UAV as shown in Figure 7.8(b) and Figure 7.20. Note that in the Figure 7.20, the GPS antenna is fully enclosed by the tail and only shown to emphasize the position relative to the VHF/UHF antenna. Measurements were taken with the VHF/UHF port terminated with a 50 Ω load. Integrated $|S_{11}|$ (dB) is shown in Figure 7.21. Simulated and measured results are in good agreement. Measured $|S_{11}|$ (dB) remains less than -10 dB from 1.137-1.968 GHz (1.73:1 bandwidth). Measured $|S_{11}|$ (dB) has a slight shift lower in frequency, due to the thin fiberglass composite of the UAV skin. To reduce the complexity of the simulation, the skin was not included.

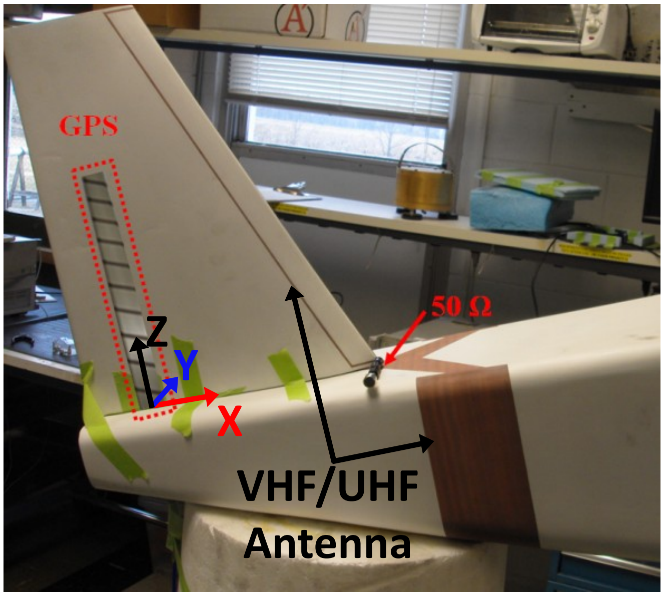

Figure 7.20: Integrated GPS antenna into Dakota UAV tail.

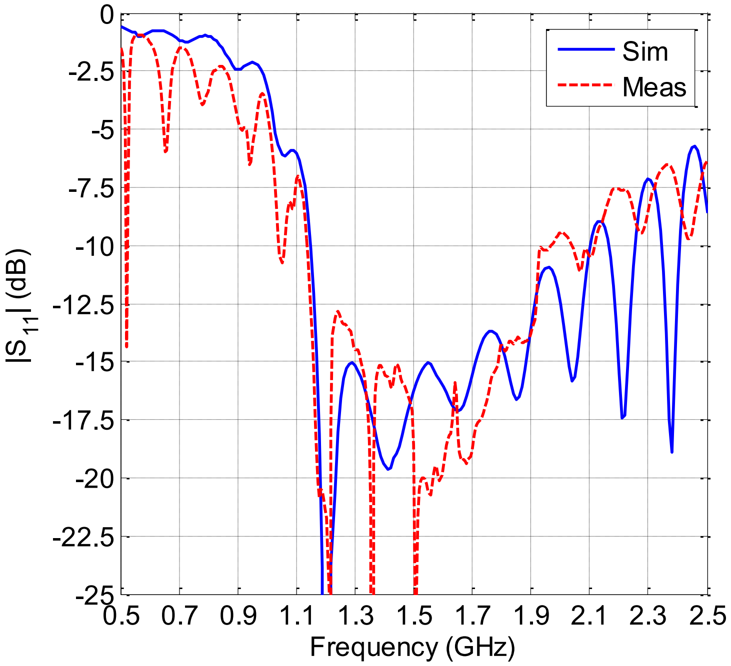

Figure 7.21: Integrated $|S_{11}|$ (dB) of 5-turn bifilar helical GPS antenna; (Blue) simulation results referenced to 200 Ω port impedance, (Red) measured results referenced to 50 Ω port impedance.

The integrated RHCP and LHCP realized gain at L5-band is shown in Figure 7.22 for both XZ- and YZ-planes. Good agreement between simulated and measured results is observed. Main integration effects are the increase in cross-polarization and slight deformation on the main beam, specifically in XZ-plane. The AR in the XZ- and YZ-planes is shown in Figure 7.23.

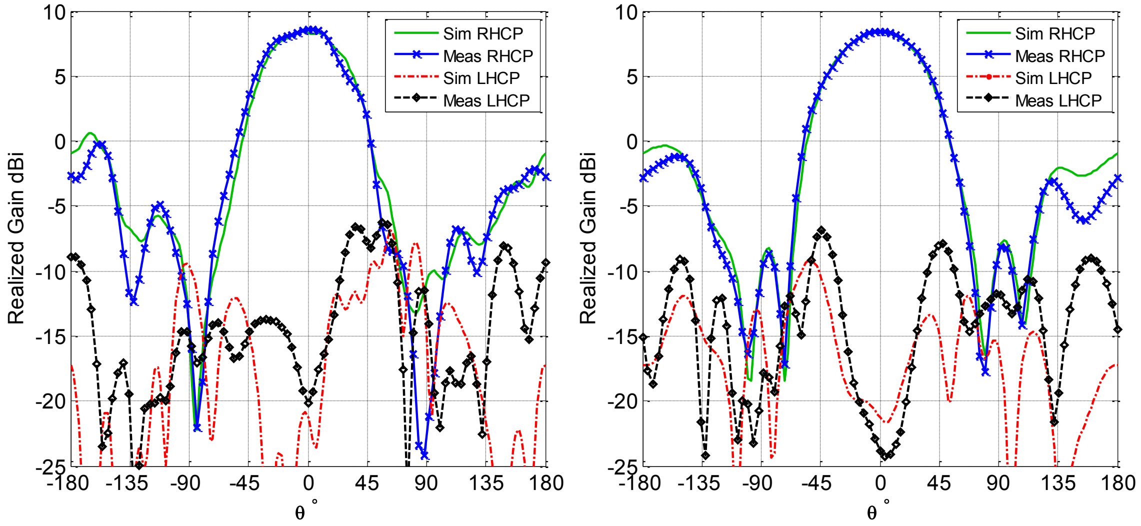

(a) (b)

Figure 7.22: L5-band realized gain (dBi) integrated into Dakota UAV tail; (a) XZ-plane, (b) YZ-plane.

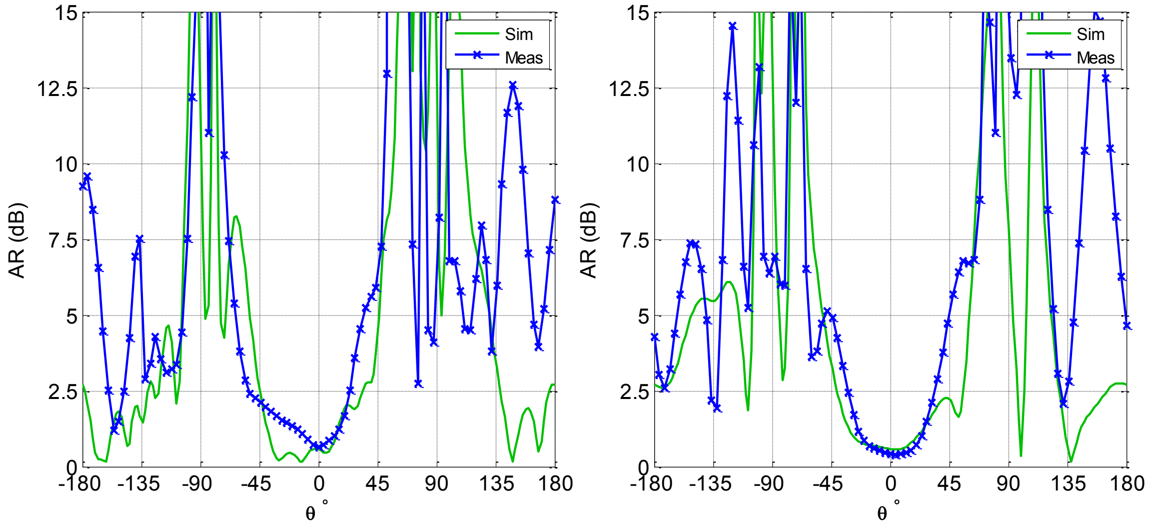

(a) (b)

Figure 7.23: L5-band axial ratio (dB) integrated into Dakota UAV tail; (a) XZ-plane, (b) YZ-plane.

The realized gain at L2-band is shown in Figure 7.24. L2-band measured gain is 1.37 dB less than simulation at boresight. Overall good agreement between simulation and measurement is achieved. The AR is shown in Figure 7.25.

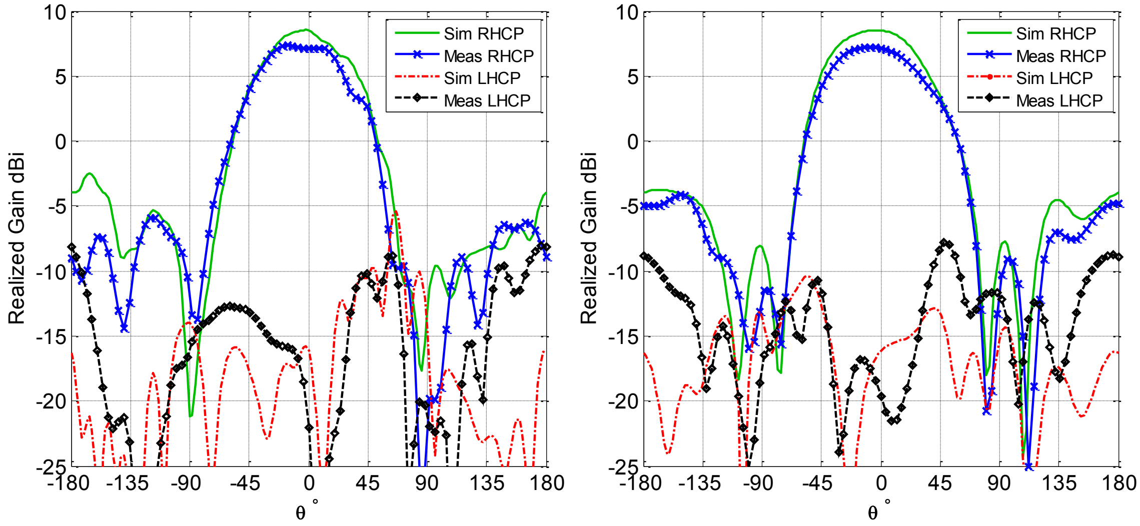

(a) (b)

Figure 7.24: L2-band realized gain (dBi) integrated into Dakota UAV tail; (a) XZ-plane, (b) YZ-plane.

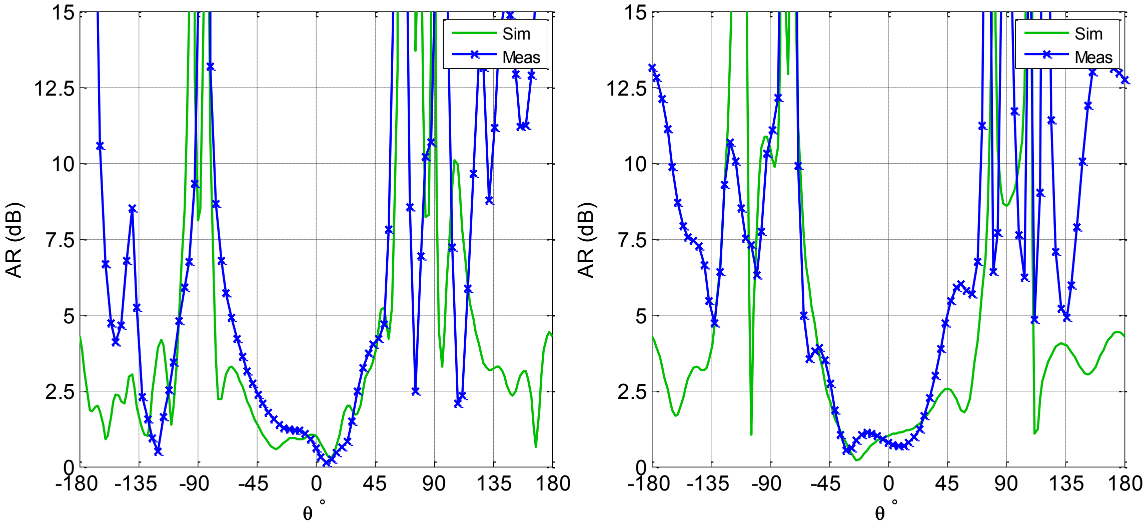

(a) (b)

Figure 7.25: L2-band axial ratio (dB) integrated into Dakota UAV tail; (a) XZ-plane, (b) YZ-plane.

The realized gain at 1.4GHz is shown in Figure 7.26 for both XZ- and YZ-planes. There is only a 0.51 dB difference between simulated and measured RHCP gain at boresight. The AR is shown in Figure 7.27.

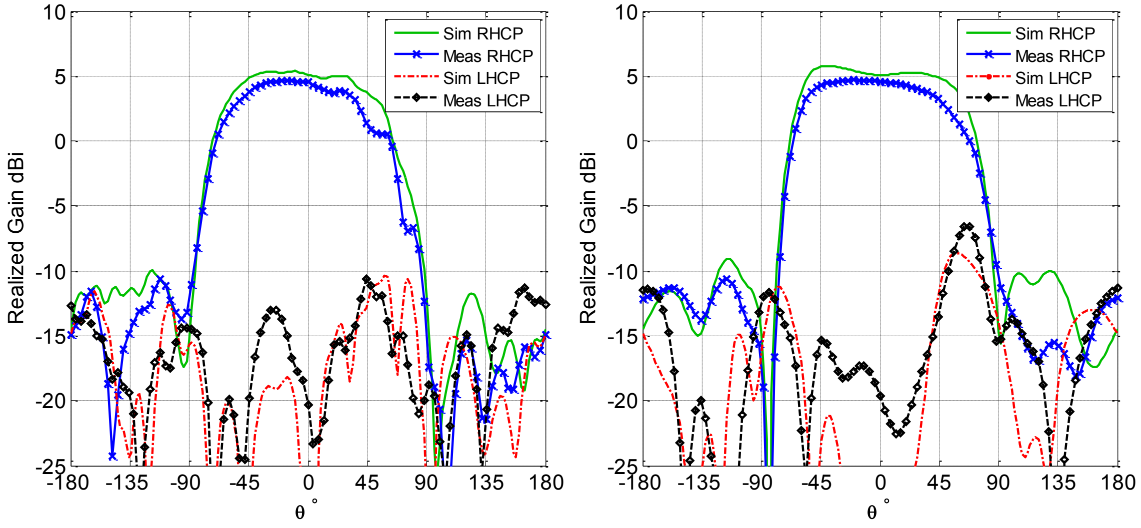

(a) (b)

Figure 7.26: 1.4 GHz realized gain (dBi) integrated into Dakota UAV tail; (a) XZ-plane, (b) YZ-plane.

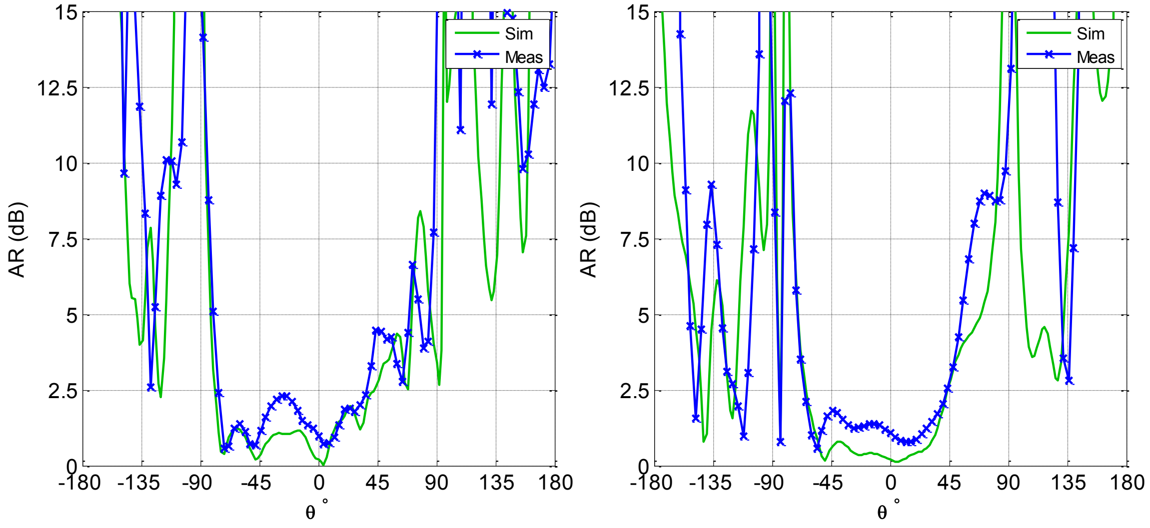

(a) (b)

Figure 7.27: 1.4 GHz axial ratio (dB) integrated into Dakota UAV tail; (a) XZ-plane, (b) YZ-plane.

The realized gain at L1-band is shown in Figure 7.28. L1-bands measured gain is 1.11 dB less than simulation at boresight. Good agreement between simulated and measured results is observed. Additionally, the AR is shown in Figure 7.29 for both the XZ- and YZ-planes.

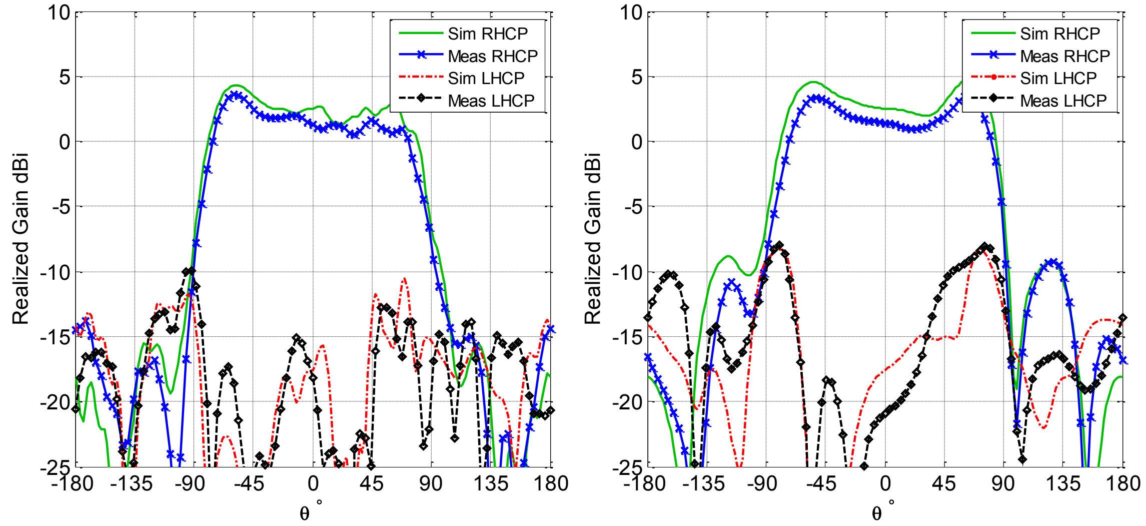

(a) (b)

Figure 7.28: L1-band realized gain (dBi) integrated into Dakota UAV tail; (a) XZ-plane, (b) YZ-plane.

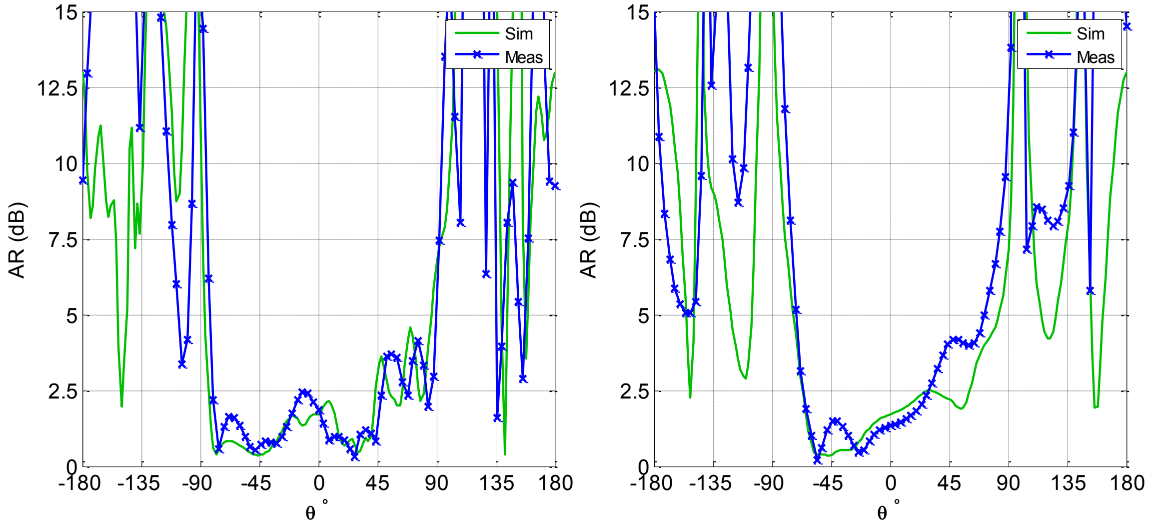

(a) (b)

Figure 7.29: L1-band axial ratio (dB) integrated into Dakota UAV tail; (a) XZ-plane, (b) YZ-plane.

The HPBW, F/B ratio, grazing angle gain level (i.e. θ = ±80˚) and AR are listed in Table 7.8 and Table 7.9 for the XZ- and YZ-plane, respectively. The HPBW is larger than 100° for L3/4- and L1-bands. The measured F/B ratio is better than 10 dB for all bands. Low grazing angle gain level (θ = 80˚) is then compared. The θ = ±80˚ grazing angle is better than -10 dB at L3/4- and L1 -bands in the XZ-plane and at L5- and L1-bands in YZ-plane. Note that L5-band is larger than -10 dBi due to a sidelobe. Finally, the AR is listed. The AR is less than 3 dB for at least 70° over the main beam for all bands.

Table 7.8: Measured integrated results in the XZ-plane HPBW, F/B ratio, realized gain at θ = 80˚ and AR

Band	HPBW (˚)	F/B (dB)	θ = 80˚ (dBi)	AR 3dB (˚)
L5	64	11.22	-18.53	83
L2	72	16.35	-10.20	85
L3/L4	106	17.43	-5.42	116
L1	145	18.08	-2.14	131

Table 7.9: Measured integrated results in the YZ-plane HPBW, F/B ratio, realized gain at θ = 80˚ and AR

Band	HPBW (˚)	F/B (dB)	θ = 80˚ (dBi)	AR 3dB (˚)
L5	74	11.20	-9.65	71
L2	81	12.15	-13.25	81
L3/L4	119	16.15	-16.60	113
L1	150	17.04	-3.14	92

7.2 Design of VHF/UHF Antenna Conformal to Dakota UAV

The VHF/UHF communication antenna is designed conformal to the tail and fuselage of the Dakota UAV. Communication antennas on UAVs generally require a vertically polarized omnidirectional pattern. The desired operating bandwidth in this design is from 30-400 MHz with a realized gain better than -15dB at 30MHz. At 30 MHz, the antenna is electrically small since the vertical height of the tail is only λ/22. Because the antenna is electrically small at 30 MHz, the goal is to design the antenna with a low Q to minimize the number of matching networks required. To lower the Q, a designer typically utilizes all available volume. However, since the GPS is integrated inside the tail, the volume available to utilize is limited.

A new design methodology was proposed which utilizes the vertical height of the Dakota Fuselage to increase the overall vertical height of the VHF/UHF antenna. Although the ultimate goal is have one matching network to cover the entire frequency band from 30-300 MHz, preliminary calculations have shown that the Q of the antenna at the lower frequencies (around 30 MHz) must be below 100, which is very difficult to achieve without sacrificing the efficiency of the antenna. The vertical height of VHF/UHF is one of the most important factors which limits the lowest possible Q of an antenna. The shorter the height of the antenna (electrically), the lower is its radiation resistance and thus the higher the Q becomes.

The design methodology for the conformal VHF/UHF antenna is as follows. First the antenna must minimize integration effects with the GPS antenna. To do this, the vertical element is placed on the front of vertical tail increasing the physical separation between antennas. To increase the vertical height, the antenna is designed conformal to the tail and fuselage of the UAV. To connect the vertical tail and fuselage elements a transition element is placed on top of the fuselage. Finally a plate is placed at the bottom of the fuselage. At 30 MHz the plate is electrically small, therefore it does not act as a ground plane but rather as a loading element to reduce the stored energy of the antenna. The VHF/UHF antenna is shown in Figure 7.30. The main sections of the antenna are highlighted. Note again that in the Figure 7.30(b), the GPS antenna is fully enclosed by the tail and only shown to emphasize the position relative to the VHF/UHF antenna.

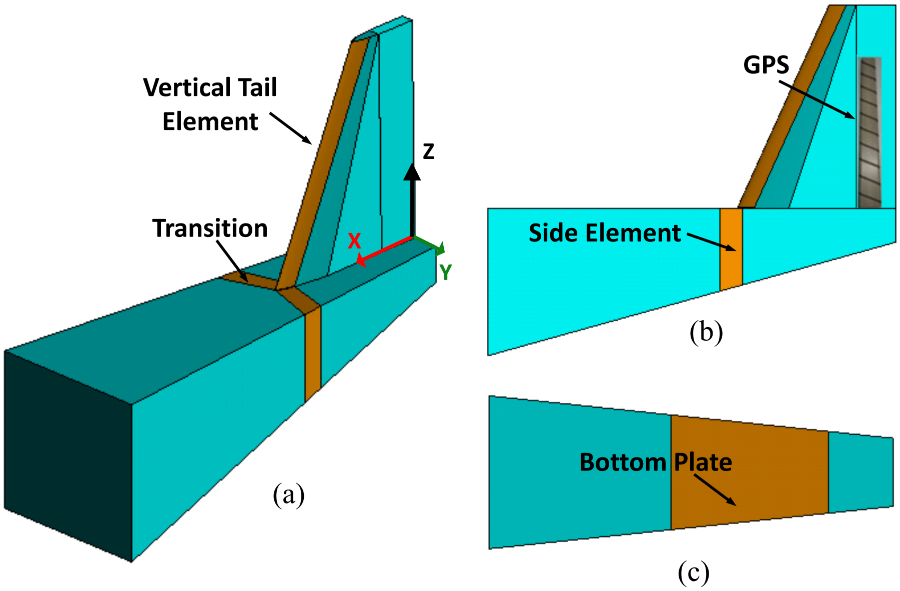

(a)

(b)

(c)

Figure 7.30: Conformal VHF/UHF asymmetrical dipole: (a) perspective view, (b) side view, (c) bottom view.

Due to the complexity of the antenna it is not obvious where to feed the antenna. Thus, a CM analysis is performed on the VHF/UHF antenna. The CM analysis provides the designer with potential feed locations. Additionally, the realistic bandwidth of the antenna is determined. The dominant CMs were identified using the resonance method outlined in Section 3.2. The reduced eigenvalue spectrum is shown in Figure 7.31. CM 1 is identified as the desired CM to excite since it radiates a near omnidirectional vertically polarized pattern. The eigen properties of CM 1 at all the modal resonant frequencies are shown in Figure 7.32-Figure 7.36. From analysis of the eigencurrent, the optimum location to excite CM 1 is on the lower region of the vertical tail (i.e. near transition of fuselage to vertical tail). Again this correspond to a dipole excitation. Note at 472.5 MHz, CM 1 no longer has an omnidirectional pattern (Figure 7.35(b)). Thus, the eigenpatterns of the higher order modes are investigated to see if the pattern bandwidth can be extended.

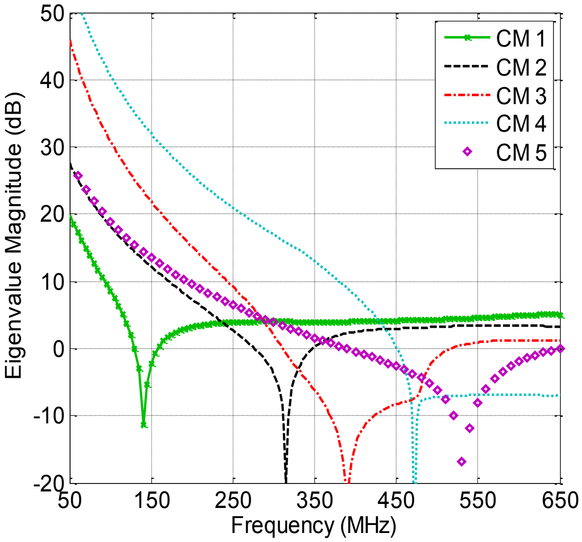

Figure 7.31: Eigenvalues spectrum of characteristic modes under consideration, $L_G = \lambda_M/8 \times W_G = \lambda_M/32$.

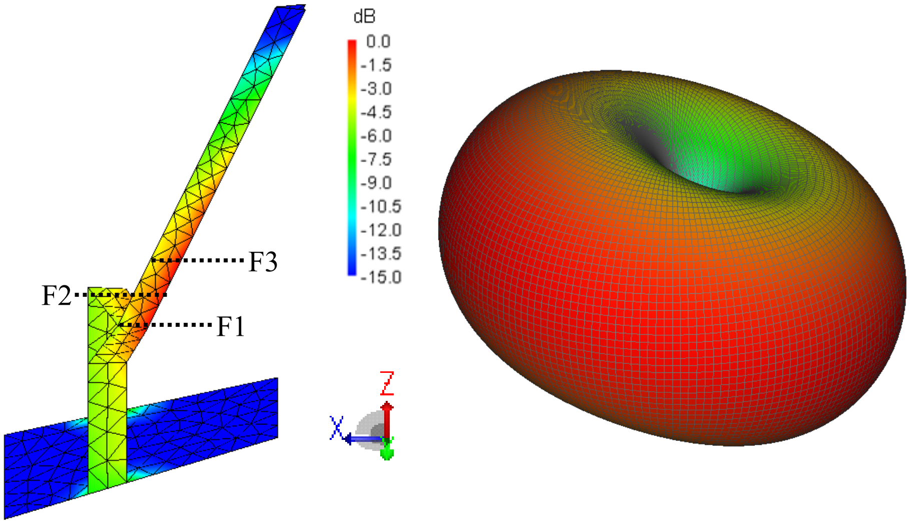

(a)

(b)

Figure 7.32: Normalized characteristic mode 1 eigen properties at 140 MHz; (a) eigencurrent, (b) eigenpattern.

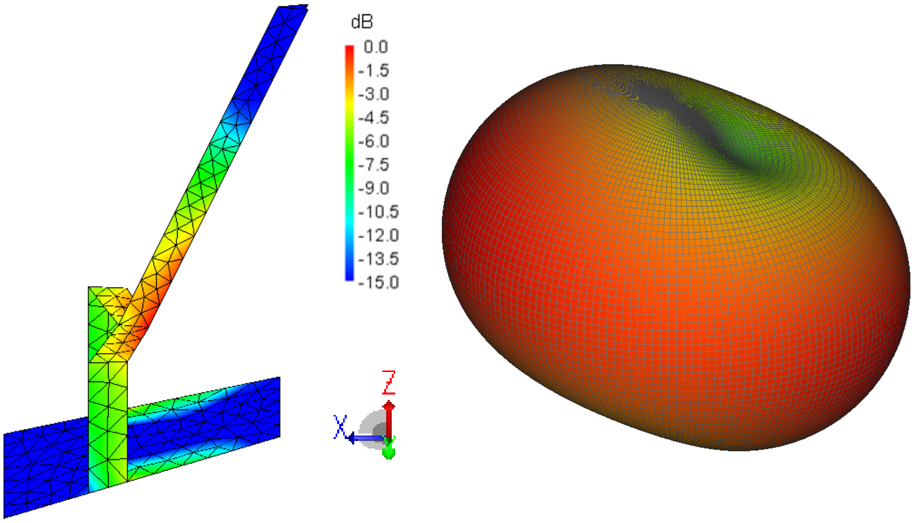

(a) (b)

Figure 7.33: Normalized characteristic mode 1 eigen properties at 315 MHz; (a) eigencurrent, (b) eigenpattern.

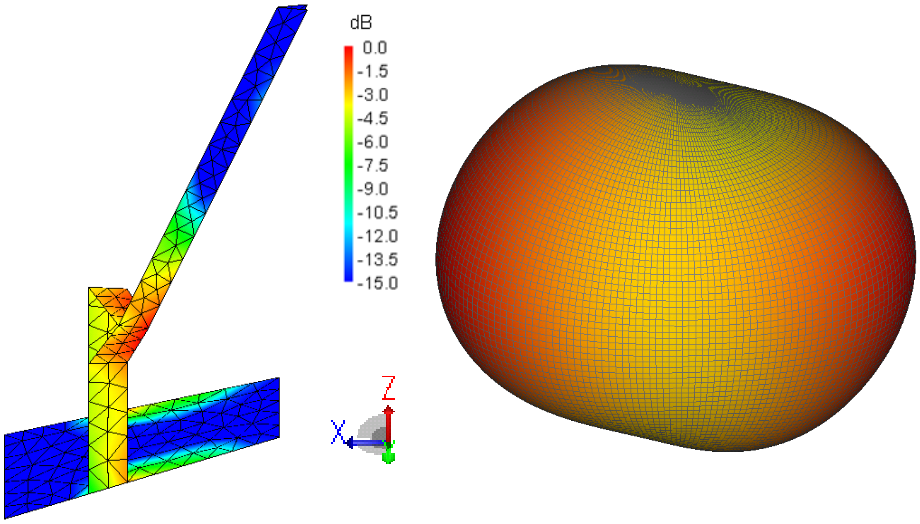

(a) (b)

Figure 7.34: Normalized characteristic mode 1 eigen properties at 390 MHz; (a) eigencurrent, (b) eigenpattern.

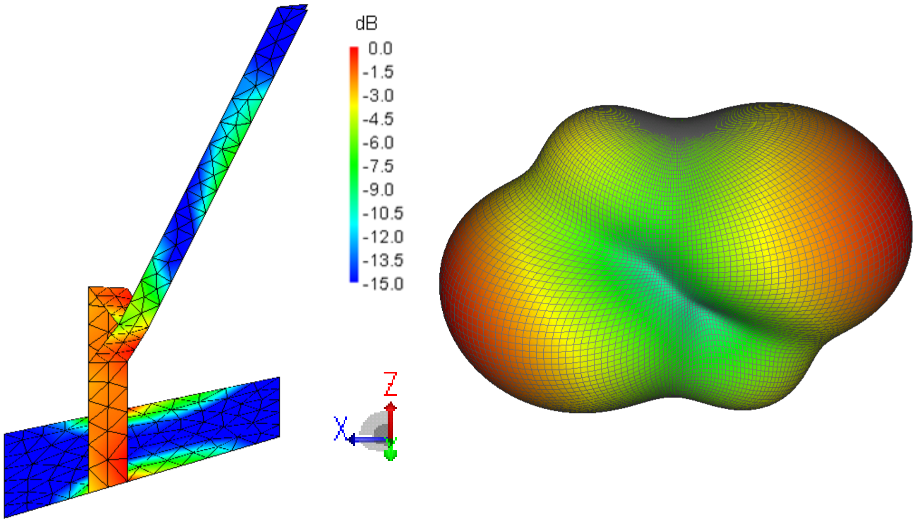

(a) (b)

Figure 7.35: Normalized characteristic mode 1 eigen properties at 472.5 MHz; (a) eigencurrent, (b) eigenpattern.

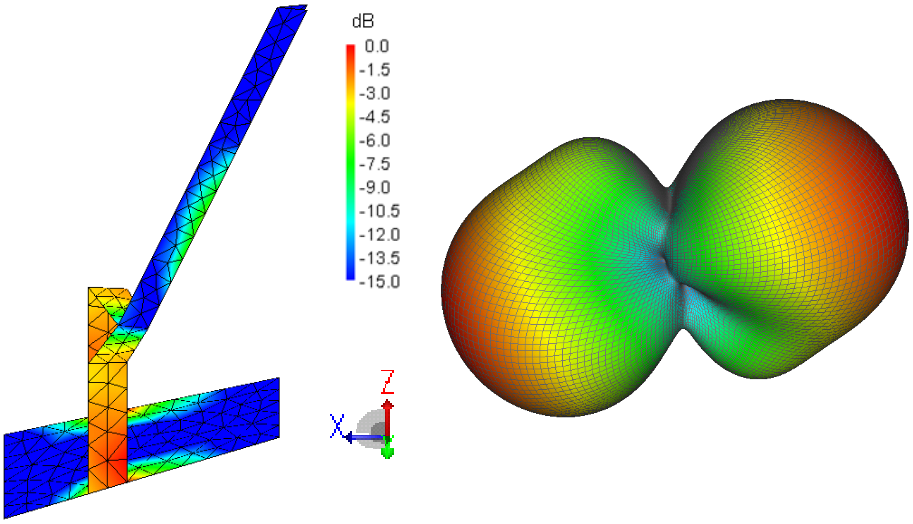

(a) (b)

Figure 7.36: Normalized characteristic mode 1 eigen properties at 530 MHz; (a) eigencurrent, (b) eigenpattern.

CM 2 is the first higher order mode investigated and is shown in Figure 7.37. The eigencurrent has a null in the preferred feed location of CM 1, thus will be weakly excited. Since CM 1 radiated a near omnidirectional pattern at 315 MHz it is not necessary to excite CM2. Next, CM 3 is analyzed and is shown in Figure 7.38. Similarly, CM 3 radiated pattern is undesirable and will not be excited by the preferred feed location of CM 1.

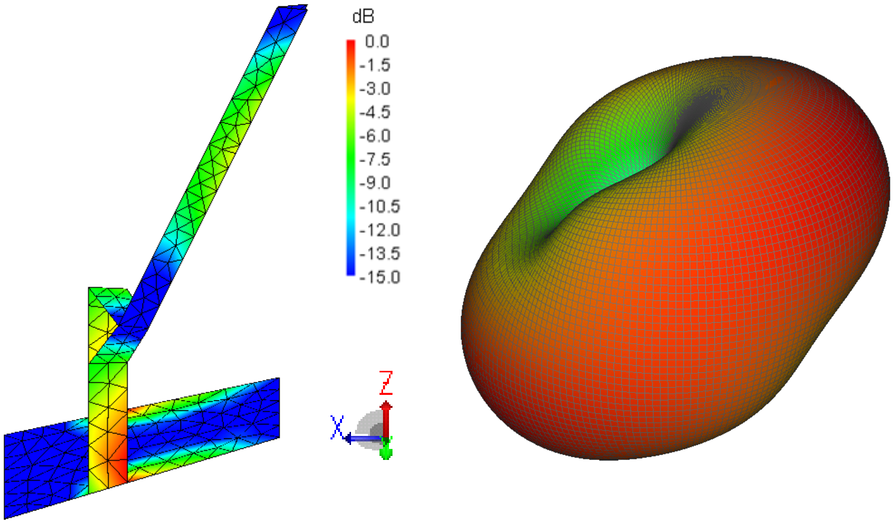

(a) (b)

Figure 7.37: Normalized characteristic mode 2 eigen properties at 315 MHz; (a) eigencurrent, (b) eigenpattern.

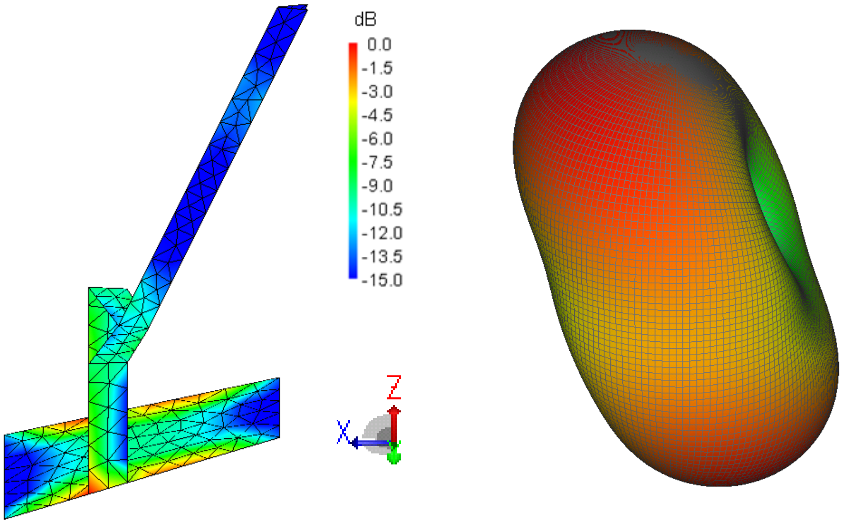

(a) (b)

Figure 7.38: Normalized characteristic mode 3 eigen properties at 390 MHz; (a) eigencurrent, (b) eigenpattern.

Finally, CM 4 and 5 are analyzed to see if the pattern bandwidth can be extended above 450 MHz. Neither eigenpattern is desirable, thus the desired omnidirectional behavior cannot be extended to higher frequencies. CM 4 will be strongly excited by the feeding network. It is not necessary to suppress this mode, since there is not a better option.

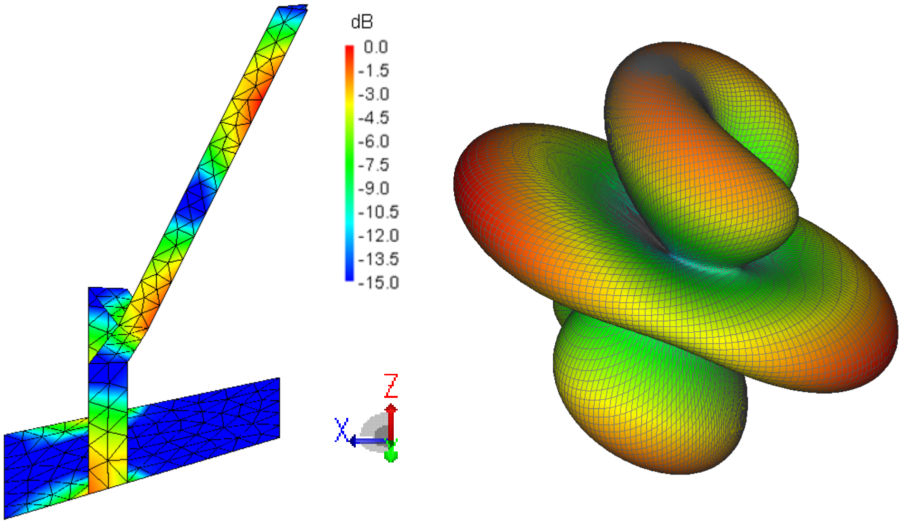

(a) (b)

Figure 7.39: Normalized characteristic mode 4 eigen properties at 472.5 MHz; (a) eigencurrent, (b) eigenpattern.

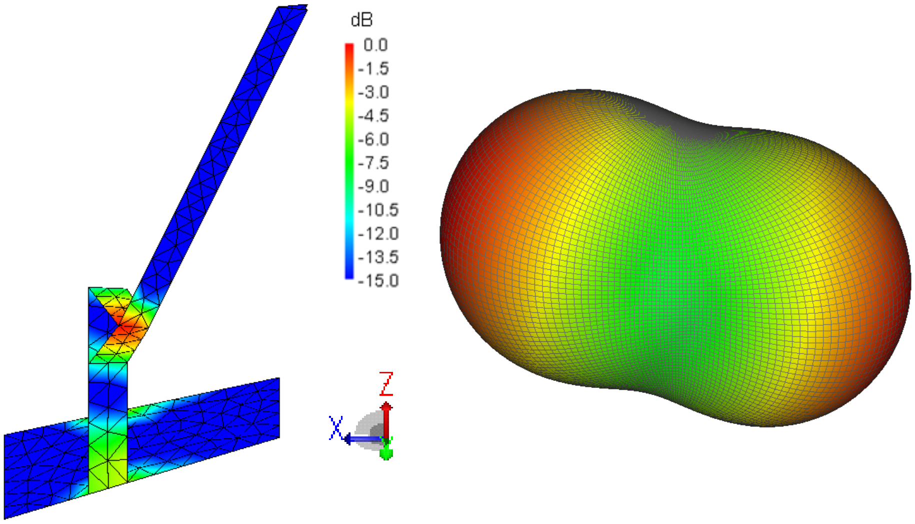

(a) (b)

Figure 7.40: Normalized characteristic mode 5 eigen properties at 530 MHz; (a) eigencurrent, (b) eigenpattern.

Based on the analysis of the dominant CMs eigen properties, it was found that CM 1 radiates the only near omni-directional pattern over the VHF/UHF band. Thus, the feed is chosen near the base of the vertical tail element, such that CM 1 is strongly excited. Furthermore, CM 2 and 3 are suppressed by the feeding network. Note CM 4 and 5 are less important when determining feed location, since CM 1 pattern no longer is omnidirectional above 450 MHz. Three feed location were tested on the vertical element and emphasized in Figure 7.32(a). F1 was placed at the bottom of the vertical tail element. F2 and F3 were placed at 5 and 10 cm from the bottom of the vertical tail element, respectively. For each feed location, both the broadside (θ = 90°) vertical and horizontal simulated realized gain is shown in Figure 7.41-Figure 7.43. There are only minor differences between feed location 1 and 2. Feed 3 develops a deep null at 310 MHz due to a stronger excitation of CM 2.

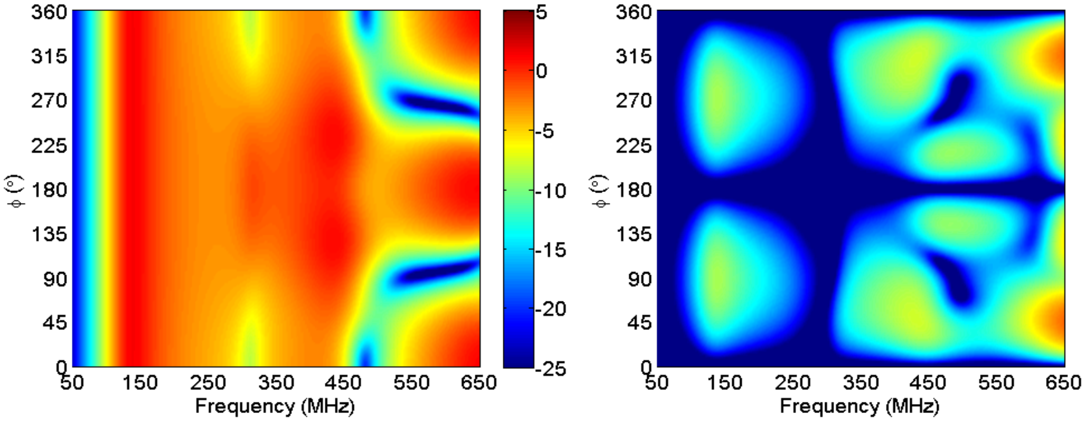

(a) (b)

Figure 7.41: Dakota UAV F1 realized gain (dBi) vs. frequency in XY-plane; (a) vertical-polarization, (b) horizontal-polarization.

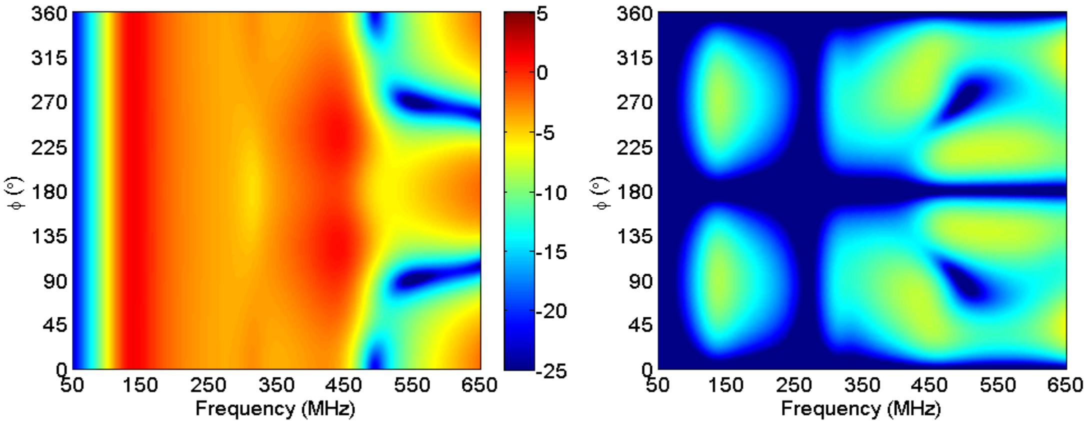

(a) (b)

Figure 7.42: Dakota UAV F2 realized gain (dBi) vs. frequency in XY-plane; (a) vertical-polarization, (b) horizontal-polarization.

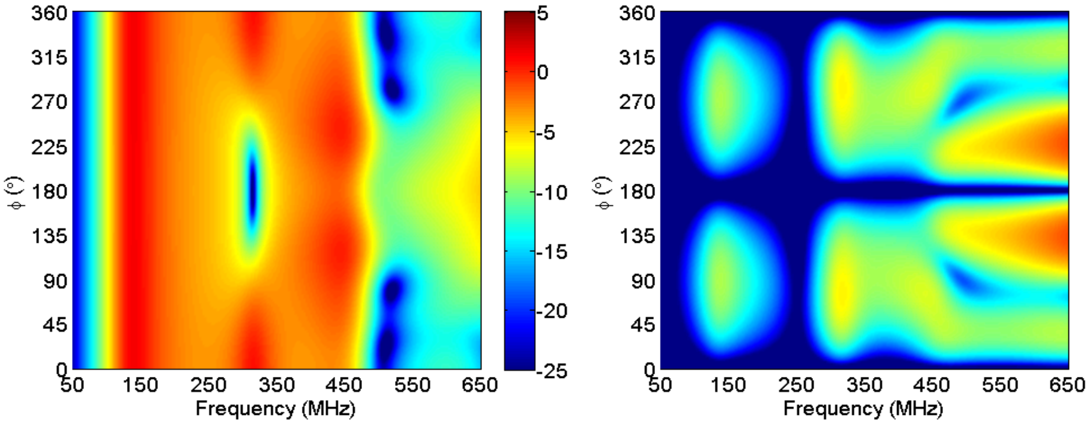

(a) (b)

Figure 7.43: Dakota UAV F3 realized gain (dBi) vs. frequency in XY-plane; (a) vertical-polarization, (b) horizontal-polarization.

7.2.1 Simulated VHF/UHF Integration Results

Finally, in this section the simulated integration effects on the VHF/UHF are presented. Currently measurements are being conducted using ESLs outdoor range, therefore only simulated patterns are shown. Since GPS simulated and measured are in good agreement, the VHF/UHF measurements are expected to match simulation.

Previously it was show that F1 and 2 have very similar performance. Therefore, F1 is chosen, mainly because it occurs at the transition between the vertical tail and the fuselage. F1 realized gain (dBi) is shown in Figure 7.44 for both vertical and horizontal polarization, respectively. The noticeable difference is the decrease in gain around 265 MHz. The integration comparison on $|S_{11}|$ (dB) and Q are shown in Figure 7.46 and Figure 7.46, respectively. Again the integration effects are negligible except at 265 MHz. Integration has a negative effect on $|S_{11}|$, directly reducing the realized gain. Very good agreement is achieved below 250 MHz. This is specifically important for the Q, since below 80 MHz the antenna requires a matching network to improve the realized gain.

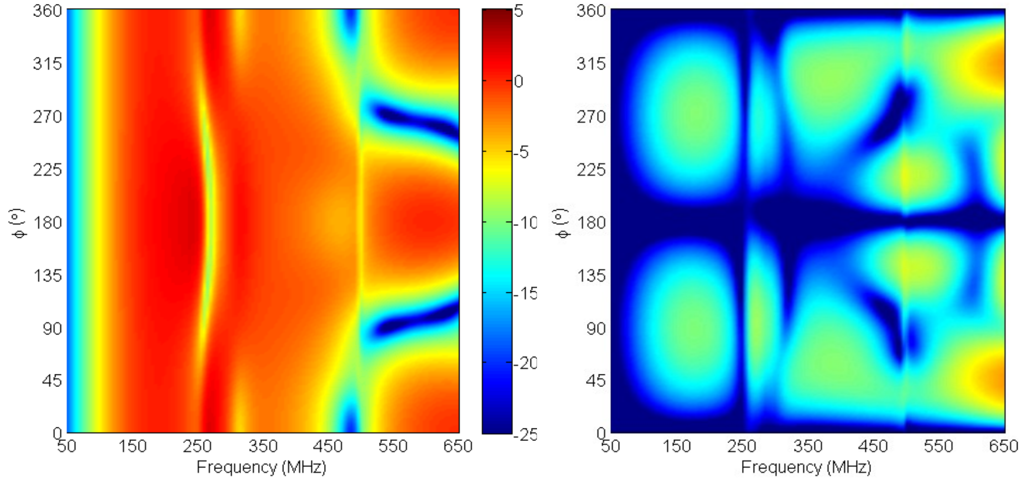

(a) (b)

Figure 7.44: Integrated Dakota UAV F1 realized gain (dBi) vs. frequency in XY-plane; (a) vertical-polarization, (b) horizontal-polarization.

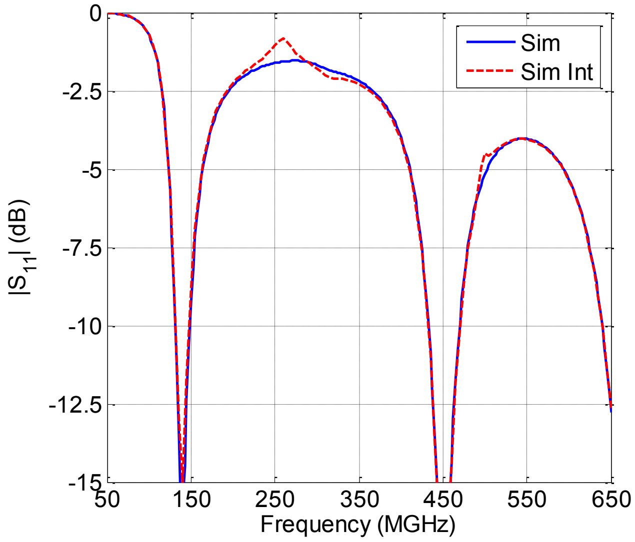

Figure 7.45: Integrated VHF/UHF $|S_{11}|$ (dB) comparison.

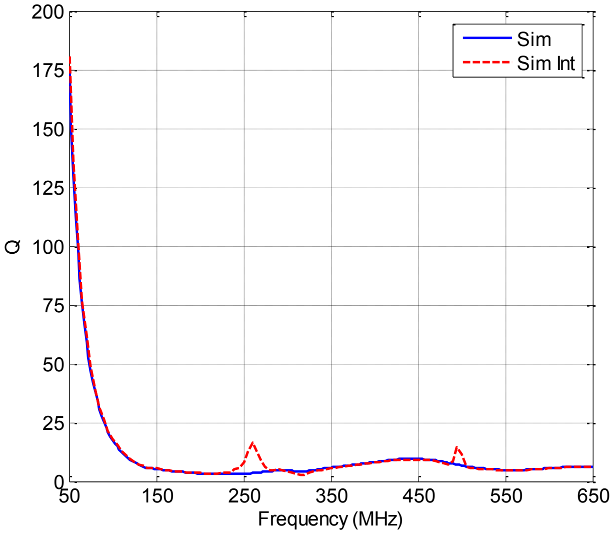

Figure 7.46: Integrated VHF/UHF Q comparison.

7.3 Summary

In this chapter a 5-turn bifilar helix was designed for the Dakota UAV. The antenna is inserted in the vertical stabilizer. The antenna was designed using a linearly varying pitch to enhance the bandwidth and was fabricated using a novel mesoplasma direct write technology. A GPS feed network insert was designed which provides an impedance match ($|S_{11}|$ <-10 dB) from 1.137-1.968 GHz (after integration), covering L1-L5 GPS bands. Simulation and measurements are in good agreement.

Additionally, CM theory was used to design a VHF/UHF antenna conformal to the tail and fuselage of the Dakota UAV. The antenna utilizes the rigorous analysis of electrically small ground planes in Chapters 4-6 and Appendix B. The vertical height of the antenna was increased by utilizing the fuselage sides. Furthermore, a plate on the bottom of the UAV was used to load the antenna resulting in a lower frequency of operation. The optimum feed location was found from CM analysis, resulting in the largest pattern bandwidth. Both GPS and VHF/UHF antennas maintain performance after integration.

Chapter 8 Conclusions and Future Work

Conformal antennas have become increasingly important for modern UAVs. Specifically, the small physical size of the UAV and the need for improved aerodynamics has created the push to design antennas conformal to the host structure. Irregular shape of host structure creates complex antenna problems, typically with no analytical solution. Often, for these antennas the designer resorts to running simulation and optimization routines to find an adequate design, but little insight is gained about the fundamental problem. Thus, there is a need for a design method which maintains the relevant physics of the problem.

In this dissertation, the theory of CMs was used for the analysis and design of complex conformal antennas. Traditionally, CM theory has been applied to electrically small to intermediate size antennas for simplicity. Furthermore, CM theory has been mainly used as an analysis tool. Complex antennas including conformal UAV antennas and antennas modeled with plates were analyzed. One of the challenges when using CM theory for the design of complex antennas is the large generalized Z-matrix. The number of CMs depends on the size of the Z-matrix. Thus, when modeling electrically large structures, the size of the Z-matrix becomes large resulting in an increased number of CMs to analyze. Therefore, a systematic approach for reducing the number of CMs in an analysis was developed. Simplifying the analysis is critical to extending CM theory to more complex structures.

Another challenge when using CM theory as a design tool is determining how to excite or suppress CMs using a feeding network. As such, port placement was thoroughly emphasized throughout this dissertation. Design methods via proper port placement were shown for determining the location for the minimum quality factor (Q_{min}), extending pattern bandwidth and cross-polarization reduction. Analysis using the modal admittance and weighting coefficient is thoroughly used to show the excitation and suppression of modes. It was shown that modes which contribute to the conductance radiate energy, whereas modes that mainly contribute to the susceptance store energy.

In Chapter 3, two systematic procedures for reducing the number of modes considered in a CM analysis were developed. This was critical to apply CM analysis to more complex antenna structures. Modes were reduced based on design criteria. Common design criteria are polarization, gain levels, pattern bandwidth and input impedance. As such, throughout this dissertation a vertically polarized omnidirectional radiation pattern was specified as the design criterion for conformal VHF/UHF UAV antennas. Although this was the specified design criteria for all antennas except for GPS antenna, the method developed here can be used for arbitrary pattern shapes.

Chapter 4 investigated antenna elements with electrically small square ground planes. The investigation identified four important CMs when the width of the ground plane was $\lambda/8$, $\lambda/16$ and $\lambda/32$ at 150 MHz. It was determined that antenna elements on electrically small ground planes should not be fed like a monopole, but rather like a dipole to achieve wideband pattern performance, specifically omni-directional at broadside. In addition to the square ground plane case, electrically small rectangular ground planes were investigated. Results are presented in Appendix B. Rectangular ground planes are the more realistic case for conformal UAV antennas since the width of the UAV is severely restricted.

Chapter 5 outlined a method to determine the Q_{min} feed location for electrically small square and rectangular ground planes. It was determined that the first undesired higher order mode (CM 2) was the mode which dictates the Q_{min} feed location. To minimize the excitation of CM 2 the feed is placed at the null of the eigencurrent specifically at its corresponding resonant frequency.

Chapter 6 investigated electrically small rectangular ground planes with an offset antenna element. Feeding network tradeoffs and limitations were discussed. As expected, when the antenna element is offset the eigenpatterns are no longer symmetric. Additionally, the eigencurrents have a large horizontal current component in the ground plane, increasing cross-polarization. Important modes are identified and a feed location to excite or suppress the modes was analyzed. Tradeoffs between bandwidth, high frequency cutoff and tolerable cross-polarization level are discussed.

Chapter 8 introduced the concept of volume integration of a GPS and VHF/UHF antenna conformal to a Dakota UAV. The design of a 5-turn bifilar helix antenna for GPS applications was presented. The GPS antenna covers L1-L5 bands and fits inside the tail of the Dakota UAV. The antenna was fabricated using mesoplasma direct write technology [16] and verified experimentally. Good agreement between simulation and measurements was achieved. Furthermore, a VHF/UHF antenna conformal to the vertical tail and fuselage was designed using the insight gained through rigorous CM analysis of UAV structures examined in Chapters 4-7.

The key contributions of this dissertation are summarized as follows:

- Development of systematic procedures for reducing the number of CMs considered for complex antenna structures. This lays the foundation for simplifying the analysis of complex antenna structures, allowing CM theory to be applied to conformal UAV antennas.
- Thorough analysis of the input admittance of CMs was conducted. It was shown for a lossless structure, that if a mode contributes to the conductance, it ultimately contributes to the radiated pattern. For higher order modes this is typically undesirable. Thus, the effects of higher order modes were suppressed by proper feed

placement. Suppressing the higher order mode resulted in increased pattern bandwidth.

- Investigation of electrically small square and rectangular ground plane effects on feed location using the theory of CMs. Analysis showed that when a designer has an electrically small ground plane the antenna should be fed like a dipole ro improve pattern bandwidth. Furthermore, it was found that placing the feed location in the eigencurrent null (at resonance) of the first higher order mode (i.e. CM 2) results in the Q_{min} feed location at VHF-band. Design tradeoffs for an offset antenna element were shown. Based on the CM properties the designer has the following tradeoffs; (1) optimize antenna for low frequency operation (VHF-band), (2) lowest cross-polarization level over desired frequency range, (3) largest bandwidth which maintains an omnidirectional radiation pattern, (4) a combination of (1)-(3). Three feed locations were chosen to emphasize tradeoffs.
- Design, fabrication and experimental verification of a 5-turn bifilar helix GPS antenna covering L1-L5 GPS bands which fits inside the tail of the Dakota UAV. The antenna was designed using a linearly varying pitch to enhance the bandwidth and fabricated using a novel mesoplasma direct write technology. A feeding network insert was designed from a microwave laminate (RO3203) providing an impedance match from 1.137-1.968 GHz, with $|S_{11}|$ less than -10 dB after integration.
- Design of a VHF/UHF antenna conformal to the tail and fuselage of the Dakota UAV by use of CM theory. The antenna utilizes the rigorous analysis of electrically small ground planes in Chapters 4-6 and Appendix B. The vertical height of the antenna was increased by utilizing the fuselage sides. Furthermore, a plate on the bottom of the UAV was used to load the antenna resulting in a lower frequency of operation. The

optimum feed location was found from CM analysis, resulting in the largest pattern bandwidth. Both GPS and VHF/UHF antennas maintain performance after integration.

Continued efforts are necessary to improve CM theory as a design tool. One area for future work includes understanding structural and material modifications to improve antenna performance. Since CMs are structural/material dependent. Changing the structure can increase or decrease the potential significance of a mode. However, the key is to understand how to modify a structure to be able to control the modes to achieve the desired performance improvement (i.e. excitation/suppression of mode, bandwidth enhancement, etc.). Potentially the designer would analyze the structure, determine the dominant mode via methods outlined in this dissertation, then modify the geometry to improve antenna performance.

Bibliography

[1] H.A. Wheeler, "Fundamental Limitations of Small Antennas," *Proceedings of the IRE*, vol. 35, pp. 1479-1484, 1947.

[2] L. J. Chu, "Physical limitations on omni-directional antennas," *Journal of Applied Physics*, vol. 19, p. 1163, 1948.

[3] A.D. Yaghjian and S.R. Best, "Impedance, bandwidth, and Q of antennas," *IEEE Transactions on Antennas and Propagation*, vol. 53, pp. 1298-1324, 2005.

[4] R. Garbacz and R. Turpin, "A generalized expansion for radiated and scattered fields," *IEEE Transactions on Antennas and Propagation*, vol. 19, pp. 348-358, 1971.

[5] R. Harrington and J. Mautz, "Theory of characteristic modes for conducting bodies," *IEEE Transactions on Antennas and Propagation*, vol. 19, no. 5, pp. 622–628, Sept. 1971.

[6] R. Harrington and J. Mautz, "Computation of characteristic modes for conducting bodies," *IEEE Transactions on Antennas and Propagation*, vol. 19, no. 5, pp. 629–639, Sept. 1971.

[7] R. Harrington and J. Mautz, "Control of radar scattering by reactive loading," *IEEE Transactions on Antennas and Propagation*, vol. 20, no. 4, pp. 446–454, Jul. 1972.

[8] R. Harrington and J. Mautz, "Pattern synthesis for loaded N-port scatterers," *IEEE Transactions on Antennas and Propagation*, vol. 22, pp. 184-190, 1974.

[9] D. Liu, R. J. Garbacz, and D. M. Pozar, "Antenna synthesis and optimization using generalized characteristic modes," *IEEE Transactions on Antennas and Propagation*, vol. 38, pp. 862-868, 1990.

[10] R. Garbacz and D. Pozar, "Antenna shape synthesis using characteristic modes," *IEEE Transactions on Antennas and Propagation*, vol. 30, pp. 340-350, 1982.

[11] S. K. Chaudhury, W. L. Schroeder, and H. J. Chaloupka, "MIMO antenna system based on orthogonality of the characteristic modes of a mobile device," *Antennas, 2007. INICA '07. 2nd International ITG Conference on*, pp. 58-62, March 2007.

[12] J. Ethier and D.A. McNamara, "An Interpretation of Mode-Decoupled MIMO Antennas in Terms of Characteristic Port Modes," *IEEE Trans. Magnetics*, vol. 45, no. 3, pp. 1128-1131, 2009.

[13] K. A. Obeidat, B. D. Raines, and R. G. Rojas, "Application of Characteristic Modes and Non-Foster Multiport Loading to the Design of Broadband Antennas," *IEEE Transactions on Antennas and Propagation*, vol. 58, pp. 203-207, 2010.

[14] K.A. Obeidat, B.D. Raines, R.G. Rojas, and B.T. Strojny, "Design of Frequency Reconfigurable Antennas Using the Theory of Network Characteristic Modes," *Antennas and Propagation, IEEE Transactions on*, vol. 58, no. 10, pp. 3106-3113, 2010.

[15] K.A. Obeidat, B.D. Raines, and R.G. Rojas, "Discussion of Series Parallel Resonance Phenomena in the Input Impedance of Antennas," *Radio Science*, vol. 45, 2010.

[16] MesoScribe Technologies. [Online]. http://www.mesoscribe.com/

[17] A. Yee and R. Garbacz, "Self- and mutual-admittances of wire antennas in terms of characteristic modes," *IEEE Transactions on Antennas and Propagation*, vol. 21, pp. 868-871, 1973.

[18] M. C. Fabres, "Systematic Design of Antennas Using the Theory of Characteristic Modes," Universidad Politechnica de Valencia, PhD Dissertation 2007.

[19] R. Harrington, "Effect on antenna size on gain, bandwidth, and effciency," *J. Res. Nat. Bur.*

Stand., vol. 64D, pp. 1-12, 1960.

[20] R. Collin and S. Rothschild, "Evaluation of antenna Q," *IEEE Transactions on Antennas and Propagation*, vol. 12, pp. 23-27, 1964.

[21] R. Fante, "Quality factor of general ideal antennas," *IEEE Transactions on Antennas and Propagation*, vol. 17, pp. 151-155, 1969.

[22] J. Mautz and R. Harrington, "Computational methods for antenna pattern synthesis," *IEEE Transactions on Antennas and Propagation*, vol. 23, pp. 507-512, 1975.

[23] O.M. Bucci, G. D'Elia, G. Mazzarella, and G. Panariello, "Antenna pattern synthesis: a new general approach," *Proceedings of the IEEE*, vol. 82, pp. 358-371, 1994.

[24] B.A. Austin and K.P. Murray, "The application of characteristic-mode techniques to vehicle-mounted NVIS antennas," *Antennas and Propagation Magazine, IEEE*, vol. 40, pp. 7 -21, 30, 1998.

[25] B. T. Strojny and R. G. Rojas, "Characteristic mode analysis of electrically large conformal bifilar helical antenna," *Proc. 4th European Conference on Antennas and Propagation*, pp. 1-5, 2010.

[26] C. A. Balanis, *Modern Antenna Handbook.*: Wiley, 2008.

[27] A.S. Meier and W.P. Summers, "Measured Impedance of Vertical Antennas over Finite Ground Planes," *Proceedings of the IRE*, vol. 37, no. 6, pp. 609-616, 1949.

[28] R.G. Fitzgerrell, "Monopole impedance and gain measurements on finite ground planes ," *Antennas and Propagation, IEEE Transactions on*, vol. 36, no. 3, pp. 431-439, 1988.

[29] M.-C. Huynh and W. Stutzman, "Ground plane effects on planar inverted-F antenna (PIFA) performance," *IEE Proc.-Microw., Antennas and Propag.*, vol. 150, no. 4, pp. 209-213, 2003.

[30] S. R. Best, "A Discussion on Small Antennas Operating with Small Finite Ground Planes," *Proc. IEEE Int Antenna Technology Small Antennas and Novel Metamaterials Workshop*, pp. 152-155, 2006.

[31] S. R. Best, "The Significance of Ground-Plane Size and Antenna Location in Establishing the Performance of Ground-Plane-Dependent Antennas," *IEEE Antennas and Propagation Magazine*, vol. 51, no. 6, pp. 29-43, 2009.

[32] B. T. Strojny and R. G. Rojas, "Integration of conformal GPS and VHF/UHF communication antennas for small UAV applications," in *Proc. 3rd European Conference on Antennas and Propagation*, 2009, pp. 2488-2492.

[33] B. T. Strojny and R. G. Rojas, "Volume integrated conformal UAV antennas," *USNC/URSI/NRSM National Radio Science Meeting*, pp. 2488-2492, 2010.

[34] Richard L. Chen, Jeffery T. Williams, David R. Jackson Lorena I. Basilio, "A New Planar Dual-Band GPS Antenna Designed for Reduced Susceptibility to Low-Angle Multipath," *IEEE Transactions on Antennas and Propagation*, vol. 55, no. 8.

[35] W. T. Patton, "The backfire bifilar helical antenna," Univ. Illinois Antenna Lab., Ph.D. Dissertation 1962.

[36] Marhefka, R. J. Kraus J. D., *Antennas for all Applications*, 3rd ed. Boston: McGraw-Hill, 2002.

[37] H. Nakano, J. Yamauchi, and S. Iio, "Tapered backfire helical antenna with loaded termination," *Electronics Letters*, vol. 18, no. 4, pp. 158-159, 1982.

[38] H. Nakano, S. Iio, and J. Yamauchi, "Improvement in front-to-back ratio of a bifilar backfire helix by a flared open end," *Antennas and Propagation, IEEE Transactions on*, vol. 41, no. 11, pp. 1591-1595, 1993.

[39] C. H. Walter, *Traveling Wave Antennas*. New York: Dover Publications Inc., 1970.

[40] R. Garbacz, "Modal expansions for resonance scattering phenomena," *Proc. IEEE*, vol. 53, pp. 856–864, August 1965.

[41] E. Newman. The electromagnetic surface patch code: Version 5, The Ohio State University. [Online]. http://esl.eng.ohio-state.edu

[42] Agilent Tech. [Online]. www.agilent.com

[43] EM Software & Systems. FEKO Website. [Online]. http://www.feko.info

[44] Ansoft LLC. Ansoft HFSS Overview. [Online]. http://www.ansoft.com/products/hf/hfss

[45] E. Telatar, "Capacity of Multi-Antenna Gaussian Channels," AT&T Bell Laboratories, Technical Memorandum June 1995.

[46] R. Allemang, "The modal assurance criterion—twenty years of use and abuse," *Sound and Vibration*, pp. 14-21, August 2003.

[47] R. E. Kalaba, K. Spingarn, and L. Tesfatsion, "Individual Tracking of an Eigenvalue and Eigenvector of a Parameterized Matrix," *Nonlinear Analysis: Theory, Methods, and Applications*, vol. 5, no. 4, pp. 337-340, 1981.

[48] K. Naishadham, T. W. Nuteson, and R. Mittra, "Parametric interpolation of the moment matrix in surface integral equation formulation," *International Journal of RF and Microwave Computer-Aided Eng.*, vol. 9, no. 6, pp. 474-489, Oct. 1999.

[49] P. Comon and G. H. Golub, "Tracking a Few Extreme Singular Values and Vectors in Signal Processing," *Proceedings of the IEEE*, vol. 78, no. 8, pp. 1372-1343, Aug. 1990.

[50] K. A. Obeidat, B. D. Raines, and R. G. Rojas, "Antenna Design and Analysis Using Characteristic Modes," *IEEE AP-S International Symposium*, 2007.

[51] K. A. Obeidat, B. D. Raines, and R. G. Rojas, "Analysis of Antenna Input Impedance

Resonances In Terms of Characteristic Modes," *IEEE AP-S Symposium*, 2009.

[52] The Mathworks, Inc. [Online]. http://www.mathworks.com

[53] R.C. Hansen, "Fundamental limitations in antennas," *Proceedings of the IEEE*, vol. 69, pp. 170-182, 1981.

[54] H.A. Wheeler, "The Radiansphere around a Small Antenna," *Proceedings of the IRE*, vol. 47, pp. 1325-1331, 1959.

[55] W. Geyi, "Physical limitations of antenna," *IEEE Transactions on Antennas and Propagation*, vol. 51, pp. 2116-2123, 2003.

[56] S. R. Best, "The Radiation Properties of Electrically Small Folded Spherical Helix Antennas," *IEEE Transactions on Antennas and Propagation*, vol. 52, pp. 953–960, Apr. 2004.

[57] R. Garbacz and E. Newman, "Characteristic modes of a symmetric wire cross," *IEEE Transactions on Antennas and Propagation*, vol. 28, pp. 712-715, 1980.

[58] W. Geyi, "A method for the evaluation of small antenna Q," *IEEE Transactions on Antennas and Propagation*, vol. 51, pp. 2124-2129, 2003.

[59] N. Inagaki and R. J. Garbacz, "Eigenfunctions of Composite Hermitian Operators with Application to Discrete and Continuous Radiating Systems," *IEEE Transactions on Antennas and Propagation*, vol. AP-30, pp. 571-575, July 1982.

[60] C. Larson and B. Munk, "The broad-band scattering response of periodic arrays," *IEEE Transactions on Antennas and Propagation*, vol. 31, no. 2, pp. 261-267, Mar. 1983.

[61] J. Mautz and R. Harrington, "Modal analysis of loaded n-port scatterers," *IEEE Transactions on Antennas and Propagation*, vol. 21, no. 2, pp. 188–199, Mar. 1973.

[62] J. S. McLean, "A re-examination of the fundamental limits on the radiation Q of electrically

small antennas," *IEEE Transactions on Antennas and Propagation*, vol. 44, p. 672, 1996.

[63] E. H. Newman, "Generation of wide-band data from the method of moments by interpolating the impedance matrix," *IEEE Transactions on Antennas and Propagation*, vol. 36, no. 12, pp. 1820-1824, Dec. 1988.

[64] D. M. Pozar, "Antenna Synthesis and Optimization Using Weighted Inagaki Modes," *IEEE Transactions on Antennas and Propagation*, vol. 38, no. 6, pp. 862-868.

[65] H. Wheeler, "Small antennas," *IEEE Transactions on Antennas and Propagation*, vol. 23, pp. 462-469, 1975.

[66] H. Wheeler, "The wide-band matching area for a small antenna," *IEEE Transactions on Antennas and Propagation*, vol. 31, pp. 364-367, 1983.

[67] R. F. Harrington and J. R. Mautz, "Characteristic Modes for Aperture Problems," *IEEE Transactions on Microwave Theory and Techniques*, vol. 33, pp. 500-505, 1985.

[68] Hsien-Peng Chang, T. K. Sarkar, and O. M. C., "Antenna pattern synthesis utilizing spherical Bessel functions," *IEEE Transactions on Antennas and Propagation*, vol. 48, pp. 853-859, 2000.

[69] B.T. Strojny and R.G. Rojas, "Asymmetrical Low Frequency Conformal Antennas for Small Unmanned Aerial Vehicles: Dipole and Monopole Tradeoffs," *Proc. Antennas Applications Symposium, Allerton, IL*, Sept 2009.

[70] B.T. Strojny and R.G. Rojas, "Investigation of Ground Plane Effects Using the Theory of Characteristic Modes," *IEEE Transactions on Antennas and Propagation*, 2011 [Under Review].

[71] Y. Zhou, C.-C. Chen, and J. L. Volakis, "Dual Band Proximity-Fed Stacked Patch Antenna for Tri-Band GPS Applications," *#IEEE_J_AP#*, vol. 55, no. 1, pp. 220-223, 2007.

[72] Zhongbao Wang, Shaojun Fang, Shiqiang Fu, and Shanwei Lu, "Dual-Band Probe-Fed Stacked Patch Antenna for GNSS Applications," *#IEEE_J_AWPL#*, vol. 8, pp. 100-103, 2009.

Appendix A Modal Quality Factor and Relationship to Total Quality Factor

A.1 Modal Q Derivation

Originally it was believed that CMs could be used to derive a modal quality factor (Q) similar to modal Q developed by Chu, because of the orthogonality properties of CMs. However, the orthogonality properties of CMs only hold in the far-field, whereas the orthogonality properties of spherical modes are enforced in the near-field on a sphere of radius a enclosing the antenna. The stored and radiated energies are then computed for all of free-space using spherical harmonics. The total radiated and stored reactive energy is the sum of each individual mode. However, the shortcoming of this prediction is you cannot accurately compute W with only far-fields. Since the orthogonality properties of CMs are enforced in the far-fields, all information about the stored energy in the near-fields is lost. Still it is possible to compute a modal Q using the modal admittance/reactance of each mode.

The definition of quality factor is the ratio of stored energy to dissipated energy. For circuit components (e.g. inductors and capacitor) the Q is given as the ratio of reactance to resistance

$$Q = 2\pi \frac{X}{R}. \tag{A.1}$$

For circuit components it is desirable to have a high Q. The radiation Q of an antenna is defined as

$$Q = 2\omega \frac{W}{P_{rad}} \tag{A.2}$$

where P_{rad} is the radiated power or the dissipated power due to radiation and W is the time-averaged, nonpropagating stored energy. Unlike circuit components it is desirable to have a low Q because the antenna is used to dissipate energy in the form of radiation. The difficulty in computing Q is accurately computing W. P_{rad} can be computed from far-fields, however since stored energy never makes it to the far-field you cannot compute W from far-fields.

Yaghjian and Best [3] derived the exact Q of an antenna tuned to have zero reactance at the frequency ω_0 (i.e. $X_0(\omega_0) = 0$) as

$$Q(\omega_0) = \left| \frac{\omega_0 X_0'}{2R_0(\omega_0)} - \frac{2\omega_0}{|I_0|^2 R_0(\omega_0)} \left[W_L(\omega_0) + W_R(\omega_0) \right] \right|. \tag{A.3}$$

Where R_0 is the input resistance, X_0' the frequency derivative of input reactance and $W_L(\omega_0)$ is the material dispersion loss given by

$$\begin{aligned} W_L(\omega_0) = \frac{1}{2Z_f} Im \int_{4\pi} &\left[\vec{H}_{I_0}' \cdot \left(\bar{\mu}_t - \bar{\mu}^* \right) \cdot \vec{H}^* + \vec{E}_{I_0}' \cdot \left(\bar{\epsilon}_t - \bar{\epsilon}^* \right) \cdot \vec{E}^* \right. \\ &\left. + \vec{H}_{I_0}' \cdot \left(\bar{\tau}_t - \bar{v}^* \right) \cdot \vec{E}^* + \vec{E}_{I_0}' \cdot \left(\bar{\tau}_t - \bar{v}^* \right) \cdot \vec{H}^* \right] dV \end{aligned} \tag{A.4}$$

and $W_L(\omega_0)$ is the far-field dispersion energy

$$W_R(\omega_0) = \frac{\omega_0}{4} Re \int_{v_a} \vec{F}_{I_0}' \cdot F^* \, d\Omega \tag{A.5}$$

The exact quality factor in (A.3) is approximated as

$$Q(\omega_0) = \frac{\omega_0}{2R_0(\omega_0)} |Z'| \tag{A.6}$$

or written in another form as

$$Q(\omega_0) = \frac{\omega_0}{2R_0(\omega_0)} \sqrt{[R'(\omega_0)]^2 + \left[X'(\omega_0) + \frac{|X(\omega_0)|}{\omega_0} \right]^2}. \tag{A.7}$$

To compute a modal quality factor input impedance can be expanded using CMs

$$Z_{in}(\omega) = \frac{V_P}{J_P(\omega)} = \frac{V_P}{\sum_n^N \alpha_n J_n} = \frac{1}{\frac{\sum_n^N \alpha_n J_n}{V_P}} \tag{A.8}$$

where V_P and J_P are the port voltage and current. The input impedance adds in parallel in terms of CMs and will be rewritten as

$$Z_{in}(\omega) = \frac{1}{\frac{1}{Z_1(\omega)} + \frac{1}{Z_2(\omega)} + \cdots \frac{1}{Z_N(\omega)}} \tag{A.9}$$

where the impedance of each individual mode is expressed as

$$Z_n(\omega) = \frac{V_P}{\alpha_n J_n}. \tag{A.10}$$

Similarly the real and imaginary part of the impedance is written as

$$R_{in}(\omega) = Re\left(\frac{1}{\sum_n^N \frac{1}{Z_n(\omega)}}\right) \tag{A.11}$$

and

$$X_{in}(\omega) = Im\left(\frac{1}{\sum_n^N \frac{1}{Z_n(\omega)}}\right). \tag{A.12}$$

The input impedance is inverted to expand in a series

$$\frac{1}{Z_{in}(\omega)} = \frac{1}{Z_1(\omega)} + \frac{1}{Z_2(\omega)} + \cdots \frac{1}{Z_N(\omega)} = \sum_n^N \frac{1}{Z_n(\omega)}. \tag{A.13}$$

The frequency derivative of (A.13) is taken using the following derivative relation

$$\frac{d}{dx}\left(\frac{u}{v}\right) = \frac{v\frac{du}{dx} - u\frac{dv}{dx}}{v^2} \tag{A.14}$$

with $u = 1$ and $v = Z_{in}(\omega)$ resulting in

$$\frac{d}{d\omega}\left(\frac{1}{Z_{in}(\omega)}\right) = \frac{-\frac{d}{d\omega}Z_{in}(\omega)}{Z_{in}(\omega)^2} \tag{A.15}$$

Therefore (A.15) can be rearranged to yield the frequency derivative of the input impedance

$$\frac{d}{d\omega}Z_{in}(\omega) = -Z_{in}(\omega)^2\frac{d}{d\omega}\left(\frac{1}{Z_{in}(\omega)}\right) \tag{A.16}$$

and expanded since the input impedance can be written in terms of modal impedances

$$\frac{d}{d\omega}Z_{in}(\omega) = -\left(\frac{1}{\sum_n^N \frac{1}{Z_n(\omega)}}\right)^2 \frac{d}{d\omega}\left(\sum_n^N \frac{1}{Z_n(\omega)}\right) \tag{A.17}$$

Therefore Eq. (A.17) can be used to for the derivative of the modal resistance and reactance and written as

$$R'(\omega_0) = Re\left(\frac{d}{d\omega}Z_{in}(\omega)\right) \tag{A.18}$$

or

$$X'(\omega_0) = Im\left(\frac{d}{d\omega}Z_{in}(\omega)\right) \tag{A.19}$$

Plugging into

$$Q(\omega) = \frac{\omega}{2Re\left(\frac{1}{\sum_n^N \frac{1}{Z_n(\omega)}}\right)}\cdot \tag{A.20}$$

$$\cdot \sqrt{\left[Re\left(\frac{d}{d\omega}Z_{in}(\omega)\right)\right]^2 + \left[Im\left(\frac{d}{d\omega}Z_{in}(\omega)\right) + \frac{\left|Im\left(\frac{1}{\sum_n^N \frac{1}{Z_n(\omega)}}\right)\right|}{\omega_0}\right]^2}$$

$$Q(\omega_0) = \frac{\omega_0}{2R_0(\omega_0)}\sqrt{[R'(\omega_0)]^2 + \left[X'(\omega_0) + \frac{|X(\omega_0)|}{\omega_0}\right]^2}. \tag{A.21}$$

Note the input impedance could be found from the input admittance, but would not simplify the analysis

$$Z_n(\omega) = \frac{G_n(\omega)}{G_n(\omega)^2 + B_n(\omega)^2} - j\frac{B_n(\omega)}{G_n(\omega)^2 + B_n(\omega)^2}. \tag{A.22}$$

The original modal Q as written in the research proposal was believed to be a weighted summation of modal Q's. However as shown in (A.18) the analytical formulation is much more involved. It was believed that each individual mode needed to be weighted according to the amount of power coupled to the mode since Q involves the ratio of energy to power. Therefore the power coupled to the mode is equal to the time-average power available for each mode. The time-average power for the antenna is given as

$$P_{av} = \frac{1}{2}Re\, J^*V = \frac{1}{2}Re\, J^*ZJ \tag{A.23}$$

The total current is expanding in terms of weighted eigencurrents

$$\vec{J} = \sum_{n}^{N} \alpha_n \vec{J}_n. \tag{A.24}$$

Multiply both sides of (A.21) by Z

$$Z\vec{J} = \sum_{n}^{N} \alpha_n Z \vec{J}_n. \tag{A.25}$$

React both sides of (A.22) with $\vec{J}^*$ resulting in

$$\langle \vec{J}^*, Z\vec{J} \rangle = \sum_{m}^{N} \alpha^*{}_m \sum_{n}^{N} \alpha_n \langle \vec{J}_m, Z\vec{J}_n \rangle. \tag{A.26}$$

Using orthogonality properties (A.23) can be written

$$\langle \vec{J}^*, Z\vec{J} \rangle = \sum_{m}^{N} \alpha^*{}_m \sum_{n}^{N} \alpha_n (1 + j\lambda_n) \delta_{nm}\,. \tag{A.27}$$

Since n=m otherwise (A.7) is zero

$$\langle \vec{J}^*, Z\vec{J} \rangle = \sum_{n}^{N} |\alpha_n|^2 (1 + j\lambda_n). \tag{A.28}$$

Equation (A.20) can be thought of as the power available for the mode, however only the real part is able to couple to the mode. Therefore the P_{av} is given

$$P_{av} = \frac{1}{2} Re \langle \vec{J}^*, Z\vec{J} \rangle = \frac{1}{2} \sum_{n}^{N} |\alpha_n|^2. \tag{A.29}$$

Then the total Q was believed to be the sum of modal Q's weighted by the power available per mode resulting in

$$Q = \frac{\sum_n^N Q_n |\alpha_n|^2}{\sum_n^N |\alpha_n|^2}. \tag{A.30}$$

The Q in (A.27) is only accurate in a single dominant mode case in which the total admittance and impedance are contributed to the dominant mode.

Appendix B Characteristic Mode Investigation of Rectangular Ground Plane Effects

The width of the fuselage is typically the limiting factor restricting the size of the ground plane. In this chapter, two rectangular ground planes (Region II of Figure 4.2) will be investigated. As in Chapter 4, λ_M is the wavelength at 150 MHz. First, in Section B.1, $L_G = \lambda_M/8 \times W_G = \lambda_M/32$. W_G is electrically small, which is a more accurate representation of modern UAVs, relative to the square ground plane case considered in Chapter 4. The height (H) and tail width (T_W) are same as Chapter 4 at 0.5 and 0.05 m, respectively. When the ground plane becomes electrically small, it is important to study the effects on the feeding network since technically it is no longer a ground plane. By shrinking the width and keeping the length the same, the effects of having an electrically small rectangular "ground plane" can be directly studied relative to the square ground plane.

In Section B.2, the length of the ground plane is reduced by a factor of 2 resulting in $L_G = \lambda_M/16 \times W_G = \lambda_M/32$. For both cases, the $|\alpha_n|$ (dB), admittance and realized gain are shown for both dipole and monopole feed excitation.

B.1 $\lambda_M/8 \times \lambda_M/32$ Rectangular Plate

Similar to the investigation of the square ground plane, the dominant CMs were identified for the rectangular ground plane using the process outlined Section 3.1. The eigenvalue spectrum (dB) vs. frequency is shown in Figure B.1. Table B.1 lists the |EV| (dB) at 50, 150, 300 and 550

MHz. The eigencurrents and eigenpatterns are shown in Figure B.2-Figure B.5. CM 1 has the lowest eigenvalue at low frequencies all the way up to 385 MHz and has a resonant frequency of 165 MHz. CM 1 eigenpattern resembles the desired vertically polarized omnidirectional pattern. Below 250 MHz, CM 1 is potentially the dominant mode on the structure depending on the feeding network since its eigenvalue is at least 10 dB lower than other dominant eigenvalues. Its eigencurrent is confined to the vertical element. CM 2 eigencurrent predominantly resides in the vertical element with a null near the center and resonates at 430 MHz. However, unlike the square ground plane, it also has a current component contained in the ground plane. CM 3 has a similar current distribution to CM 2, (lower section of vertical plate) with a different pattern. CM 4 has two nulls in the eigencurrent causing multiple nulls in the radiated pattern. The eigenvalue corresponding to CM 4 is very high relative to other modes and will have minimal contribution until higher frequencies. One of the more noticeable effects is the decrease in CM 3 resonant frequency down to 627 MHz. Previously this mode did not resonate in the frequency range of interest (50-650 MHz).

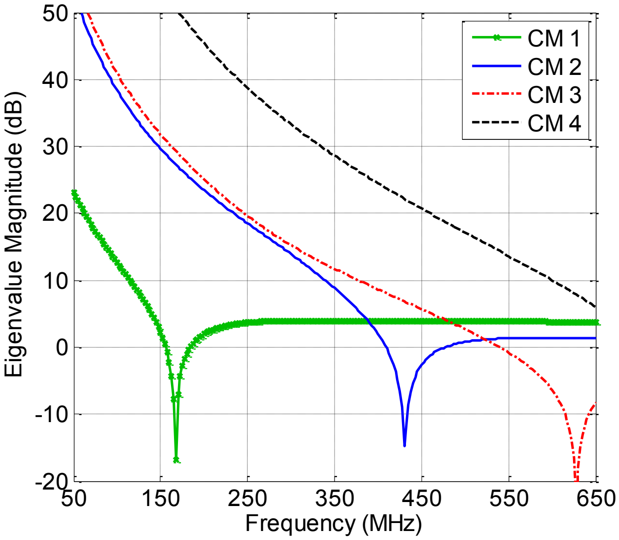

Figure B.1: Eigenvalue spectrum of characteristic modes under consideration ($L_G = \lambda_M/8 \times W_G = \lambda_M/32$).

Table B.1: |EV| (dB) when $L_G = \lambda_M/8 \times W_G = \lambda_M/32$

CM	50 MHz	150 MHz	300 MHz	550 MHz
1	23.23	2.27	3.97	3.95
2	53.39	29.66	13.91	1.34
3	56.20	31.81	15.24	-0.79
4	87.10	53.99	33.28	13.62

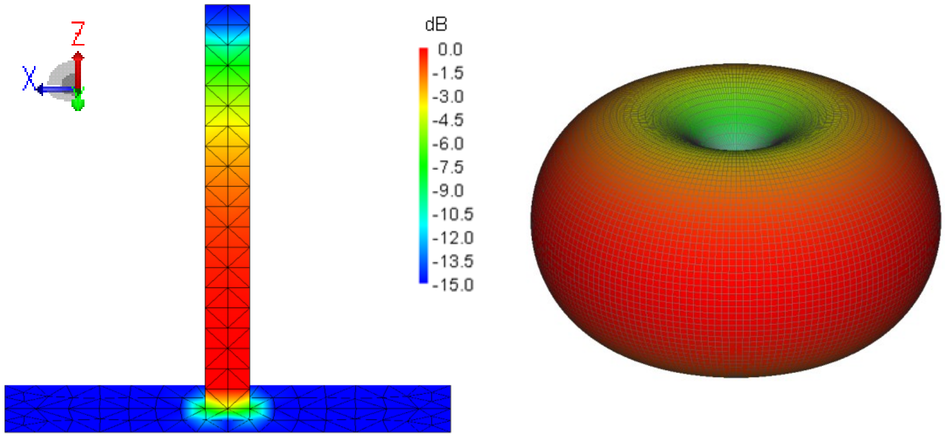

(a) (b)

Figure B.2: Normalized characteristic mode 1 eigen properties at 150 MHz; (a) eigencurrent, (b) eigenpattern.

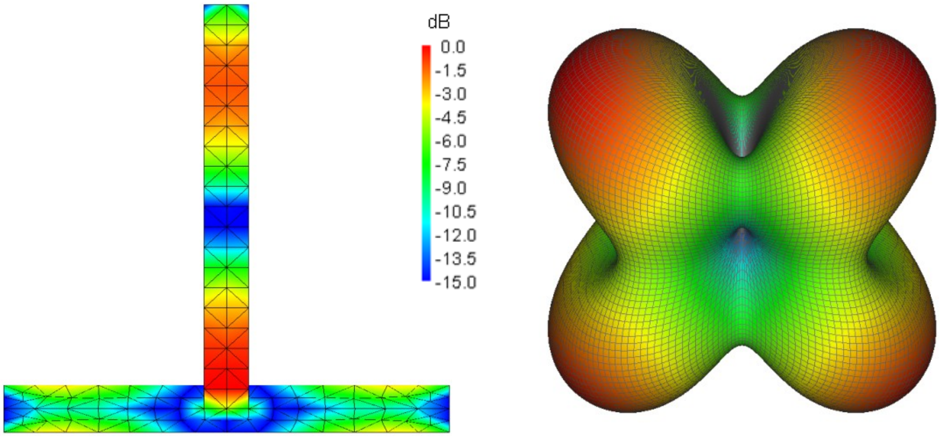

(a) (b)

Figure B.3: Normalized characteristic mode 2 eigen properties at 150 MHz; (a) eigencurrent, (b) eigenpattern.

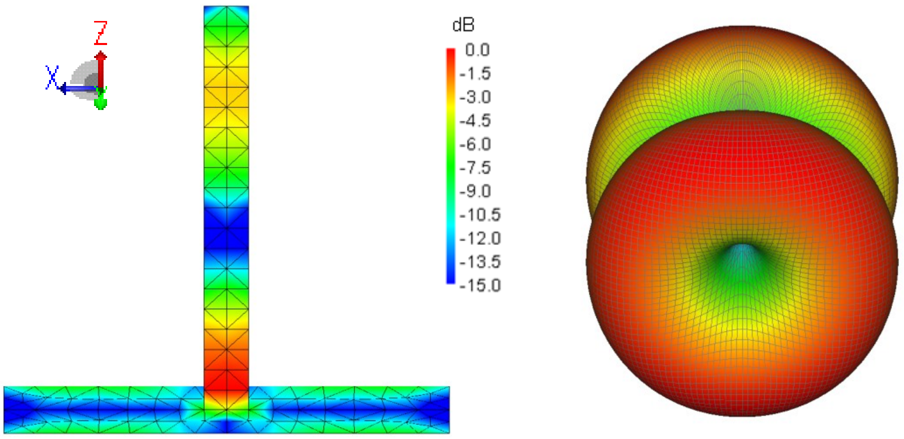

(a) (b)

Figure B.4: Normalized characteristic mode 3 eigen properties at 150 MHz; (a) eigencurrent, (b) eigenpattern.

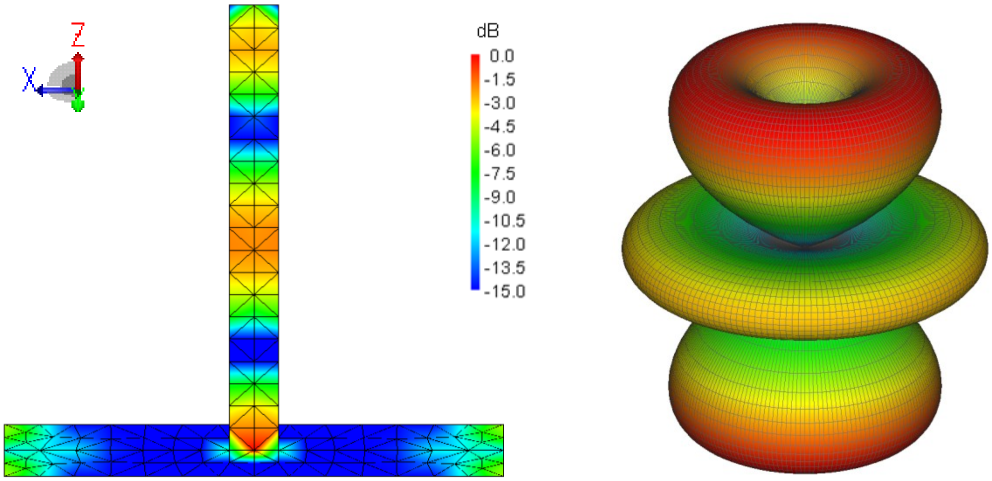

(a) (b)

Figure B.5: Normalized characteristic mode 4 eigen properties at 150 MHz; (a) eigencurrent, (b) eigenpattern.

B.1.1 Dipole Feed $\lambda_M/8 \times \lambda_M/32$ Rectangular Plate

The dipole feed is the same as the one described in Section 4.2.1 The $|\alpha_n|$ (dB) of the dominant modes are shown in Figure B.6. As expected, the dipole feed configuration strongly excites CM 1. CM 1 remains the dominant mode excited up to 500 MHz. Above 500 MHz, CM 3 transitions into the dominant mode excited, but all modes remain within 7 dB of maximum, therefore contribute to input admittance and radiated pattern. The dominant mode's contribution to the total conductance is shown in Figure B.7(a). It can be seen that with the dipole feed, the total conductance and CM 1 conductance match from 50 to 450 MHz. At 450 MHz the total conductance and that of CM 1 diverge because CM 2 is getting excited. The sum of all four dominant CMs' conductance is also shown Figure B.7(a), where the total and sum agree. The susceptance comparison is shown in Figure B.7(b). The total and CM 1 susceptance agree well at low frequencies and diverge around 250 MHz.

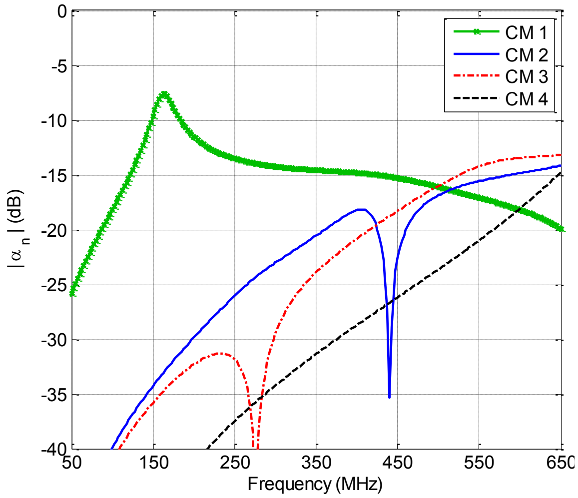

Figure B.6: $|\alpha_n|$ (dB) of characteristic modes under consideration for dipole feed ($L_G = \lambda_M/8 \times W_G = \lambda_M/32$).

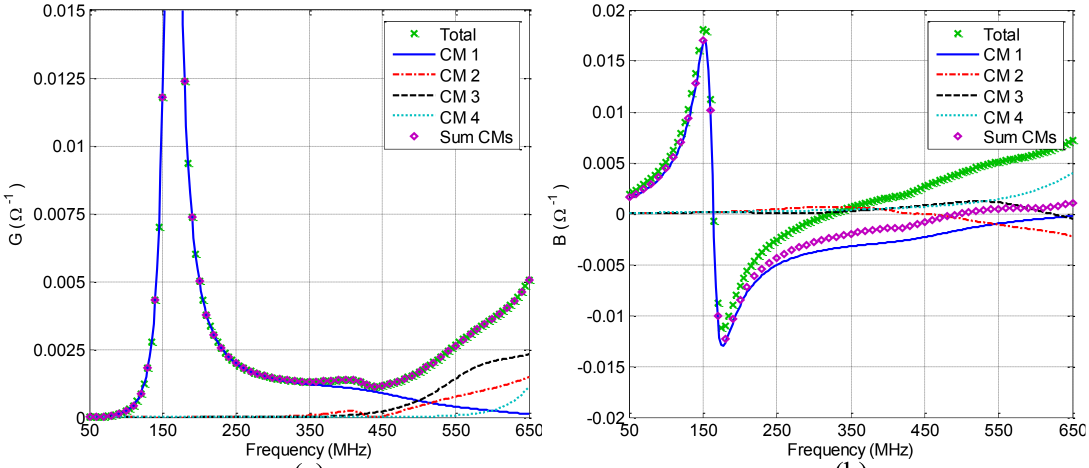

(a) (b)

Figure B.7: Dipole feed comparing total, characteristic mode and sum of characteristic mode admittance; (a) conductance, (b) susceptance.

The realized total gain (referenced to 50 Ω) of the dominant modes is shown in Figure B.8 for the XZ-plane at 250, 350, 450 and 550 MHz. As expected, when the ground plane is rectangular, symmetry between the XZ- and YZ-plane is lost especially at higher frequencies. Thus, the radiated pattern in the YZ-plane is shown in Figure B.9 at 450 and 550 MHz. Below 250 MHz, CM 1 is the dominant mode contributing to the radiated pattern. Note CMs 2-4 at 250 MHz, 4 at 350 and 450 MHz have realized gains less than -25 dBi and thus do not show up in the figures. At 550 MHz all modes have contributions to the radiated pattern. When the four dominant modes are summed the resulting pattern matches the total pattern. Again with the dipole feed there are no major nulls at broadside. However, a major difference is a decrease in symmetry of the pattern in the XZ- and YZ-plane at 450 and 550 MHz. The decrease in symmetry is due to the rectangular ground plane relative to square ground plane shown last chapter.

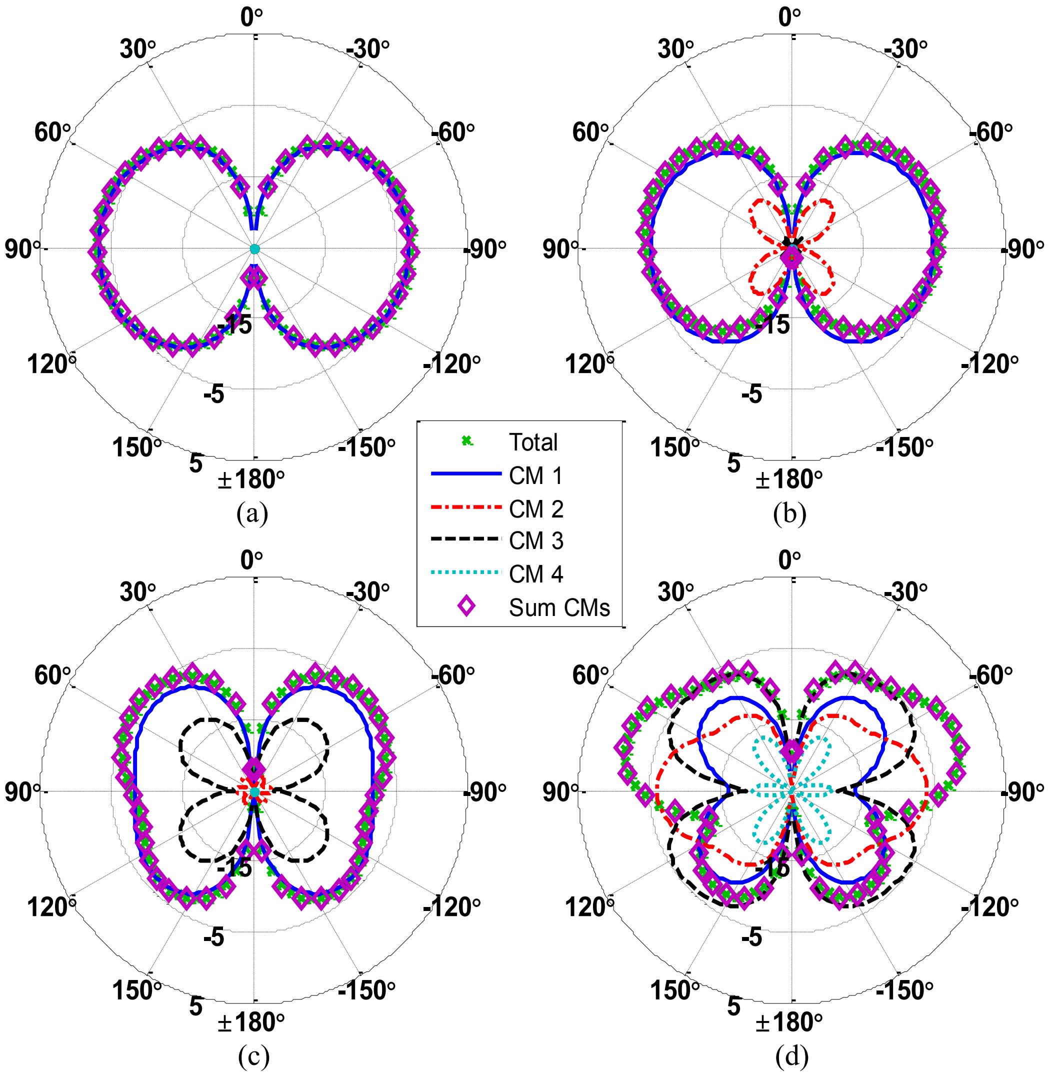

Figure B.8: Dipole feed realized total gain (dBi) comparing total pattern, eigenpatterns and sum of eigenpatterns in the XZ-plane; (a) 450 MHz, (b) 550 MHz.

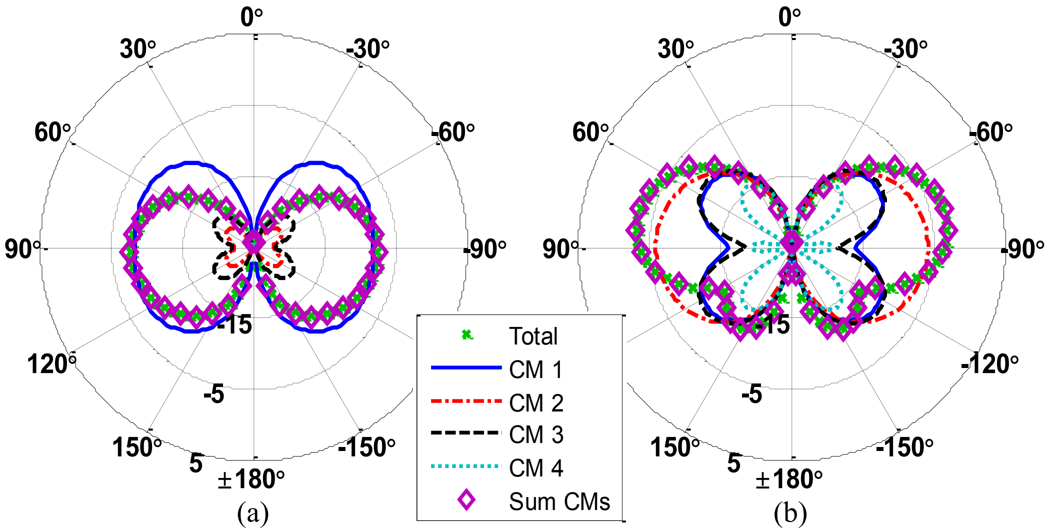

(a) (b)

Figure B.9: Dipole feed realized total gain (dBi) comparing total pattern, eigenpatterns and sum of eigenpatterns in the YZ-plane; (a) 450 MHz, (b) 550 MHz.

The patterns in the XY-plane are shown in Figure B.10. It is desirable for the pattern to remain omnidirectional in the XY-plane. CMs 2-4 at 250 MHz, CM 4 at 350 and 450 MHz have realized gains less than -25 dBi, thus do not show up in the corresponding figures. The total and CM 1 radiation pattern match at 250 and 350 MHz. Between 450 and 550 MHz CM 2 becomes the dominant mode. Also the pattern starts to resemble a square shape.

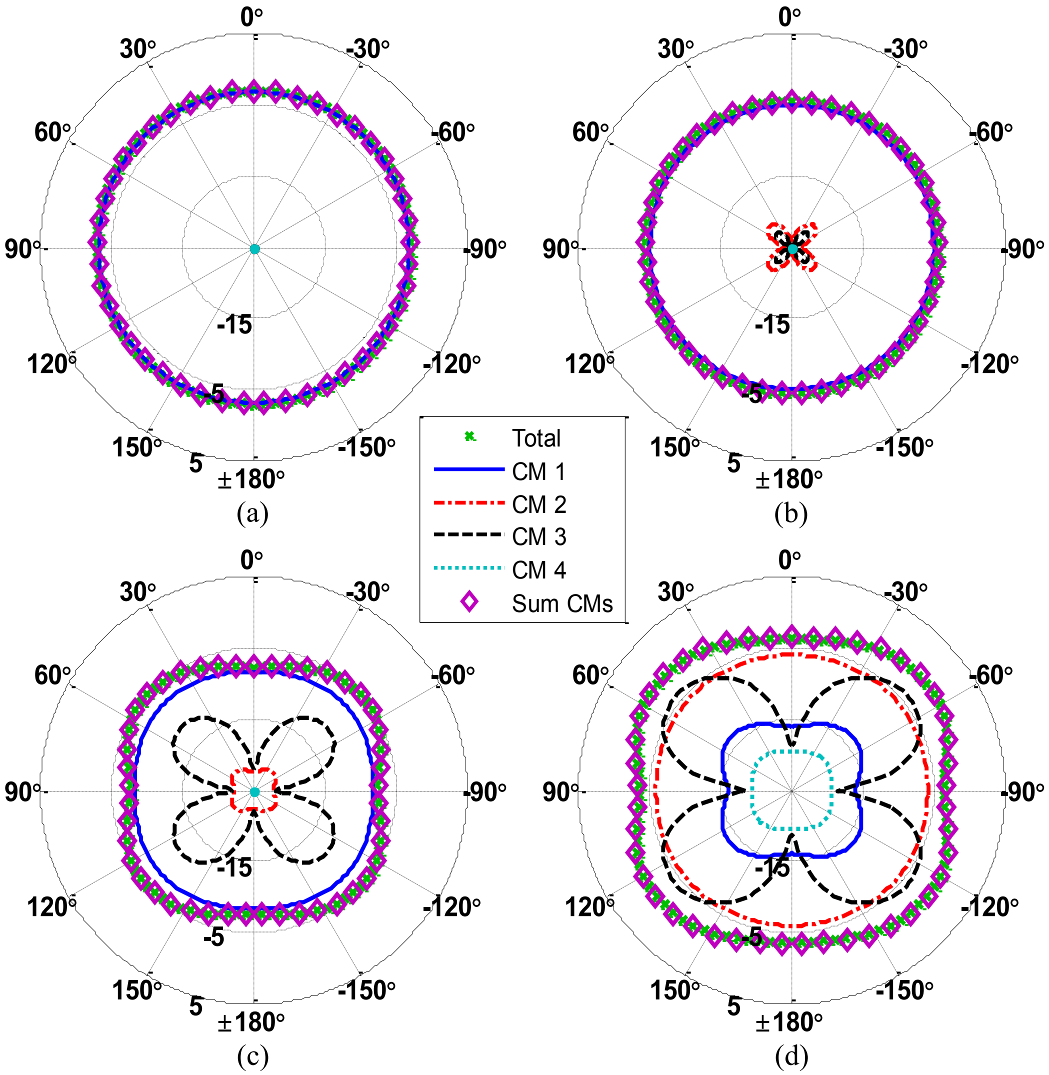

(a) (b) (c) (d)

Figure B.10: Dipole feed realized total gain (dBi) comparing total pattern, eigenpatterns and sum of eigenpatterns in the XY-plane; (a) 250 MHz, (b) 350 MHz, (c) 450 MHz, (d) 550 MHz.

Similar to the square case, a modal transition occurs. Above 450 MHz the eigenpatterns of CM 1 and CM 2 start to switch. CM 1 develops a null at broadside whereas CM 2 becomes more omnidirectional. The change in pattern can be explained by the change in eigencurrent of the modes. At 150 MHz, CM 1 eigencurrent has near constant amplitude starting near the base of the ground plane and extends to the top where it transitions into a null (Figure B.2(a)). As frequency increases, the eigencurrent null moves down the vertical element towards the ground plane. At 550 MHz the null resides near the middle of the vertical element with another strong current component forming near the top as shown in Figure B.11(a). The change in eigencurrent results in an eigenpattern with a null near broadside as shown in Figure B.11(b). CM 2 eigencurrent starts out with multiple dominant current components resulting in an eigenpattern with a null at broadside (Figure B.3). As frequency increases the current component near the top of the vertical element moves towards the bottom, while the one at the bottom becomes weaker. The result is one current component offset near the top of the vertical element as shown in Figure B.12(a). Since one current component resides on the element, the radiated pattern is near omnidirectional as shown in Figure B.12(b). It should be re-emphasized that these effects are believed to be caused by the plate loading the antenna. The switching of the modes does not occur without the plate.

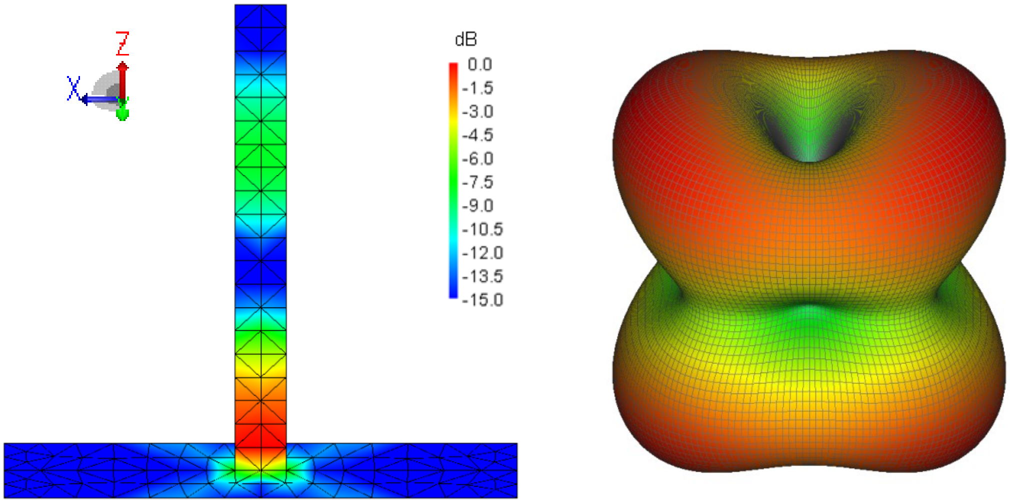

(a) (b)

Figure B.11: Normalized characteristic mode 1 eigen properties at 550 MHz; (a) eigencurrent, (b) eigenpattern.

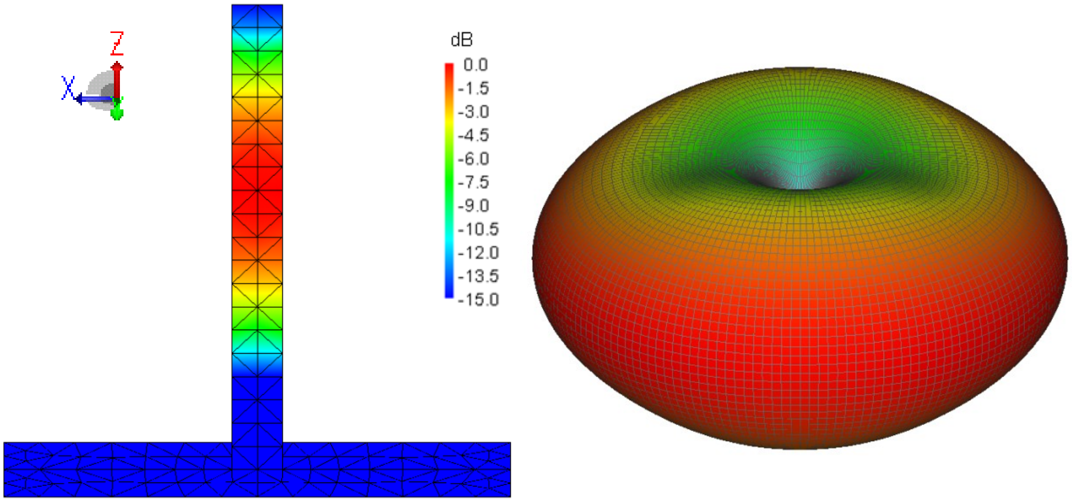

(a) (b)

Figure B.12: Normalized characteristic mode 2 eigen properties at 550 MHz; (a) eigencurrent, (b) eigenpattern.

B.1.2 Monopole Feed $\lambda_M/8 \times \lambda_M/32$ Rectangular Plate

The monopole feed for the rectangular ground plane case is now considered. The feed is the same as that described in 4.2.2. Figure B.13 shows the $|\alpha_n|$ (dB) for the dominant CMs and Figure B.13 shows the admittance. No major differences occur in conductance and susceptance relative to the square ground plane case.

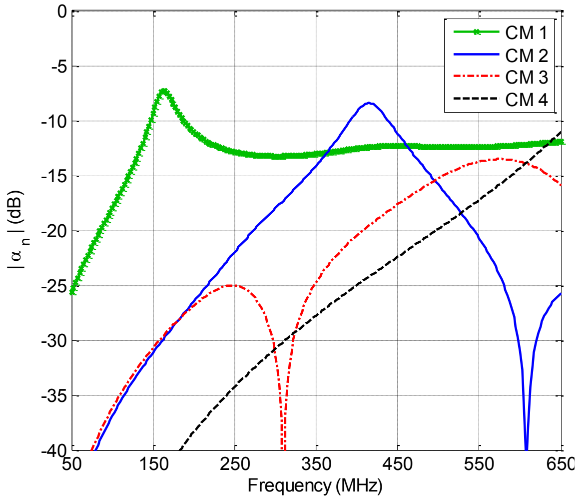

Figure B.13: $|\alpha_n|$ (dB) of characteristic modes under consideration for monopole feed ($L_G = \lambda_M/8 \times W_G = \lambda_M/32$).

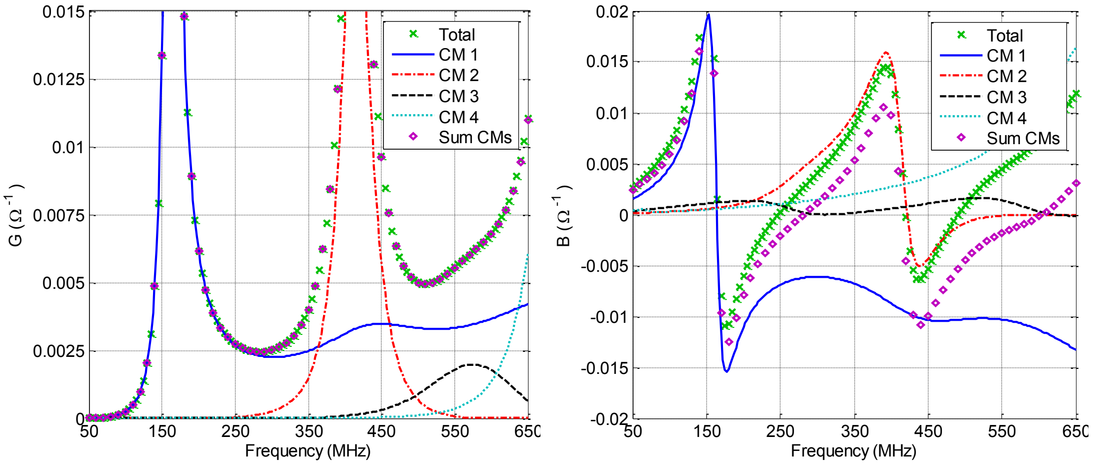

(a) (b)

Figure B.14: Monopole feed comparing total, characteristic mode and sum of characteristic mode admittance; (a) conductance, (b) susceptance.

The realized total gain (referenced to 50 Ω) of the dominant modes is shown in Figure B.15 for the XZ-plane at 250, 350, 450 and 550 MHz. Also Figure B.16 shows the YZ-plane at 450 and 550 MHz. At 250 and 350 MHz CM 3 and 4 have a realized gain below -25 dBi. At 450 and 550 MHz all modes have contributions to the radiated pattern. When the four dominant modes are summed the resulting pattern matches the total pattern. With the monopole feed a null at broadside starts to form at 450 MHz and completely forms at 550 MHz.

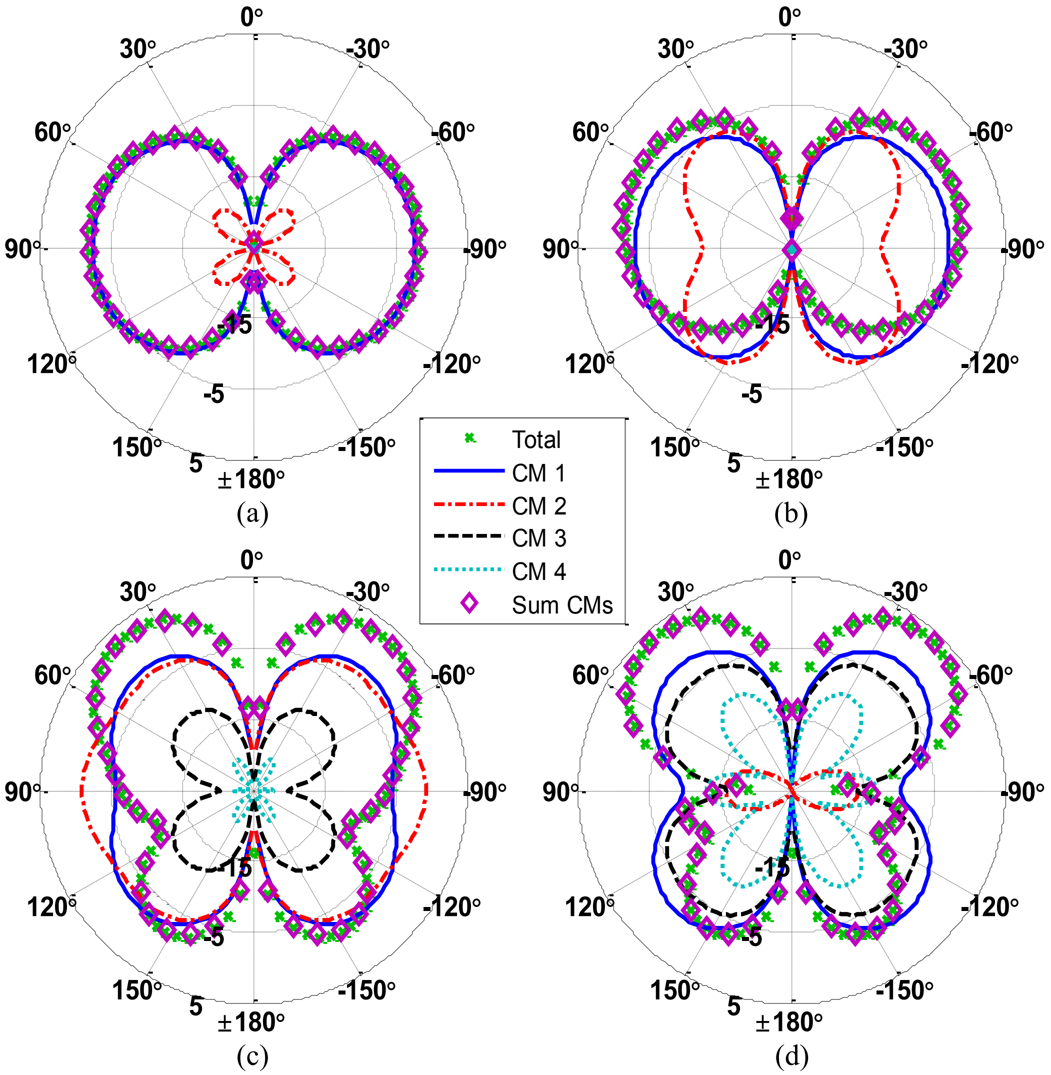

Figure B.15: Monopole feed realized total gain (dBi) comparing total pattern, eigenpatterns and sum of eigenpatterns in the XZ-plane; (a) 250 MHz, (b) 350 MHz, (c) 450 MHz, (d) 550 MHz.

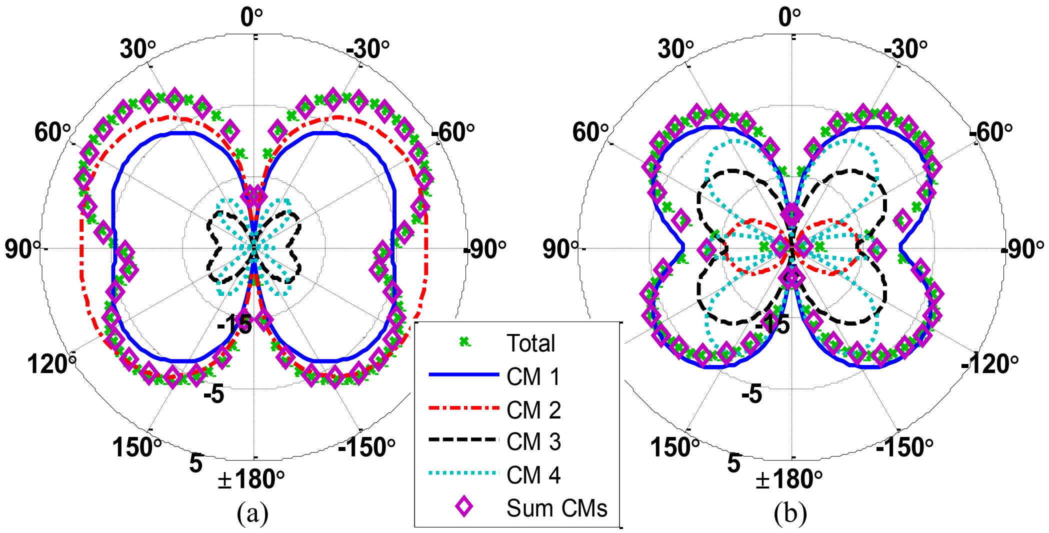

(a) (b)

Figure B.16: Monopole feed realized total gain (dBi) comparing total pattern, eigenpatterns and sum of eigenpatterns in the YZ-plane; (a) 250 MHz, (b) 350 MHz, (c) 450 MHz, (d) 550 MHz.

The patterns in the XY-plane are shown in Figure B.17. CMs 2 and 4 at 250 MHz and CM 4 at 350 MHz have realized gains less than -25 dBi thus do not show up in the corresponding figures. The total and CM 1 radiation pattern match at 250 and 350 MHz. Between 350 and 450 MHz CM 2 becomes the dominant mode. Major nulls form at φ = 0, ±90 and 180° at 550 MHz in which CM 3 and the total realized gain have good agreement.

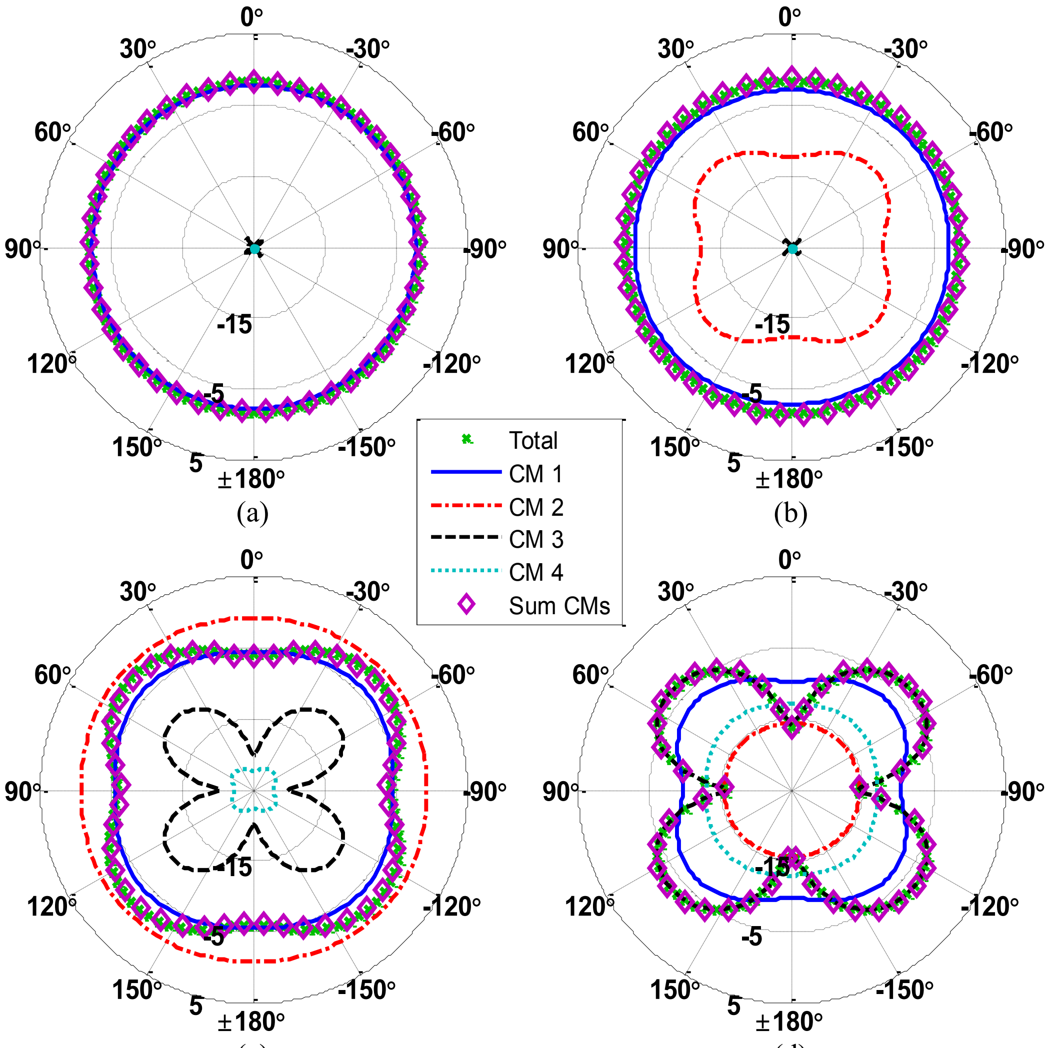

(a) (b)

(c) (d)

Figure B.17: Monopole feed realized total gain (dBi) comparing total pattern, eigenpatterns and sum of eigenpatterns in the XY-plane; (a) 250 MHz, (b) 350 MHz, (c) 450 MHz, (d) 550 MHz.

B.2 $\lambda_M/16 \times \lambda_M/32$ Rectangular Plate

Similar to the $\lambda_M/8 \times \lambda_M/32$ case, a CM analysis of the antenna when $L_G = \lambda_M/16 \times W_G = \lambda_M/32$ is analyzed. Four dominant CMs were identified and their eigenvalue spectrum vs. frequency is shown in Figure B.18. Table B.2 lists the eigenvalues at 50, 150, 300 and 550 MHz for each mode. Each mode's eigencurrent and eigenpattern is shown in Figure B.19-Figure B.22. CM 1 closely resembles the desired criteria, while CMs 2-4 are higher order modes. CM 1 and 2 resonate at 190 and 452.5 MHz, respectively. Both CMs' resonant frequency increases by 22.5 MHz. CM 3 no longer resonates in the frequency range of interest.

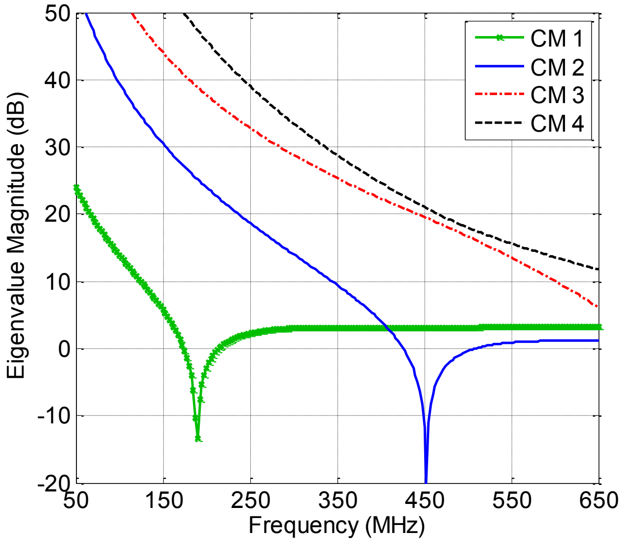

Figure B.18: Eigenvalues spectrum of characteristic modes under consideration ($L_G = \lambda_M/16 \times W_G = \lambda_M/32$).

Table B.2: |EV| (dB) when $L_G = \lambda_M/16 \times W_G = \lambda_M/32$

CM	50 MHz	150 MHz	300 MHz	550 MHz
1	24.05	5.80	3.03	3.24
2	54.60	30.50	14.03	0.90
3	67.94	44.02	28.80	13.50
4	87.60	54.49	33.50	15.63

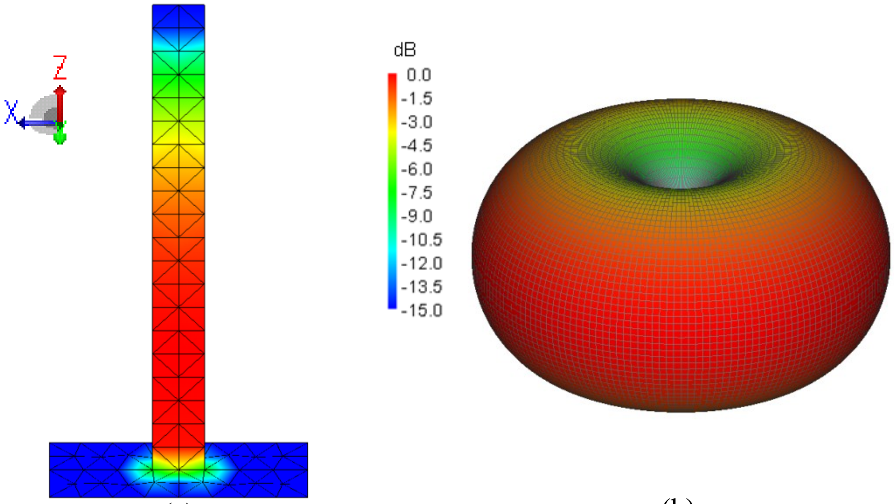

(a) (b)

Figure B.19: Normalized characteristic mode 1 eigen properties at 190 MHz; (a) eigencurrent, (b) eigenpattern.

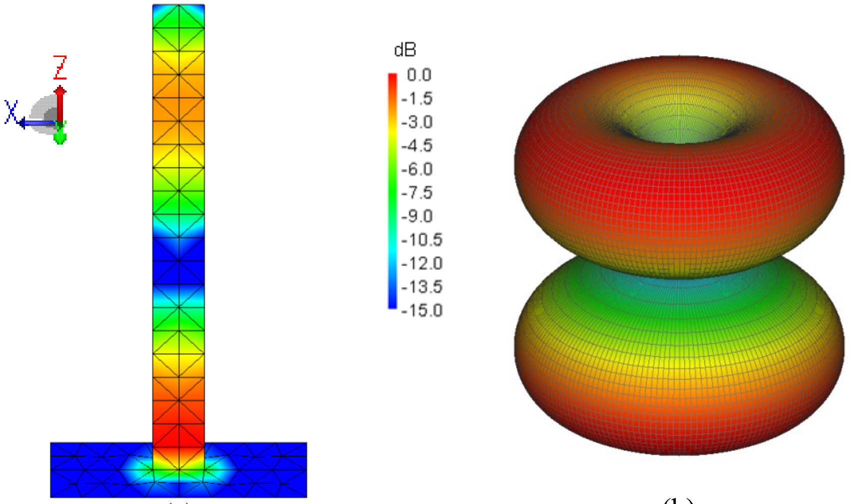

(a) (b)

Figure B.20: Normalized characteristic mode 2 eigen properties at 190 MHz; (a) eigencurrent, (b) eigenpattern.

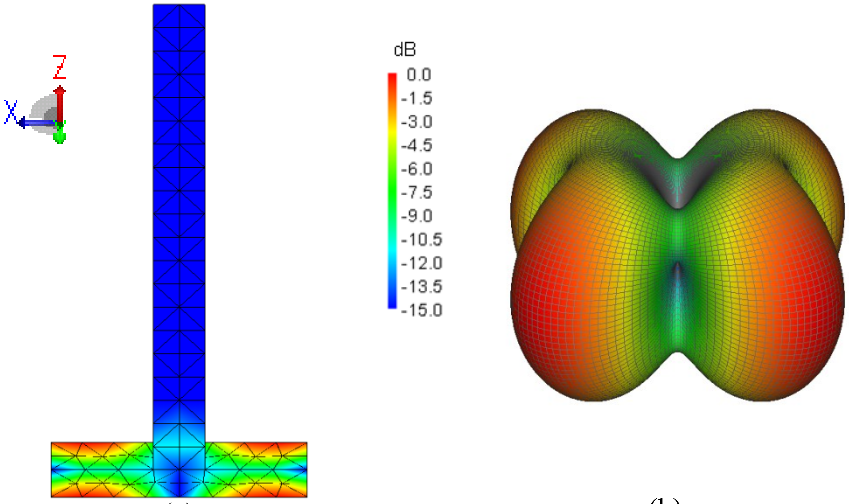

(a) (b)

Figure B.21: Normalized characteristic mode 3 eigen properties at 190 MHz; (a) eigencurrent, (b) eigenpattern.

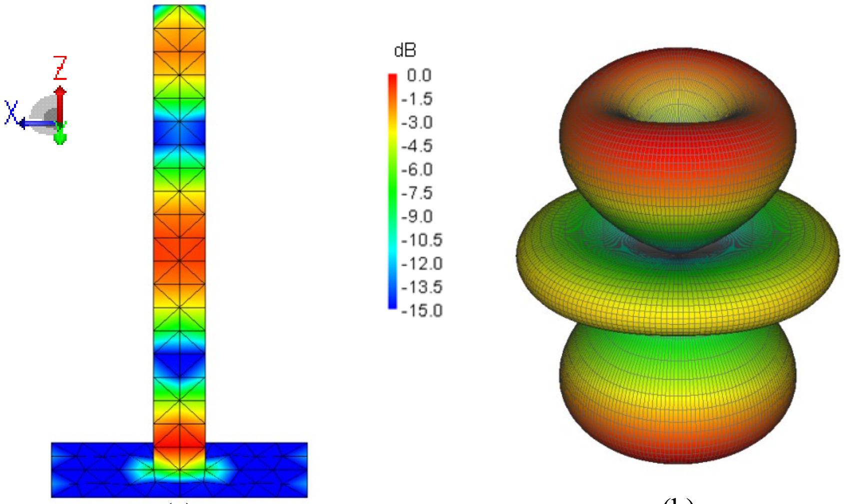

(a) (b)

Figure B.22: Normalized characteristic mode 4 eigen properties at 190 MHz; (a) eigencurrent, (b) eigenpattern.

B.2.1 Dipole Feed $\lambda_M/16 \times \lambda_M/32$ Rectangular Plate

The $|\alpha_n|$ (dB) of the dominant modes is shown in Figure B.23. The admittance and impedance of the dipole feed is shown in Figure B.24. With the dipole feed, CM 1 almost entirely makes up the total conductance except near the resonant frequencies of CM 2 and above 550 MHz. Therefore the total pattern will closely resemble CM 1 over the entire band, in other words the dipole feed suppresses CM 2 and CM 3 (higher order modes) over the frequency band.

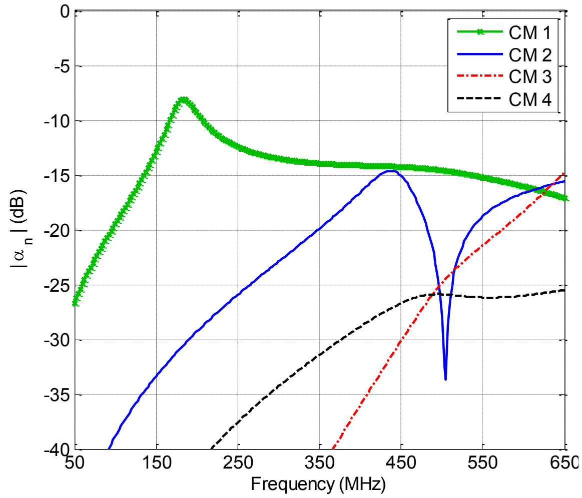

Figure B.23: $|\alpha_n|$ (dB) of characteristic modes under consideration for dipole feed ($L_G = \lambda_M/16 \times W_G = \lambda_M/32$).

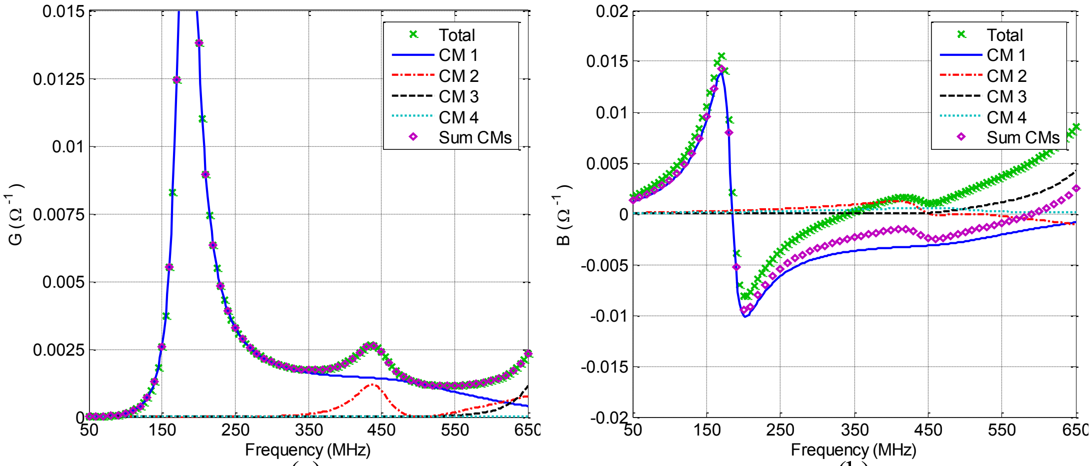

(a) (b)

Figure B.24: Dipole feed comparing total, characteristic mode and sum of characteristic mode admittance; (a) conductance, (b) susceptance.

The realized total gain (referenced to 50 Ω) of the dominant modes is shown in Figure B.25 for the XZ-plane at 250, 350, 450 and 550 MHz. Below 250 MHz, CM 1 is the dominant mode contributing to the radiated pattern. Note CMs 2-4 at 250 MHz, 3 and 4 at 350 and 450 MHz and

CM 4 at 550 MHz have realized gains less than -25 dBi and thus do not show up in the figures. When the four dominant modes are summed the resulting pattern matches the total pattern. Again with the dipole feed there are no major nulls at broadside. However, a major difference between the rectangular cases is that when $L_G = \lambda_M/16$, the symmetry between XZ- and YZ-planes is restored similar to the square case. Due to the symmetry between planes, the YZ-plane is omitted for brevity.

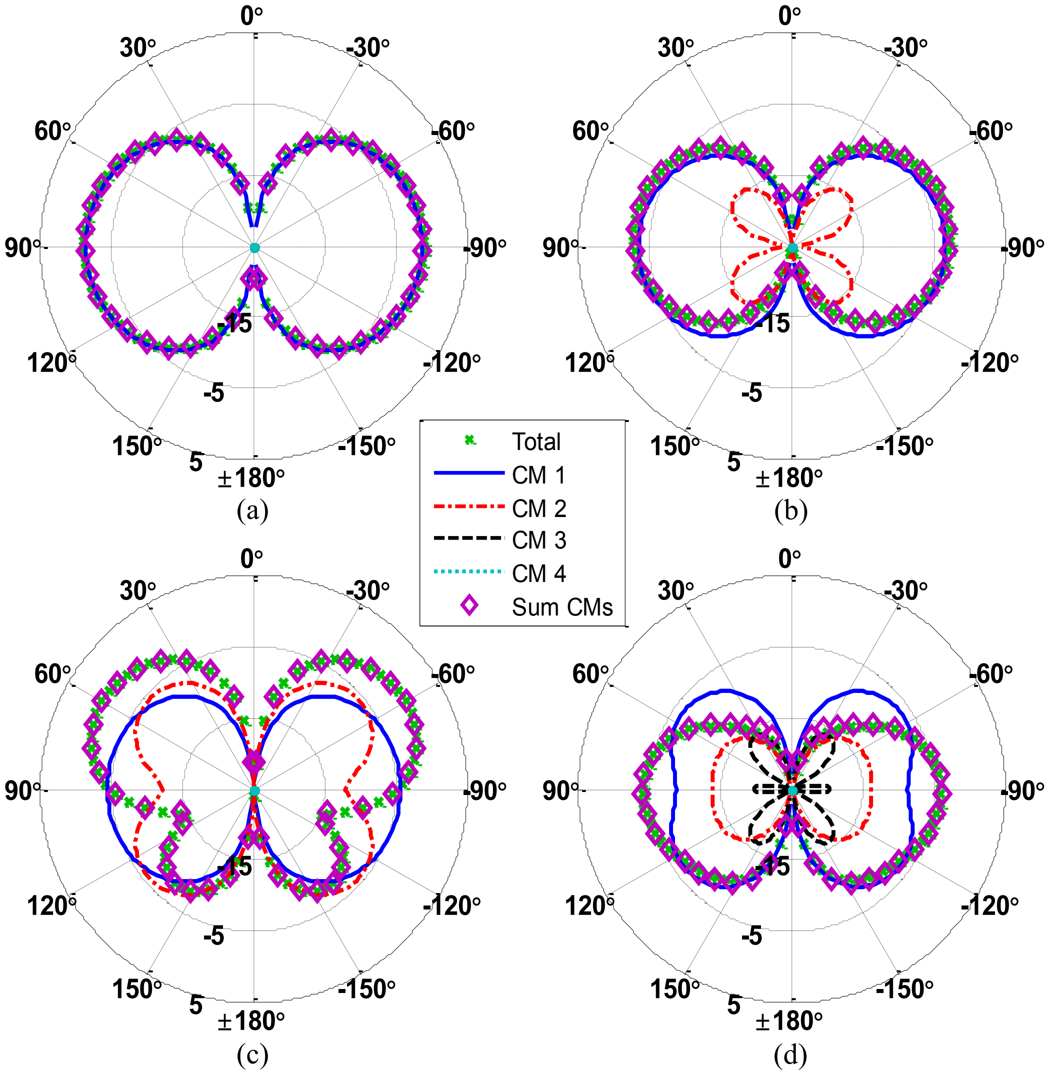

(a) (b) (c) (d)

Figure B.25: Dipole feed realized total gain (dBi) comparing total pattern, eigenpatterns and sum of eigenpatterns in the XZ-plane; (a) 250 MHz, (b) 350 MHz, (c) 450 MHz, (d) 550 MHz.

In Figure B.26 the total realized gain is shown in XY-plane. The patterns remain omnidirectional with a realized gain better than -5 dBi. CM 1 and the total pattern have good agreement except at 550 MHz where multiple modes have contributions to the total pattern. CM 4 is less than -25 dBi for all frequencies shown. As expected with the dipole feed the major null at broadside is avoided.

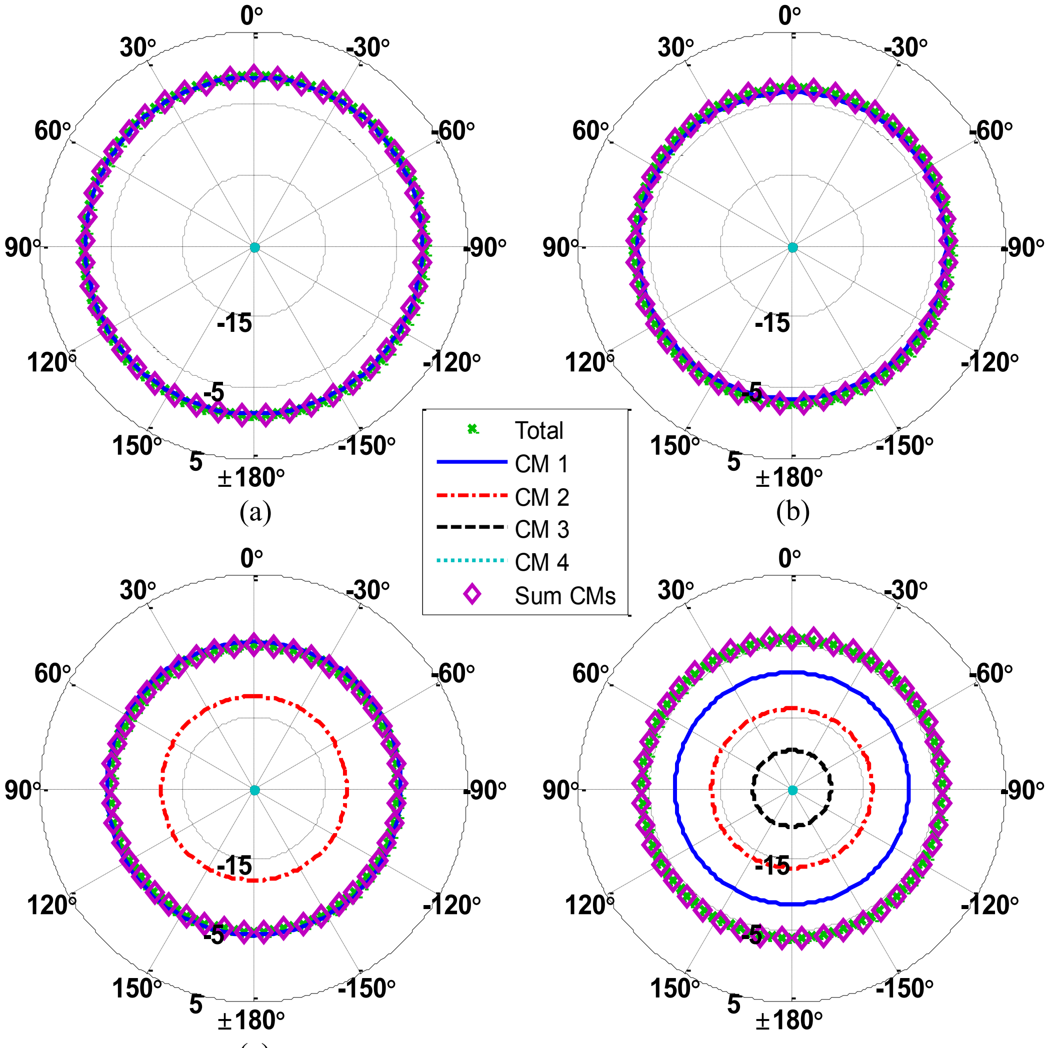

(a) (b) (c) (d)

Figure B.26: Dipole feed realized total gain (dBi) comparing total pattern, eigenpatterns and sum of eigenpatterns in the XY-plane; (a) 250 MHz, (b) 350 MHz, (c) 450 MHz, (d) 550 MHz.

B.2.2 Monopole Feed $\lambda_M/16 \times \lambda_M/32$ Rectangular Plate

The monopole feed for the rectangular ground plane case is considered. The feed is the same as that described in 4.2.2. Figure B.27 shows the $|\alpha_n|$ (dB) for the dominant CMs and Figure B.28 shows the admittance. No major differences occur in conductance and susceptance relative to the square ground plane case.

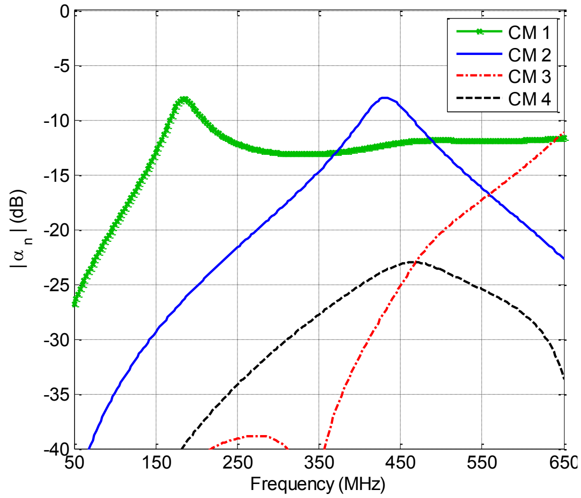

Figure B.27: $|\alpha_n|$ (dB) of characteristic modes under consideration for monopole feed ($L_G = \lambda_M/16 \times W_G = \lambda_M/32$).

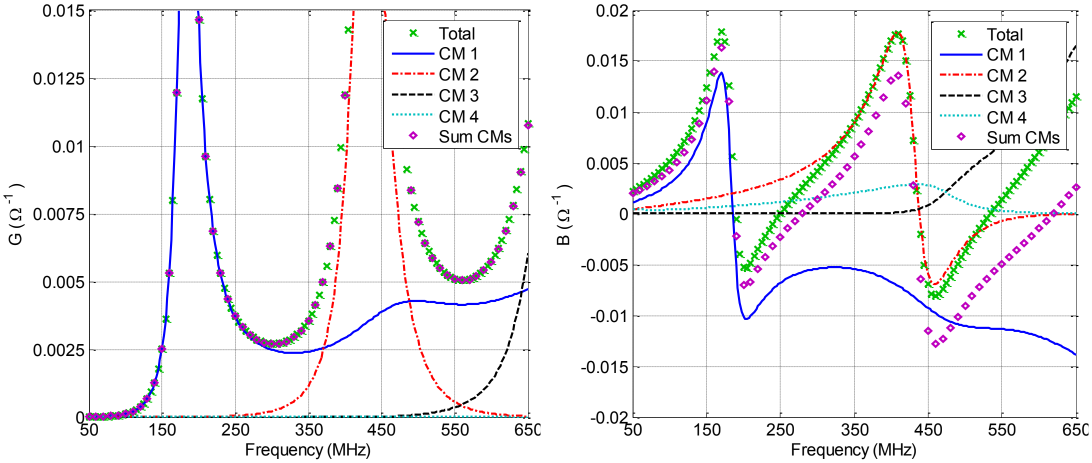

(a) (b)

Figure B.28: Monopole feed comparing total, characteristic mode and sum of characteristic mode admittance; (a) conductance, (b) susceptance.

The realized total gain (referenced to 50 Ω) of the dominant modes is shown in Figure B.29 for the XZ-plane at 250, 350, 450 and 550 MHz. Note CMs 3 and 4 at 250 and 350 MHz, 4 at 450 and 550 MHz have realized gains less than -25 dBi and thus do not show up in the figures. When the four dominant modes are summed the resulting pattern matches the total pattern. With the monopole feed the CMs destructively interfere forming a major null at broadside starting at 450 and fully forming at 550 MHz.

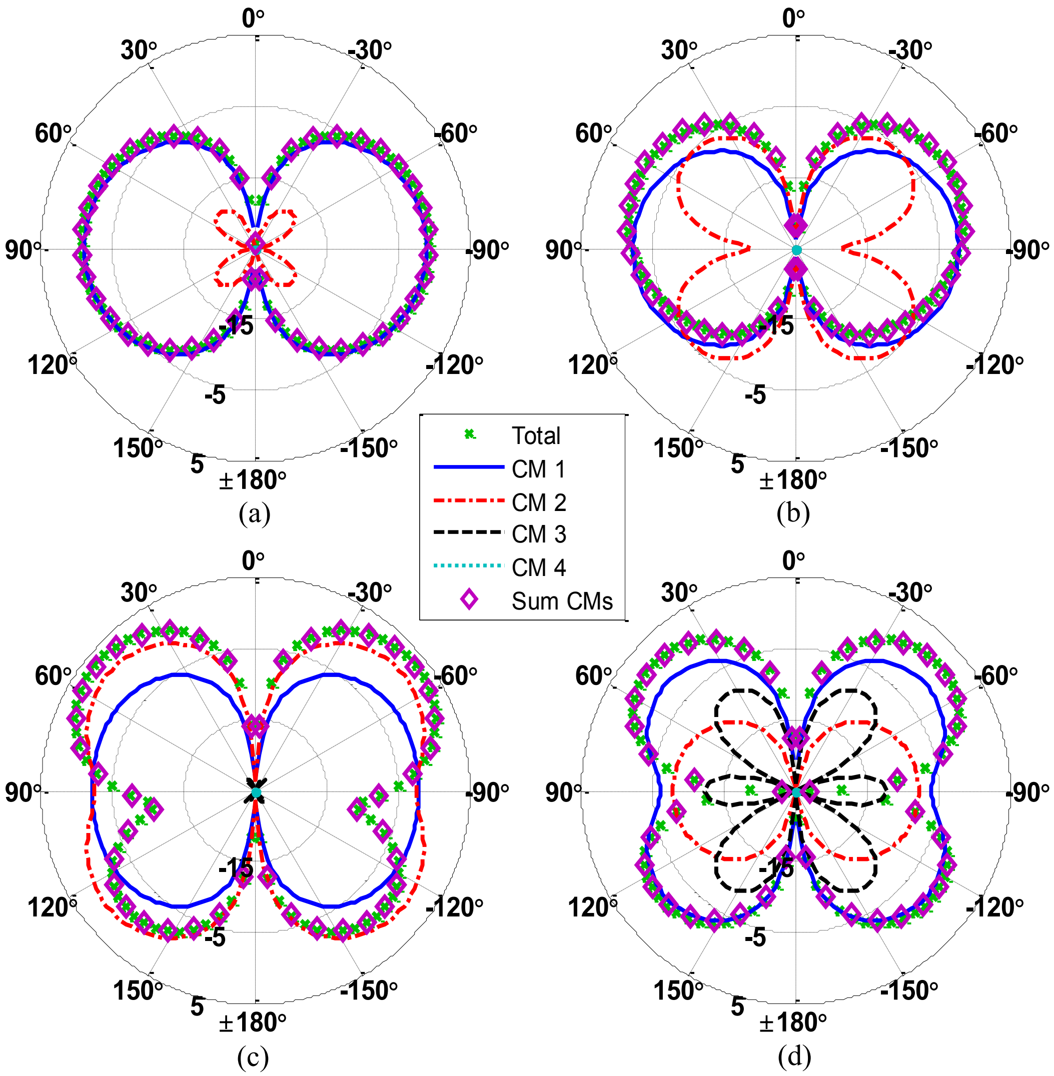

(a) (b) (c) (d)

Figure B.29: Monopole feed realized total gain (dBi) comparing total pattern, eigenpatterns and sum of eigenpatterns in the XZ-plane; (a) 250 MHz, (b) 350 MHz, (c) 450 MHz, (d) 550 MHz.

In Figure B.30, the total realized gain is shown in XY-plane. The pattern remains omnidirectional at all frequencies except 550 MHz. CM 1 and the total pattern have good agreement at 250 and 350 MHz. At 450 MHz both CM 1 and 2 have realized gains larger than the total gain. This occurs because they are destructively interfering reducing the gain. The destructive interference increases resulting in a null at 550 MHz.

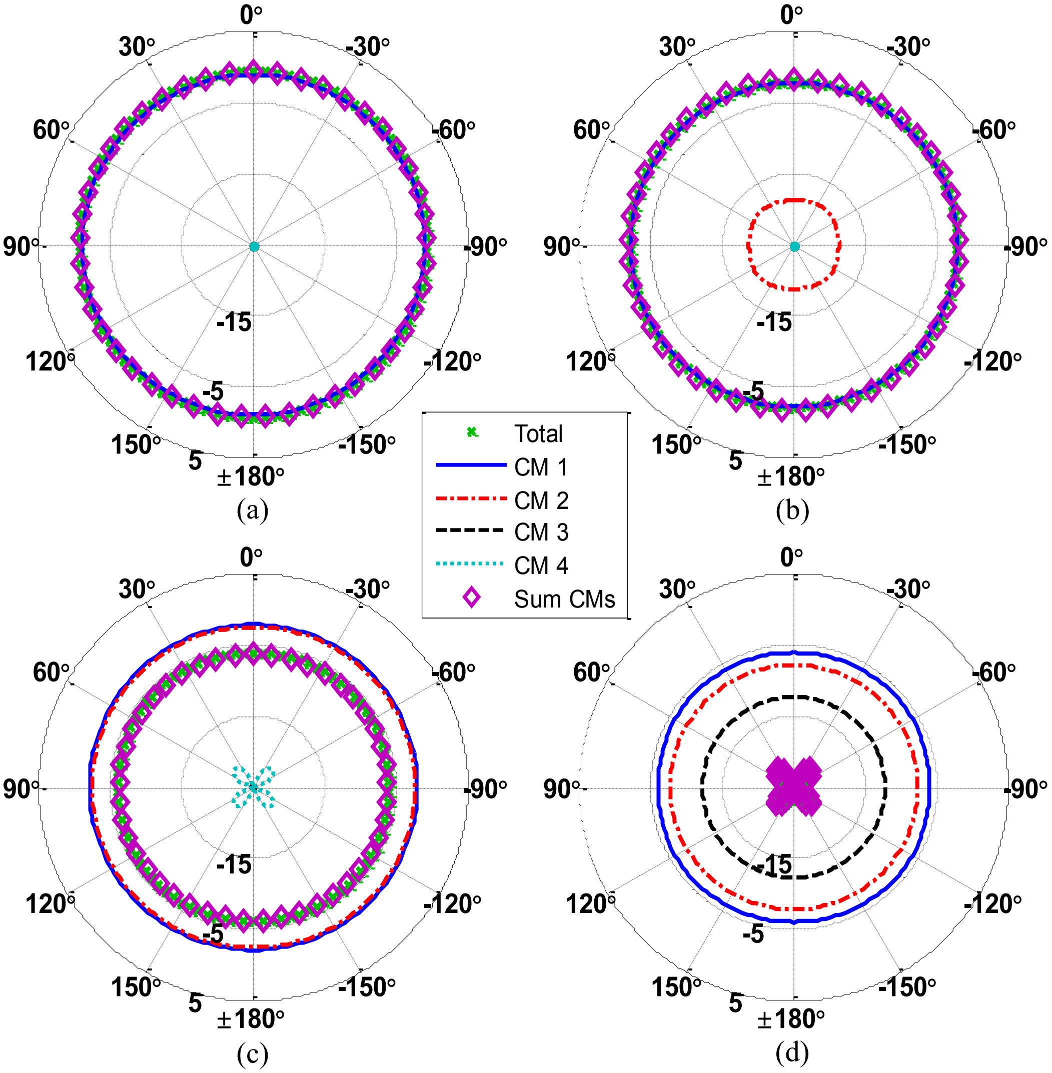

(a) (b) (c) (d)

Figure B.30: Monopole feed realized total gain (dBi) comparing total pattern, eigenpatterns and sum of eigenpatterns in the XY-plane; (a) 250 MHz, (b) 350 MHz, (c) 450 MHz, (d) 550 MHz.

B.3 Summary

Rectangular electrically small ground plane effects were investigated in this chapter. Both dipole and monopole excitations were investigated similar to the square case. Results were shown when $L_G = \lambda_M/8 \times W_G = \lambda_M/32$ and $L_G = \lambda_M/16 \times W_G = \lambda_M/32$. The dipole feed extends the pattern bandwidth of the antenna relative to the monopole feed. CM 1 for both rectangle cases closely resemble CM 1 of the square cases. A major difference relative to the square case is the loss of symmetry between the XZ- and YZ-planes, when $L_G = \lambda_M/8$. The asymmetry stems from CM 2. When $L_G = \lambda_M/16$ CM 2 eigenpattern returns to that of the square case, thus the symmetry is restored.

For both feed types (i.e. dipole and monopole) the conformal antennas radiate an omnidirectional radiation pattern below 350 MHz. At 550 MHz the dipole feed maintains an omnidirectional radiation pattern, whereas the monopole feed has a null at broadside. Similar to the square case, a mode switch occurs where CM 2 transitions into the omnidirectional mode at high frequencies. The result of the mode transformation is that the dipole feed location is preferred as it excites an omnidirectional pattern over the entire frequency band.

The resonant frequency of CM 1 without a plate was 267.5 MHz. Adding the rectangular plate increases the occupied volume of the antenna. When $L_G = \lambda_M/8 \times W_G = \lambda_M/32$ the resonant frequency of CM 1 is reduced by 38.32% to 165 MHz. Although W_G is severely restricted, the reduction in resonant frequency approaches the 43.93% reduction of the $\lambda_M/8$ square case. Similarly, the resonant frequency of CM 1 is reduced by 28.97% when $L_G = \lambda_M/16 \times W_G = \lambda_M/32$ which approaches the 35.51% reduction of the $\lambda_M/16$ square ground plane.

Appendix C Ground Plane Effects for Conformal UAV Antennas

With limited vertical height and fuselage width it is necessary to understand the design tradeoffs and limitations of conformal low frequency UAV antennas. Derivatives of dipole and monopole antennas are commonly used for VHF/UHF communication. Typically monopole antennas are preferred over dipoles due to their lower operation frequency for a fixed height; however, a monopole antenna requires a ground plane. The fuselage of the UAV is used for this purpose but is limited by the width typically resulting in a rectangular ground plane. Further, the monopole element is often not in the center of the ground plane. It is desirable for the ground plane radius to be larger than $\lambda/4$ at operation frequency. Small UAVs have very limited area to create a ground plane so the question becomes whether it is better to create a monopole with an electrically small ground plane or use the available height to create a dipole.

This research focuses on an asymmetrical conformal dipole and monopole antenna of the same vertical height and occupied volume. Both antennas will be designed using the tail section and fuselage plate of a Dakota UAV. To simplify the model, while maintaining the relevant physics, the fuselage will be modeled by a planar rectangular plate. At 50 MHz the length of a Dakota UAV is approximately $\lambda/3$ and vertical height of the tail is approximately $\lambda/13$. The effects on radiation pattern, bandwidth, feed location, quality factor (Q) and input impedance will be studied while changing the dimensions of the fuselage plate. Also the -20 dBi realized vertical gain point will be illustrated. Realized gain above -20 dBi is often the most challenging performance metric to meet because at VHF the UAV becomes electrically small. To achieve the best low frequency performance, monopole antennas are generally used because they can operate at frequencies twice as low as corresponding dipole antennas.

C.1 UAV Description

The Dakota UAV shown in Figure C.1(a) is under investigation in this research for the analysis of low frequency antenna performance. This geometry is a simplified version of a more accurate model but is sufficient for the present purposes. The UAV is divided into three regions. Region I represents the tail section to which the antenna element is conformal to. This region is commonly utilized for the design of conformal VHF/UHF antennas, because it is one of the few vertical locations on the UAV yielding a vertically polarized antenna. Region II represents the fuselage plate which is the main parameter under investigation. This region can be used to create a ground plane for monopole type antennas. Region III is the fuselage of the UAV which, in this paper, will be removed. The fuselage skin is made of a fiberglass/epoxy composite and will not be considered for simplicity. The Dakota UAV is simplified further to only include the tail section and fuselage plate (i.e. Region I and II), shown in Figure C.1(b-d).

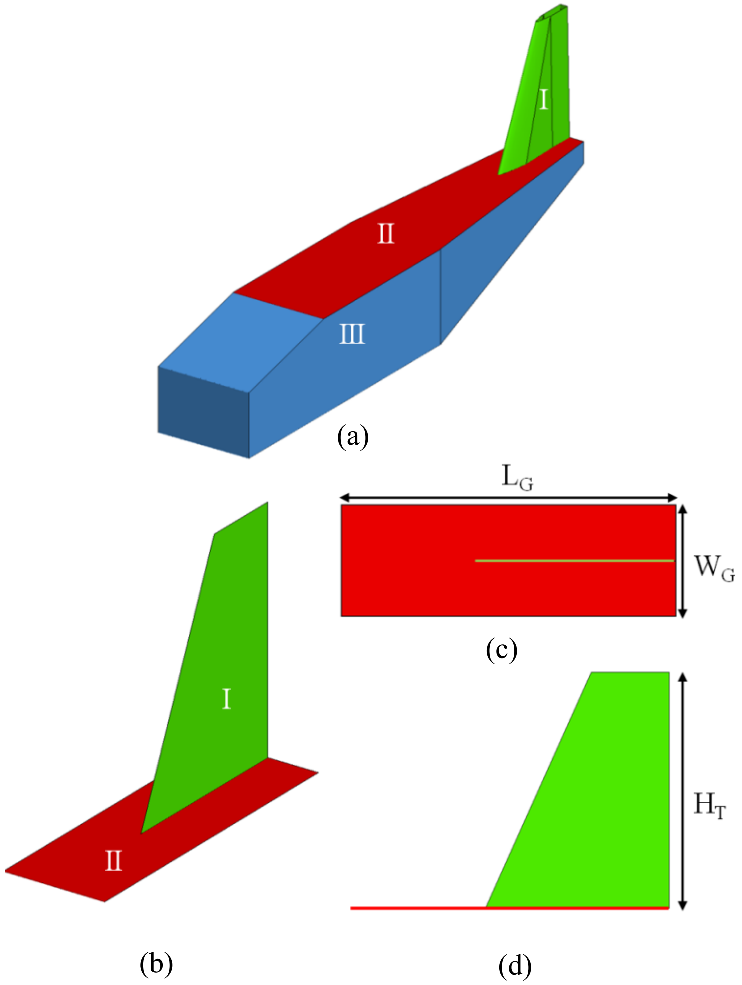

Figure C.1: Simplified dakota UAV model; (a) UAV sections: tail (Region I), fuselage plate (Region II), fuselage (Region III), (b) perspective view, (c) top view, (d) side view.

The parameters under investigation are the width (W_G) and length (L_G) of the fuselage plate, Region II. The vertical height of the Dakota UAV tail (H_T) is fixed at 0.454 m. The vertical height and occupied volume are the physical properties establishing the low frequency antenna performance [2]. Mainly the vertical height establishes the radiation resistance, while the occupied volume determines the antenna's bandwidth. At 50 MHz the electrical height of the Dakota UAV tail is approximately $\lambda/13$, thus the antenna is electrically small.

Two approaches to design an asymmetrical conformal UAV antenna will be taken. The first is to excite the tail as a dipole antenna. This involves creating a slot in the tail section to separate the arms as depicted in Figure C.2(a). The second approach is to excite the tail as a monopole. This involves creating a gap between the tail section and fuselage plate as shown in Figure C.2(b). In both cases the tail is modeled as a flat copper plate. For each antenna configuration, four fuselage plate cases will be investigated (also simulated as copper). The cases are listed in Table C.3.

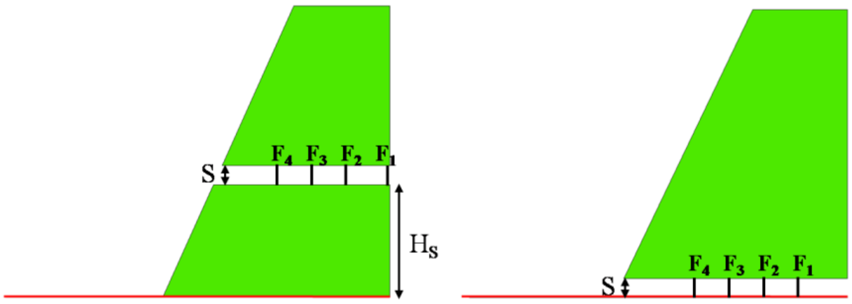

(a) (b)

Figure C.2: Antenna comparison with four feed locations; (a) dipole, (b) monopole.

Table C.3: Fuselage plate dimensions

	W_G (m)	L_G (m)
Case 1	0.1	0.4
Case 2	0.1	0.6
Case 3	0.2	0.4
Case 4	0.2	0.6

C.2 Reference Antennas

To start the analysis, reference dipole and monopole antennas will be used. The reference antennas give a baseline performance metric and illustrate the advantage of using the monopole for low frequency operation. Each antenna is modeled using four different cases. The antenna element is initially modeled as a wire. The element is then modeled as a flat plate while varying the plate width (P_W) using widths of 5, 10 and 15 cm shown in Figure C.3. A P_W of 15 cm is representative of the maximum available tail width before the tapered region of the tail begins. The height (H) of the element is fixed at 0.454 m. A finite square ground plane for the monopole antenna was created. The width of the ground plane (W_G) is λ/2 at the λ/4 monopole operation frequency of 165.2 MHz.

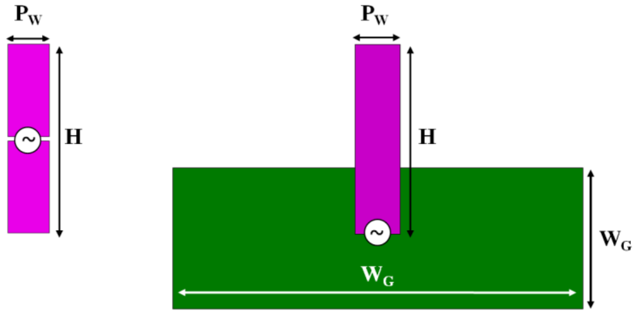

(a) (b)

Figure C.3: Reference antennas; (a) dipole, (b) monopole.

The realized vertical gain (dBi) vs. frequency for the reference antenna is shown in Figure C.4. For the wire case the gain peaks near the expected λ/2 and λ/4 (i.e. 330.4 and 165.2 MHz) operation frequencies for the dipole and monopole antennas, respectively. Both antennas are narrowband due to the limited volume they occupy. The elements are then simulated as a flat plate while varying the width P_W. As the width increases the realized gain increases and the low frequency performance is improved. The -20 dBi realized gain frequencies are shown in

Table C.4 and it is very clear the monopole has the low frequency performance advantage. For completeness, the $|S_{11}|$ (dB) is shown in Figure C.5. As expected, the impedance match is greatly improved when the width of the plate is increased.

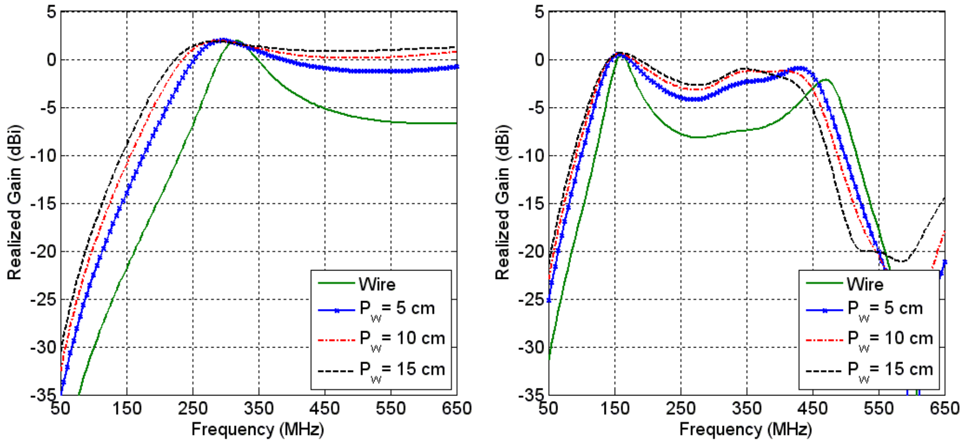

(a) (b)

Figure C.4: Reference antenna’s realized vertical gain (dBi); (a) dipole, (b) monopole.

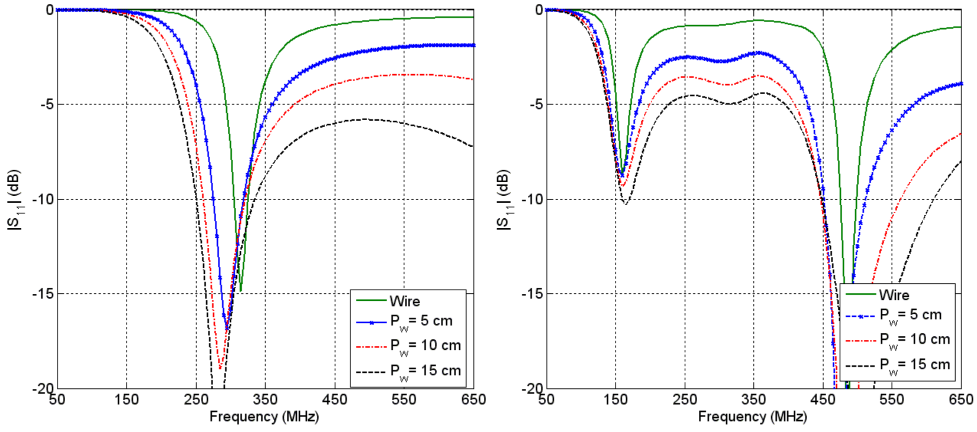

(a) (b)

Figure C.5: Reference antenna’s $|S_{11}|$ (dB); (a) dipole, (b) monopole.

Table C.4: Reference antennas’ lowest -20 dBi realized vertical gain and –3 dB $|S_{11}|$ frequencies (MHz)

	-20 dBi		-3 dB $\lvert S_{11}\rvert$	
Antenna Element	Dipole	Monopole	Dipole	Monopole
Wire	162.00	85.79	284.3	146.1
5 cm	113.20	64.81	242.2	134.1
10 cm	97.83	58.24	223.2	129.9
15 cm	88.15	53.92	210.0	127.5

C.3 Asymmetrical Conformal Dipole Antenna

The asymmetrical conformal dipole is created by making a slot in the tail section at a height H_S from the fuselage plate as shown in Figure C.2(a). Arm 1 is formed by the top part of the tail while arm 2 is formed by the lower part of the tail and the fuselage plate. The arm separation S is 3 mm. The H_S was chosen to be 0.175 m determined from a CM analysis. This analysis showed a dominant mode similar to the fundamental dipole mode and was omitted for brevity. Four feeding locations (F_1 - F_4) are considered for each case (see Figure C.2(a)). The $|S_{11}|$ (dB) of each case is shown in Figure C.6 referenced to 50 Ω. As expected, the feed location has a significant effect on input impedance. Feed location F_1 (green curve) has the largest mismatch loss for all cases. It is also important to note that changing the width of the fuselage plate has minimal effects on input impedance whereas changing the length has a significant impact. The -3 dB frequencies are listed in Table C.5.

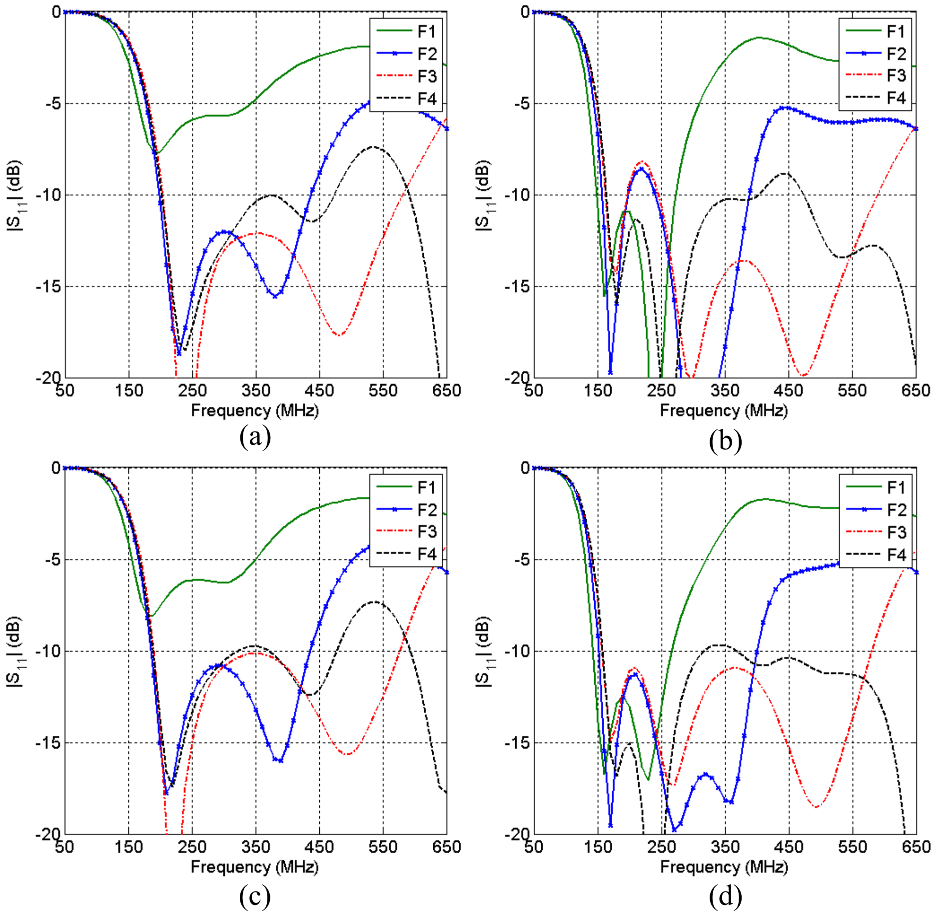

(a) (b) (c) (d)

Figure C.6: Dipole antenna feed comparison $|S_{11}|$ (dB); (a) case 1, (b) case 2, (c) case 3, (d) case 4.

Table C.5: Dipole antennas lowest -3 dB $|S_{11}|$ frequency (MHz)

	Case 1	Case 2	Case 3	Case 4
F1	151.2	127.9	142.5	122.3
F2	162.9	135.4	152.8	130.1
F3	166.8	139.1	156.0	132.4
F4	164.5	139.7	154.1	132.7

The realized vertical broadside gain (i.e. $\theta=90°$) (dBi) vs. frequency for each feed location is considered for all cases (Figure C.7-Figure C.10). Similar to the impact on input impedance, changing the width of the fuselage plate has negligible effects on radiation pattern. However, changing the length has noticeable effects. It is important to note that for all cases F_1 has the largest null in radiation pattern starting at 300 MHz while F_3, has the most uniform radiation pattern over a large frequency range. The performance is attributed to having the feed near the center of the dipole arms. Table C.6 list the frequency points in which the realized vertical gain reaches -20 dBi. The results show that increasing the size of the plate effectively loads the antenna, improving low frequency performance.

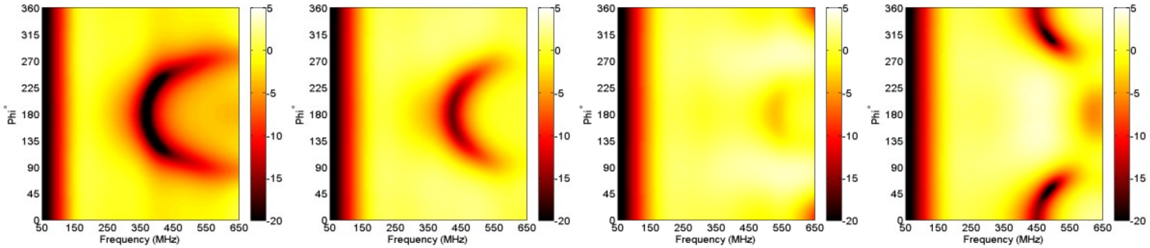

(a) (b) (c) (d)

Figure C.7: Dipole realized vertical gain (dBi) case 1; (a) F_1, (b) F_2, (c) F_3, (d) F_4.

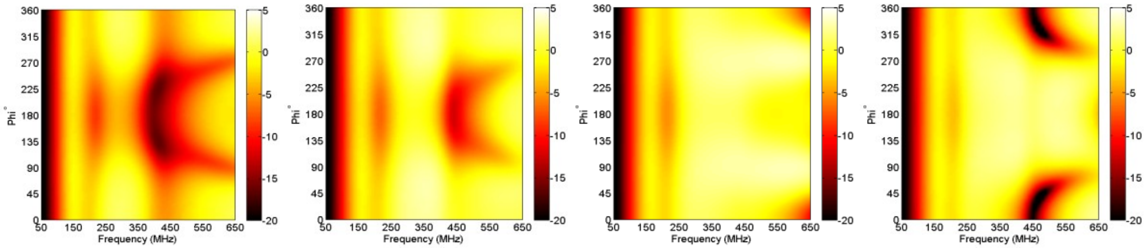

(a) (b) (c) (d)

Figure C.8: Dipole realized vertical gain (dBi) case 2; (a) F_1, (b) F_2, (c) F_3, (d) F_4.

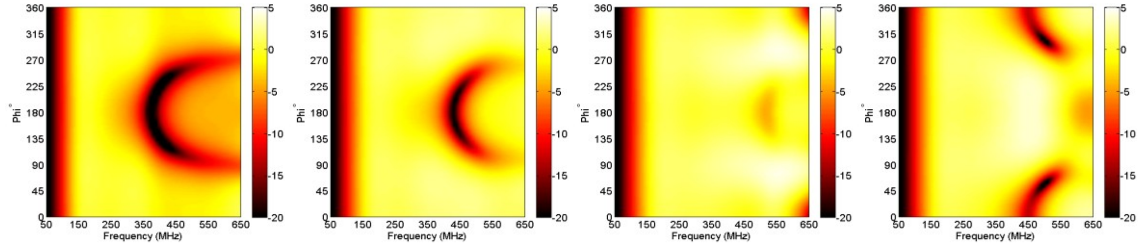

(a) (b) (c) (d)

Figure C.9: Dipole realized vertical gain (dBi) case 3; (a) F_1, (b) F_2, (c) F_3, (d) F_4.

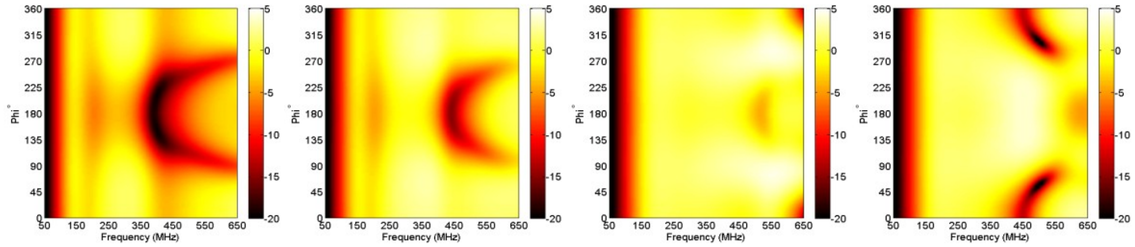

(a) (b) (c) (d)

Figure C.10: Dipole realized vertical gain (dBi) case 4; (a) F_1, (b) F_2, (c) F_3, (d) F_4.

Table C.6: Dipole antenna's; lowest -20 dBi realized vertical gain frequencies (MHz)

Feed	Case 1	Case 2	Case 3	Case 4
F1	67.38	63.34	63.56	60.11
F2	68.70	64.52	64.71	61.21
F3	69.00	64.82	64.97	61.48
F4	68.70	64.62	64.69	61.26

C.4 Conformal Monopole Antenna

The conformal monopole antenna is formed by removing the slot in the tail section and creating a gap S of 3 mm between the fuselage plate and tail section as shown in Figure C.2(b). In this case, the fuselage plate is used as a ground plane. The $|S_{11}|$ (dB) vs. frequency and -3 dB frequencies are shown in Figure C.11 and Table C.7, respectively, referenced to 50 Ω. The -3 dB $|S_{11}|$ frequency has increased by at least 42.6 MHz in cases 1 and 3 compared to the 15 cm reference monopole. The electrical dimensions of the fuselage plate at the monopole operation frequency of 165.2 MHz are $\lambda/18.16 \times \lambda/4.54$ and $\lambda/9.08 \times \lambda/4.54$ for case 1 and 3 respectively. Cases 2 and 4 frequencies are also increased but not as drastically.

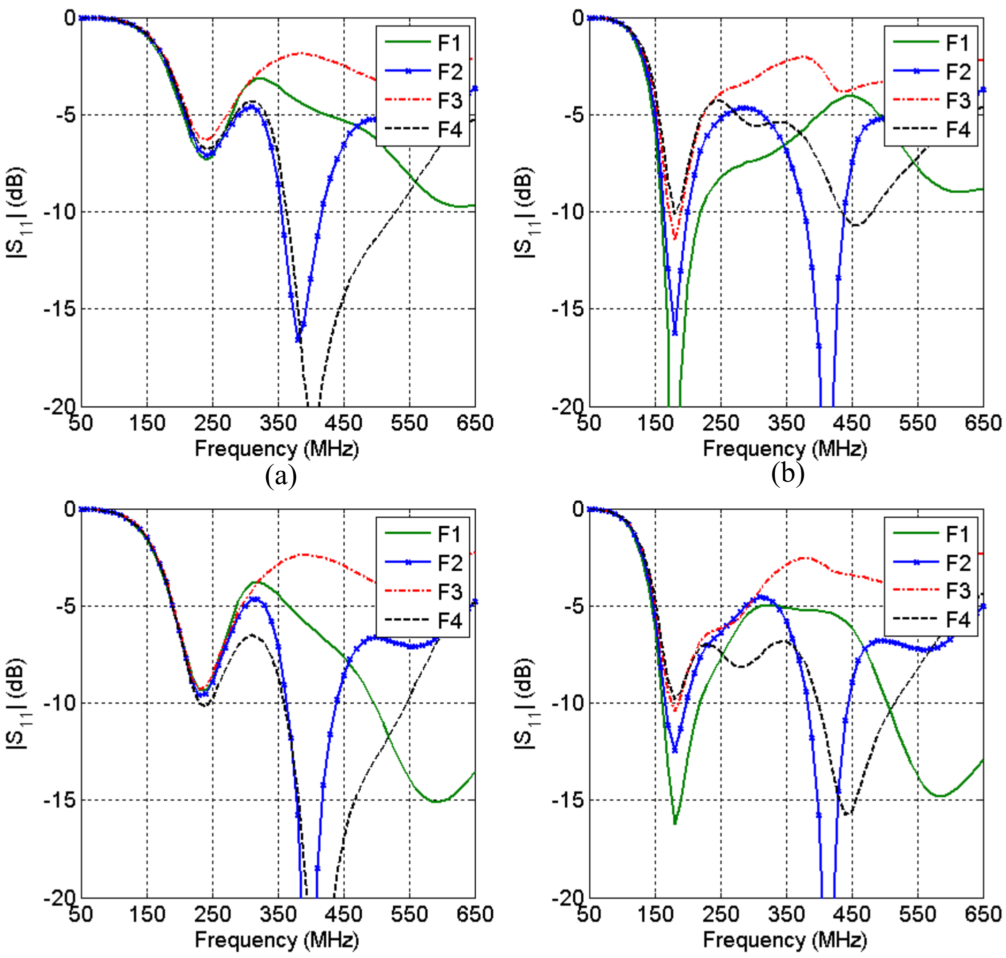

(a) (b) (c) (d)

Figure C.11: Monopole antenna feed comparison $|S_{11}|$ (dB); (a) case 1, (b) case 2, (c) case 3, (d) case 4.

Table C.7: Monopole antenna; lowest -3 dB $|S_{11}|$ frequency (MHz)

Feed	Case 1	Case 2	Case 3	Case 4
F1	184.4	136.5	170.1	133.5
F2	188.4	140.2	172.0	136.2
F3	191.0	143.1	172.8	138.5
F4	189.1	144.6	171.3	139.2

The realized vertical broadside gain (dBi) vs. frequency for each feed location is considered for all cases (Figure C.12-Figure C.15). Similar to the impact on input impedance, changing the width of the fuselage plate has negligible effects on radiation pattern, however changing the length has noticeable effects.

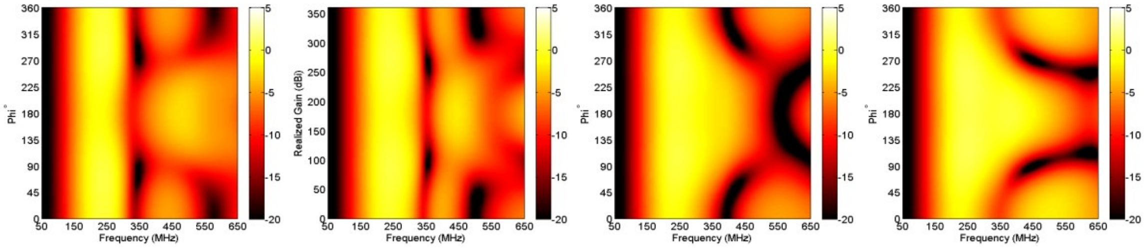

(a) (b) (c) (d)

Figure C.12: Monopole realized vertical gain (dBi) case 1; (a) F_1, (b) F_2, (c) F_3, (d) F_4.

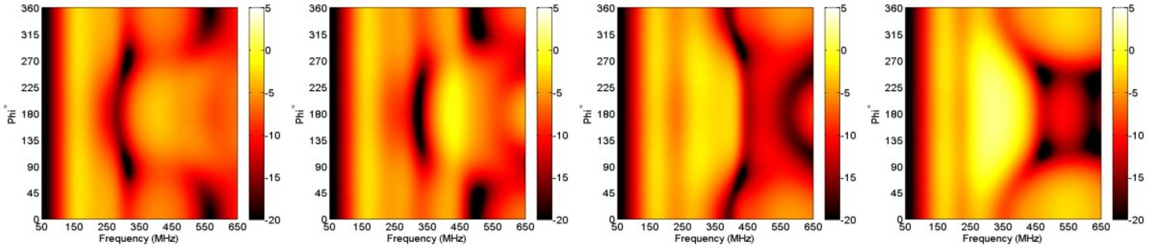

(a) (b) (c) (d)

Figure C.13: Monopole realized vertical gain (dBi) case 2; (a) F_1, (b) F_2, (c) F_3, (d) F_4.

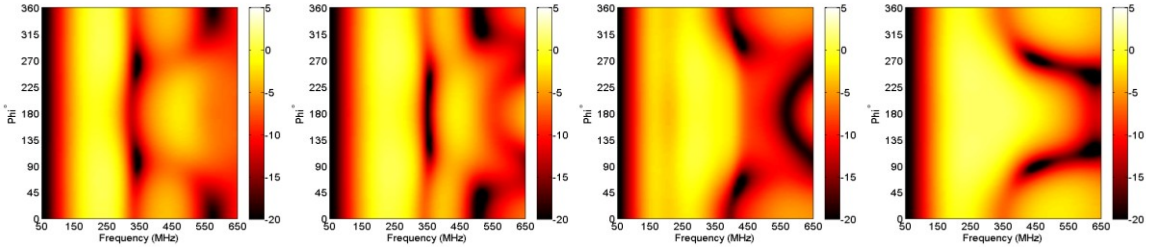

(a) (b) (c) (d)

Figure C.14: Monopole realized vertical gain (dBi) case 3; (a) F_1, (b) F_2, (c) F_3, (d) F_4.

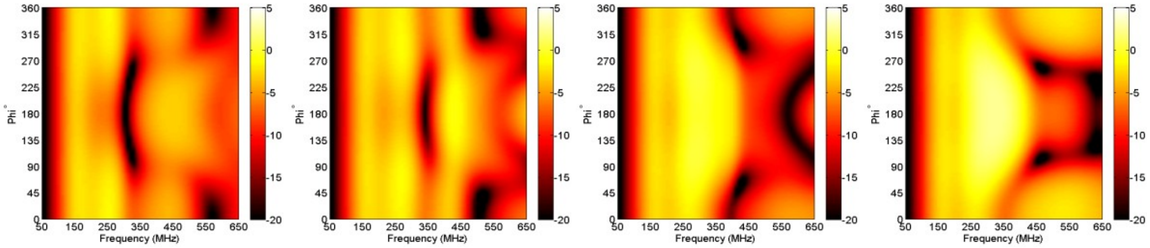

(a) (b) (c) (d)

Figure C.15: Monopole realized vertical gain (dBi) case 4; (a) F_1, (b) F_2, (c) F_3, (d) F_4.

Table C.8: Monopole antenna's; lowest -20 (dBi) realized vertical gain frequencies (MHz)

	Case 1	Case 2	Case 3	Case 4
F1	74.59	66.32	65.29	60.19
F2	75.22	66.87	65.72	60.66
F3	75.53	67.30	65.92	60.86
F4	75.24	67.17	65.67	60.67

C.5 Quality Factor Comparison

The Q is another important performance metric for antennas. The quality factor is inversely related to the bandwidth of the antenna. Similarly, the Q gives insight into the bandwidth of a matching network. When the antenna becomes electrically small the Q becomes very large and the radiation resistance becomes very small. A matching network can be used to improve the realized gain, but if the Q is very high the bandwidth of the matching network may be very limited. The Q for the reference antennas vs. frequency is shown in Figure C.16 and frequencies in which the Q is equal to 50 are shown in Table C.9. It is desirable to have a Q around 50 or less when creating a matching network. For Q>50, a matching network can still be used, however, the bandwidth will be limited.

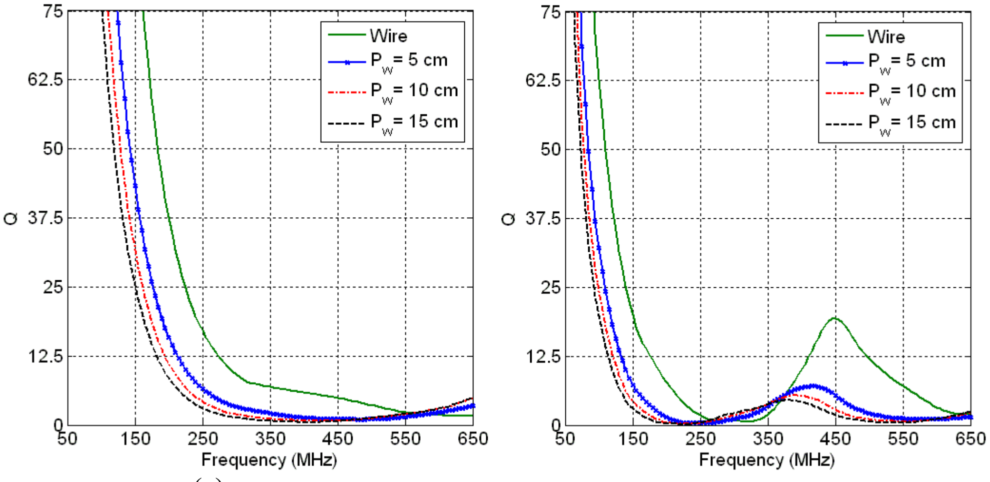

(a) (b)

Figure C.16: Quality factor comparison for reference antennas; (a) dipole, (b) monopole.

Table C.9: Frequencies (MHz) in which the reference antennas' quality factor is equal to 50

Antenna Element	Dipole	Monopole
Wire	184.1	109.7
5 cm	143	84.86
10 cm	128.8	77.81
15 cm	119.1	73.28

The Qs for asymmetrical dipole and monopole antennas are calculated for the optimum feed location and shown in Figure C.17. The optimum feed location for both antennas was F3. This location provides the best tradeoff between $|S_{11}|$ and uniform pattern vs. frequency. The Q=50 frequencies are shown in Table C.10. As expected as the size of the fuselage plate increases the Q decreases.

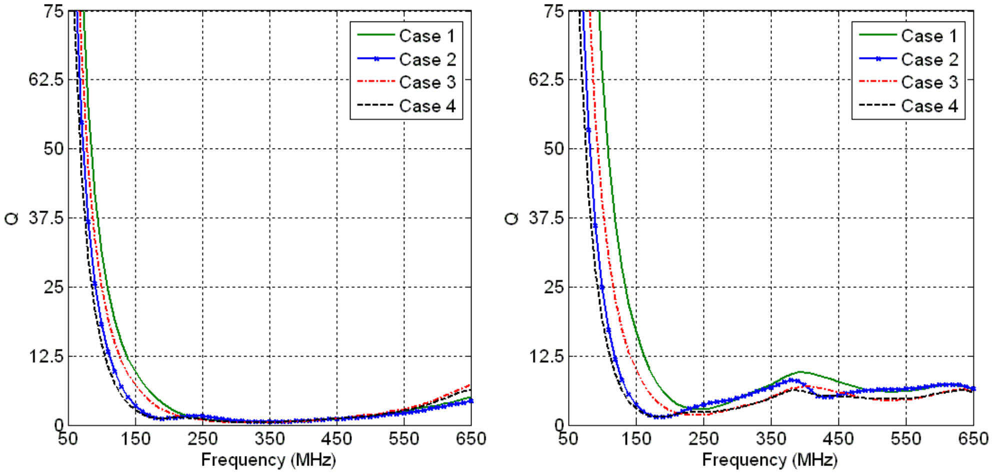

(a) (b)

Figure C.17: Quality factor comparison for asymmetrical antennas; (a) dipole, (b) monopole.

Table C.10: Frequencies (MHz) in which the asymmetrical antennas' quality factor is equal to 50

	Dipole	Monopole
Case 1	84.81	109.0
Case 2	72.68	93.65
Case 3	78.30	81.98
Case 4	68.16	75.99

C.6 Comparison of Dipole and Monopole Antennas

For both antennas the most noticeable effect on input impedance and radiation pattern occurs when the length of the fuselage plate was changed. Changing the width of the fuselage plate has negligible effects. Increasing the length of the fuselage plate lowered the operating frequency for both antennas. The monopole resonant frequency decreases to 165 MHz when the fuselage plate was increased to 0.6 m (i.e. case 2 and case 4). This results in the monopole operating near the expected λ/4 resonant frequency.

The feed location effect on pattern can be explained by the changes between the distance of the primary radiation point and secondary radiation points. The primary radiation point is directly related to feed location, however secondary radiation points exist at the junction between Region I and II. Secondary radiation points also exist at the ground plane ends. Depending on the electrical distance, the radiation from the secondary radiation points can either constructively or destructively interfere with the primary radiation point causing a non-uniform radiation pattern. For the asymmetrical dipole the electrical distance from F1 to the front intersection between Region I and II is near 180° at 380 MHz. This secondary radiation point will destructively interfere causing a null in the pattern as seen in Figure C.7(a) - Figure C.10(a). Similarly, the physical distance between F2 and the front intersection between Region I and II shrinks causing the destructive interference to occur at a higher frequency point with respect to F1.

The deterioration of the monopole performance can be attributed to the electrically small ground plane. Typically monopole ground planes are greater than λ/2 in diameter (circular ground plane), however due to the restrained width of the UAV fuselage plate the ground plane is electrically small degrading the performance. The bandwidth of the asymmetrical monopole antenna is acceptable, however with a rectangular electrically small ground plane the realized gain level decreases and the pattern is no longer uniform vs. azimuth. The reference monopole antennas realized vertical gain for ground plane widths of λ/2, λ/4 and λ/8 is shown in Figure C.18. When the ground plane shrinks with a fixed element size the operation frequency increases. The shift in operation frequency is shown in Figure C.19 and Table C.11.

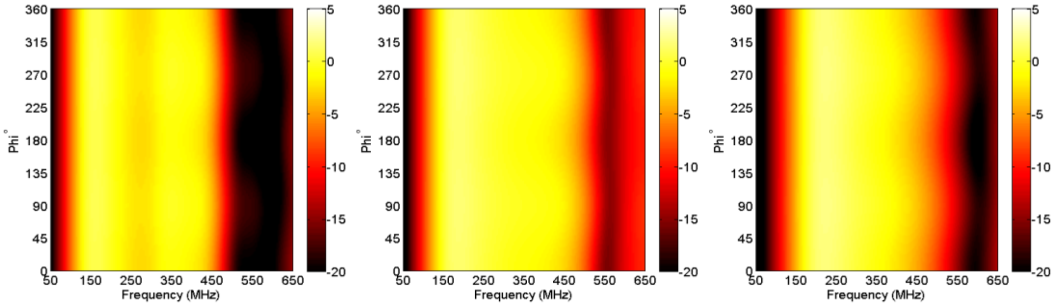

Figure C.18: Reference monopole square ground plane comparison realized vertical gain (dBi); (a) λ/2, (b) λ/4, (c) λ/8.

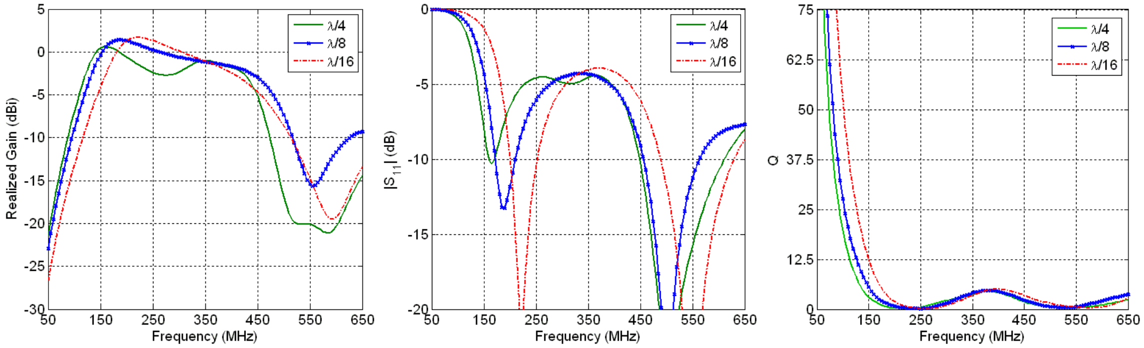

Figure C.19: Reference monopole square ground plane comparison; (a) realized vertical gain (dBi), (b) $|S_{11}|$ dB, (c) Q.

Table C.11: Reference monopole's -20 (dBi) realized vertical gain, –3 dB $|S_{11}|$ and Q=50 frequencies (MHz)

W_G	-20 dBi	-3 dB $\|S_{11}\|$	Q
λ/2	53.97	127.5	73.28
λ/4	58.49	141.5	81.04
λ/8	71.51	169.9	101.8

The quality factor for the asymmetric dipole was reduced when increasing the fuselage plate length. When adding the fuselage plate to the dipole arm, the occupied volume of the antenna is increased reducing the stored energy lowering the Q. For the monopole, since the ground plane size is reduced from the reference case the occupied volume is reduced increasing the stored energy and thus resulting in an increased Q. For VHF communication design applications, it is very important to choose the antenna with a lower Q to try to cover the 30-80 MHz frequency band since a matching network will be required to achieve an acceptable gain level.

C.7 Summary

An asymmetrical conformal dipole and monopole VHF/UHF UAV antenna were investigated in this research. The fuselage plate parameters and feed location were varied and the effects on input impedance, radiation pattern and Q were compared. Results show that changing the width of the fuselage plate has minimal effects on input impedance and radiation pattern. For both antennas, F3 (near center fed) provides the best low frequency performance combine with uniform radiation pattern among all cases. It was shown that the asymmetrical dipole has superior performance compared to the monopole antenna. Monopole antennas typically have better low frequency performance over dipole antennas, which was illustrated by the reference antennas performance, however due to the electrically small ground plane the monopole's performance was severely degraded. Results show that for the Dakota UAV, a conformal dipole antenna will provide better antenna performance for VHF/UHF applications. At low frequencies, the quality factor for the asymmetrical dipole was lower than the monopole, thus making it easier to design a matching network. Having a lower Q will increase the bandwidth of a matching network. These findings are believed to be general. If the UAV has an electrically small ground plane, the antenna performance will be better in terms of radiation pattern and input impedance if fed like a dipole.